Fatigue Behaviour of Aluminum Friction Stir Welds Under Highway Bridge Loading Conditions

by

Shi Hui Guo

A thesis

presented to the University of Waterloo

in fulfillment of the

thesis requirement for the degree of

Master of Applied Science

in

Civil Engineering

Waterloo, Ontario, Canada, 2018

AUTHOR'S DECLARATION

This thesis consists of material all of which I authored or co-authored: see Statement of Contributions included in the thesis. This is a true copy of the thesis, including any required final revisions, as accepted by my examiners.

I understand that my thesis may be made electronically available to the public.

Statement of Contributions

The main original contributions of this thesis include the following:

- Fatigue testing of structural friction stir welded (FSW) joints with various common defect types intentionally introduced to study their effect.

- Fatigue testing of FSW joints under variable amplitude (VA) loading conditions typical of highway bridge applications.

I am the author of this thesis. Technical supervision was provided by Professors Scott Walbridge and Adrian Gerlich. This included input on the test program design and specimen fabrication, testing protocols, and interpretation of the results. The fatigue tests were completed with technical support provided by Richard Morrison and Peter Volcic, with assistance from Rakesh Ranjan. Aspects of the metallurgical analysis of the test specimens were performed by Luqman Shah with my assistance, as noted in the thesis.

Abstract

Friction stir welding (FSW) is a solid state joining process performed by rotating a cylindrical tool with a short protrusion between the two metal pieces to be joined. The combination of frictional and deformation heating leads to the consolidation of the joint. This welding method is rapidly growing in popularity in many applications, particularly in aluminum alloys for transportation vehicle (rail cars, ships) and bridge applications. Across North America, over 150,000 bridges have been identified as "structurally deficient" or "functionally obsolete". Since FSW has the potential to have a positive influence on their durability and economics, the Aluminum Association of Canada (AAC) has identified the possibility of replacing promoting aluminum bridge decks as a means of replacing existing deficient concrete decks. However, currently available codes and guidelines for aluminum welded joints only address structures made with conventional welding methods. Therefore, bridge designers are lacking the necessary knowledge to use FSW joints in their designs. The main objective of this thesis is to present a fatigue testing study to support the development of improved "performance-based" code provisions for the quality control and fatigue design of FSW joints by examining the durability of FSW joints with prescribed flaws. In order to obtain the experimental results, various intentionally flawed aluminum FSW samples were fabricated for fatigue testing under constant amplitude (CA) and simulated in-service variable amplitude (VA) loading conditions. A statistical analysis of the results has been performed to assess the influence of the various defect types. It has also been shown how finite element (FE) analysis using the software ABAQUS can be used to assess the influence of the defects on the local stresses within the welded joints. Lastly, it is shown how the fatigue performance of the welds can be predicted using linear elastic fracture mechanics (LEFM). The results of this research will contribute to an improved understanding of the behaviour of imperfect FSW joints under fatigue loading conditions, which simulate in-service vehicular bridge VA loading. The main conclusions of this research include the following: 1) The worst fatigue lives were observed in the specimens with "kissing bond" defects at the weld root (on the order of approximately 1 mm in depth), 2) toe flash, undercut, and worm hole defects, as well as surface improvement by polishing were seen to have a much lower influence on fatigue performance, 3) a novel "lap joint" specimen simulating an extruded bridge deck joint was also observed to fail at the root at a nominal stress level lower than that of a properly-welded butt joint.

Acknowledgements

Table of Contents

List of Figures

List of Tables

Chapter 1
Introduction

1.1 General

Over the past decade, there has been an increased awareness of the poor condition of the existing highway bridges in North America. The National Research Council Canada has identified that over one third of Canada's 80,000 highway bridges are either "structurally deficient" or "functionally obsolete" with short remaining service lives. The maintenance cost to repair those deficient bridges will be considerable (Huijbregts, 2013).

The Aluminum Association of Canada (AAC) has identified aluminum as an alternative construction material for vehicular bridges with the potential to yield a reduction in life cycle and maintenance costs (Walbridge & de la Chevrotière, 2012). Aluminum alloys have much to offer for bridge applications, and continue to be used where its high strength-to-weight ratio, high corrosion resistance, and extrudability characteristics make aluminum an ideal choice. Although there is significant potential to use aluminum in bridge applications to help address the current infrastructure crisis, there is a lack of competence in working with aluminum due to limited fundamental knowledge and supporting applied research. Since aluminum is difficult to weld using conventional fusion welding methods, friction stir welding (see Figure 1.1) has been proposed as an alternative.

Figure 1.1 Friction stir welding process

Friction stir welding (FSW) is a solid state joining process performed by rotating a cylindrical tool with a short protrusion between the two metal pieces to be joined. The combination of frictional and deformation heating leads to the consolidation of the joint. This welding method is rapidly growing in popularity in many applications, particularly in aluminum alloys for transportation vehicle (rail cars, ships) and bridge applications. In an effort to promote using aluminum in civil infrastructure such as highway bridges, a new chapter in the CSA Canadian Highway Bridge Design Code (CAN/CSA S6-14) was developed and first published in 2011. It is expected that the 2019 version of this structural design code will – for the first time – acknowledge FSW as a viable welding process for vehicular bridge applications such as aluminum bridge decks.

Fatigue failures are often observed in structures subjected to repeated loading conditions, such as vehicular bridges. Many factors affecting a weld make it critical in a structure under fatigue loads, as virtually every welded joint contains discontinuities. Residual stresses and stress raisers such as the weld toe, the weld root, internal voids, and misalignment are major causes of weld failure in service. The calculated nominal stress range of the weld detail should be less than the fatigue resistance defined in fatigue design curves provided in standards. A full understanding of the application of FSW in aluminum structures can help increase the competence of bridge designers in using aluminum as a structural material and developing long-life structures with a reduction in maintenance costs.

1.2 Objective

The main objective of this thesis is to present a fatigue testing study to support the development of improved "performance-based" code provisions for the quality control and fatigue design of FSW joints by examining the effectiveness of FSW joints with inherent flaws. In order to obtain the experimental results, various intentionally flawed aluminum FSW samples were fabricated for fatigue testing under constant amplitude (CA) and simulated in-service variable amplitude (VA) loading conditions. Each of the investigated defected types was described using various destructive and non-destructive evaluation methods.

A statistical analysis of the results was performed to assess the influence of the various defect types. It is also shown how finite element (FE) analysis using the software ABAQUS can be used to assess the influence of the defects on the local stresses within the welded joints. Lastly, it is shown how the fatigue performance of the welds can be predicted using linear elastic fracture mechanics (LEFM). The results of this research will contribute to an improved understanding of the behaviour of imperfect FSW joints under fatigue loading conditions, which simulate in-service vehicular bridge VA loading. This thesis will present this research, along with key findings concerning the influence of defect quality on fatigue performance.

1.3 Scope

The experimental study presented in this thesis is limited to two plate thicknesses (9.1 mm and 9.5 mm), two aluminum alloys, and a finite set of weld defect types (kissing bond, toe flash, undercut, and wormhole). The fatigue tests have all been performed under tension only loading with either a CA loading history or a VA loading history corresponding to the support reaction of a short span bridge flexural element.

The subsequent analysis is limited to a statistical analysis of the stress-life data, a metallurgical analysis to assess the metallurgy and defect geometry for the various specimen types, a FE analysis to determine the significance of the local stress raisers (e.g. in the toe flash and lap joint specimens) using the FE analysis software ABAQUS, and a fatigue life prediction for the various defect types using a linear elastic fracture mechanics (LEFM) analysis.

Due to the limitation of fatigue testing frames and research budget, the experimental program was limited to small-scale specimens with an intended maximum of twelve specimens for each weld flaw type for aluminum alloy grades 6061 and 5083. The specimens were designed to accommodate the physical constraints of the available frames in the University of Waterloo Structural Testing Laboratory. Differences in the material properties in the distinct weld zones that result from the heat generated during the solid state joining process –

including the weld nugget zone, heat affected zone, the thermomechanical affected zone, and the parent material – were ignored in the ABAQUS modelling, as a simplification.

1.4 Thesis Outline

This thesis is organized as follows:

- Chapter 2 presents a literature review on the most recent research with regards to aluminum applications in bridges, past fatigue testing on aluminum FSW joints, and currently available codes and standards for aluminum weld design.

- Chapter 3 discusses the fatigue test program conducted for this research project, including the design of the specimen geometry, fabrication process, and quality control of each defect type. The metallurgical testing methods performed in conjunction with the fatigue testing are also described in this chapter.

- Chapter 4 presents and discusses the results of the fatigue testing program and the metallurgical analysis of the various specimen types.

- Chapter 5 presents the statistical analysis of the stress-life data obtained from the fatigue tests. It also presents the FE analyses used in order to establish elastic stress concentration factors, as well as the fracture mechanics analysis.

- Chapter 6 presents conclusions and recommendations based on this research.

Chapter 2

Literature Review

2.1 Aluminum Development

Aluminum is considered to be one of the newer metals discovered, as it was not discovered until the 19th century, and does not occur naturally in its elemental form. The Bayer process was invented to refine the abundant ore, Bauxite, to produce alumina, and the Hall-Héroult process was invented to enable the production of aluminum from alumina using electrolysis (Gitter, 2006). The production of aluminum using the Bayer and Hall-Heroult processes nowadays has enabled the rapid growth of aluminum applications.

2.1.1 Aluminum Properties

Aluminum is the second most abundant metallic element, comprising 8% by weight of the Earth's crust. Aluminum has been used as a suitable material for load bearing structures for over a century (Gitter, 2006). The main advantages of the material include:

i.   low density at 2.70 grams per cubic centimeter (g/cm^3)

ii.   corrosion resistance resulting from a 4 nanometer (nm) thin oxide film when exposed to air that protects the underlying aluminum from further oxidation; and

iii.   excellent recyclability without degrading in quality and quantity.

Aluminum is in solid form with a melting point of 660.3 degrees Celsius (^{o}C) at room temperature. The linear thermal expansion coefficient of aluminum is 23×10^{-6}/^{o}C, which is twice that of steel. Thermal dilatation (expansion or contraction) has to be taken into account with drastic ambient temperature changes in Canada when designing with multiple structural materials (Walbridge & De La Chevrotière, 2012). The elastic modulus of aluminum is 70 GPa, which is about one third the modulus of steel. The section geometry design depends on the elastic modulus, which governs the deflection of beams or bearing capacity of columns. If replacing a steel section with aluminum by keeping the same stiffness, thickening by a factor of 3 is not effective, since the relation of specific weight of the two materials is also approximately 3. The same stiffness of an aluminum section can be achieved by increasing all dimensions with the exception of width by a factor of 1.4 (Gitter, 2006). In this way, an

aluminum structure results with the same stiffness as steel structure and half of its weight.

Pure aluminum itself has a tensile strength of around 40 MPa and a proof strength of around 10 MPa. The strength of pure aluminum is relatively low for most applications in civil engineering (Gitter, 2006). Aluminum alloys, or mixtures combined with other suitable metals provide far improved mechanical properties compared with its high purity form.

2.1.2 Aluminum Alloys

In pure aluminum, plastic flow in the individual crystals occurs along specific slip planes, which provide the lowest resistance to internal shear stresses. The general mechanical strength of aluminum will be enhanced if the shear strength is improved (Gitter, 2006). The lattice imperfections due to foreign materials act as shear dowels, which can improve the shear strength. One suitable element for improve the strength of aluminum is magnesium. Aluminum-magnesium alloys are, in fact, the predominant choice for structural applications. Only a few elements are suitable as alloying elements in aluminum, including magnesium (Mg); silicon (Si); manganese (Mn); copper (Cu); and zinc (Zn). Two of the most common aluminum alloys in bridge applications are 6061 and 5083 (see Table 2.1).

Table 2.1 Composition of aluminum alloys

Element	6061	5083
Aluminum	85.85 - 98.56 %	92.4 - 95.6 %
Magnesium	0.8 - 1.2 %	4.0 - 4.9 %
Silicon	0.4 - 0.8 %	≤ 0.4 %
Iron	≤ 0.7 %	≤ 0.4 %
Copper	0.15 - 0.4 %	≤ 0.1 %
Zinc	≤ 0.25 %	≤ 0.25 %
Titanium	≤ 0.15 %	≤ 0.15 %
Manganese	≤ 0.15 %	0.4 - 1.0 %
Chromium	0.04 - 0.35 %	0.05 - 0.25 %
Others	0.05%	0.15%

The system of designation of the *Aluminum Association* is the most common, together with *European Aluminum Standards* which also follow a numerical nomenclature based on chemical composition. The numerical designation consists of a four-digit number for each aluminum alloy. The 5000 series aluminum alloys are called non-heat-treatable alloys. They gain their strength by alloying and work hardening. The 6000 series aluminum alloys are heat-treatable alloys, which gain their strength by alloying but make use of precipitation hardening as the main strengthening mechanism (Gitter, 2006).

Non-heat-treatable alloys such as 5083, can be further strengthened through various degrees of cold working or strain hardening. These different temper conditions have to be described in the designation to characterize the aluminum alloys accurately indicated in Table 2.2. The letter "H" followed by first number denotes the specific condition obtained from strain hardening, and second number indicates the degree of strain hardening. In the case of the 5083-H321 alloy, "-H321" denotes alloys that are strain hardened less than the amount required for a controlled "-H32" temper.

Table 2.2 Tempers used in work hardened products for non-heat-treatable alloys

Symbol	Description
O	Annealed, soft
H1	Strain hardened only
H2	Strain hardened and partially annealed
H3	Strain hardened and stabilized
Hx2	Quarter hard
H14	Half hard
H18	Full hard

Similar to non-heat-treatable alloys, heat-treatable alloys such as 6061 are produced in many tempers, as listed in Table 2.3. In order to get the highest strength, the material is kept for sufficient time at the correct solution heat temperature followed by quenching and then

aging. In the case of the aluminum 6061-T6 alloy, the "-T6" means solution heat-treated and then artificially aged. The suffixes may include additional numbers, such as "-T651", which would indicate the alloy was solution heat-treated, stress-relieved by stretching, and artificially aged to reduce the possibility distortion in machined parts.

Table 2.3 Tempers used in precipitation hardened products for heat-treatable alloys

Symbol	Description
T4	Solution heat-treated and then naturally aged to a substantially stable condition
T5	Cooled from an elevated temperature shaping and then artificially aged
T6	Solution heat-treated and then artificially aged
T64	Solution heat-treated and then artificially aged, but not fully so in order to improve formability
T7	Solution heat-treated and over-aged
Tx51 Tx510 Tx511	These suffixes stand for a controlled stretching to relief internal stresses coming from manufacturing

2.2 Aluminum in Bridge Applications

Aluminum applications in bridges were first motivated by the increase in price for steel from 1958 to 1963 during a period of construction of many bridges in the United States for grade separations providing controlled access on superhighways (Siwowski, 2006). Due to the increased volume of bridge construction projects, the availability of steel became limited, which caused increased steel process and long lead times to obtain steel in some cases (Das & Kaufman, 2007). The return of the steel supply following this period brought the structural application of aluminum to a halt, mainly due to the lack of codes and specifications for designers when considering aluminum as a construction material.

2.2.1 Design Considerations

Across North America, over 150,000 bridges have recently been identified as "structurally deficient" or "functionally obsolete" according to the data from the US Federal Highway Administration (Bridges & Structures, 2016). In order to improve these bridges, several factors must be evaluated for considering aluminum as a construction material, in particular for the application of deteriorated bridge deck replacement, repair and reconstruction of existing bridges, movable bridge construction, and pedestrian bridges.

Deicing salt has been commonly used in North America where snow or ice can be a seasonal roadway safety hazard. Sodium chloride ($NaCl_2$), also known as rock salt, is the most commonly used deicing product, following by calcium and magnesium chloride, which are all corrosive (Houska). Despite the associated environmental concerns, these products can deteriorate steel by gradually absorbing water to form a corrosive chloride solution when critical temperatures are reached. Corrosion induced by deicing salt is the most important factor responsible for the majority of structurally deficient bridges made of steel and concrete (Siwowski, 2006). Aluminum as an alternative construction material, can prevent corrosion by forming a thin, protective oxidize layer on the surface. As a result, aluminum bridges offer the potential for lower life-cycle costs and increased durability due to the excellent corrosion resistance, eliminating the need to apply a protective coating (i.e. paint), resulting in lower maintenance cost (Das & Kaufman, 2007). Aluminum bridges are especially favoured in marine environments, where the corrosion risk level is relatively high.

Aluminum alloys were used for the first time for rehabilitation of bridge decks in 1933 on Pittsburgh's Smithfield Stress Bridge because their light weight was needed to achieve a higher live-load carrying capacity (Das & Kaufman, 2007). One of the foremost advantages of aluminum alloys is its low density at 2.7 g/cm^3, which is one third of that of steel. Over the past decades, there was an obvious increase in traffic volume and truck sizes. Replacing the aged concrete steel bridge decks with extruded aluminum decks can significantly increase the live load carrying capacity with a reduction in the dead load (self-weight). The increase in live load capacity can be cost effective as the structure does not need to be redesigned or

reinforced. A reduction of the dead load to the foundation can eliminate the need to remediate the substructure during the rehabilitation of a structure. Despite the fact that aluminum weighs less than steel, the strength can be as high as mild steel, making the aluminum bridge deck more efficient than steel or concrete components. Reducing the weight of the structure while maintaining its strength, aluminum is more effective than steel and concrete due to its particularly high strength-to-weight ratio (Siwowski, 2006).

Another significant advantage of aluminum in structural applications is ease of fabrication. Complex aluminum extrusions can be fabricated easily and optimized for structural design and assembly. The complex extrusions can be prefabricated in large sections that can be shipped to site due to their light weight and installed quickly and more effectively. Especially for bridges, simple erection procedures with fewer components save construction time, which minimizes traffic delays (Siwowski, 2006). Extrusions can be designed in stiffer structural shapes, while avoiding excessive welding and bolting typical in build-up sections.

The light weight of aluminum structures not only offers benefits in service, but can also be critical during transportation and construction. The lighter aluminum structure simplifies the erection phase, as prefabricated components can be transported from the fabrication facility to the construction site with less fossil fuel consumption.

Despite all of the advantages of using aluminum in bridge applications, aluminum structures can have a severe loss in strength due to the high temperature of local melting during the welding process. This decrease in strength must be taken into account, which forms an important aspect of the verification of the design of structure. The fatigue strength of aluminum is about one third of that of steel, which implies that aluminum structures are more prone to fatigue failure. Another disadvantage of using aluminum as a construction material is the higher initial cost for aluminum components over concrete and steel components. Although the maintenance cost can be reduced over the lifetime of the bridge, the construction and maintenance costs are usually budgeted separately (Das & Kaufman, 2007). However, the existing Life Cycle Cost Analysis (LCCA) shows that aluminum replacement decks lead to a benefit over the lifetime of the bridge (Siwowski, 2006).

Since the education system focuses on concrete and steel as building blocks, most engineers are hesitated to use aluminum as a structural material due to a lack of knowledge and a lack of design rules in structural applications. The successful applications of aluminum bridges are reviewed in the next section.

2.2.2 Historical Review of Aluminum Bridge Structures

The first documented application of bridge deck rehabilitation using aluminum as a construction material was the *Smithfield Street Bridge* in Pittsburgh, Pennsylvania built in 1882. The replacement of the deck structure enabled the bridge to carry the new electrified trolley cars introduced at the time in the city of Pittsburgh (Das & Kaufman, 2007). The replacement of the existing heavy steel and wood deck of Smithfield Street Bridge with aluminum 2014-T6 and an asphalt wearing course allowed a 3.5x higher live load carrying capacity with a reduction of the bridge self-weight by 675 tons. The replaced deck served until 1967 before a more corrosion resistant aluminum 6061-T6 alloy with polyester and a sand wearing course was installed and remained in service until 1995 (Walbridge & De La Chevrotière, 2012). In the subsequent 50 years, there were approximately 100 aluminum vehicle and pedestrian bridges constructed (Siwowski, 2006).

The first highway bridge constructed entirely using aluminum was the *Arvida Bridge* over the Saguenay River in Arvida, Quebec, Canada in 1950. The main span of the bridge is a riveted arch structure 88.4 m long and 14.5 m high, with multiple approach spans 6.1 m long on each end. The width is 9.75 m with a total length of 153 m over the span of Saguenay River in Quebec (Siwowski, 2006). All the structural supports are made of aluminum. The aluminum grid superstructure consists of longitudinal stringers and cross beams, supporting a reinforced concrete deck. The whole structure was made of 2014-T6 aluminum readily available at the time of construction. It weighs approximately 150 tons (Siwowski, 2006).

From 1958 to 1963, aluminum started being used as a construction material in bridges in the US. The first two of these aluminum bridges used a relatively conventional design of built-up plate girders. The *Clive Road Bridge*, located in Des Moines, Iowa, consisted of a four-span

structure supporting two lanes of traffic on 86th Street over I-80. The superstructure was constructed of welded 5083-H113 aluminum plate girders with 5183 filler wires supporting a concrete deck (Das & Kaufman, 2007). The 5000 series aluminum alloys were comparatively new and featured higher strength, weldability, and corrosion durability than the 2000 series alloys. The bridge remained in service until 1993, when a new design of the intersection was introduced so that a bridge was no longer required. Tensile and fatigue testing was conducted on the removed aluminum bridge girder components. The test results indicated that the aluminum components had a similar performance to when it was first erected after 40 years in service (Das & Kaufman, 2007). The second bridge was constructed in 1960. It was a twin structure, consisting of two lanes on each supporting structure on the I-495 in Jericho Turnpike, New York. The superstructure was constructed of 6061-T6 plates with 2117-T4 riveted connections supporting a concrete deck (Das & Kaufman, 2007). The bridge was replaced in 1992 when the intersection was re-designed.

The last four aluminum bridges constructed during the period adopted the "Fairchild Design", which consisted of rolled plates and extruded angles with unique rivets forming stiffened triangular box beam girders adopting the aircraft design concept at the time (Das & Kaufman, 2007). The cross-section of the "Fairchild Design", illustrated in Figure 2.1, is a series of triangular box beams with common upper or lower flanges, plus end frames. To validate the effectiveness of this structure, a full-scale 50-foot long "Fairchild Bridge" with a composite concrete deck was designed, fabricated, and tested by the Fritz Engineering Laboratory at Lehigh University. This type of design resulted a very stiff semi-monocoque structure, in which the skin absorbs all or most of the stresses to which the spans are subjected. The result confirmed that the dead load could be significantly reduced, allowing a lighter substructure with a reduction in cost for transportation and erection.
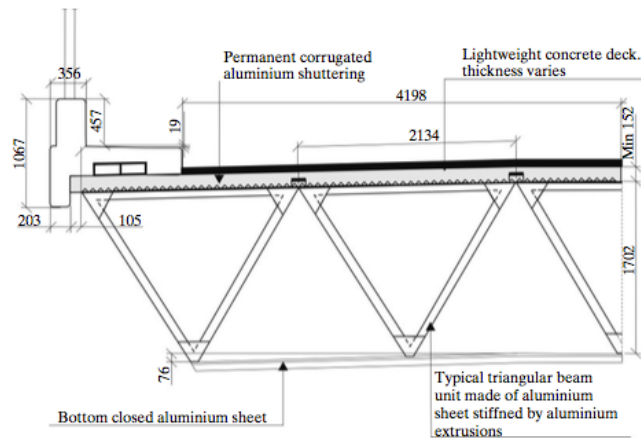
Figure 2.1 Fairchild bridge system (Das & Kaufman, 2007)

The first of the four "Fairchild Bridges" was erected in 1961 in Petersburg, Virginia, as a single-span, two-lane bridge with concrete deck on Route 36 over the Appomattox River. The superstructure was constructed using 2.5 mm 6061-T6 aluminum sheet. The second bridge, *Sykesville Bypass Bridge* using the "Fairchild Bridge" design was constructed on Maryland Route 32 over the Patapsco River with a three-span structure carrying two lanes of traffic in Sykesville, Maryland. The bypass bridge was replaced in 2004 primarily because of galvanic corrosion due to a failure to isolate the aluminum components from the steel bearings, and an inadequate internal drainage system for the hollow sections. The final two "Fairchild Bridge" designs were constructed in Amityville, New York, where four-span structures carried three lanes of traffic on Route 110 over the Sunrise Highway.

2.2.3 Current Aluminum Bridge Applications

Most bridges currently in service have been designed to support freight loads of only one-half of the load presently considered in the design of modern bridges (Gagnon, Gaudreault, & Overton, 2008). There is an estimated need for $140 billion US dollars to be spent to upgrade the 60,000 existing US bridges – around 25% of which have been deemed to be either structurally deficient or functionally obsolete. In 2007, the total value of the bridges and roads in Canada was estimated to be $23.9 billion and $170.1 billion respectively (Gagnon, Gaudreault, & Overton, 2008).

In the mid-90s in the United States, the Alumadeck aluminum bridge deck shown in Figure 2.2 was developed (Siwowski, 2006). The first deck of this kind was installed on the *Corbin Bridge* in 1996. The second bridge, after a comprehensive study, was installed to replace a functionally obsolete four-lane bridge over Little Buffalo Creek in Mecklenburg County, Virginia. Due to the lightweight characteristic of aluminum, the deck system was assembled on-site with several separate prefabricated deck panels. The prefabricated deck panels were achieved by welding individual extrusions consisted of a hollow two-voided extrusion 0.305 m wide and 0.203 m high, together at the top and bottom flanges to the designed dimensions. The deck was oriented with the extrusion aligned parallel to the bridge girders providing a stiff deck system. A 0.05 m haunch was constructed on the girders' top flanges to achieve composite action and prevent galvanic actions between the aluminum deck and steel girders. Magnesium phosphate grout was injected into the full length of the extrusion above each girder connecting the deck and shear studs (Siwowski, 2006).
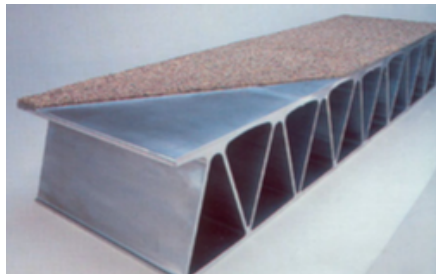
Figure 2.2 Alumadeck bridge deck

There are a great number of aluminum alloys to be selected for aluminum bridge or bridge deck construction, but the most highly recommended and used due to their superior combination of strength, corrosion resistance, and ease of fabrication are 5000 series and 6000 series extruded shapes (Walbridge & De La Chevrotière, 2012).

The "Fairchild Bridge" aluminum bridge design concept would likely not be considered in the current day. The complex buildup of sheets and extrusion components with riveted construction is labour intensive, and thus expensive compared with other girder designs. Current design practice involves the use of structural aluminum decks in combination with

14

steel or reinforced concrete girders (Das & Kaufman, 2007). Much of the recent effort to introduce aluminum in vehicular bridge construction has focused on the development of deck replacement products. The main motivation is to carry modern truck loads by increasing the capacity of deteriorated aged bridges with lighter aluminum structures.

Three most commonly used aluminum bridge deck systems are (see also Figure 2.3):

- the Alcoa Bridge Deck System developed in the mid-60s in the United States,
- the Alumadeck system developed by the Reynolds Metals Company, and
- the Svensson deck developed by L. Svensson in Sweden.

Arrien et al. (1995) and Roy et al. (1999) have compared these bridge deck systems in detail. The Alcoa and Alumadeck bridge decks are more sensitive to fatigue than other bridge deck systems in Figure 2.3 due to the extensive fusion welding practices. A more effective joining method – friction stir welding – was introduced in the 1990s for aluminum bridge applications.

a) Alcoa bridge deck system   b) Alumadeck system

c) Svensson bridge deck system
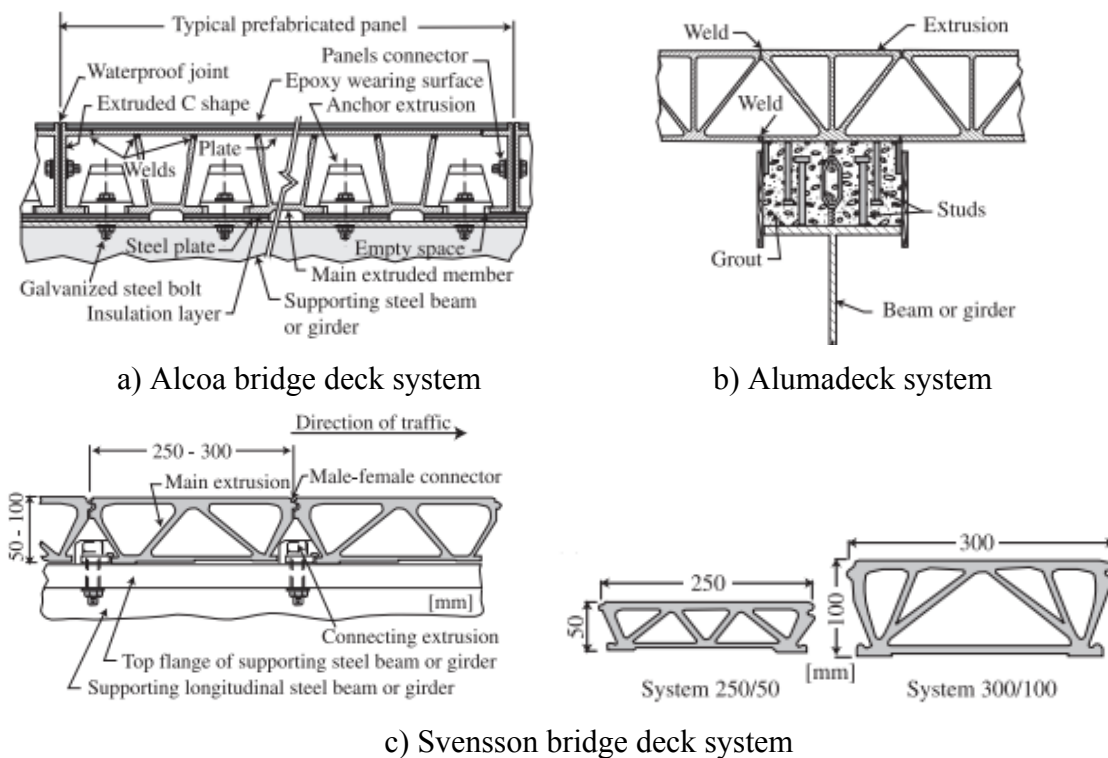
Figure 2.3 Aluminum bridge deck systems (Arrien, Bastien, & Beaulieu, 2001)

2.3 Fatigue of Friction Stir Welded Aluminum Structures

The long-term performance of aluminum structures is often controlled by the fatigue behaviour of the welds, because the welds are highly susceptible to damage under repeated loads. A structural component subjected to repetitive stresses will fail at a stress much lower than the load required to fail it in a single application. Despite the fact that welded aluminum structures were being built, a comprehensive fatigue design specification for aluminum did not exist until 1986 in the United States, where only experimental results for small specimens under constant amplitude loading were available (Menzemer, 1992). It is evident, even today, that the existing codes and standards for the fatigue assessment of aluminum alloy structures, especially those made with friction stir welded (FSW), need to be further expanded with supporting experimental data. Based on the currently available testing data and making assumptions concerning the FSW joint fatigue performance, guidance on welding, quality control, and the design of welded joints, along with qualification of welding operators and procedures are outlined by the North America and Europe code committees.

2.3.1 Introduction to Fatigue

There are four phases during the fatigue loading of a structural component, including crack initiation, stable crack growth, rapid crack propagation, and final rupture.

The location of the initiation of a crack can be the result of a local sudden geometry change, initial defects, material softening in the heat-affected zone, tensile residual stresses, and the mechanical properties of the base metal. High stress concentrations result from local geometry changes in the vicinity of welds, abrupt changes in cross section, flaws in the material, or surface scratches caused by handling the material. These stress concentrations lead to a reduction in the fatigue resistance at the weld. In practice, higher stress concentrations are observed with more intensive changes in geometry, which in turn leads to lower fatigue strengths. The various defects during the welding process can cause the structural components to fail at a faster rate under cyclic loading than they would otherwise. The heat generated during the welding process in aluminum components can reduce the

material strength in the heat affected zone by removing the effects of cold-working (Coughlin & Walbridge, 2012). Tensile residual stresses are generated due to the differential cooling in the material away from the weld. Aluminum structures are particularly prone to fatigue failure modes due to their lower absolute fatigue strength in comparison with steel.

Fatigue problems can be categorized as involving either low or high cycle fatigue. During low cycle fatigue, the stresses are usually high enough for plastic deformation to occur. The employed design approach for low cycle fatigue is the strain-life approach for predicting the number of cycles until crack initiation. On the contrary, high cycle fatigue results when the stresses are low with only elastic deformations occurring. The crack propagation life is estimated by the fracture mechanics method under high cycle fatigue. This study will focus on high cycle fatigue, with predictions made using a fracture mechanics model.

A material's performance is commonly characterized by Wohler's stress-life (S-N) curves, which is a graph of the magnitude of cyclical stress (ΔS) against the logarithmic scale of the number of repeated cycles of loading (N) that a material will undergo before it fails.

2.3.2 Friction Stir Weld Process

Friction stir welding (FSW) is a solid-state joining process that involves rotating a cylindrical tool with a short protrusion between aluminum plates or other low melting point alloys (see Figure 2.4). It was developed by TWI in the early 1990s. The plates to be joined are clamped with a sturdy fixture to the backing plate with an anvil piece of hardened steel underneath the path of the FSW tool, counteracting the vertical and horizontal force arising during welding. The combination of frictional and deformation heating with high temperature (still below the melting temperature) around the immersed rotating probe, and at the interface between the shoulder of tool and the plates leads to the consolidation of the two joining metal sheets as the tool traverses along the joint line (Svensson, Karlsson, Larsson, Fazzini, & Karlsson, 2000). The shear stress within the stir zone drops rapidly as the temperature increases. Therefore, the plasticized material flows from the leading to trailing side of the tool in a counter-clockwise motion (Thomas, Johnson, & Wiesner, 2003).
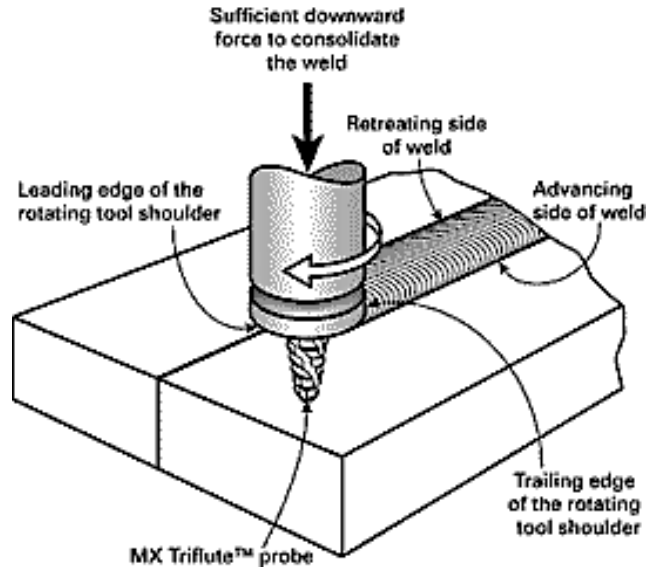
Figure 2.4 Principles of friction stir welding (Thomas, Johnson, & Wiesner, 2003)

2.3.2.1 Advantages and Disadvantages of Friction Stir Welding

FSW has multiple advantages over the conventional fusion welding methods:

- temperatures generated from the FSW process are below the melting point, which allows thin or soft plates to be welded;
- thermal distortion is reduced, along with residual stresses;
- the stirring of the tool minimizes the risk of having excessive local amounts of inclusions, resulting in a homogenous and void-free weld;
- the process is environmentally friendly due to the lack of need for a consumable electrode – a pin made of hardened steel can weld over 1 km of aluminum;
- improved safety due to the absence of toxic fumes or spatter of molten material;
- it can be performed on milling machines requiring low setup cost and training;
- the weld appearance of FSW joints is relatively smooth, which reduces the need for expensive machining afterwards;
- excellent mechanical properties result, as proven by fatigue, tensile and bend tests;
- it is tolerant to imperfect weld preparation – a thin oxide layer can be accepted.

18

FSW also has a few disadvantages compared with conventional fusion welding:

- a keyhole impression when the tool is removed at the end of weld;
- large horizontal and downward forces are required with heavy-duty clamping necessary to hold the plates in place;
- limited flexibility in comparison with manual/arc processes (non-linear welding);
- design of the FSW machine fixture and backing plate is of utmost importance since the forces exerted by the tool are large;
- welding speeds are moderately slower than those of some fusion welding processes;
- repair of welds in the field is generally not possible.

FSW is particularly well suited for aluminum alloys as they are often difficult to weld using fusion welding without hot cracking, porosity, or distortion occurring (Zhou, Yang, & Luan, 2005). An important source of information on the subject of FSW is the currently evolving document ISO 25239 "Friction Stir Welding – Aluminium" (ISO, 2011). This document handles issues of specification and qualification of welding procedures, qualification of welding operator, fabrication, quality and inspection requirements, and design of welds. However, the developing document lacks guidelines on fatigue performance of the welded joints.

2.3.2.2 Microstructure of Friction Stir Welds

The general microstructure of the FSW zone and the effect of welding on the fine scale precipitation in aluminum alloys are discussed in this section. The microstructure in a cross-section of a FSW joint is comprised of four characteristic regions. These regions are labelled Zones A, B, C, and D in Figure 2.5. The can be described as follows:
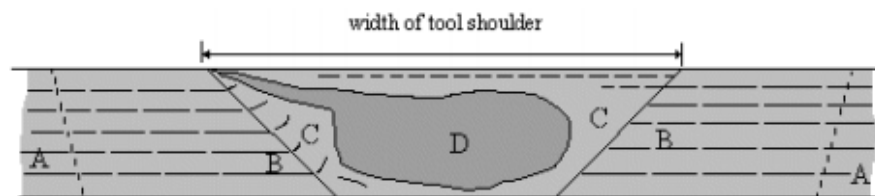
Figure 2.5 Cross section of friction stir weld zones (Mishra & Mahoney, 2007)

i.   Zone A is the parent material, which is not affected by the heat or mechanical deformation in the FSW process. The grains are elongated as a result of the rolling operation during the plate fabrication phase.

ii.   Zone B is the "heat affected zone" (HAZ), which is only affected by heat. The material has experienced a thermal cycle, which modifies the microstructure and mechanical properties without plastic deformation. There is no apparent differences with the parent material in this region under optical microscopy. However, the hardness in Zone B is lower compared to the parent material indicating that heat generated from the welding process caused the material to over age.

iii.   Zone C is the "thermomechanically affected zone" (TMAZ), which can be distinguished with an inverted trapezoidal shape as a distinct boundary between HAZ and TMAZ. In the TMAZ, the joint effect of high temperature and large strains causes the deformation of the grain structure without recrystallization.

iv.   Zone D with a characteristic 'onion ring' structure also refers as the "nugget zone" (NZ), which usually has a fine grain size as a result of the full dynamic recrystallization process under the high levels of plastic strain induced in the weld. The nugget has an asymmetric shape caused by material being preferentially sheared from one side of the tool and drawn into the centre.

FSW joints are not symmetric about the weld centreline due to the tool rotation: the side of the weld on which the rotational velocity of the tool has the same direction as the welding velocity is designated as the advancing side (AS) of the weld; the side of the weld on which the two velocities are in opposite directions is the retreating side (RS) of the weld. The soft material is mashed by the leading face of the pin profile and transported to the trailing face of the pin where it consolidates and cools to produce a high integrity weld (Salerno, 2007). Due to the different residual stresses and strains at each side, it is important to distinguish between the advancing side and retreating side (James, Hattingh, & Bradley, 2003).

Depending on the aluminium alloy types and selected welding procedures, a variety of microstructure grain sizes in FSW zones are presented with a typical value of less than 10

microns (μm) (Itharaju, 2004). For instance, 2 – 4μm diameter equiaxed grains are observed for 7075 – T6 alloy, while 10 μm grain diameters are reported in the weld zone of 6061 – T6, in contrast with an average grain size of 100 μm in the base metals.

The strength of the HAZ is typically weaker than the strength of the NZ. In the case of the annealed material, tensile tests usually fail in the unaffected parent material away from the welding zones. The welded properties of fully hardened (cold worked or heat treated) alloys can be further improved by controlling the thermal cycles, in particular by reducing the annealing and over aging effects in the TMAZ, where the lowest hardness and strength are reported after welding. Heat treatment after welding can improve the optimum strength of the material, although it is not a practical solution for many applications.

2.3.2.3 Friction Stir Weld Welding Parameters

FSW defects are relatively difficult and expensive to detect, especially internal defects, because the defects can occur in any orientation and form (James, Hattingh, & Bradley, 2003). The relative difficulty of detecting defects in FSW joints makes it imperative to fully understand the relation between the welding parameters and quality of welds. A number of parameters to be determined in a controlled environment when performing FSW are tool type, probe angle, tool plunge depth, travel speed, rotational speed, and clamping force:

i.   Tool Type: The tool bit shape and material affect the heating temperature, plastic flow, and forging pattern, which makes welding tool design critical in FSW. Optimizing tool geometry shape to obtain more efficient stirring improves mixing of the oxide layer and yields a higher welding speed (ESAB, 2017). Fujii et al. (2006) investigated the effects of three different tool geometric designs, including: a column without threads, a column with threads, and a triangular prism shape, on the mechanical properties and microstructures of 5 mm thick aluminum plates. It was concluded that a columnar tool without thread produced defect-free welds for soft aluminum alloys 1050, while a triangular prism-shaped tool was appropriate for hard aluminum alloys 5083 with a high rotational speed and all three types of tool

geometry were indifferent for 6061 aluminum alloys.

ii. Travel Speed: Fatigue resistance is improved at relatively low welding speed due to the increased amount of heat supplied to the weld per unit length (Ericsson & Sandström, 2003). The optimum travel speed has to be determined prior to fabrication depending on the alloy type. To assure good weld quality, it is critical that the stirred material is hot enough to plasticize with a suitable travel speed. Insufficient heat input due to a fast travel speed can cause the formation of micro-void coalescence. There is a wide acceptable range in travel speed for 6061 and 5083 alloys as shown in Figure 2.6, based on studies by Gharaibeh et al. (2016) and Kim (2008). The highest ultimate tensile strength was observed at 90 mm/min and 127 mm/min for 6061 and 5083 at given rotational speeds of 1120 rpm and 1600 rpm. However, a range of travel speeds in general result in quality welds, with a poor result only seen at 342 mm/min, as identified by Kim (2008), for the 5083 alloy.
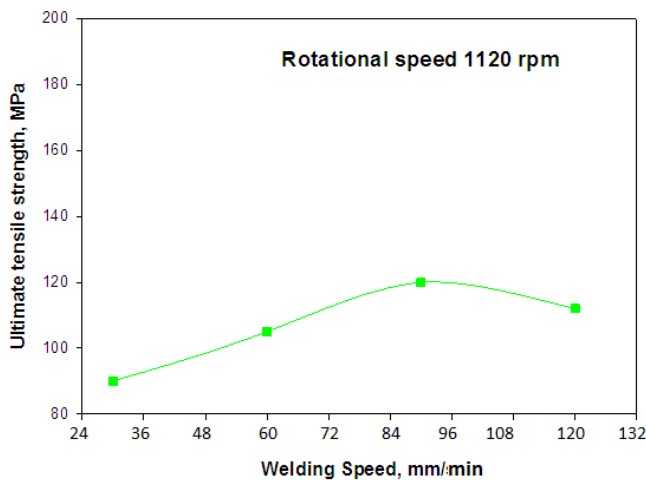
(a) 6061 (Gharaibeh, Al-Jarrah, & Sawalha, 2016)
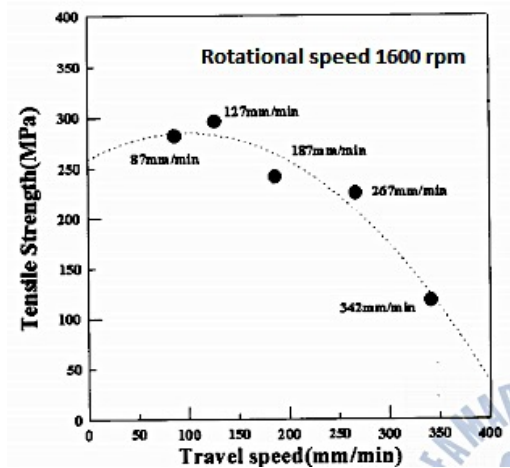
(b) 5083 (Kim, 2008)

Figure 2.6 Tensile strength vs. travel speed for 6061 and 5083 alloys

iii. Rotational Speed: Similar to travel speed, rotational speed needs to be investigated prior to the fabrication phase in combination with the travel speed on different aluminum alloys. The highest strength joint for the 6061 alloy was detected at a

rotational speed of 900 rpm, as shown in Figure 2.7 (a). It was produced by a triangular pin profile, as sufficient heat was generated by the higher shoulder area compared to the square or hexagonal pin profiles (Gharaibeh, Al-Jarrah, & Sawalha, 2016). Chandrashekar et. al. (2016) identified a difference in tensile strength depending on the threaded and unthreaded pin profiles for 5083 alloys at a travel speed of 50 mm/min as shown in Figure 2.7 (b). The optimum results were found at 1000 rpm for a tapered unthreaded tool profile, whereas 600 rpm for the tapered threaded pin profile was found to be the optimal rotational speed.
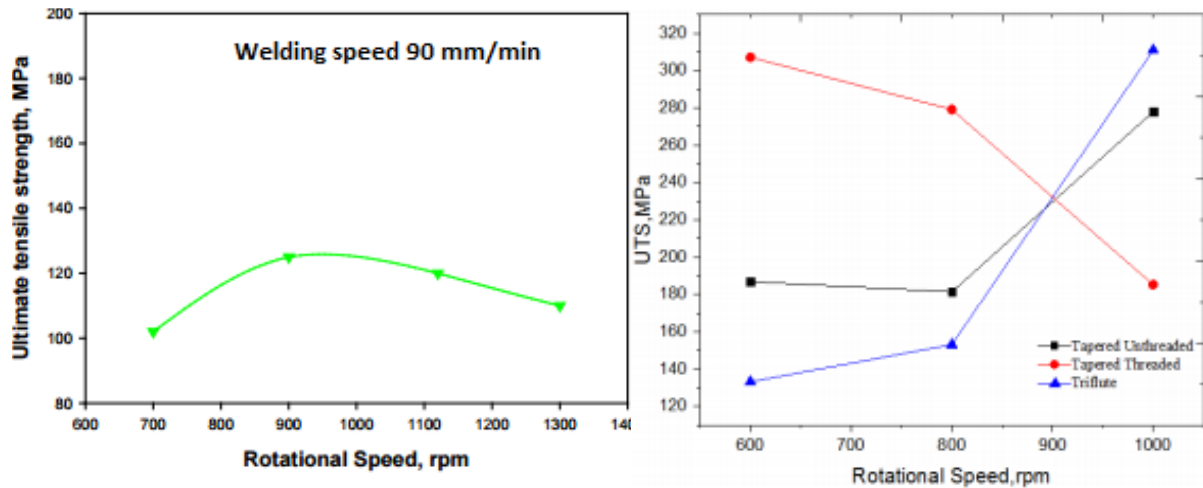
(a) 6061 (Gharaibeh, Al-Jarrah, & Sawalha, 2016)

(b) 5083 (Chandrashekar, Reddappa, & Ajaykumar, 2016)

Figure 2.7 Tensile strength vs. rotational speed for 6061 and 5083 alloys

iv. Clamping Force: The two plates to be joined must be in contact with each other with the tool probe positioned over the middle of the two joining plates. During the FSW process, large forces in both planar directions are generated. An effective clamping system for the FSW plates is a vital element for obtaining a defect free weld, as large gaps between the plates tend to reduce the strength of the joint due to void formation.

In order to achieve high quality FSW joints, the ratio between the traverse speed, v, and the rotational speed, w, known as welding pitch, k, is critical. High welding pitch means higher

traverse speed and lower rotational speed, which leads to a 'cold' weld. Insufficient heat input due to high welding pitch may cause internal defects, such as wormholes. Decreasing the welding pitch can enhance the joint quality with an increase in heat input.

2.3.2.4 Friction Stir Weld Defects

There are certain inherent flaws in fabricated FSW joints that are not fully known or have not being properly investigated in terms of their effect on fatigue performance. During the FSW fabrication process, flaw-free welds will only be produced if the welding parameters are within an optimized "tolerance box" for a particular aluminum alloy. Although the majority of FSW joints will be free of flaws as the tolerance windows are wide, it is still possible to fabricate flawed welds with welding parameters outside the tolerance box (Dickerson & Przydatek, 2003). For instance, to achieve a higher productivity rate, one may decide to increase the travel speed on the boundary or beyond the designated speed. Once the appropriate welding parameters are selected for a particular alloy, including tool type, probe angle, tool plunge depth, travel speed, rotational speed, clamping fixtures, it should not be easy for the fabricator to produce flawed welds. As the welding parameters are usually determined from experimental trial runs on test plates, the effects of variation of the described welding parameters and their associated defect types on the fatigue performance need to be further investigated. According to Menzemer (1992), welded aluminum joints subjected to repeated loading tend to exhibit subcritical crack growth along the joint line. Particularly in FSW joints, the fracture is often in the vicinity of advancing side due to the higher stress concentration and residual stress observed over the retreating side. The fatigue lives of FSW joints with defects are consumed at an early stage with macro-crack development. FSW defect types including: toe flash (underfill), kissing bond (lack of penetration), lap joints, and wormhole (porosity) can be described as follows,

i. **Toe Flash (TF)**

Toe flash defects co-exist with underfill, they form when the spinning tool pushes the joining material downwards below the surface of the plates causing excess material to be expelled along the weld toe. High stress concentrations developed due to the

24

discontinuity in material. Minor toe flash is acceptable. However, excessive toe flash can be an indication of improper FSW practices (McDonnell & Miller, 2011). Toe flash or underfill defects in FSW joints can be easily identified by visual inspection. Depending on the amount of toe flash, with the corresponding underfill, the fatigue strength can be significantly reduced due to the discontinuity in material and reduction in cross sectional area along the joint (see Figure 2.8).

Figure 2.8 Macrograph of FSW joint with toe flash (Podržaj, Jerman, & Klobčar, 2015)

Similar to kissing bond defects, toe flash can be removed by polishing. However, the process productivity can be greatly reduced as a result of additional polishing on the joints. In order to avoid the formation of toe flash, the welding operators should make sure the appropriate plunging depth and tool pin length are selected for the given plate thickness, and enough clamping force is applied.

ii. **Kissing Bond (KB)**

Kissing bond defects, also known as lack of penetration defects, consist of two solid-state bonding surfaces in contact except the weld root with little or no metallurgical bonding in a welded joint. Based on research conducted by Lamarre, Dupuis, and Moles (2009), kissing bond occurs due to the lack of penetration of the spinning tool, which prevents the weld root region from being properly stirred and solidified.

It is critical to identify kissing bond defects, because they are difficult to detect using non-destructive testing methods. This type of defect is critical in terms of fatigue performance, as the unbonded region can be seen as an initial crack perpendicular to the direction of loading, which can reduce fatigue life depending on the depth of the unbonded region. Figure 2.9 illustrated an example of kissing bond defect.
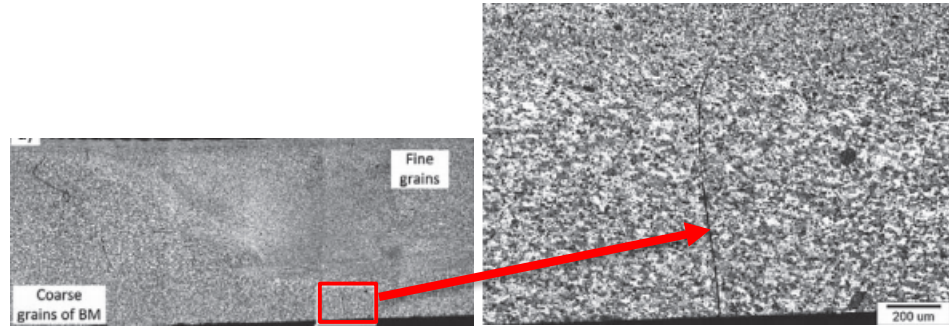
Figure 2.9 Macrograph of 5083 kissing bond defect (Podržaj, Jerman, & Klobčar, 2015)

Mitigation of kissing bond can be achieved by removing the layer at the bottom surface of the joint in order to eliminate root flaws. This mitigation method can reduce productivity, as post-machining has to be done, it may also affect the fatigue resistance of the joint due to higher stress concentration induced at the weld root and modified residual stress profile. Another mitigation method for kissing bond defects is to carefully select the appropriate pin penetration depth over the full plate thickness and position the tool to allow material movement at the root of the joint through the action of tool stirring (Gemme, Verreman, Dubourg, & Wanjara, 2011).

iii. **Lap Joint (LJ)**

FSW lap joints are widely used in applications where two pieces overlap each other along the weldment, with the typical geometry in a T-joint configuration as shown in Figure 2.10 a) or overlap each other as shown in Figure 2.10 b). For a lap joint to be made using FSW, the probe of the tool is pushed through the top plate and only a small distance into the bottom plate. Three common lap joint defects were identified by Bisadi et. al. (2011), including top sheet thinning, kissing bonds, and hooking defects. It is critical to exam the lap joints where the crack opening is in the direction of loading resulting a possible decrease in fatigue strength.

a) T-Joint Configuration   b) Overlap Configuration
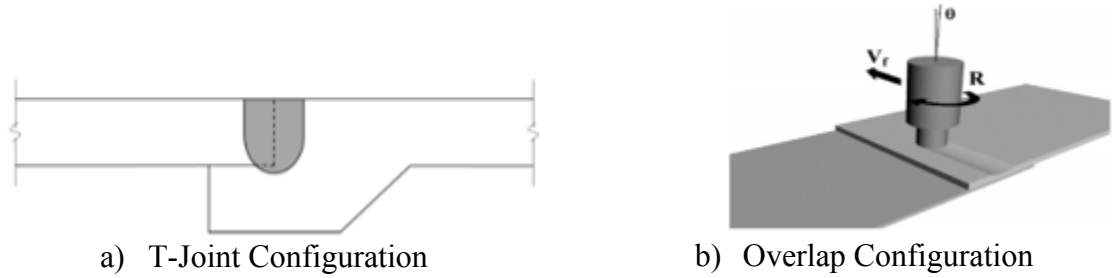
Figure 2.10 Lap detail illustrations

As a result of asymmetrical weld formation in FSW, namely advancing side and retreating side depending on the welding direction, Buffa et. al. (2009) examined lap joints by varying the joint configuration as summarized in Figure 2.11. The mechanical properties of Case a) was superior to those of Case b) as a result of hooking effect. Therefore, it can be concluded that to optimize an FSW lap joint, welding with the advancing side at the hook should be avoided.

a) Retreating side at hook   b) Advancing side at hook
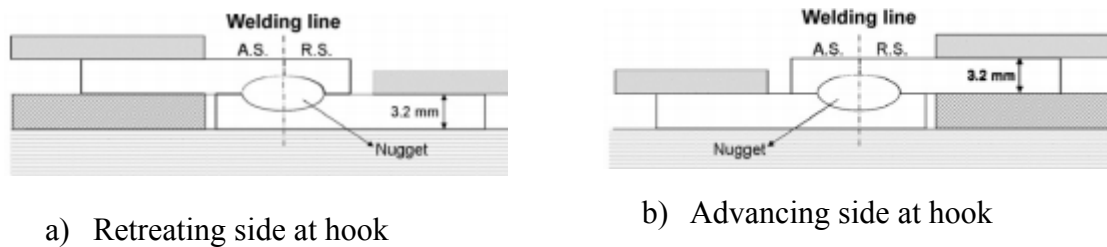
Figure 2.11 Lap joint configurations

Another factor affecting lap joint strength is the penetration depth. This factor was studied by Elrefaey et. al. (2004), who observed that a slight difference in this depth has a significant effect on the performance of the lap joint.

iv.   **Wormhole (WH)**

Wormholes inside FSW joints, also known as porosity or cavity, are long, tube like regions with a lack of bonding on or below the weld surface as shown in Figure 2.12. The major cause of this type of defect is abnormal material flow during the welding process due to inappropriate tool design or low rotational speed and high traverse rate resulting low heat input. Porosity can severely weaken the mechanical bonding of the

material. It is important to detect this type of defect, because modelling wormhole defects inside of welds is particularly difficult due to the limitation of the numerical methods used for dynamic flow modelling (Threadgill, Leonard, Shercliff, & Withers, 2009). Surface wormholes can be visually observed, whereas internal wormholes are difficult to detect using non-destructive testing methods.
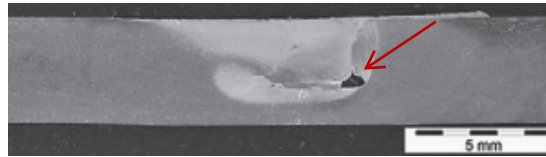
Figure 2.12 Macrograph of FSW joint with porosity (Podržaj, Jerman, & Klobčar, 2015)

Unlike kissing bond and toe flash defects, internal wormhole defects are considered as the most detrimental defect for fatigue strength of FSW joints as it is not possible to remove the defects after welding and to detect the defects using non-destructive testing methods is difficult. Internal wormholes are associated with the chaotic nature of the plastic deformation below the tool shoulder where the defect is affected by tool rotational speed, traverse speed, and geometry of the tool pin.

2.3.2.5 Effect of Polishing Friction Stir Welds

It has been hypothesized that the performance of FSW joints can be improved by polishing. It is typical that the reduction in thickness of the polished weld is in the range of 0.1 mm to 0.2 mm. The material flash and rippled structure caused by the rotating tool is removed by manual polishing. Bussu and Irving (2003) have studied polished FSW joints. They found that fatigue behaviour is significantly improved when the weld face is polished.

2.3.3 Fatigue Resistant Design

The fatigue behaviors of each specimen type can be modelled by stress-life curves consisting of CA and VA loading. CA loading is when the cyclic loads are applied with the same maximum and minimum loads in each cycle resulting a constant amplitude and mean load. One of the most used CA fatigue loads applied in many fatigue experiments is in the form of sinusoidal wave as shown in Figure 2.13.
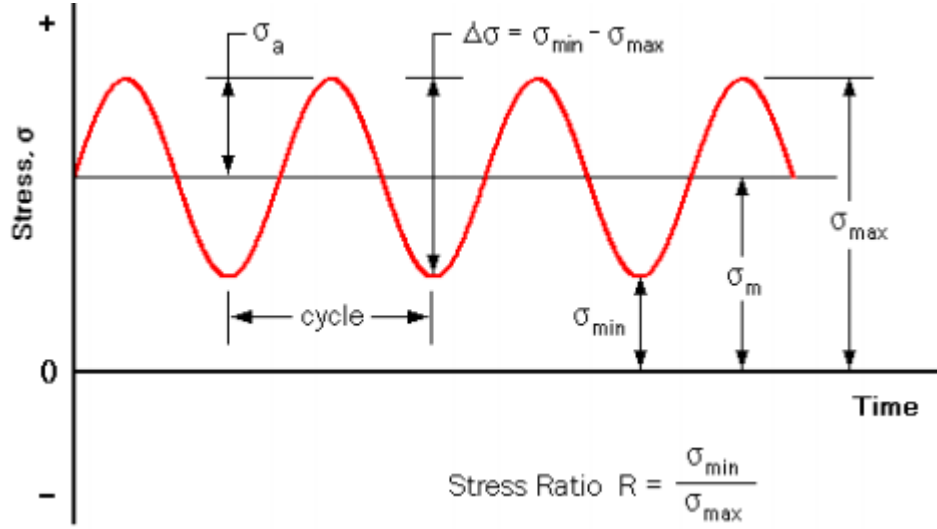
Figure 2.13 Sinusoidal cyclic loading

In practice, a complex or a random sequence of loads applied to mechanical parts is known as VA loading. Each stress cycle is associated with a particular stress range for the VA loading which requires proper contribution of each stress range to the total fatigue damage. The stress history is divided into repeated cycles with one stress range that are summed up to a distribution of stress ranges. This distribution of stress ranges is called a stress histogram or a stress spectrum consisting a number of constant stress range blocks. A histogram of cyclic stress is created from either the reservoir method or the rainflow analysis that reduces the complex loadings into series of simple cyclic loads. The cumulative damage is calculated from the fatigue resistance curve for each stress level. The effect of the individual contributions is combined using an algorithm called Miner's rule.

Fatigue resistance or stress-life (S-N) curves relate the nominal applied stress range, ΔS, and the number of stress cycles to failure, N. Numerous testing procedures are available to collect data for a proper S-N plot, where the S-N plots are usually represented on a log-log scale. The S-N curve can be approximated by a straight line as shown in Figure 2.14, formulated as a power law equation:

29

$$N_1 = N_2 \left(\frac{S_1}{S_2}\right)^{\frac{1}{m}} \qquad (2.1)$$

where,

S_1 is the nominal stress at point 1

S_2 is the nominal stress at point 2

N_1 is the number of cycles to failure at point 1

N_2 is the number of cycles to failure at point 2

m is the slope of the line, also referred as the *Basquin slope*, given as:

$$m = \frac{-(logS_1 - logS_2)}{logN_2 - logN_1} \qquad (2.2)$$
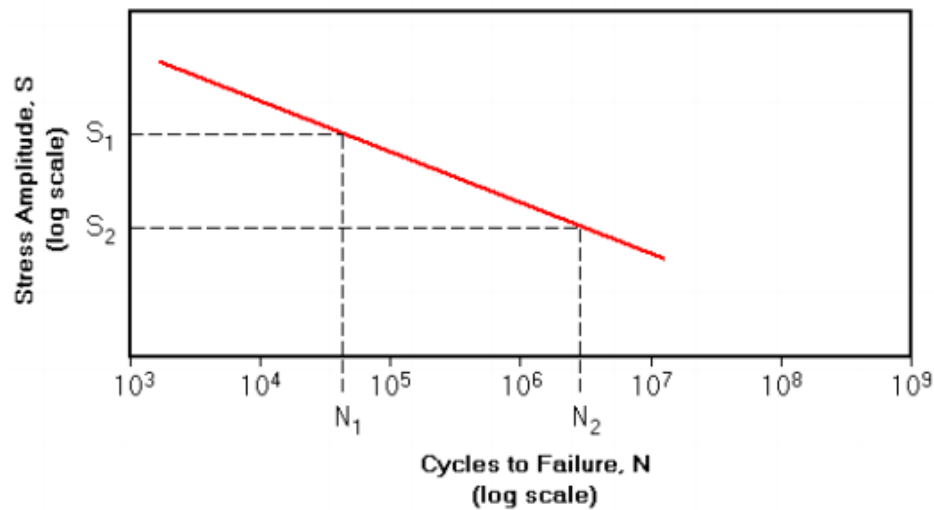
Figure 2.14 Idealized S-N curve

The most frequent constant amplitude S-N data collected in the laboratory is usually in the form of fully-reversed stress cycle with a mean stress, σ_m, on which the oscillatory stress is superimposed as indicated in Figure 2.13.

The stress range, $\Delta\sigma$, is the algebraic difference between the maximum and minimum stress in a cycle:

$$\Delta\sigma = \sigma_{max} - \sigma_{min} \tag{2.3}$$

The stress amplitude, σ_a, is defined as one half of the stress range:

$$\sigma_a = \frac{\sigma_{max} - \sigma_{min}}{2} \tag{2.4}$$

The mean stress, σ_m, is one half of the algebraic summation of the maximum and minimum stresses in a cycle:

$$\sigma_m = \frac{\sigma_{max} + \sigma_{min}}{2} \tag{2.5}$$

The R-ratio, R, is the ratio between minimum stress and maximum stress in a cycle:

$$R = \frac{\sigma_{min}}{\sigma_{max}} \tag{2.6}$$

The Palmgren-Miner linear damage hypothesis or Miner's rule is applied to evaluate the cumulative damage, D for structural elements subject to varying fatigue loads. The expressions of Miner's rule are stated in Equations (2.7) and (2.8):

$$D = \frac{n_1}{N_1} + \frac{n_2}{N_2} + \cdots + \frac{n_k}{N_k} = \sum_{i=1}^{k} \frac{n_i}{N_i}, \text{where } 0.7 \leq D < 2.2 \tag{2.7}$$

$$N_f = \sum n_i \tag{2.8}$$

where,

D is the fraction of fatigue life subjected to the cycles at varying CA stress range, ΔS_i

n_i is the number of cycles of CA stress range, ΔS_i

N_i is the number of cycles for a design S-N at CA stress range, ΔS_i constitutes failure

N_f is the number of cycles to failure

For design purpose, a structural element is designed safely against fatigue if D is less or equal to 1, with the assumption that the total damage is obtained as a linear combination of the damage due to all the applied stress reversals at varying stress amplitudes. Miner's rule is used in conjunction with design S-N curves to determine fatigue life in many design codes or specifications.

A set of equally spaced S-N curves are plotted on a log-log scale to allow detailed categories to be classified for a particular structural detail. The constant amplitude fatigue limit (CAFL) is a threshold value of the stress amplitude where the stress amplitude below this level do not always lead to failure. Any stress cycles below the CAFL are considered as non-damaging, where the component is considered to have an infinite life. An endurance limit can disappear in a design application due to the following reasons, periodic overloads, corrosive environments and high temperatures. Under VA loading, no fatigue damage assessment has to be carried out if no stress range applied in the full spectrum of VA exceeds the fatigue limit. However, if at least one stress range exceeds the fatigue limit, a damage calculation applying Palmgren-Miner's rule has to be performed indirectly with an equivalent constant amplitude stress range representing the variable spectrum loading. The following form employs Miner's sum:

$$\Delta S_{eq} = \left(\frac{\sum n_i \cdot \Delta S_i^m}{\sum n_i} \right)^{\frac{1}{m}} \tag{2.9}$$

where,

ΔS_{eq} is the equivalent constant amplitude stress range

ΔS_i is the stress range at i

n_i is the number of cycles for a given stress range i

N_i is the number of cycles to cause failure under stress range I

m is the slope of the design S-N curve

Since the equivalent stress range, ΔS_{eq}, only depends on the fatigue load spectrum and the slope constant, m, the equivalent stress range can be calculated without knowledge of the vertical position of the S-N curve.

In practice, almost all structural members contain some form of geometrical or microstructural discontinuities that result in a local maximum stress, S_{max} greater than the nominal stress, σ_n of the members. In ideally elastic members, the ratio of these stresses is designated as the stress concentration factor, K_t:

$$K_t = \frac{S_{max}}{\sigma_n} \tag{2.10}$$

The stress concentration factor is solely dependent on the geometry and the mode of loading.

Several codes and standards exist for designing aluminum details under fatigue loadings, however they were developed unparalleled with each other by different code committees. The similarities and differences of the current available fatigue design curves are discussed in the following section.

2.4 Current Fatigue Design Curves

The fatigue failure of structural members, comprising crack initiation, crack propagation and final fracture is an extremely localized process in its origin. Therefore, the local parameters of geometry, loading and material have a major influence on the fatigue strength and service life of structural members. They must be taken into account as close to reality as possible when performing fatigue strength assessments and especially so when optimizing a design in respect of fatigue resistance.

Extensive laboratory testing and analysis of the fatigue performance of welded aluminum structures has been undertaken over the past 20 years promoted by the lack of fatigue design standards (Maddox, 2003). The S-N curves obtained from fatigue tests on specimens containing the weld detail of interest are used in many design codes and standards. Several codes and specifications are developed concurrently for the fatigue design and analysis of

welded aluminum alloy structures as welded parts can exhibit poor fatigue behaviour. The following listed design codes and specifications for welded aluminum alloys, in chronological order are reviewed and compared,

- BS 8118-1:1991: 'Structural Use of Aluminum – Part 1 Code of Practice for Design', British Standard Institution (BSI), London, 1991
- ECCS: 'European Recommendations for Aluminum Alloy Structures, Fatigue Design', European Convention for Constructional Steelwork, Document No. 68, 1992
- Canadian Standards Association CAN/CSA S6-14: 'Aluminum Structures', 1992 (Revised, 2014)
- The Aluminum Association: 'Specifications for Aluminum Structures', Washington DC, 1994 (Revised, 2015)
- IIW: 'Fatigue Design of Welded Joints and Components', Abington Publishing, 1996
- Eurocode 9: 'Design of Aluminum Structures: Part 2: Structures Susceptible to Fatigue', ENV, 1999-2: 1998, CEN Brussels, 1998

All of the above provide a selection of design S-N curves with particular weld details expressed in terms of nominal stress ranges. Since the S-N curves refer to particular weld details, there is no need for the user to attempt to quantify the local stress concentration effect of the weld detail itself. Thus, the curves are used in conjunction with the nominal stress range near the detail. There are significant differences between the S-N curves in the rules and how they are used, and hence the different specifications will lead to different estimations of fatigue life. In order to provide a basis for judging their applicable to welded aluminum structures, key features are compared and where possible assessed in the light of relevant published data.

2.4.1 British Standard Institute

As a starting point in developing aluminum fatigue standards in 1979 with the observation of a good correlation between fatigue crack growth data for steel and aluminum on the basis of $\Delta K/E$, the steel bridge design standards, BS 5400, was simply factored in accordance with

the different in Young's modulus between steel and aluminum (Maddox, 2003). The fatigue design stresses of steel divided by 3 were adopted to design welded aluminum alloys with support from published data. However, some designers felt that the approach was too simplistic and penalized aluminum alloys as a construction material in compare to steel.

British Standards Institute: Structure Use of Aluminum – Part I Code of Practice for Design (BS 8118-1:1991) was published in 1992 to replace its predecessor *The Structural Use of Aluminum* (CP 118:1969). BS 8118 provided design methods for the fatigue resistance of aluminum alloys, including nine detailed categories, represented by a two-slope fatigue resistance S-N curves with initial slopes, m_1, ranges from 3.0 to 4.5 as shown in Figure 2.15. The design S-N curves in this code are set at two standard deviations below the mean of experimental data.
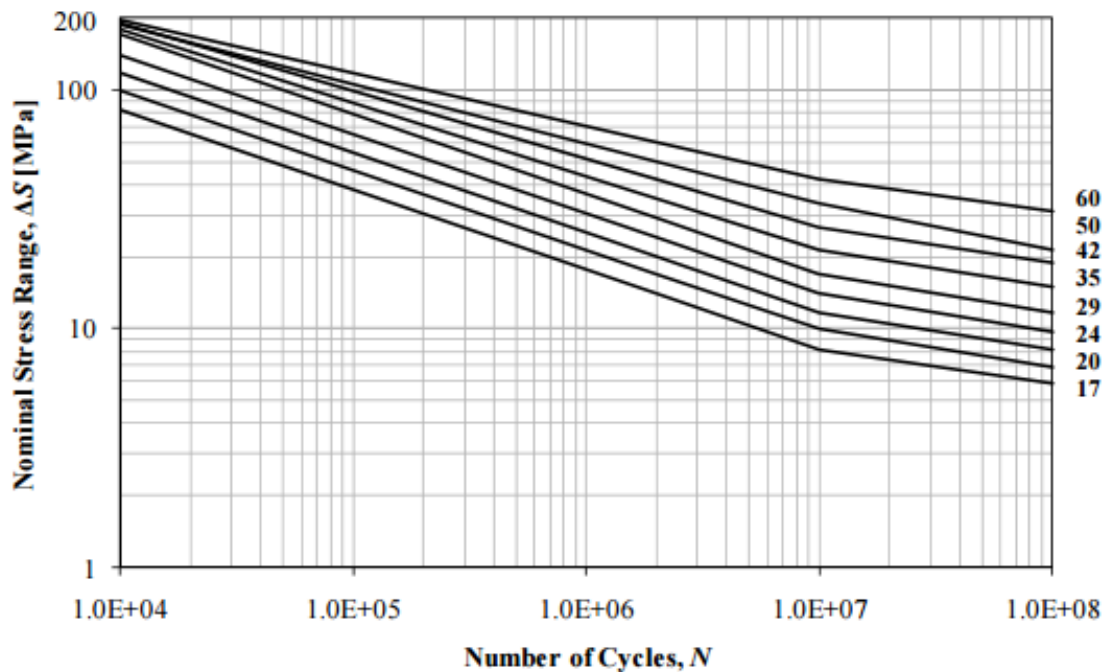
Figure 2.15 BS 8118 design S-N curve

Each fatigue detail is represented by a two-slope fatigue curve identified by the fatigue strength at 2 x 10^6 cycles listed at the right side of Figure 2.15. The knee point of the design S-N curve is located at 10^7 cycles where second slope of $m_2 = m_1 + 2$ is used up to the

35

variable amplitude cut-off stress at 10^8 cycles. The second slope beyond 10^7 stress cycles assumes that in a variable load spectrum, stress cycles below the constant amplitude fatigue limit (CAFL) at 10^7 cycles can be damaging. Safe life design is based on the design principle and the code using the Palmgren-Miner Rule as the failure criterion for general or variable amplitude loading satisfying the following condition with the recommendation that the cumulative damage cannot exceed 1.0 (BSI, 1992).

Many other design aspects should be taken into consideration along with the design S-N curve. One of the design aspects is the scale effect, relating the collected fatigue data obtained from small-scale specimens to real structures. The influence of tensile residual stresses is inevitable in real structures, but could be absent in small-scale samples. The thickness of the sample can also influence the fatigue strength and should be specified in the classification system.

2.4.2 European Convention for Constructional Steelwork (ECCS)

The initial review of fatigue data for welded joints in aluminum alloys included a wide scatter of existing data for welds that were smaller size and of unspecified quality. The newly formed ECCS Committee was focused on realistic structural specimens, and charged with the task of drafting a European Standard. Alusuisse and a number of other European projects made a large database available to the committee. To some extent, the same database was used to review the BS 8118 Draft for Public Comment and the fatigue rules were revised slightly as a result. *'European Recommendations for Aluminum Alloy Structures, Fatigue Design', Document No. 68, 1992* was drafted. The endurance limit for constant amplitude loading is assumed at the first knee point of 5 x 10^6 cycles, whereas the S-N curves for variable amplitude loading used in the calculation of damage accumulation are elongated with a further decrease into the high-cycle range (Radaj, Sonsino, & Fricke, 2006).
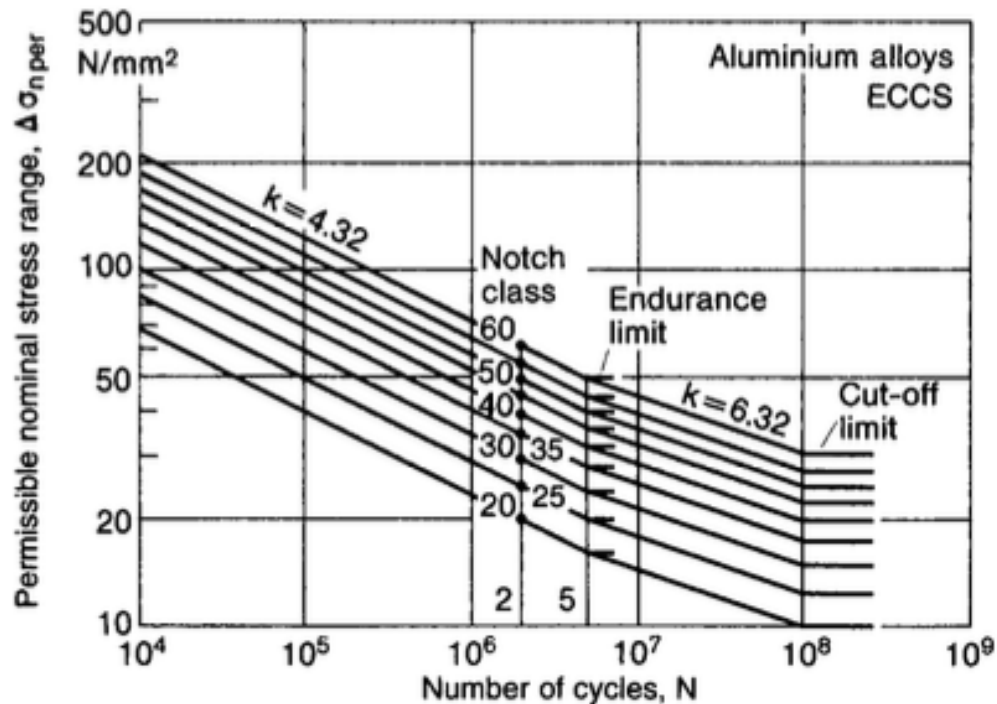
Figure 2.16 ECCS design S-N curves for aluminum alloys

Each fatigue detail is represented by a two-slope fatigue curve identified by the notch classes. The knee point of the design S-N curve with initial slope, m_1 at 4.32 is located at 5×10^6 cycles where second slope of $m_2 = 6.32$ is used up to the variable amplitude cut-off stress at 10^8 cycles as shown in Figure 2.16. The second slope provided beyond 5×10^6 stress cycles assumes that in a variable load spectrum, stress cycles below the CAFL can be damaging.

The resulting ECCS and BS 8118 fatigue rules were finally considered together as the basis of the new Eurocode 9 in the early 1990s. Even more large-scale specimen data were available by then and so the final form of Eurocode 9 is different from both BS 8118-1:1991 and the ECCS specifications.

2.4.3 Canadian Standards Association

Except Manitoba, all provinces and territories have mandated the use of CSA S6-14 under their jurisdictions (CSA, 2014). Development of one single code ensured consistency in highway bridge design across Canada, and made consulting easier without interpretations

from multiple codes. The only design code developed in Canada for the design, fabrication, and erection of aluminum structures is the eleventh edition of *Canadian Highway Bridge Design Code – Section 17 Aluminum Structures* (CSA S6-14) with the most recent revision released in 2014. The exact same design S-N curves are also adopted in ADM standards further discussed in Section 2.4.4. For the purpose of fatigue design, the aluminum design S-N curves currently are single-slope curves with different initial slopes, m, range from 3.45 to 6.85 (see Table 2.4), where the fatigue design S-N curve is plotted in Section 2.4.4 in Figure 2.19.

Table 2.4 Fatigue life constants amplitude threshold stress ranges **(CSA, 2014)**

Detail category	Fatigue life constant, γ	Fatigue life constant, m	Constant amplitude threshold stress range, F_{srt}, MPa	Damage equivalence factor, λ
A	21.7×10^{18}	6.85	70.0	0.65
B	199×10^{12}	4.84	37.2	0.60
C	894×10^{9}	3.64	27.7	0.55
D	206×10^{9}	3.73	17.3	0.55
E	31.1×10^{9}	3.45	12.6	0.54

Based on the requirement set out in *Welded Aluminum Construction CSA-W59.2-M1991 (R2013)* in accordance with *Certification of Companies for Fusion Welding of Aluminum CSA W47.2-11 (R2013)*, all welds must be visually inspected by a certified welding supervisor before, during and after welding. When inspections are required by contract, non-destructive weld testing shall be performed by a registered laboratory certified by the Canadian Welding Bureau in accordance with the requirements of *Certification of Welding Inspection Organizations CSA-W178.1-14* and *Certification of Welding Inspectors CSA-W178.2-14*. The laboratory shall also interpret the results.

CSA-W59.2-M1991 outlined the acceptance criteria for welded joints including material, weld profile, surface defects, internal defects, and surface finish. The acceptable groove weld profile in butt joint welded from one side is as shown in Figure 2.17.
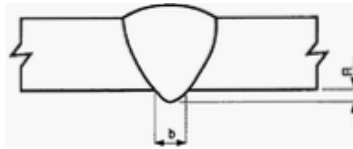
Figure 2.17 Butt joint weld profile

where,

   R is the convexity of the weld

   b is the weld width

For statically loaded structures,

$$R \leq (1 + 1.2b) \leq 5 \tag{2.11}$$

For dynamically loaded structures,

$$R \leq (1 + 0.6b) \leq 4 \tag{2.12}$$

Clause 6.3 and 6.4 in *W59.2-M1991* outlined the conditions of weld which are not permitted for surface and internal defects respectively.

For surface defects, surface crack, lack of fusion, and weld termination craters are not permitted; the section shall also be inspected for internal porosity if surface finish reveals porosity.

For internal defects, cracks are not permitted; dispersed and linear porosity shall not exceed the limits listed in Table 2.5 and Figure 2.18 respectively, individual discontinuities such as porosity, lack of fusion, and incomplete penetration shall not exceed the limit specified in Table 2.5, and roughness of the surface finish shall not exceed 12 μm.

Table 2.5 Acceptance criteria for dispersed porosity

Type of discontinuity	Maximum size of discontinuity allowed	
	Statically loaded joints in tension	Dynamically loaded joints in tension
Individual (only one in a length of 6t)	2/3 throat thickness but not more than 20 mm. The discontinuity shall not be closer than three times its greatest dimension to the end of a groove weld.	1/3 throat thickness but not more than 13 mm. The discontinuity shall not be closer than five times its greatest dimension to the end of a groove weld.
Aligned linear discontinuities at least one of which has a dimension 1 mm or larger	In any length of 6t, the sum of the greatest dimension of all discontinuities larger than 0.5 mm shall not exceed t. When the length of weld being examined is less than six times the effective throat, the permissible sum of the greatest dimensions shall be reduced proportionally.	In any length of 6t, the sum of the greatest dimensions of all discontinuities larger than 0.5 mm shall not exceed 0.5t. When the length of weld being examined is less than six times the effective throat, the permissible sum of the greatest dimensions shall be reduced proportionally.

Note: *t is the plate thickness.*

Pores shown are approximately 1.2 mm, 0.8 mm and 0.4 mm in diameter.

Number of Pores shown = 10, with the following breakdown: Number of 1.2 mm Pores = 3 Number of 0.8 mm Pores = 3 Number of 0.4 mm Pores = 4

PORES IN ASSORTED SIZES

Pores shown are approximately 1.2 mm in diameter.

Number of Pores shown = 7

LARGE-SIZE PORES

Pores shown are approximately 0.8 mm in diameter.

Number of Pores shown = 13

MEDIUM-SIZE PORES

Pores shown are approximately 0.4 mm in diameter.

Number of Pores shown = 18

FINE

WELDS OVER 6 mm TO 13 mm THICK

Figure 2.18 Acceptance criteria for linear porosity defects

Nondestructive testing including liquid penetrant inspection, radiographic inspection, and ultrasonic testing are outlined in Clause 7.5, 7.6, and 7.7 correspondingly, and only individuals qualified for Level II or III can perform this nondestructive testing.

Under Clause 5.12 in *W59.2-M1991*, a contractor can take corrective actions where defects can be repaired by properly preparing the defect sites before re-welding. The defects can be either removed or replaced as follows:

a) The excess weld metal due to overlap or excessive convexity can be reduced by removal

b) Additional weld metal can be deposited where excessive concavity of weld, undersize welds, and undercutting were detected

c) The portion where excessive weld porosity, excessive oxide inclusions, and incomplete fusion exists can be removed and rewelded

d) Cracks in welds or base metal shall be removed and rewelded

Under Clause 5.13 in *W59.2-M1991*, members required rectifications due to welding distortions can be straightened at ambient temperatures by mechanical means with a controlled amount of localized heat. Depending on the type of aluminum alloys, the maximum holding times at different temperatures varies. For 5000 (Al-Mg) series alloys, the distortion correction should be performed between a temperature from 230 to 300°C with a maximum holding time of 50 hours. For 6000 series alloys, the distortion correction should be completed below 230°C with a maximum holding time varying from 5 minutes to 50 hours depending on the holding temperature.

Under Clause C8 in *W59.2-M1991*, post weld operations on aluminum are suggested using portable milling machine to remove the reinforcement on butt welds.

CSA had outlined the acceptance level for surface and internal defects associated with FSW and their corresponding mitigation methods. The narrow tolerance window for each of the defects suggested that the fatigue performance of those samples were not taken into account in the S-N curve.

2.4.4 The Aluminum Association

The Aluminum Association: Aluminum Design Manual (ADM) Part I: Specification for Aluminum Structures applies to design of aluminum load-carrying structures, members, and connections (2015). The design manual referred to was published in 2015, and has served as the primary source for designing using aluminum alloys in the United States. The specification referred to multiple documents, including Aluminum Association, American Association of State Highway and Traffic Officials (AASHTO), American Institute for Steel Construction, American Society for Nondestructive Testing (ASNT), American Society of Civil Engineers (ASCE), American Society of Mechanical Engineers (ASME), American Welding Society (AWS), and ASTM International. The design S-N curves were derived directly from experimental results from ATLSS Laboratory at Lehigh University with the focus on full-scale welded beam members (Menzemer & Fisher, 1993). As a general provision in *Design for Fatigue* (ADM 2015), the plane of fatigue crack is expected to grow perpendicular to the nominal stress range applied under elastic conditions, and the requirements under static loading should be met after the welded detail was subjected to 100,000 cycles or more. ADM provided a set of seven detail categories as indicated in Table 2.6 and Figure 2.19 with single-slope design S-N curves for characterizing fatigue resistance, with each curve representing the specified fatigue detail accounting for the effect of stress concentrations. Many other factors, including temperature, corrosive substances, weld defects, and post-weld mechanical treatment can have an effect on fatigue strength, but are not addressed by this specification.

Six detail categories are included in Figure 2.19 with variable slopes, ranges from 3.42 to 6.85 with a constant amplitude fatigue limit at 5×10^6 cycles. Detail category F1 has a CAFL of 10^7 cycles with a single-slope of 7.31 is not plotted in Figure 2.19 for neatness of the graph.
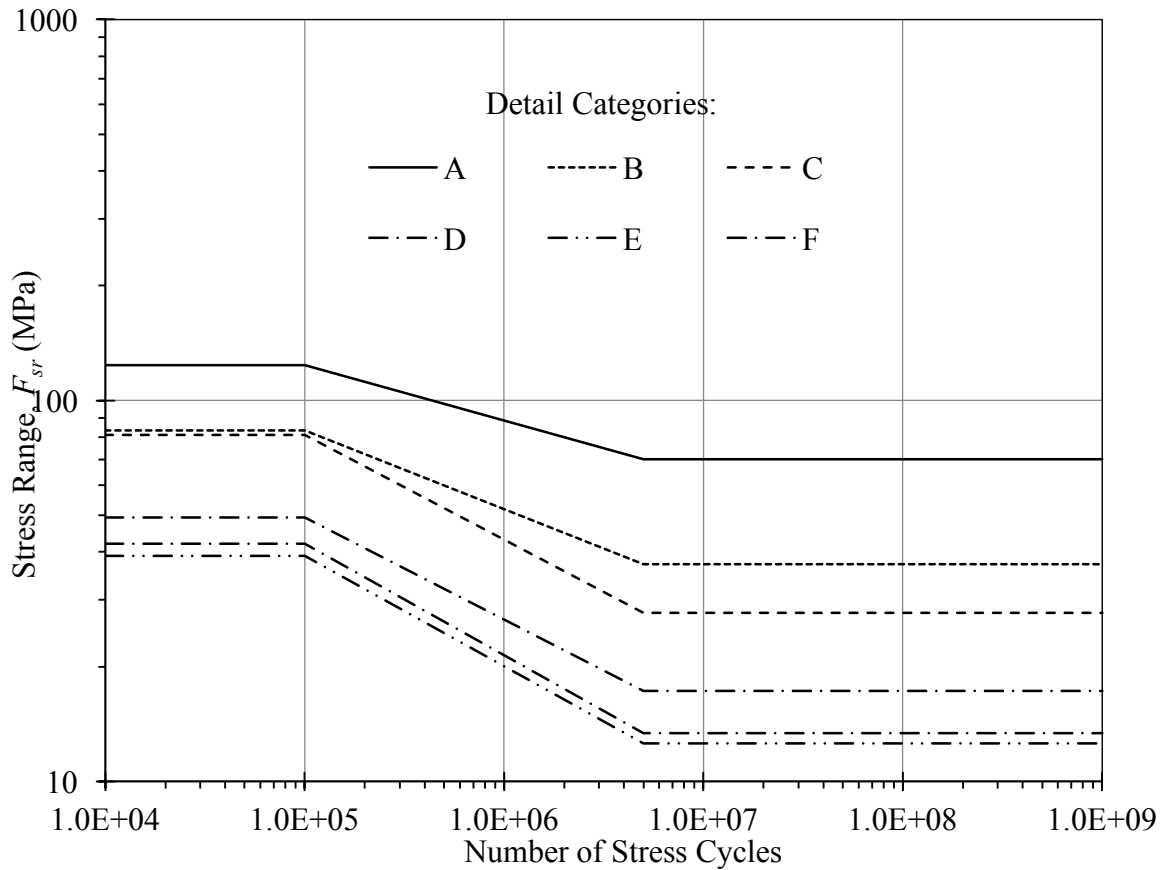
Figure 2.19 ADM design S-N curve

Under constant amplitude loading, if the applied stress range is less than the CAFL given in Table 2.4, further fatigue assessment is not required. However, the design S-N curve does not provide a second slope beyond the CAFL for variable amplitude loading due to limited testing data under variable amplitude loading. Structures subjected to variable amplitude loading may not exhibit a fatigue limit because a crack can be initiated by the higher stress cycles of the spectrum and propagate at stresses below the fatigue limit. As indicated in Figure 2.19, the Aluminum Association makes a conservative approach in formation of the variable amplitude by extending beyond the CAFL (Menzemer & Fisher, 1993). Under variable amplitude loading, if the maximum stress range in the spectrum is less than the constant amplitude fatigue limit, no further fatigue assessment is required. Palmgren-Miner's

rule is used to determine the effects of the cumulative damage from variable loading spectra (Aluminum Association, 2015).

In addition to visual inspection, which is always necessary to achieve compliance with code requirements listed in Table 2.6, three nondestructive testing (NDT) methods are provided by *AWS D1.2/D1.2M* (2014), including, radiographic testing (RT), ultrasonic testing (UT), and the liquid penetrate test (PT).

Table 2.6 Visual inspection criteria

Issue	Statically Loaded Structures	Cyclically Loaded Structures
Cracks	None	None
Fusion between adjacent layers of weld metal and between weld metal and base metal	Required	Required
Fillet maximum convexity Width of Weld Face or Individual Surface Bead ≤5/16 [8] >5/16 [8] to <1 [25] ≥1 [25]	Maximum Convexity 1/16 [2] 1/8 [3] 3/16 [5]	Maximum Convexity 1/16 [2] 1/8 [3] 3/16 [5]
Fillet maximum concavity	Throat shall not be undersize	Throat shall not be undersize
Craters	Underfilled craters in fillet welds are acceptable	Craters must be filled
Fillet weld maximum undersize over no more than 10% of the weld length Specified Weld Size ≤3/16 [5] 1/4[6] ≥5/16 [8]	Maximum Undersize 1/16 [2] 3/32 [2.5] 1/8 [3]	Maximum Undersize 1/16 [2] 3/32 [2.5] 1/8 [3]
Groove weld maximum reinforcement t ≤ 3/8 [10] 3/8 [10] < t ≤ 3/4 [20] t > 3/4 [20]	3/32 [2.5] 1/8 [3] 3/16 [5]	3/32 [2.5] 1/8 [3] 3/16 [5]
Groove welds maximum underfill	None	None
Undercut limits	For material ≤1 [25] thick, undercut <1/32 [1] except undercut <1/16 [2] for any cumulative length up to 2 [50] in 12 [300]. For material >1 [25] thick, undercut <1/16 [2].	No more than 0.01 [0.25] for welds transverse to tensile stress; otherwise no more than 1/32 [1]
Scratch or arc strike maximum depth	Same as undercut	Same as undercut
Surface porosity	Shall not exceed limits given in 5.15.1	Shall not exceed limits given in 5.15.2

As specified in *Quality Control and Quality Assurance* (Aluminum Association, 2015), the welding inspection personnel shall be welding inspectors or higher as defined in AWS B5.1, *Standard for the Qualification of Welding Inspectors.* Non-destructive testing personnel shall be qualified in accordance with the American Society for Nondestructive Testing (ASNT) CP-189, *Standard for Qualification and Certification of Nondestructive Testing Personnel*, only individuals who qualify to SNT-TC-1A NDT Level II may perform NDT without supervision. The acceptance criteria for ultrasonic testing shall be as required by *AWS D1.2/D1.2M)* (2014) (Aluminum Association, 2015).

RT and UT are used to detect both surface and internal discontinuities, PT is used to detect discontinuities open to the surface. The maximum acceptance discontinuities in any 3 inch long weld under RT are listed in Table 2.7, whereas UT is not treated in detail in AWS D1.2 because of the lack of consensus, it is about formulating a simple procedure giving satisfactory results. Other standards and codes provide applicable information for UT including, ASTM E164, *Standard Recommendation Practice for Ultrasonic Contact Examination of Weldments*; and Section V of ASME *Boiler and Pressure Vessel Code, Non-Destructive Examination.*

Inclusions, remnant oxides, and underfill cannot exceed the required sizes listed in Table 2.8, whereas cracks, lack of bonding, and voids are unacceptable under the RT inspection.

Table 2.7 Maximum acceptance discontinuity in radiographs for 3 inch length of weld

(E) Weld Size[c]		Total Area Allowed		Large Discontinuities			Medium Discontinuities			Fine Discontinuities		
				Major Dimension		Max. No.	Major Dimension		Max. No.	Major Dimension		Max. No.
in	mm	in²	mm²	in	mm		in	mm		in	mm	
1/8	3	0.008	5	0.031	0.79	9	0.025	0.64	16	0.018	0.46	31
1/4	6	0.017	11	0.063	1.60	4	0.032	0.81	21	0.020	0.50	54
3/8	10	0.024	15.5	0.094	2.39	3	0.037	0.94	23	0.022	0.56	65
1/2	13	0.033	21	0.125	3.17	2	0.041	1.04	25	0.026	0.66	62
5/8	16	0.042	27	0.156	3.96	3	0.043	1.09	28	0.029	0.74	63

[a] Discontinuities may be circular, elliptical, conical, or irregular in shape. The major dimension shall be measured in determining the size of an indication. The discontinuities may be a void or a tungsten or nonmetallic inclusion. Copper or ferrous inclusions shall not be allowed in the welds.
[b] Only discontinuities whose major dimension exceeds 1/64 in [0.4 mm] shall be considered relevant in evaluating the RT soundness criteria.

Table 2.8 Inspection acceptance criteria for FSW

Issue	Cyclically Loaded Structures	Statically Loaded Structures
Cracks	none	none
Lack of bonding	none	none
Voids (internal or open to surface)	none	none
Inclusions and remnant oxides (1) individual size (maximum) (2) spacing (minimum) (3) cumulative length in any 3 in [75 mm] of weld (maximum)	lesser of 0.33T or 0.06 in [1.5 mm] 4 × size of larger adjacent inclusion lesser of 1.33T or 0.25 in [6 mm]	lesser of 0.50T or 0.09 in [2.3 mm] 2 × size of larger adjacent inclusion lesser of 1.33T or 0.25 in [6 mm]
Underfill maximum depth, measured from adjacent base metal surface	0.05T	0.075T
Weld flash (maximum height)	remove if WPS requires removal	remove if WPS requires removal

Note: T = nominal thickness of the parts joined.

2.4.5 International Institute of Welding

The International Institute of Welding: Recommendations for Fatigue Design of Welded Joints and Components (IIW document IIW-2259-15 ex XIII-2460-13/XV-1440-13) is meant to provide the basis for the design and analysis of welded components loaded with fluctuating forces by avoiding failure by fatigue (Hobbacher, 2016). The most updated IIW document in its second edition was revised by a Commissions XIII and XV in 2014, the main revisions topics include, but are not limited to: structural hot spot stress, aluminum using the effective notch stress method, and fracture mechanics. The design S-N curves in IIW recommendations distinguish the characteristic fatigue strength of details as fatigue classes (FAT) defined by their corresponding stress ranges at 2×10^6 cycles. For instance, an aluminum transverse butt weld is categorized as FAT class 28 with a stress range of 28 MPa at 2×10^6 cycles indicated in Figure 2.20. The structural details are usually assessed on the basis of the maximum principal stress range in the section where potential fatigue cracking is expected. The butt weld is acceptable if the misalignment is within 10% of the plate thickness. Two-slope design S-N curves for 14 detailed categories under constant and variable amplitude are included in the IIW recommendations.
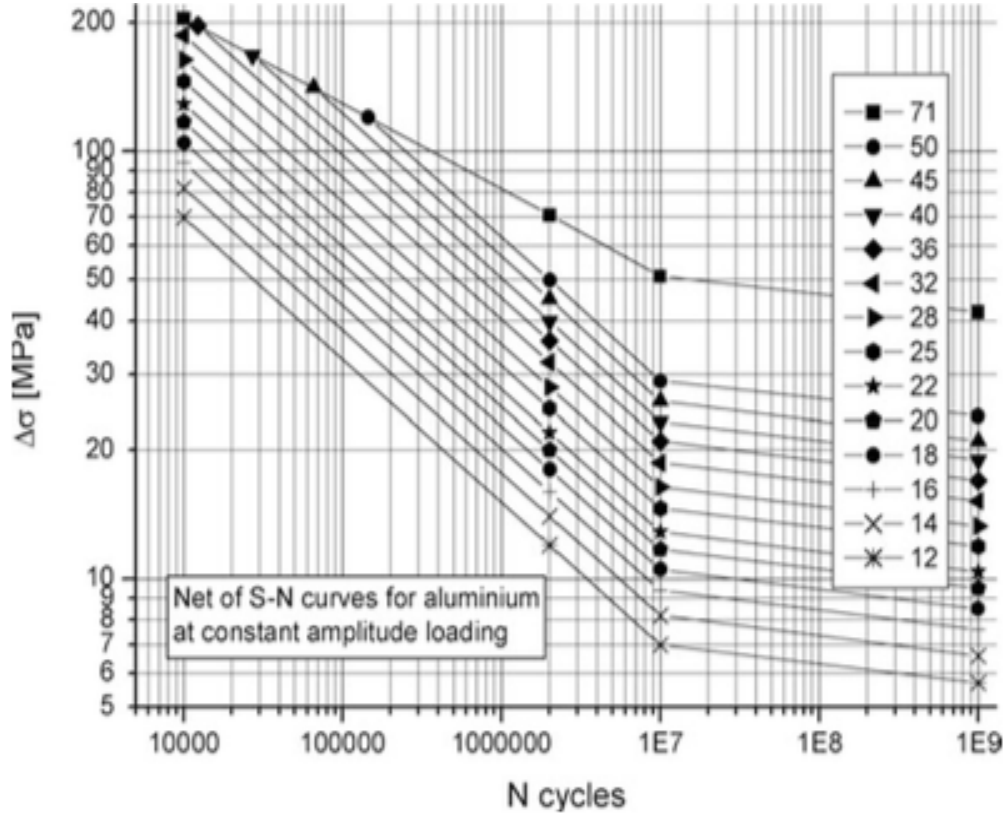
Figure 2.20 Fatigue resistance S-N curves for IIW recommendation

For constant amplitude loading, the slope of the fatigue strength S-N curves for details assessed on the basis of normal stresses, m_1 is 3.0, except FAT 71 which has a slope of 5.0. The constant amplitude knee point is assumed to correspond to 10^7 cycles, known as the constant amplitude fatigue limit (CAFL). The nominal stress based characteristic S-N curves are presented with an extrapolation beyond 10^7 cycles at a slope of 22 for all FAT classes. Traditionally, CAFL defines the corresponding fatigue endurance on the S-N curve. However, new experimental data indicate that a CAFL does not exist and the S-N curve should continue on the basis of a further decline in the stress range of about 10% per decade in terms of cycles, which corresponds to a slope of $m = 22$ (Hobbacher, 2016).

Under VA loading, a cumulative damage procedure, usually modified "Palmgren-Miner" rule and associated resistance S-N curves, are applied. A number of codes and standards follow this procedure, however, recent research indicates that assuming a specified damage sum or

fatigue damage ratio $D = 1.0$ can be non-conservative. IIW recommends a lower critical damage ratio of 0.5 instead of 1.0. In some cases, an equivalent constant amplitude stress range may need to be determined and compared directly with the constant amplitude resistance curve.

The characteristic of each FAT class in Figure 2.21 can be modified further according to stress ratio, plate thickness, and post welding treatments. For variable amplitude loading, the Palmgren-Miner rule is modified with the design stress range multiplied by the partial safety factor γ_F and the design resistance stress range divided by the partial safety factor γ_M. Similarly, the secondary bending stress caused by axial or angular misalignment needs to be considered if the misalignment exceeds the amount (10% of plate thickness) which is already covered by the fatigue resistance S-N curve for the structural detail. This is done by the application of an additional stress magnification factor $k_{m,eff}$. Either the applied stress is multiplied by or the fatigue resistance is divided by it.
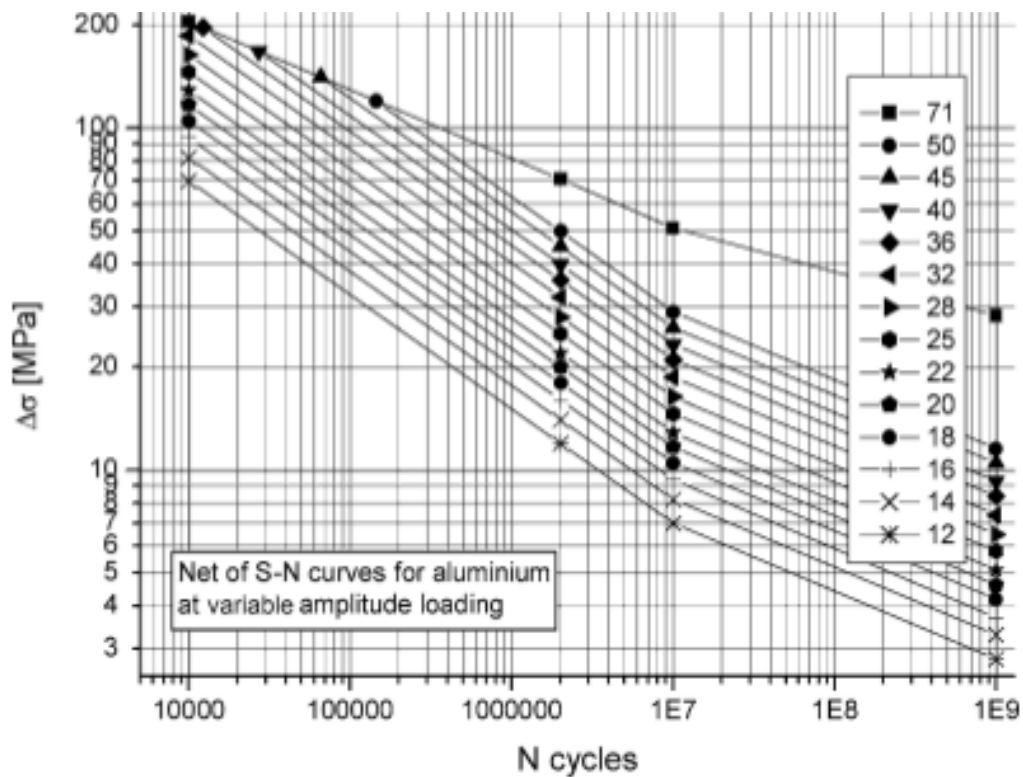
Figure 2.21 Modified design S-N curve for aluminum

48

The design S-N curves are the same before the knee point at 10^7 with an initial slope of m_1 equal to 3. Whereas, the slope beyond the knee point is modified according to the expression $m_2 = 2 \cdot m_1 - 1$. Therefore, the second slope modified by IIW is 5.0 for all welded fatigue details, except FAT 71 with a slope of 9.0

Since the current system of *Welding-Fusion Welded Joints in Steel, Nickel, Titanium and Their Alloys – Quality Levels for Imperfections* (ISO 5817:2006) is not consistent in terms of fatigue properties (Hobbacher, 2016). Three types of imperfection are outlined in Table 2.9 and discussed individually. It is assumed that any of the imperfections not included, can be assessed by assuming similar imperfections with comparable notch effects.

Table 2.9 Categorization and assessment procedure for weld imperfections

Effect of imperfection		Type of imperfection	Assessment
Increase of general stress level		Misalignment	Formulae for stress magnification factors
Local notch effect	additive	Weld shape imperfections, undercut	Tables given
	competitive	Porosity and inclusions not near the surface	Tables given
Crack-like imperfection		Cracks, lack of fusion and penetration, all types of imperfections other than given here	Fracture mechanics

Misalignment: The IIW recommendations already include stress magnification factors (see Table 2.10) to account for the increase of stress in the welded joint due to misalignment in axial loading conditions. For instance, an additional 30% increase in stress is directly applied due to misalignment for butt welded joints (Hobbacher, 2016). Use of an effective stress magnification factor $k_{m,eff}$ is required when the effect of misalignment is larger than specified, and $k_{m,eff}$ is calculated as:

$$k_{m,eff} = \frac{k_{m,calculated}}{k_{m,alreadycovered}} \qquad (2.13)$$

Table 2.10 Stress magnification factors due to misalignment

Type of k_m analysis	Nominal stress approach	Structural hot spot, effective notch and fracture mechanics appoach	
Type of welded joint	k_m already covered in FAT class	k_m already covered in SN curves	Default value of effective k_m to be considered in stress
Butt joint made in shop in flat position	1.15	1.05	1.10*
Other butt joints	1.30	1.05	1.25*
Cruciform joints	1.45	1.05	1.40*
Fillet welds on one plate surface	1.25	1.05	1.20**
Fillet welds on both plate surfaces	1.25	1.05	1.10***

* but not more than $(1 + 2.5 \cdot e_{max}/t)$, where e_{max} = permissible misalignment and t = wall thickness of loaded plate
** but not more than $(1 + 0.2 \cdot t_{ref}/t)$, where t_{ref} = reference wall thickness of fatigue resistance curves
*** but not more than $(1 + 0.1 \cdot t_{ref}/t)$, where t_{ref} = reference wall thickness of fatigue resistance curves

Undercut: The IIW recommendation assesses weld toe undercut with the ratio of depth of undercut, u to plate thickness, t as indicated in Table 2.11.

Table 2.11 Acceptance levels for weld toe undercut in aluminum

Fatigue class	Allowable undercut u/t	
	Butt welds	Fillet welds
50	0.025	Not applicable
45	0.05	Not applicable
40	0.075	0.05
36	0.10	0.075
32	0.10	0.10
28 and lower	0.10	0.10

Porosity and Inclusions: The IIW recommendation suggests to assessing the embedded volumetric discontinuities using NDT when in doubt. The detected porosity or inclusion should be combined to be treated as one large imperfection whether they are the same or of different types. Table 2.12 assesses inclusions by their maximum length, which porosity is evaluated as the maximum percentage of projected area.

Table 2.12 Acceptance levels of porosity and inclusion in aluminum welds

Fatigue class	Max. length of an inclusion in mm ** As-welded	Limits of porosity in % of area * **
40 and higher	1.5	0 +)
36	2.5	3
32	4	3
28	10	5
25	35	5
15 and lower	no limit	5

Crack-like Imperfections: Crack-like defects can be idealized as elliptical cracks, which is defined by two half-axes, *a* and *c* as identified in Figure 2.22. The stress intensity factor as a result of such cracks can be calculated using equations provided in Section 2.5.1.2.
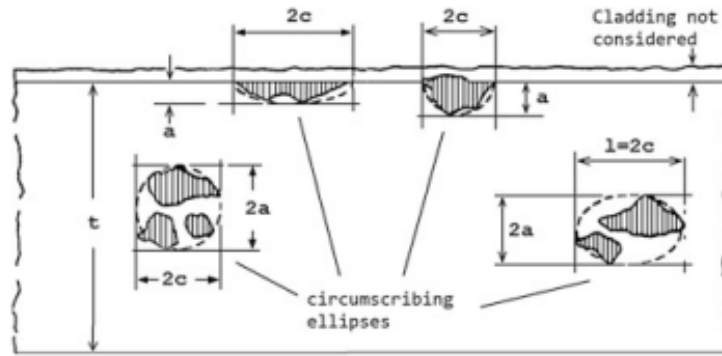
Figure 2.22 Crack-like Defects Transferred into Elliptic Cracks

IIW recommendations assumes the parameters of the Paris power law and threshold data for aluminum in Table 2.13 when the specified or measure material parameters are absent.

Table 2.13 Parameters of the Paris Power Law and Threshold Data for Aluminum

Units	Paris power law parameters	Threshold values ΔK_{th}			
		$R \geq 0.5$	$0 \leq R \leq 0.5$	$R < 0$	Surface crack depth < 1 mm
K [N · mm$^{-3/2}$] da/dN [mm/cycle]	$C_0 = 1.41 \cdot 10^{-11}$ m = 3.0	21	56.7– 72.3 · R	56.7	≤ 21
K [MPa$\sqrt{m}$] da/dN [m/cycle]	$C_0 = 4.46 \cdot 10^{-10}$ m = 3.0	0.7	1.8– 2.3 · R	1.8	≤ 0.7

51

2.4.6 European Committee for Standardization

Eurocode 9: Design of Aluminum Structures Part 1-3: Structures Susceptible to Fatigue (UNI EN 1999-1-3: 2007) is a European Standard applied to the design of buildings and civil engineering and structural works in aluminum, it provides the basis for the design of aluminum alloy structures with respect to the limit state of fracture induced by fatigue. EN 1999 is only concerned with requirements for resistance, serviceability, durability and fire resistance of aluminum structures. EN 1999 provides eight fatigue strength curves for over 50 detail types with 54 associated detail categories for plain members, different weld types, and bolted connections to determine fatigue resistance.

The basis of Eurocode 9 was formed as a result of BS 8118 and ECCS fatigue guidelines in the early 1990s. Initially, the statistical regression analyses were based on small specimens. Until the 1980's, larger specimens experiments were conducted at TUM that formed the basis for the first European document. A large volume of research work has accumulated in Europe for fatigue design of aluminum structural components. The two existing aluminum fatigue databases at Iowa State University and the Technical University of Munich (TUM) was united by the Committee for Aluminum Fatigue Data Exchange and Evaluation and maintained at Technical University of Munich for many years. During the second phase of developing Eurocode 9, a considerable amount of full-scale specimens experiments were carried out by TUM, with small-scaled specimens used to differentiate the impact of R-ratio and plate thickness. All of the evaluations that have emerged since used the baselines for the first draft of Aluminum Fatigue Design in Eurocode 9 in the third phase, with a further enhancement for materials and a number of comparative analyses used on other concurrent codes – IIW Recommendations, and ADM, following with a few new issues by re-evaluate the available data. Since the fatigue data used in *Design for Structures Susceptible to Fatigue* (EN 1999-1-3) is not accessible to the general public, data in the form of S-N design curves is used for designing aluminum structures.

Based on the quality level of butt weld (see Table 2.14), three separate groups of structural detail types were established by S-N curves with different slope values, m_1 of 7.0, 4.3 and

3.4. This recognized that the predicted fatigue performance is highly dependent on the quality levels of the welded details. Eurocode 9 adjusted the prediction according to *ISO 10042:2005 Welding – Arc-welded Joints in Aluminum and Its Alloys – Quality Levels for Imperfections.* For example, butt welded plates with full penetration on one side is categorized as 45-4.3 or 40-4.3 depending on the quality level based on criteria listed in ISO 10042:2005 (as indicated in Table 2.14). All of the S-N curves in the code are two-slope curves as shown in Figure 2.23, excluding those associated with detail categories from plain member and bolted joints, which are single-slope curves. The second slope beyond the CAFL takes the form of $m_2 = m_1 + 2$. The S-N curves are set two standard deviations below the mean of experimental data.
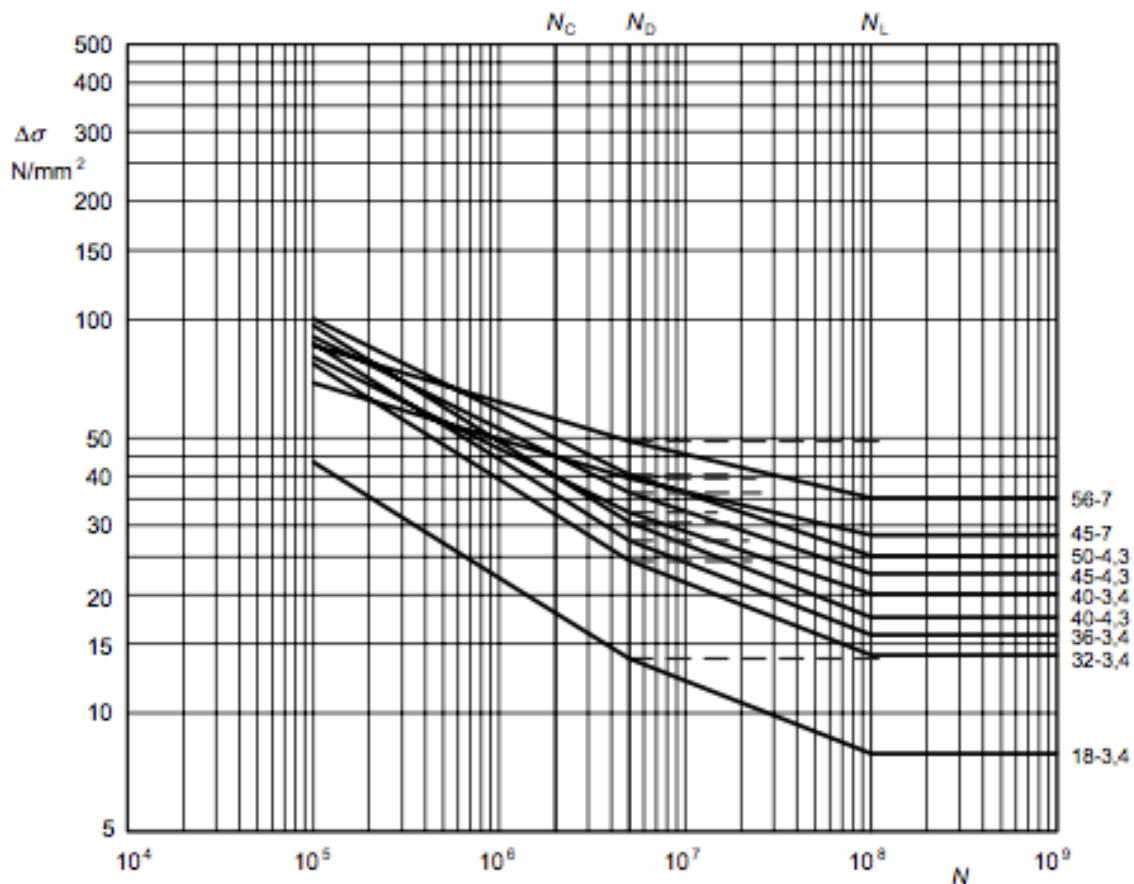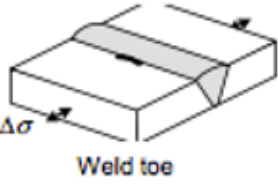

Figure 2.23 S-N design curve Eurocode 9

Table 2.14 Quality level of butt welded details

Detail type	Detail category $\Delta\sigma - m_1$ [1]	Constructional detail / Initiation site	Type of weld	Joint Part	Stress analysis	Welding requirements	Execution requirements Quality level [3]		additional
							internal	surface and geometric	
7.4.1	45-4.3	$\Delta\sigma$ / Weld toe	Welded one side only, full penetration without backing	Flats, solids	used on ends, cut off a		B	B	5) 6)
7.4.2	40-4,3						C	C	
7.4.3	32-3,4			Open shapes, hollow, tubular			C	C	6)

There are nine S-N curves provided for varying butt welded joint detail categories, each represented by a two-slope fatigue curve identified by the fatigue strength in MPa at 2×10^6 cycles (N_C) and its initial slope m_1, denoted on the right side of Figure 2.23. The constant amplitude fatigue limit for all fatigue details occurs at 5×10^6 cycles (N_D). Although constant amplitude stress cycles below the CAFL are considered non-damaging, the code notes that occasional loading events above will cause a crack to propagate, thus allowing stress cycles under the CAFL to cause further damage. Therefore, the code uses a second slope, between 5×10^6 and 10^8 cycles. The code notes that the second slope may be conservative for certain loading spectra. A cut off limit is provided at 10^8 cycles (N_L), thus implying that any stress cycles below this limit cause no damage. For safe life design, the code uses the Palmgren-Miner rule with the recommendation that the cumulative damage should not exceed 1.0, although the code does offer different levels of allowable cumulative damage in the annex (CEN, 2007).

Eurocode 9 permits a damage-tolerant approach to fatigue design when the crack growth can be predicted, along with a suitable inspection regime.

2.4.7 Specification Comparison

Each of the provisions for fatigue design of aluminium structures exhibits similarities as well as discrepancies in philosophy because they were developed over time based on the previous

findings and were also improved based on the current database. The development of each specification in chronological order are BS 8118, ECCS, CSA, ADM, IIW, and Eurocode 9. The differences in philosophies separated the specifications into two broad groups, the ECCS and CSA considered fatigue strength to be a function of loading, in another words, as a function of R-ratio, whereas BS8118 and ADM assumes R-ratio independence (Menzemer & Fisher, 1993). In the early stage of specification development, there was a lack of experimental results on fatigue damage subjected to VA fatigue loading. Over the years, variable amplitude fatigue damage was accounted for through the application of Miner's rule for all specifications. Except the ADM, specifications all employed a second slope ($m_2 > m_1$) for VA loading, implying the damage accumulates at different rates for different load regime. The majority of specifications assume a CAFL at 5×10^6 cycles, except BS 8118 and IIW, where a CAFL at 10^7 cycles was assumed. Due to the significant differences proposed by each specifications, the fatigue life design of a certain detail can vary depending on the specification used (Maddox, 2003). All of the specifications specify a series of S-N curves for welded details, with a classification scheme developed by joint committee members with different perspectives. Detail classifications in Eurocode 9 outlined joint type, type of joint part, loading direction, and quality control criterions as shown in Table 2.14, whereas, less comprehensive guidance on weld details is provided by CSA, ADM and IIW, which only include joint type and loading direction.

The historical developments of many fatigue design specifications were reviewed and compared by Maddox (2003) to identify discrepancies during their developments. As a starting point in the 1970s, British Standard Institute developed the most comprehensive standards for aluminum on the same basis as steel. The aluminum standard at the time was not widely accepted as it was too simplistic or conservative. Most of the initial fatigue data for welded aluminum joints were obtained from small-scale specimens of variable, unspecified qualities, making the data widely scattered. Small-scale specimens do not truly represent full-scale beams or elements because they did not account for higher tensile residual stress in the full-scale beams or elements. More realistic fatigue data were then

developed by the ECCS Committee for drafting European Standards, containing large-scale data from Alusuisse and new European projects. Based on the European standards, the drafting of fatigue design rules by the Aluminum Association and Canada Standard Association were developed thereafter.

To illustrate the differences between the mentioned codes and recommendations, one detail category: a one-sided butt weld, from each set of standards was compiled for comparison in Figure 2.24.
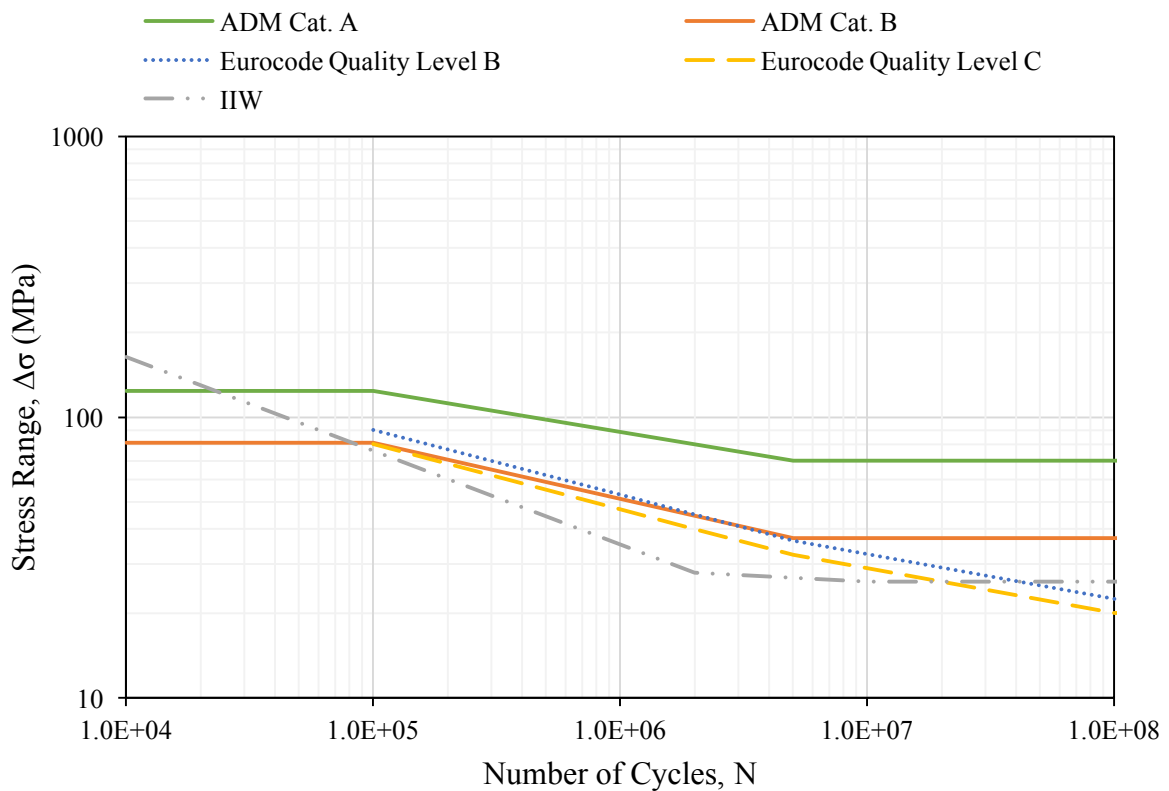

Figure 2.24 Design S-N curves comparison for butt weld

The variation for each of the design S-N curves for butt weld can be explained by the fact that test data were only applied under specific manufacturing and quality control procedures stated in each of the design specifications. Extrapolations to other conditions of manufacturing and service should be handled with care.

The classification of weld quality through allowable imperfections was undertaken after the document EN ISO 10042. Certain inconsistencies may arise in this procedure, as comparative studies at TUM with respective national specifications have shown. The issue of relevance to fatigue behaviour is not yet evaluated for specific imperfections in this code. The quantification of the quality classes and the harmonization of imperfection limit sizes will be one of the main challenges in the coming years.

2.5 Fracture Mechanics

Fracture mechanics analysis is a useful tool to evaluate the fatigue behaviour of aluminum welds beyond the limited fatigue test data. Fracture mechanics theory is concerned with the load bearing capacity of a structural component containing an initial crack or flaws. The majority of initial cracks in welded joints initiate from small, sharp crack-like intrusions at the weld toe, or from the crack-like lack of penetration at the weld root. The rate at which a crack will grow characterizes a material's resistance to fracture. Development of a crack initiation phase is suppressed for a welded joint in which crack propagation commences at the beginning of fatigue life (Gurney, 2006). The fatigue life of a structural component can undergo three phases or less, including the crack initiation, crack propagation and final fracture stages as illustrated in Figure 2.25.

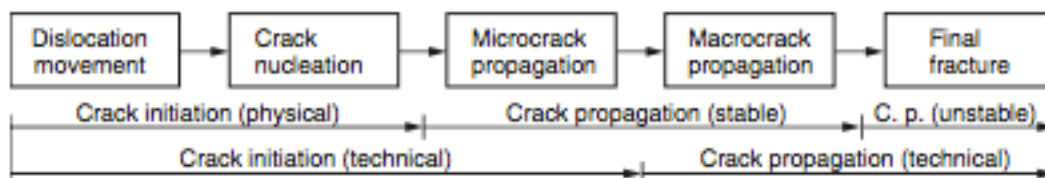**Figure 2.25** Micro- and macrophenomena of material fatigue (Radaj, Sonsino, & Fricke, 2006)

The fatigue life, N_{total} can be modeled as shown below,

$$N_{total} = N_i + N_p \tag{2.14}$$

where,

N_{total} represent the total fatigue life

N_i represent the crack initiation stage of the fatigue life

N_p represent the crack propagation stage of the fatigue life

Two of the most widely employed methods used to predict fatigue life are the strain-life approach and the fracture mechanics approach, where each represents a distinctly different philosophy. Strain-life techniques are used to determine the crack initiation life at a specimen, while fracture mechanics techniques are usually to predict the crack propagation phase of fatigue life. The crack initiation stage of the fatigue life can be viewed as the number of cycles required for a crack defect at a given size to develop, which can be detected by common technical means, i.e. 1 mm (Radaj, Sonsino, & Fricke, 2006). Fracture mechanics is then used to determine the number of cycles required for the initial crack to grow to a critical crack length, which constitutes failure. In a smooth coupon with no explicit consideration of defects, the components spend most of the fatigue life in the crack initiation stage at low fatigue lives. However, for welded structures where dominant flaws are a direct consequence of welding, the components spend the majority of their fatigue life in the crack propagation phase.

As listed in the IIW recommendations, fracture mechanics is used for the following purposes:

a) to evaluate fractures, especially brittle fracture, in a component containing cracks or crack-like details,

b) to assess the fatigue behaviours in a component containing cracks or crack like defects, such as welded joints, and

c) to predict the fatigue properties of severely notched components (welded joints) with no or a relatively short crack initiation stage.

2.5.1 Linear Elastic Fracture Mechanics

For low toughness material, the critical stress is linearly related to the fracture toughness, K_{IC} in the linear elastic region. Precipitation hardened aluminum 6061 is indicated to have a linear elastic fracture behaviour for which linear elastic fracture mechanics (LEFM) is applicable. The conventional approach considers crack propagation exclusively under mode I

crack tip loading conditions, where the crack growth occurs along the crack plane perpendicular to the applied external loading mode (Radaj, Sonsino, & Fricke, 2006).

LEFM was developed to predict the fatigue behaviour of the structural components containing defects. To apply LEFM concepts, a mathematical relationship between applied stress, and flaw size have to be established. LEFM under constant amplitude loading was verified with the test data at Lehigh University (Menzemer & Fisher, 1993). The LEFM model was further enhanced under variable amplitude loading to simulate more realistic traffic loading data. Three chosen stress spectrums, including constant, linear and Rayleigh stress distributions were applied to obtain the desired stress range values for LEFM analysis. According to a IIW recommendation, the fatigue resistance can be determined by an integration of a fatigue crack growth rate in terms of the fracture mechanics stress intensity factor parameter ΔK. The critical crack size for failure can be found if the fracture toughness K_{IC} is known using the crack propagation equation originally proposed by Paris and Erdogan known as the Paris' law. The crack growth rate during cyclic loading was assumed to follow the Paris' law,

$$\frac{da}{dN} = C \cdot \Delta K^m \text{ if } \Delta K > K_{th} \text{ else } \frac{da}{dN} = 0 \tag{2.15}$$

where,

    C is a material constant of the power law

    m is the exponent of the power law

    ΔK is the range of the cyclic stress intensity factor

    ΔK_{th} is the threshold value of the stress intensity factor range, under which no crack propagation is assumed

    da/dN is the crack growth rate

2.5.1.1 Material Parameters

The material parameters *m* and *C* in the Paris' law (crack propagation) equation solely depend on the stress ratio and material's composition and microstructure with certain environmental conditions (Radaj, Sonsino, & Fricke, 2006). The IIW recommendation listed values in Table 2.15 for the parameters of the Paris' law in the absence of measured parameter data.

Table 2.15 Parameters of the Paris' power law and threshold data for aluminum

Units	Paris power law parameters	Threshold values ΔK_{th}			
		$R \geq 0.5$	$0 \leq R \leq 0.5$	$R < 0$	Surface crack depth < 1 mm
K [N · mm$^{-3/2}$] da/dN [mm/cycle]	$C_0 = 1.41 \cdot 10^{-11}$ m = 3.0	21	56.7– 72.3 · R	56.7	≤21
K [MPa√m] da/dN [m/cycle]	$C_0 = 4.46 \cdot 10^{-10}$ m = 3.0	0.7	1.8– 2.3 · R	1.8	≤0.7

Several approximations have been proposed in respect of the influence of the stress ratio (inclusive of welding residual stresses) on the threshold stress intensity factor (Radaj, Sonsino, & Fricke, 2006).

$$\Delta K_{thR} = \Delta K_{th} \cdot (1 - R) \tag{2.16}$$

where,

R is the stress intensity factor ratio $R = K_{min}/K_{max}$

ΔK_{th} is the stress intensity factor for $R = 0$

ΔK_{thR} is the threshold stress intensity factor for $R > 0$

The IIW recommendation for aluminum alloys:

$$\Delta K_{th} = 63N/mm^{3/2} \ (R = 0) \tag{2.17}$$

$$\Delta K_{thR} = (63 - 48R)N/mm^{3/2} \ (R > 0) \tag{2.18}$$

2.5.1.2 Initial Crack Size and Aspect Ratio

In numerical LEFM analysis, the initial crack size is directly related to the fatigue strength of the material. In reality, it can always be assumed that all welds contain defects, in the form of porosity, incomplete penetration, sudden geometry changes, and material disturbance. The flaws tend to be in the problematic region from which crack propagates. Detecting flaws in the material using non-destructive methods can be time consuming and costly with inspection limitations. The IIW recommendation assessed welded joints without detected imperfections by using a fracture mechanic method. The initial crack is assumed to occur at multiple locations with openings equal to 0.1 mm. According to Radaj (2006), the initial crack size should not be underestimated, $a \geq 0.1$ mm as the crack propagation life is highly depended on the initial crack size. The aspect ratio a/c is a significant parameter for the stress intensity factor. It has to be taken into consideration in fracture mechanics calculations. The aspect ratio can be illustrated in Figure 2.26.

t = distance to nearest surface   b = distance to nearest edge
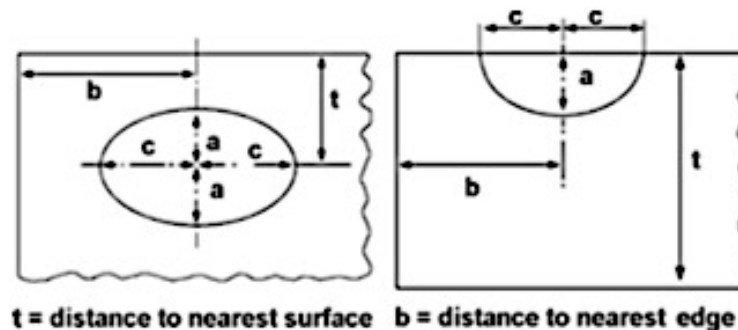
Figure 2.26 Crack parameter aspect ratio

The aspect ratio can be calculated in different ways:

a) Direct determination and calculation of crack growth in c-direction.
b) Application of formulae and values which have been derived from toes of fillet welds by fitting of experimental data
c) The crack depth of $a = 0.15$ or 0.1 mm may be used to calculate the effective SIF at the surface for crack propagation in c-direction
d) A constant aspect ratio of $a/c = 0.1$ may be taken as a conservative approach

The initial crack sizes were documented in experimental data, and an empirical crack shape expression was developed. Menzemer (1992) observed initial crack size by examining the histogram of 100 measurement using Scanning Electron Microscopy (SEM) tests. Three most frequent initial crack sizes were assumed 0.0127 mm (0.0005 in), 0.0254 mm (0.001 in), and 0.0508 mm (0.002 in). An empirical crack shape that accounts for multiple crack initiations was suggested:

$$c = 3.274 \cdot a^{1.241} \tag{2.19}$$

where,

c is the crack half-width

a is the crack depth

The EUREKA project is similar to the experiment done by Menzemer. Three initial crack sizes were assumed, 0.05 mm, 0.15 mm, and 0.5 mm. An initial crack size of 0.05 mm used in a fracture mechanics analysis was found to best match with the experimental data.

Burk and Lawrence (1978) analyzed by assuming the crack initiation stage is complete. Providing there are no cracks or crack-like defects prior to the start of loading, the crack length was determined under the assumption of a size greater than the threshold crack size, which is defined as,

$$a_{th} = \frac{1}{\pi} \cdot (\frac{\Delta K_{th}}{\Delta S})^2 \tag{2.20}$$

where,

a_{th} is the threshold crack size

ΔK_{th} is the threshold stress intensity factor

ΔS is the applied stress range

By assuming an initial crack size of 0.25 mm (0.01 in), fracture mechanics was employed to determine the fatigue propagation life.

2.5.1.3 Stress Intensity Factor

The stress intensity factor (SIF) range ΔK is a parameter to describe the fatigue behaviour in terms of crack propagation with the SIF for a center crack in an infinite plate, defined as,

$$\Delta K = \sigma \cdot \sqrt{\pi a} \tag{2.21}$$

where,

σ is the applied stress range

a is one half of the width of the through crack

The prediction of crack growth rate depends on the accuracy of the stress analyses for a structural component. Crack correction factors are applied to account for the differences of crack configurations and geometrical shapes in the structural components. Newman and Raju (1981) used a three-dimensional finite element method to obtain the SIF variations along the crack front for various crack shapes. An empirical equation was presented for the SIF as a function of parametric angle, crack depth, crack length, plate thickness and plate width for a plate subjected to tension and bending loads with the assumption of semielliptical surface cracks in finite elastic plates. The SIF empirical equation combined tension and bending loads is,

$$K_I = (S_t + H S_b) \sqrt{\pi \frac{a}{Q}} F\left(\frac{a}{t}, \frac{a}{c}, \frac{c}{b}, \phi\right) \tag{2.22}$$

where,

Subscript 'I' in K_I denotes the mode of loading, in this case the loading is in mode I for $0 < a/c \leq 1.0, 1 \leq a/t < 1.0, c/b < 0.5, and\ 0 < \Phi \leq \pi$

S_t is the remote uniform tension stress

S_b is the remote outer fiber bending stress for the applied bending moment M

A useful approximation for Q developed by Rawe is given as,

$$Q = 1 + 1.464(\frac{a}{c})^{1.65} \tag{2.23}$$

The boundary correction factor for tension and bending are defined as functions of F and product of H and F respectively. The function F was obtained from a systematic curve-fitting procedure by using a double series polynomial in terms of $a/c, a/t$, and angular function of Φ. The function F is,

$$F = [M_1 + M_2 \left(\frac{a}{t}\right)^2 + M_3 \left(\frac{a}{t}\right)^4]f_\phi g f_w \tag{2.24}$$

where,

$$M_1 = 1.13 - 0.09(\frac{a}{c}) \tag{2.25}$$

$$M_2 = -0.54 + \frac{0.89}{0.2 + \dfrac{a}{c}} \tag{2.26}$$

$$M_3 = 0.5 - \frac{1.0}{0.65 + \dfrac{a}{c}} + 14(1.0 - \frac{a}{c})^{24} \tag{2.27}$$

$$g = 1 + [0.1 + 0.35 \left(\frac{a}{t}\right)^2](1 - sin\phi)^2 \tag{2.28}$$

The function f_Φ, an angular function from the embedded elliptical-crack solution, is

$$f_\phi = [\left(\frac{a}{c}\right)^2 cos^2\phi + sin^2\phi]^{\frac{1}{4}} \tag{2.29}$$

The function f_w, a finite-width correction, is

$$f_w = [sec\left(\frac{\pi c}{2b}\sqrt{\frac{a}{t}}\right)]^{\frac{1}{2}} \tag{2.30}$$

The function H, developed herein also by curve fitting and engineering judgment, is

$$H = H_1 + (H_2 - H_1)\sin^p \phi \qquad (2.31)$$

where,

$$p = 0.2 + \frac{a}{c} + \frac{0.6a}{t} \qquad (2.32)$$

$$H_1 = 1 - \frac{0.34a}{t} - \frac{0.11a}{c}\left(\frac{a}{t}\right) \qquad (2.33)$$

$$H_2 = 1 + G_1\left(\frac{a}{t}\right) + G_2\left(\frac{a}{t}\right)^2 \qquad (2.34)$$

where,

$$G_1 = -1.22 - \frac{0.12a}{c} \qquad (2.35)$$

$$G_2 = 0.55 - 1.05\left(\frac{a}{c}\right)^{0.75} + 0.47(\frac{a}{c})^{1.5} \qquad (2.36)$$

The empirical equations solutions were within ±5% of the finite element results if $a/t \leq 0.8$. Otherwise, the accuracy has not been established. The correcting factors account for the following parameters: crack shape, distance from an edge, finite width, wall thickness, and embedded crack located inside of a plate.

Chapter 3
Testing Program

The primary objective of the testing program described in this chapter is to support the development of improved "performance-based" code provisions for the quality control and fatigue design of FSW joints by examining the decrease in fatigue strength of FSW joints with intended flaws. In the following sections of this chapter, the fatigue testing program and the methods used in the metallurgical analysis of the test specimens are described.

3.1 Specimen Design and Fabrication

This section describes the preparation phase prior to fatigue testing. It includes a discussion of the decisions made in the experimental design on such things as the specimen design, the fabrication process, the investigated material types, the defect types, and the testing apparatus.

3.1.1 Specimen Design

Since the FSW joints are of interest of this study, fatigue cracks initiating at the joints were desired. Dog-bone shaped specimens were therefore designed to achieve high stress levels in the FSW joint region. Due to the dimensional constraints of the testing frame, which the maximum specimen width was limited to 90 mm with a minimum grip length of 80 mm. In order to prevent slipping of the specimen during the test, a grip area of 90 mm by 120 mm was chosen. The geometry of the specimen was then determined by modelling the specimen using the FE analysis software ABAQUS to determine the stresses in the specimen under uniform axial loading. The sharper the radius between the wide and narrow regions of the specimen, the higher the stress concentration is; on the other hand, the more gradual the radius, the more material is required – therefore, the radius at the transition from the grip to the FSW region was modelled in ABAQUS to establish the minimum radius that would result in the stress concentration at the transition resulting in a local stress no greater than that in the region of the weld. On this basis, transition radii of 70.25 mm, 85 mm, and 96.5 mm were compared to optimize the design of the dog-bone specimen. A radius of 85 mm was

found to be optimal and was therefore chosen for the design, as it resulted in an acceptably gradual stress concentration transition with a manageable specimen length. The selected geometry of the designed specimen with a transition radius of 85 mm is shown in Figure 3.1.
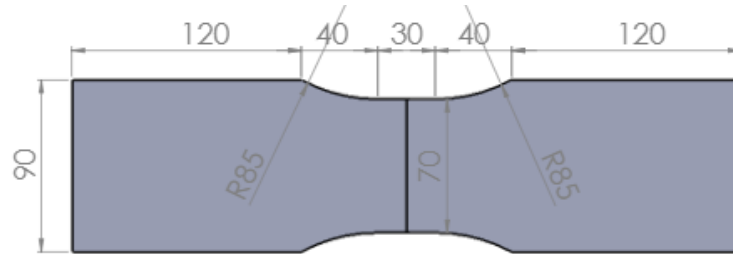

Figure 3.1 Dog-bone specimen (dimensions in mm).

Dog-bone specimens were fabricated from commercially available 3/8" (9.53 mm) thick 6061-T651 aluminum sheets and 0.36" (9.1 mm) thick 5083-H321 aluminum sheets. Both of these materials are widely used aluminum alloys in structural applications in North America due to their high strength, excellent corrosion resistance, and (in the case of 6061) extrudability. Typical physical design variables of 6061 and 5083 alloys are summarized in Table 3.1.

Table 3.1 Physical properties of aluminum alloys

Physical Properties	Unit	6061-T651	5083-H321
Modulus of Elasticity, E	GPa	68.9	70.3
Ultimate Tensile Strength, σ_u	MPa	310	317
Tensile Yield Strength, σ_y	MPa	276	288
Elongation at Break	-	12%	22%

3.1.2 Fabrication Process

To make the welded plates from which the specimens were subsequently fabricated, two plates of equal size (175 mm by 420 mm) were prepared and welded along the rolling direction (see Figure 3.2) in house by Shah – doctoral candidate from the Waterloo MME Department. These were the maximum plate dimensions possible for the milling machine's

backing plate attachment, which was custom made for this research project (note that clamping of the two plates to the table is critical for ensuring that the plates don't spread apart during the welding process).
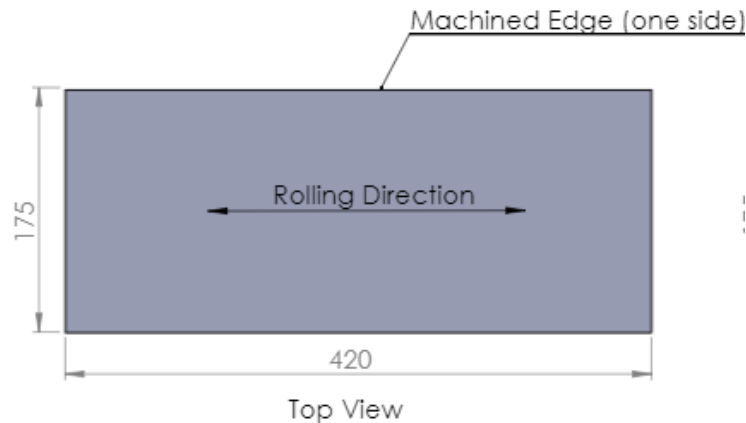

Figure 3.2 Friction stir weld plate (dimensions in mm)

The welding edges were all cleaned before welding to avoid contamination potentially leading to voids and unexpected defects. The plates were held in place using clamps mounting on the backing plate with both vertical and horizontal forces as indicated in Figure 3.3. The joints were welded together with the parameters discussed in Section 3.1.3.
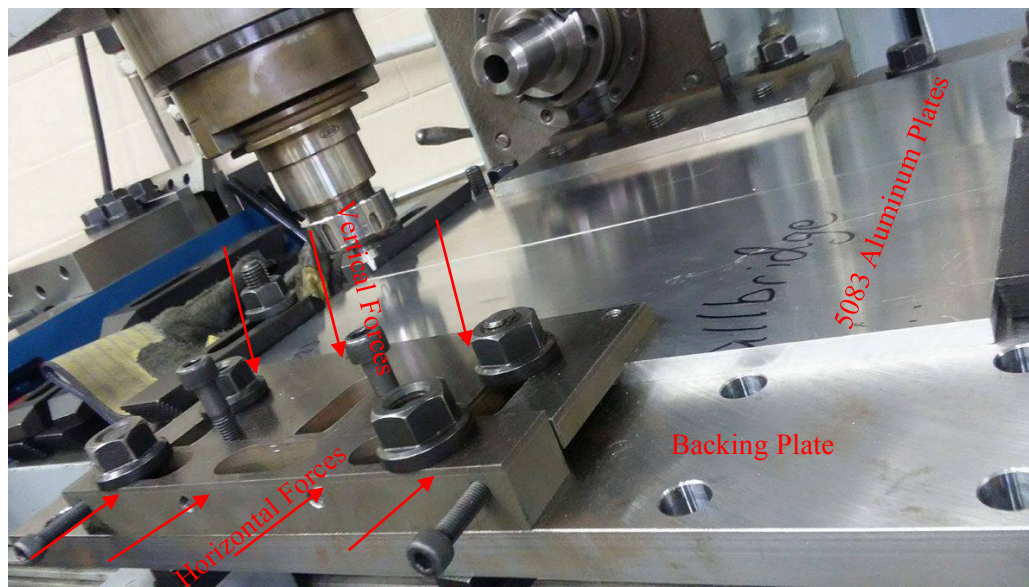

Figure 3.3 FSW setup

A test matrix was developed to allow the effects of different defect types on the fatigue life of the material (listed in Table 3.2) to be determined with a sufficient number of similar specimens fabricated to ensure statistically meaningful results. Spare specimens for each set of tests were made in case problems were encountered in a given test. A minimum of twenty-four pairs of plates were joined together, including 15 pairs of 9.53 mm 6061 plates and six pairs of 9.1 mm 5083 plates. In addition, a special lap joint detail was investigated, which simulated a lap joint between extrusions in a multi-extrusion bridge deck panel. The lap joint detail was customized by grinding down 3/4" (19.05 mm) 6061 aluminum plates to half of their thickness or 3/8" (9.53 mm), but keeping an L-shaped joint geometry on one end. The profile of the lap joint detail is shown in Figure 3.4.
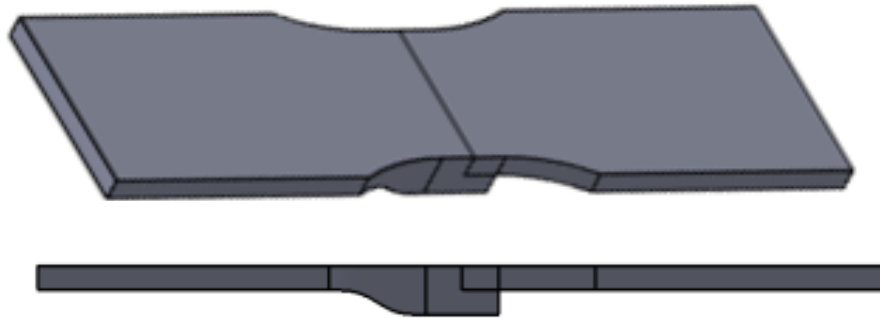

Figure 3.4 Lap joint profile

Each of the FSW joined plates was then cut into four dog-boned specimens using a CNC machine, as illustrated in Figure 3.5. As the spindle was rotating counter-clockwise, the advancing side was as indicated in Figure 3.5 (b). Note that the material between each specimen was saved for subsequent metallurgical analysis. Specifically, the three small pieces between each dog-bone specimen were reserved for further microstructural analysis, as they can represent the weld structure of the fatigue specimens, and can be used for destructive metallurgical testing without damaging the specimens.
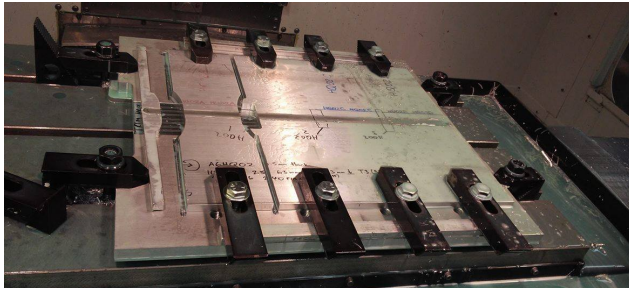
(a) Fabricate specimens in CNC machine   (b) Schematic of the dog-bone specimens
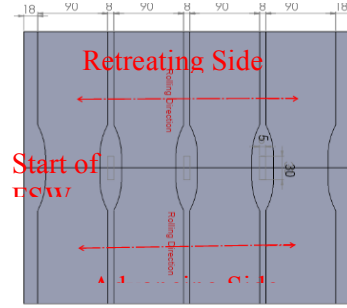
Figure 3.5 Dog-bone specimens fabrication

Each of the specimen was labelled with the type of alloy, the welding conditions, the plate number, and the specimen order using letter and number classifications. Each plate rendered four fatigue specimens, subsequently labeled by letter A, B, C, and D from the start of the weld to the end of the weld. For instance, specimen labelled as A6PW01C is made of 6061 as the third specimen from the start of weld in plate number 01 under properly welded (PW) condition. Seven groups of specimens were tested in this study including: 6061 Properly Welded (A6PW), Polished (A6PL), Kissing Bond (A6KB), Toe Flash (A6TF), Lap Joint (A6LJ), and 5083 Properly Welded (A5PW) and Wormhole (A5WH).

Table 3.2 Fatigue test matrix

Aluminum Alloy	Welding Condition	CA Loading	VA Loading
6061	Properly Welded	5	5
	Polished	5	5
	Toe Flash	5	5
	Kissing Bond	5	5
	Lap Joint	5	5
5083	Properly Welded	5	5
	Wormhole	5	5

70

In general, the penetration depth of the FSW pin is approximately 0.2 mm above the bottom of the welded plate, as the shearing action from the tool pin is sufficient to fuse the weld at the bottom and also to protect the backing plate from deforming due to the high heat input. For the 6061 plate, the penetration depth was 9.3 mm for all conditions with a plate thickness of 9.5 mm, except that the penetration depth for creating the kissing bond defect was 8.5 mm in order to ensure an initial opening at the bottom of the weld and a penetration depth of 11 mm for the lap joint detail was used in order to ensure the weld penetrated through the 9.5 mm plate to create a horizontal initial crack-crack defect. Similarly, for the 5083 plate, the penetration depth was 8.9 mm for 9.1 mm aluminum plates. The optimum travel speed and rotational speed for both 6061 and 5083 are 63 mm/min and 1120 rpm respectively. In order to generate wormhole defects in the 5083 plate material, the travel speed and rotational speed were set at 90 mm/min and 1120 rpm, resulting in less heat input than other welding conditions.

3.1.3 Quality Control

To ensure the desired quality for each weld type, several measurement methods were utilized. Metallographic analysis was performed on scrap weld samples left over from the dog-bone specimen fabrication as indicated in Figure 3.5. By properly documenting the initial specimen condition of each plate, its metallography provides a powerful quality control parameter as well as a valuable investigation tool. The area of interest was preserved by sectioning and casting 5 mm by 30 mm samples in a plastic resin as shown in Figure 3.6.
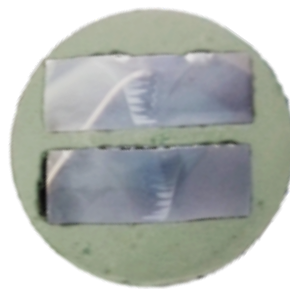

Figure 3.6 FSW sectioning samples in resin

Sectioning was performed in the Engineering Machine Shop (EMS) at the University of Waterloo. The prepared casting resins were polished using planar grinding down to 1 μm diamond media available in the nearby Materials Lab to remove all surface imperfections due to cutting in accordance with *Struers Metallographic Preparation of Aluminum and Aluminum Alloys* manual. Etching was used to optically enhance microstructural features in order to view them in a high-power microscope. Visual inspection was performed for all specimens and each specimen was photographed using a high resolution camera.

3.1.3.1 Properly Welded Condition

All of the properly welded plates were inspected visually to confirm that no major toe flash nor initial crack-like defects were identified possible. In the absence of significant weld defects, the major stress concentration in a specimen containing a transverse butt weld in the proper weld condition occurs at the weld toes. In such cases, it is expected that fatigue failure is most likely to initiate from this location. Thus, the propagating crack is initially located either just in the weld metal or in the HAZ of the parent material at this location.

3.1.3.2 Polished Condition

Any toe flash on the polished plates was first ground down using a milling machine just touching the top surface of the plate as shown in Figure 3.7. Polishing was then performed using 800 fine sand paper. The surface was then measured using a ruler to identify possible geometric variations. Figure 3.8 presents the state of the FSW plates after polishing. Note that the polishing action was performed just over the edge of the weld toe.

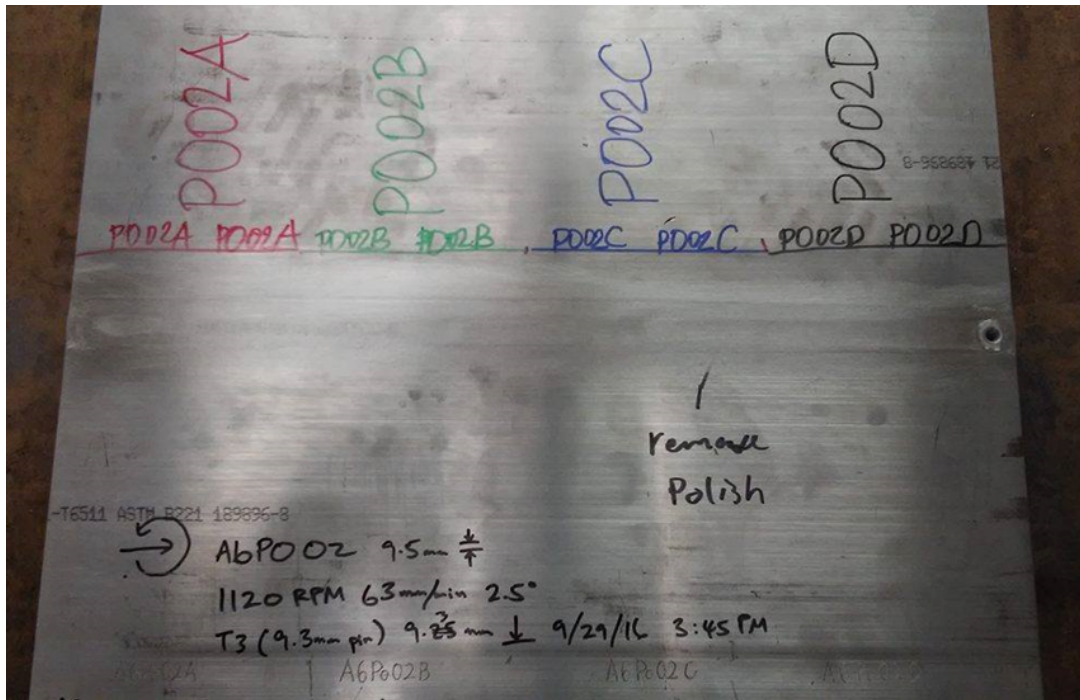**Figure 3.7** Milling of the toe flash for polished condition

Figure 3.8 After polishing

3.1.3.3 Kissing Bond Defect Condition

With a tool pin penetration gap of approximately 1 mm, kissing bond defects with a depth of close to 1 mm were expected for the specimens fabricated with this condition. These bond defects are too small and thin to be seen with the naked eye. The welded plates containing

this defect type were therefore sent to a professional non-destructive test facility: Certified Testing Systems (CTS) in Waterloo, Ontario. Several non-destructive tests (NDT) were performed on the root of the FSW welds, including a radiographic inspection test (RT), a liquid penetrant (LP) inspection, and an ultrasonic inspection (UT). The conclusion from CTS was that the defects were too shallow for UT/RT to detect. Normally a 1.5 mm or greater crack depth would be detectable by these testing methods. However, the LP method suggested that kissing bond defects were present at the root of the plates at various locations as indicated in the report provided by CTS (see Appendix B). Before the fatigue specimens were tested, dye penetrant was applied on the root of the specimens and recorded using a high resolution camera.

Further NDT was performed by Eclipse Scientific (ES) in Waterloo, Ontario using the UT method. Specifically, the tests were performed using the eddy current and ultrasonic phased array method. Different phased array tests were performed using specialized software in the Omniscan MX Phased Array instrument. The 68°, 55°, and 45° linear techniques were implemented for kissing bond Plate 1 with the 45° linear technique illustrated in Figure 3.9 resulting in the best detection capability.
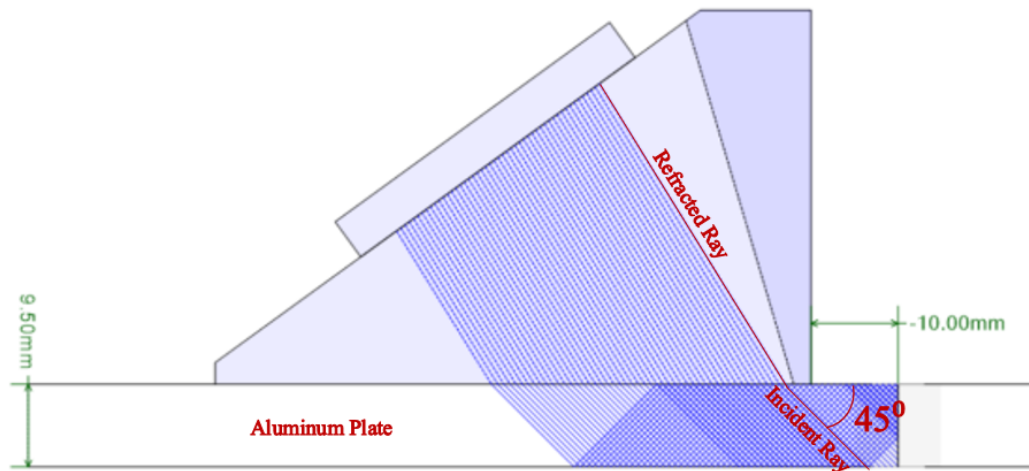

Figure 3.9 45° linear technique used by ES

The 45° linear technique produced the highest amplitude response from discontinuities in the weld. Upon scanning, signals are visible over the full length of the weld as displayed in

Figure 3.10. The flaw height was estimated at 0.8 mm at its larger vertical component, however the corner effect in a 45° beam may oversize the flaw height measurement. The eddy current method is well suited for locating surface breaking defects, so the method was chosen for checking the finds with the ultrasonic phased array scans, although eddy currents cannot give reliable depth estimates. The result indicates that the full extent of the weld produced a signal in the eddy current instrument consisting of a crack-like indication, except for two areas approximately 10 mm long on the scanned Plate 1.
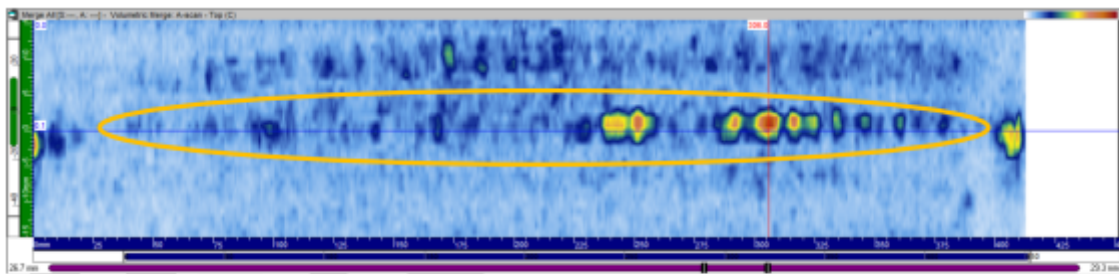

Figure 3.10 Ultrasonic 45° scans result from ES

Plate 2 and Plate 3 were also analyzed by ES. Given the findings from Plate 1, only the 45° setup was used to identify the kissing bond defect.

The full reports from CTS and ES can be found in Appendix B and Appendix C.

3.1.3.4 Toe Flash Defect Condition

The plates with toe flash/underfill defects were made by using the 8.5 mm T3 tool with a penetration depth of 9.3 mm. The resulting weld surface is approximately 1 mm below the parent material surface. The excess material was pushed along the edge of the tool shoulder, resulting in toe flash, which measured 3 to 5 mm in height above the welding surface. The sudden geometry change of the specimen is expected to result in higher stresses around the weld toe, which can reduce the fatigue life compared to a properly welded sample.

3.1.3.5 Lap Joint Condition

The lap joint specimens consist of two portions, one L-shaped portion as shown in Figure 3.4 and one straight portion as shown in Figure 3.2. Due to frictional heat during the welding

process, some distortion of the lap joint was observed. This distortion was quantified using images of the prepared material samples for the defect set.

3.1.3.6 Wormhole Defect Condition

The original plan was to create wormhole defects by increasing the tool travel speed to 350 mm/min, i.e. much greater than the optimum tool travel speed for the 6061 aluminum plates of 63 mm/min. However, the pin thread of the tool broke when this was attempted.

A travel speed of 180 mm/min was subsequently attempted. Unfortunately, the weld created in this way was found to be defect free, with no visible wormhole detected. Another trial run with a travel speed of 250 mm/min was also conducted and found to be defect free.
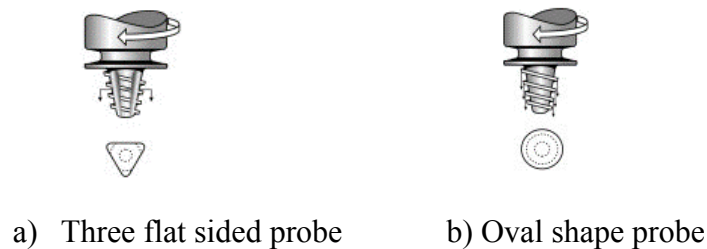

a) Three flat sided probe   b) Oval shape probe

Figure 3.11 Probe shapes

An oval shaped probe (see Figure 3.11) was subsequently used to try to generate wormholes in the 6061 aluminum welds. As suggested by TWI (Thomas, Johnson, & Wiesner, 2003), the flow dynamics using the oval verses three-flat sided probe were expected to increase the chance of producing a defect. However, attempts to create a defect with this tool shape were also unsuccessful. Due to the multiple fail attempts to create wormholes in the 6061 plates, an attempt was made in 5083 by varying the travel speed with 45 mm/min, 90 mm/min, 180 mm/min, and 355 mm/min. The weld cross-sectional macrograph for each speed was inspected for any void formations as shown in Figure 3.12, where the subsurface voids were pointed out by white arrow (Shah, 2017). Therefore, 5083 aluminum alloy was used to generate wormhole defects with a travel and rotation speed of 90 mm/min and 1120 rpm respectively. Surface wormholes were observed and internal wormholes were found using NDT methods performed by ES. The wormholes were observed to range from 1 mm to 3 mm

in the long direction. Further efforts to characterize the wormhole geometry were made subsequently by destructive metallurgical analysis of the weld samples.
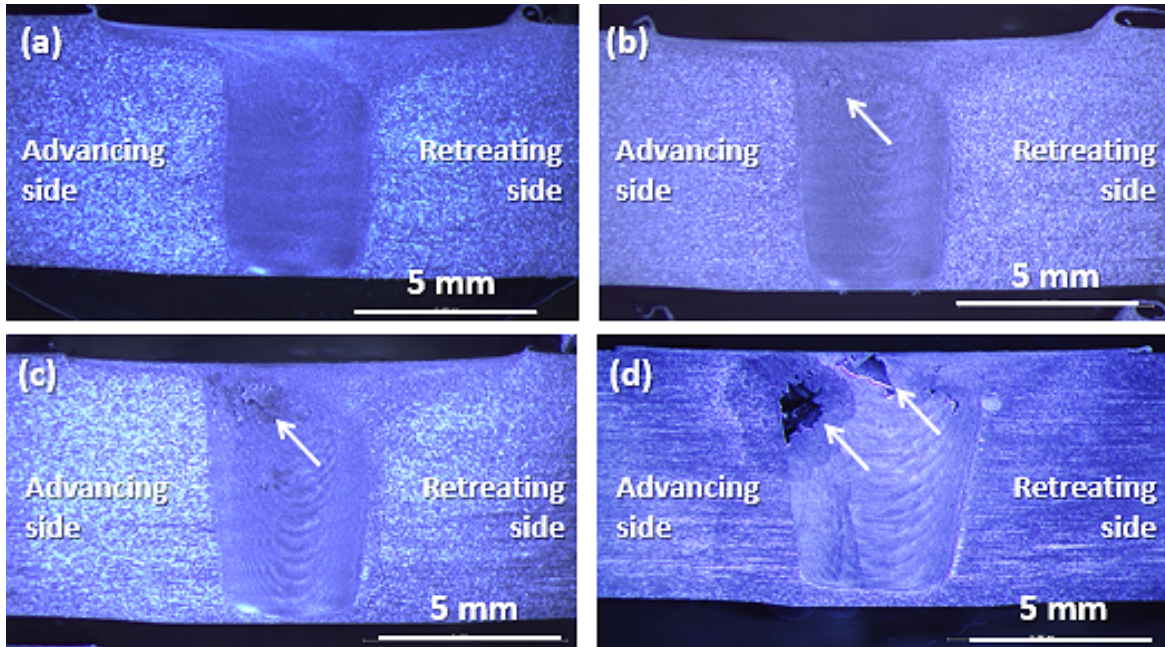

Figure 3.12 5083 weld macrograph with varying travel speed (a) 45 mm/min (b) 90 mm/min (c) 180 mm/min (d) 355 mm/min

3.1.4 Fatigue Testing Program

The fatigue testing program conducted for this study included 92 dog-boned FSW joint details tested under constant (CA) and variable (VA) amplitude, tension only axial loading conditions using a 500 kN MTS structural testing frame.

The testing under CA loading was conducted at an R-ratio (S_{min} / S_{max}) of 0.1 at varied nominal stress ranges, ΔS, to establish the slope and position of the S-N curve for the respective detail categories. A majority of the tests were conducted at stress ranges between 30 to 150 MPa and at a frequency of 10 Hz, except that some tests were run at a frequency of 15 Hz in order to save time for the prolonged lower stress range tests.

Fatigue testing under VA loading was performed using a loading history for a bridge girder subjected to Ontario traffic (generated by passing trucks over the influence line for the

support reaction of a 15 m girder) data to simulate realistic cyclic loading conditions (see Figure 3.13). This history has a total of 29065 stress peaks. A shorter random (1007 peak) sample from this history was extracted and used for the VA fatigue tests.
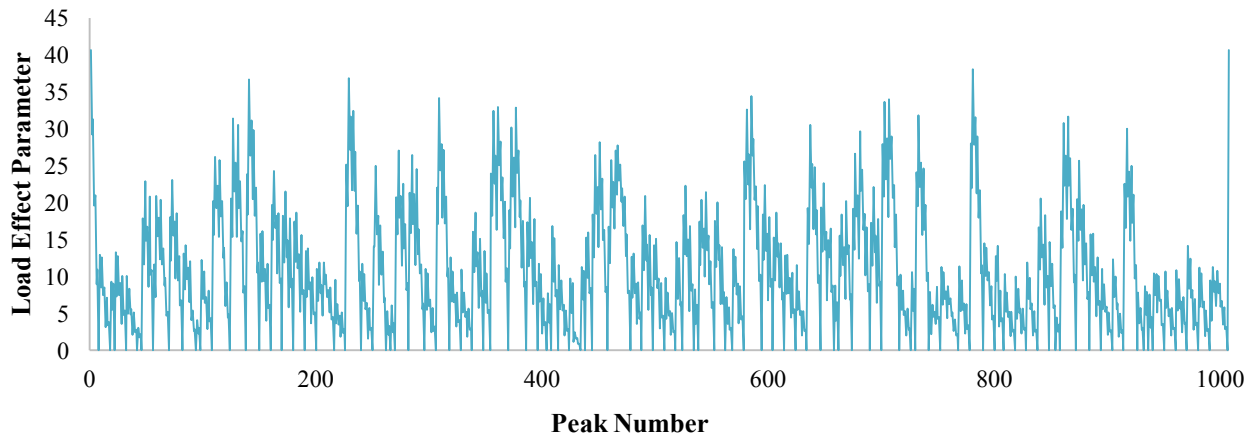

Figure 3.13 Variable amplitude loading history

An R-ratio of 0.1 was maintained for the VA loading tests by scaling/shifting the load history, and equivalent stress ranges were obtained by applying Miner's sum with an S-N curve slope of 4.84 for AASHTO Detail Category B for a single sided transverse butt weld. The specimen cross section areas used to calculate the stress levels were the nominal areas of 666.75 mm^2 and 637 mm^2 for the 6061 and 5083 plates respectively, unless otherwise specified. For plotting the test results, the cross-sectional area of the FSW region in each dog-bone specimen was measured using a caliper, and the results were adjusted based on the true measurement. The matrix (specimen and loading type, stress range, stress ratio, and frequency) for the fatigue testing program is reported in the fatigue testing results section.

3.1.5 Fatigue Testing Equipment

An MTS structural testing frame was used for the fatigue tests. This frame is part of an integrated testing system with a load range from 5 kN to 500 kN, equipped with hydraulic controls, hydraulic power and hydraulic actuated grips as shown in Figure 3.14. The axial loading is applied using a closed-loop servohydraulic controller connected to a personal computer. The principle of operation includes generating an input signal of load, strain, or

displacement using a function generator, applying this input through a hydraulic actuator, and finally measuring the specimen response via a load cell, a clip gage, or a linear variable differential transducer (LVDT) and comparing the measured response with the specific input. Operation of the frames is controlled using a personal computer and commercial software.

Figure 3.14 MTS material testing system

The MTS Station Manager Software package uses MultiPurpose TestWare® to meet the demands of the test requirements, including performing CA and VA loading spectrums and setting station limits. The fatigue testing was conducted under load control with varying ranges. The peak axial loads and displacements were recorded in a text file through the MTS MultiPurpose TestWare® software. The hydraulic actuated grips are 100 mm wide by 80 mm in length. One end of the specimen is placed in the stationary grip at the bottom, and the other end is placed to the crosshead at the top of the test frame, which is able to rotate. Two L-shaped brackets were carefully placed on the opposite sides of the crosshead on the top and the bottom. A specimen strain gauged on each side near the welds (see Figure 3.15) was

79

prepared and loaded statically in order to adjust the crosshead and the brackets for the specimen to be loaded vertically without bending stresses. The durations of the fatigue tests were governed by the specimen's fatigue lives to failure at a cycling frequency (e.g. 10 or 15 Hz). The station limits for axial load and axial displacement were set to trip at the onset of specimen failure, stopping the test if the axial load or displacement changes dramatically. The axial load limit was set to ±5 kN which, if exceeded, stopped the test due to excessive drift of the applied load peaks. The axial displacement limits were set to ±0.2 mm which, if exceeded stopped prior to complete specimen failure. With the axial displacement limits set, the tests generally stopped around the time that a visible crack first appeared.
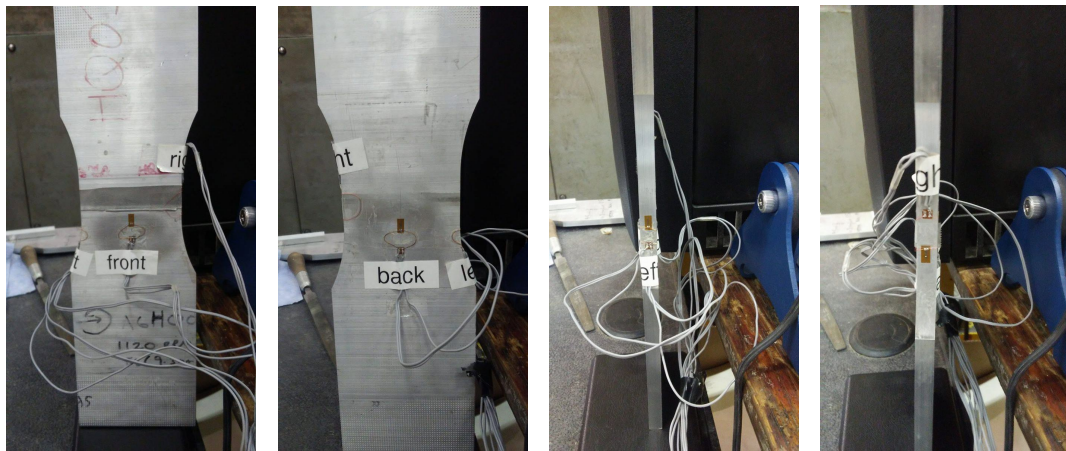
(a) Front   (b) Back   (c) Left   (d) Right

Figure 3.15 Strain gauged dog-bone specimen

Dye penetrant, Magnaflux Spotcheck SKL-SP1 was used to detect any cracks that are not easily seen by the naked eye and to obtain the crack shape when the crack first appeared. The dye penetrant was allowed to cure for a minimum of 3 hours. The specimen was then cyclically loaded to complete failure, under the same loading conditions. Upon complete failure, where the specimen was separated into two pieces, a crack shape was fit to the dye penetrant region of the failure surface to obtain the pre-failure crack shape measurements. In this way, the half semi-elliptical width and depth can be measure for all specimens tested.
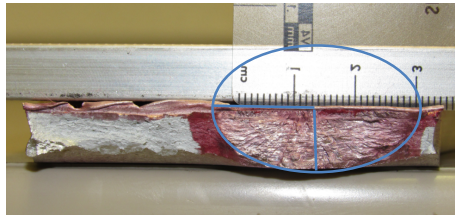
Figure 3.16 Failure surface of A6PW01C

A specimen photo is shown in Figure 3.16 to illustrate the crack shape measurement for a test specimen where the crack initiated from the weld toe.

3.2 Microhardness Testing

The frictional heat generated during the welding procedure for heat-treated alloys, such as the 6061-T651 aluminum alloy will alter the material properties in the vicinity of the weld. This phenomenon can be investigated through microhardness measurements. The hardness profile along the middle of the weld covering BM, TMAZ, HAZ and NZ was measured for this purpose.

3.2.1 Microhardness Testing Program

For each weld type, microhardness tests were performed on seven samples, including 6061 (PW, PO, KB, TF, LJ) and 5083 (PW, WH). The specimens were prepared by cold-mounting the small samples obtained during the fabrication phase into epoxy resins as shown in Figure 3.17. The mounted samples were then polished and etched to reveal the microstructural details in accordance to *Struers Metallographic Preparation of Aluminum and Aluminum Alloys* manual in collaboration with Shah.

Each specimen was subjected to Vickers microhardness testing along a horizontal cross-section of the weld profile at mid-thickness with approximately 57 points 0.5 mm apart as shown in Figure 3.17. Additionally, a square of 9 points 0.5 mm apart was measured to determine the hardness at the crack initiation point as indicated in Figure 3.17. For the specimen with a toe flash defect, the initiation crack point occurred at the weld toe of the advancing side.
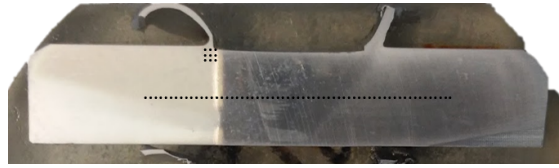
81

Figure 3.17 Traverse cross-section of welded specimen (toe flash), with testing locations of microhardness indentation indicated by dots

3.2.2 Microhardness Equipment

For the microhardness testing, a 200 g force load was applied with a 10 s dwell time using the Vickers hardness machine to indent the surface, leaving a diamond shaped indent. An optical microscope was used to measure the dimensions of the Vickers indents by adjusting two parallel lines in the microscope display. After measuring the diagonal dimensions D1 and D2, the Vickers hardness can be calculated for each indent.

Figure 3.18 Vickers hardness apparatus

3.3 Microstructural Analysis

Microstructural analysis is indispensable for determining the weld joint quality through observations of the weld region grain sizes or potential defects. Due to the distinct thermal cycles in the different regions along the welding profile, the microstructural grain sizes of each region including the TMAZ, HAZ, and nugget zone show observable differences from the BM. The HAZ regions were negatively affected (softened) during the welding process

due to the thermal cycle caused by the weld process. Microstructural analysis is also an inexpensive way to examine external and internal defects present in the weld region in comparison with other non-destructive testing methods.

3.3.1 Microstructural Analysis Program

The microstructural analysis program was conducted in parallel with the fatigue testing program in collaboration with doctoral candidate L. Shah. With three 8 mm by 50 mm samples cut in the transverse direction through each welded plate, there were 84 samples in total. Not all of the prepared samples were tested – only the ones expected to yield results of interest for this study. Table 3.3 shows the number of samples and expected microstructural characteristics for each defect type.

Table 3.3 Microstructural samples

Aluminum Alloy	Defect Types	Samples	Characteristics
6061	Proper Weld	12	no significant defect
	Polished	6	leveled welded surface
	Kissing Bond	8	lack of penetration at the weld root
	Toe Flash	9	enhanced geometry change at weld toe
	Lap Joint	9	horizontal gap due to plate overlap
5083	Proper Weld	12	no significant defect
	Wormhole	15	inclusions or porosity
Total		84	

The cut-out samples were also observed using a Scanning Electron Microscope (SEM), which is able to produce cross-sectional images of the samples at a much higher magnification. The specimen topography was captured and saved digitally for identifying any defect.

3.3.2 Microstructural (SEM) Equipment

Resin samples with an approximate diameter of 4 mm were prepared to fit in the specimen chamber of the SEM equipment as shown in Figure 3.19. The SEM was able to generate topographical images of each weld sample in a digital form for subsequent metallurgical analysis.
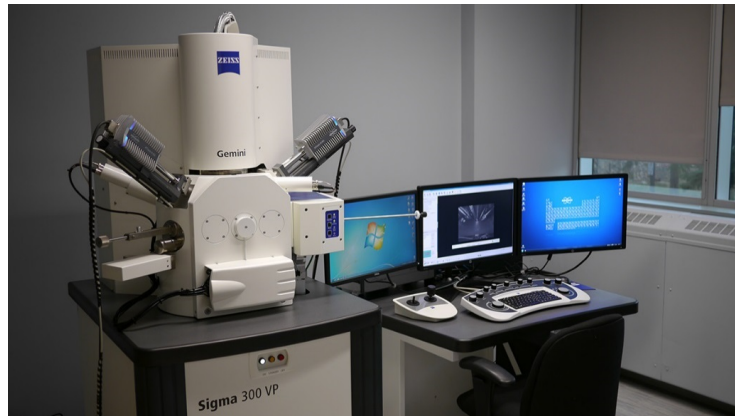

Figure 3.19 Scanning electron microscope

Chapter 4

Evaluation of Fatigue Testing Results

Fatigue testing results for various butt-welded, dog-bone specimens under constant and variable amplitude load histories are presented and analyzed in this chapter. A general testing plan was presented in Chapter 3. This chapter outlines the fatigue testing results, and microhardness results.

4.1 Fatigue Testing

Results of the fatigue tests under constant and variable amplitude loading with R-ratio of 0.1 on various 6061 and 5083 butt-weld dog-bone specimens are presented in this section. The conditions of each specimen prior to the fatigue testing were discussed in Section 3.1.3, which described the associated characteristics of the weld. The tests were conducted using the equipment and test procedures outlined in Section 3.1.5.

4.1.1 Fatigue Test Results

The CA fatigue tests were conducted with different stress ranges and the VA fatigue tests were conducted with the proposed loading history shown in Figure 3.13. The experimental fatigue test results are presented in four figures with the proper weld specimens as a baseline for both 6061 and 5083 aluminum alloys, including:

i. Figure 4.1 – S-N Curves of 6061 proper welds (A6PW) and 6061 polished welds (A6PO)

ii. Figure 4.2 – S-N Curves of 6061 proper welds (A6PW) and 6061 toe flash defects (A6TF)

iii. Figure 4.3 – S-N Curves of 6061 proper welds (A6PW), 6061 kissing bond defects (A6KB), and 6061 lap joint specimens (A6LJ)

iv. Figure 4.4 – S-N Curves of 6061 proper welds (A6PW), 5083 proper welds (A5PW), and 5083 wormhole defects (A5WH)

The stress-life test results are plotted on log-log scales, and the results are compared with the ADM design curve of Detail Category B, which is representative of a full-penetration butt-weld made from one side and an ADM design curve of Detail Category A for base metal as a reference. The CA results are plotted as solid markers, whereas the VA results are plotted with hollow markers, all of the runouts are represented with arrows. A detailed report recording measured cross sectional area, type of loading, stress range, stress ratio, location of fracture, etc. is attached in Appendix D for reference.

i.   **6061 Proper Welds (PW) vs. 6061 Polished Welds (PO)**

Both CA fatigue data shown as solid square and diamond in Figure 4.1 for A6PW and A6PO indicated limited scatter, and they can be modelled with straight lines of slope (Equation 2.2) -3.48 and -3.15 respectively on a log-log scale.
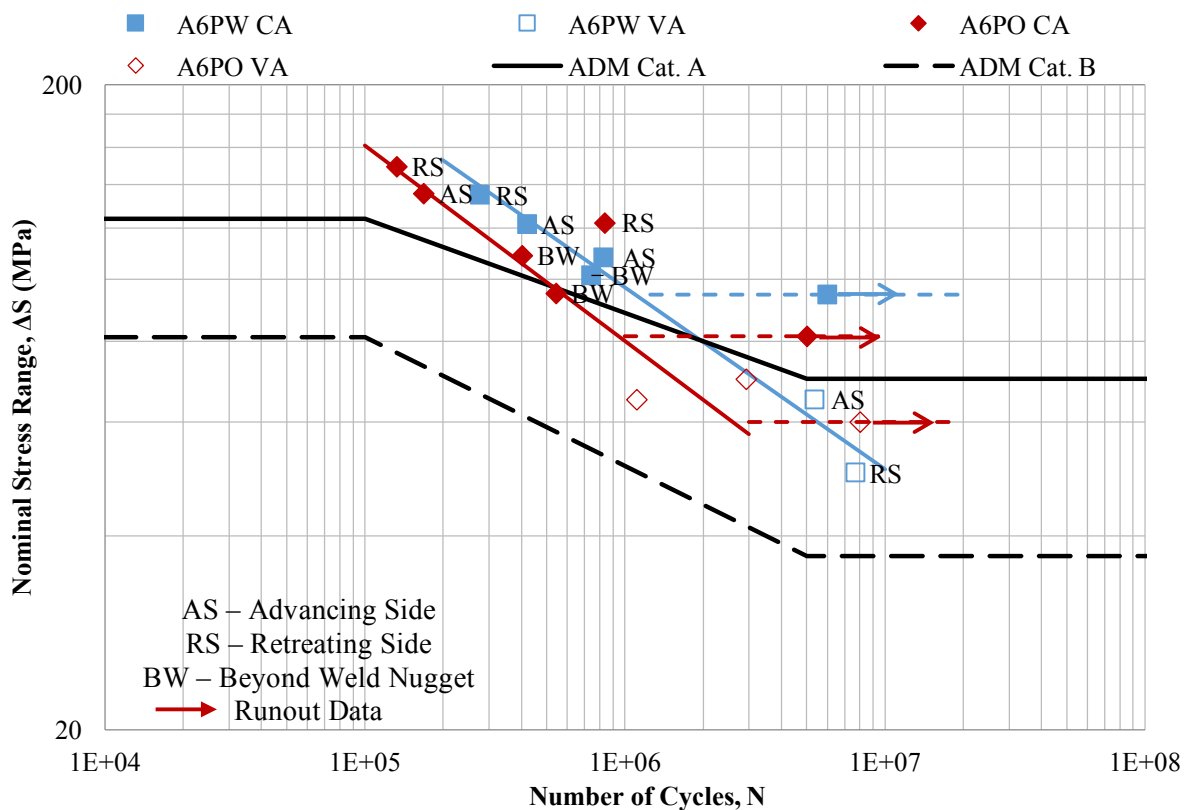

Figure 4.1 Fatigue test results of 6061 proper welds (A6PW) and polished (A6PO) FSW joints compared with ADM curves

Their correspondent CAFLs were estimated to be 94.5 MPa and 81.5 MPa based on the nearest fractured specimens and limited by the intercept of the best fit line with a fatigue life of 5 million cycles (note: horizontal gridlines in Figure 4.1 indicate increments of 20 MPa). It was noted that the A6PO S-N curve has a similar slope with the A6PW S-N curve at a lower CAFL. Based on the results, it did not appear that polishing improved the fatigue performance. However, it should be noted that fractures mainly initiated from the side of the machined section, and not the milled top surface, and so these edge surfaces may have played an overriding role in the fatigue performance after milling the top surface. However, both A6PW and A6PO mean design curves were "safe" according to the Category B butt welded design curves in the ADM standard. Since aluminum alloy types were not specified in the standards, the design S-N curves in both standards were conservative in comparison with the experimental A6PW and A6PO S-N curves for aluminum alloy 6061.

The VA fatigue test results shown as hollow square and diamond in Figure 4.1 for both A6PW and A6PO were plotted using equivalent stress range, ΔS_{eq} calculated by applying Palmgren-Miner's rule as outlined in Section 2.3.3. Detailed sample calculations are included in Appendix E. The variable amplitude tests were conducted at an equivalent stress range, where the maximum stress was below the yield stress of the welded material. The VA test data and the CA test data for A6PW were fitted with one straight line in log-log scales, where a slope (Equation 2.2) of -3.48 was adopted. Due to the steeper slope of A6PW fatigue test data for variable amplitude loading than slope of the corresponding ADM standard, an equivalent stress range below 37.16 MPa or 20 MPa would not pass the ADM standards for the A6PW FSW design. The CAFL for polished specimens was estimated to be 60 MPa and additional specimens for proper welds are to be conducted to obtain the CAFL under VA loading.

ii.   6061 Proper Welds (PW) vs. 6061 Toe Flash Defects (TF)

The CA A6TF results are shown as circles in Figure 4.2. The mean S-N curve for CA A6TF has a slope of -4.74 based on calculation of Equation 2.2. Both of the mean S-N curves for A6PW and A6TF shared similarities in slopes. However, due (it is hypothesized) to the

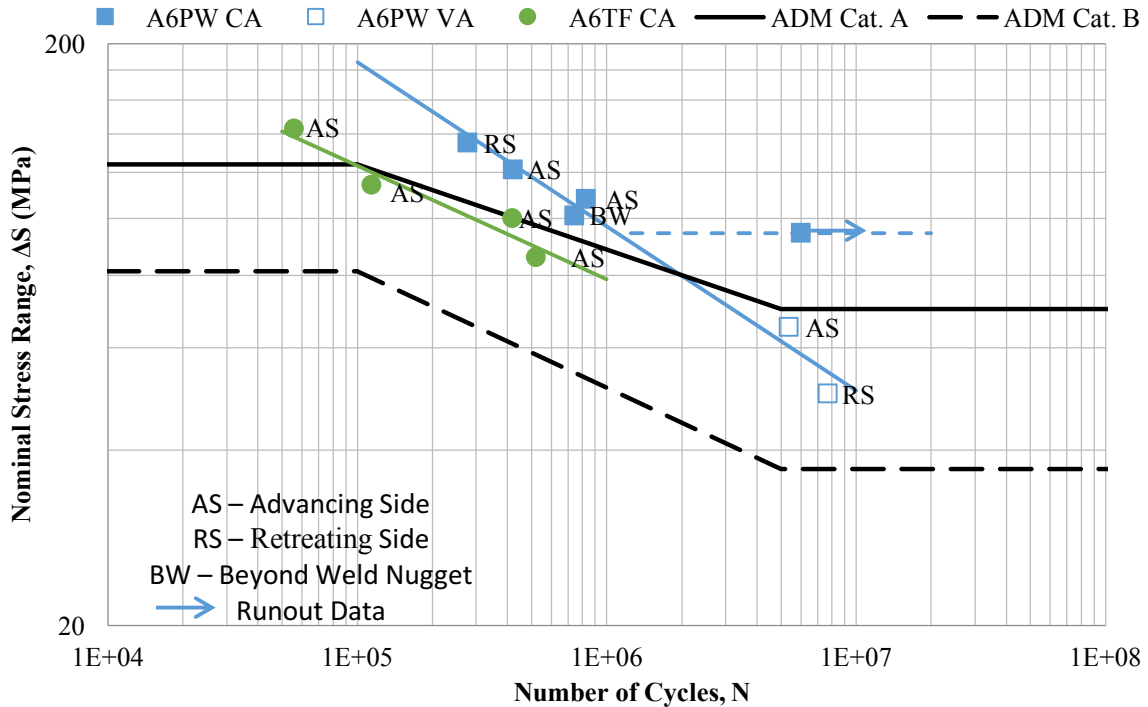reduction in area and sudden geometry change at the weld toe, a significantly lower fatigue life was observed.

Figure 4.2 Fatigue test results for 6061 proper welds (A6PW) and toe flash (A6TF) FSW joints compared with ADM curves

The fracture locations consistently occurred at the advancing side of the weld for the A6TF specimens. This is consistent with the finding that higher stress concentrations were observed on the advancing side over the retreating side as a result of the asymmetric stirring action. Only four constant amplitude A6TF tests were conducted due to unexpected weld root (WR) failures as a result of potential kissing bond defects found in the following tests. Even with a reduction of approximately 1 mm or 10% in thickness, the A6TF fatigue results were still above the ADM Detail Category B design curve for butt welds made from one side.

iii.   **6061 Proper Welds (PW) vs. 6061 Kissing Bond Defects (KB) and 6061 Lap Joint Specimens (LJ)**

Both A6KB and A6LJ specimens were fabricated with an initial crack-like weld root (WR) and hook opening (HK) defect, which caused a significant reduction in fatigue life (see

Figure 4.3). Both of the fatigue test results exhibit minimal scatter, and were fitted with straight power lines with slopes of -4.95 and -3.80 calculated based on Equation 2.2, respectively, for their CA S-N curves.
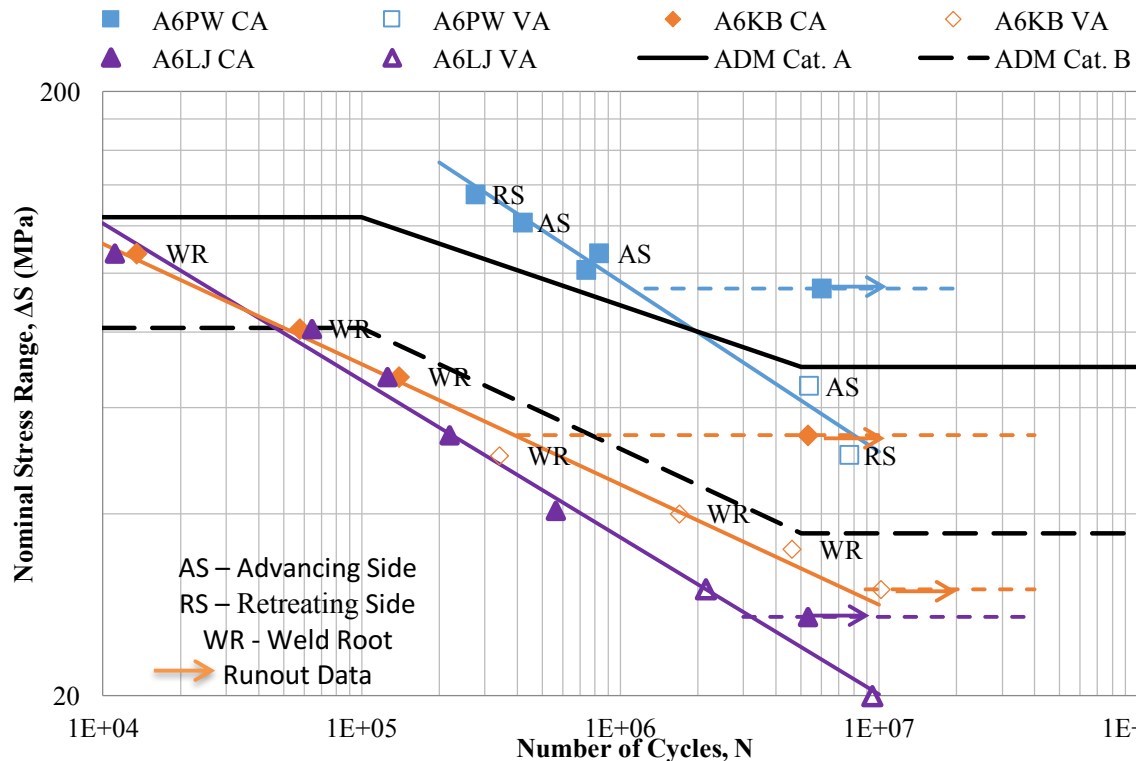

Figure 4.3 Fatigue test results for 6061 proper welds (A6PW), kissing bond (A6KB), and lap joint (A6LJ) FSW joints compared with ADM curves

The corresponding CAFLs were determined to be 54 MPa and 27 MPa based on the closest fracturing specimen with a fatigue life below 5 million cycles. The LJ specimens had a lower CAFL value than the KB specimens, which suggests that the fatigue performance of the LJ specimens is slightly worse than the specimens fabricated with a KB defect. This could be due to the LJ specimens having a larger initial crack-like defect or out-of-plane bending stresses due to the non-symmetrical geometry of the lap joint specimens.

The VA fatigue test results shown as hollow diamonds and triangles in Figure 4.3 for the A6KB and A6LJ specimens were plotted using an equivalent stress range, ΔS_{eq} calculated by applying Palmgren-Miner's rule as outlined in Section 2.3.3. The variable amplitude tests

were conducted at lower equivalent stress ranges, where the maximum stress was around the CAFL. Due to limited VA test data obtained, the slopes of mean S-N curves for A6KB and A6LJ VA fatigue test data were assumed to be the same for their corresponding CA slopes. The data sets for both specimens clearly fall below the equivalent butt welded Category B in the ADM standard. It can therefore be concluded that the defects present in these specimens should either result in rejection – if detected – or the requirement to design the weld using a lower detail category (e.g. C or D).

iv.   6061 Proper Welds (A6PW) vs. 5083 Proper Welds (A5PW) and 5083 Wormhole Defects (A5WH)

The constant amplitude loading fatigue test results for the A5PW specimens shown limited scatter with a slope of -15.15 (calculated based on Equation 2.2), which has a dramatically different slope than the A6PW specimens as shown in Figure 4.4.
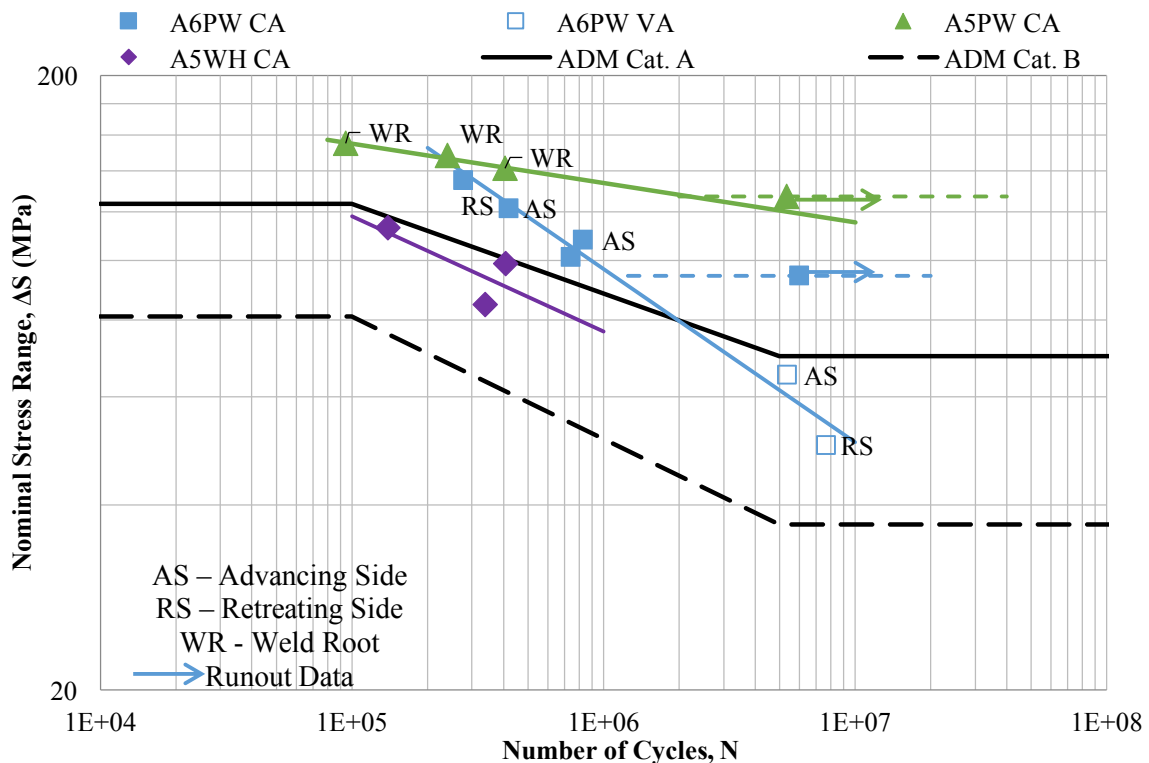

Figure 4.4 Fatigue test results of 6061 proper welds (A6PW), 5083 proper welds (A5PW) and wormhole (A5WH) FSW joints compared with ADM standards

90

In comparison with the A6PW welds, A5PW welds exhibited a higher CAFL. It is hypothesized that this is because there was a softening effect of the HAZ in the heat-treatable alloy 6061 during the FSW process, where the precipitation hardening was disturbed. As a result, the fatigue loading applied to the A6PW welds would result in local plastic deformation in the softer zone at a lower nominal applied stress range than it would for the A5PW welds. Similar conclusions to those made for the A6PW welds can also be made for the A5PW welds in comparison with the ADM design curves. The test results are well above both design curves, suggesting that a higher design curve for properly welded FSW joints may be warranted. In order to make such a change with confidence, however, further testing with large-scale specimens and a wider range of alloys would be needed.

Due to the inconsistency in wormhole production for each A5WH specimen, the fatigue test results exhibited a much higher degree of scatter with a straight line slope of -2.97. One of the specimens, with a particularly large defect, was tested at 71 MPa and had a fatigue life of 2951 cycles, which is below the horizontal axis range in Figure 4.4. The surface wormhole (see Figure 4.5) acts as an initial discontinuity, which significantly reduces or eliminates the crack initiation life.

(a) A5WH01C weld surface   (b) A5WH01D weld surface

Figure 4.5 Surface conditions of 5083 WH defect specimens

4.2 Crack Shape Measurements

The final fatigue crack shape prior to fracture was examined for all tested fatigue specimens. Due to the variation in the final fracture condition, out of the 46 fractured specimens, only 20 semi-elliptical shapes on the specimens fracturing surface can be clearly identified and measured, including 14 for the 6061 alloy and 6 for 5083. In general, these fatigue cracks initiated at the weld toe on either the AS or RS. Cracks emanating from weld root defects, tended to be linear (i.e. with $a/c = 0$), as these defects tended to extend across the entire specimen width. A histogram of the measured crack shapes for the aluminum 6061 and 5083 alloys is presented in Figure 4.6, and photos of each fracture surface are included in Appendix F for reference.
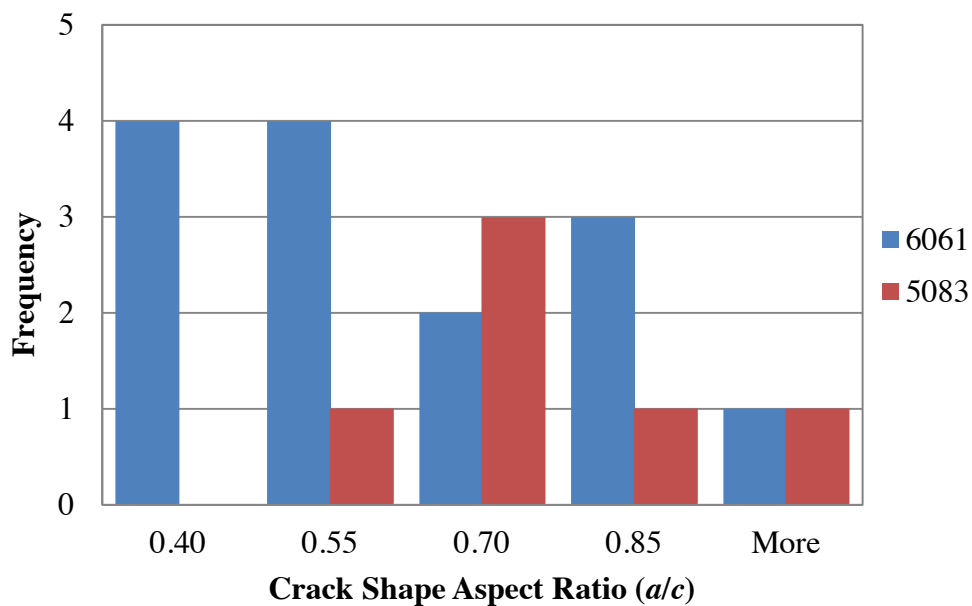

Figure 4.6 Histograms of measured crack shape aspect ratios

For the 6061 alloy, the mean crack shape aspect ratio of the 14 semi-elliptical crack shapes (on 13 fractured specimens) measured had an average value of 0.55 and a standard deviation of 0.19 as shown in Table 4.1. The maximum and minimum crack shape aspect ratios measured were 0.88 and 0.25, respectively.

Table 4.1 Summary of crack shape ratio for 6061 and 5083

Descriptions	6061	5083
Semi-Elliptical Shapes	14	6
Fractured Specimens	13	5
Average Ratio	0.55	0.65
Max Ratio	0.88	0.99
Min Ratio	0.25	0.43
Standard Deviation	0.19	0.20

Similarly, for the 5083 alloy, the measured mean value for the 6 semi-elliptical crack shapes (on 5 fracture specimens) was 0.65 with a standard deviation of 0.20 as shown in Table 4.1. The maximum and minimum crack shape aspect ratios were 0.99 and 0.43. The obvious difference between the selected aluminum alloy materials was the minimum value of the crack shape ratio. A higher value for the minimum crack shape aspect ratio was observed for the 5083 alloy, indicating "rounder" crack shapes in comparison with the 6061 alloy. Due to the limited number of measurable shapes obtained, variations can exist for the measurements in Table 4.1.

The measured crack shape ratios in this study were plotted against the empirical equation (2.19) proposed by Menzemer in Figure 4.7. It can be seen that there is no clear trend in the measured data in terms of a relationship between crack depth and aspect ratio. All of the measured data falls above the empirical equation proposed by Menzemer (1992). However, it is important to note that the detail on which Menzemer performed his crack shape measurements was a cruciform weld detail, which has a higher stress concentration at the surface than a butt joint, which explains why his model predicts a lower aspect ratio.
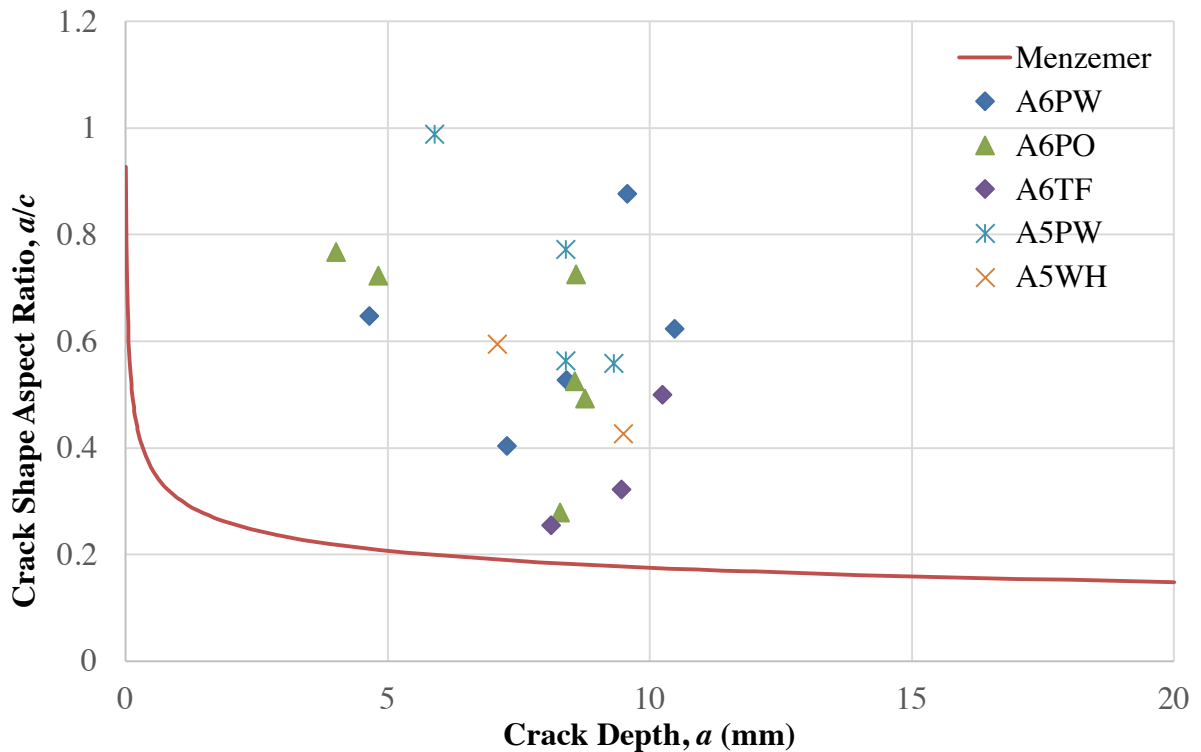
Figure 4.7 Crack shape measurements

4.3 Microhardness Testing

Microhardness specimens were fabricated concurrently with the dog-bone specimens by cutting a 5 mm by 30 mm rectangular samples between the two dog-bone specimens using a CNC machine. The detailed specimen fabrication drawings were drafted in Solidworks and are shown in Appendix G. Microhardness measurements were conducted on the A6PW, A6TF, A6LJ, and A5PW welds at their mid-thickness and critical fracture points. Due to the marginal differences in welding parameters from the properly welded samples, the microhardness studies were only exercised at the critical fracture points for the A6PW, A6TF, A6KB, A6LJ and A5PW welds. The aim for this microhardness testing was to provide data for indirectly determining other material properties in the four different weld regions, and the most critical points in the samples, which are highly correlated with hardness.

4.3.1 Microhardness Testing Results

The microhardness tests were performed using a Vickers hardness scale, with the following expression,

$$HVN = \frac{1854.4 \cdot F}{d^2} \tag{4.37}$$

where, HVN is Vickers hardness

F is the load applied by the indenter in grams

d is the pyramid diagonal length in micrometers

The diagonal length of the pyramid was measured by adjusting the angle and distance of two parallel lines under the microscope as shown in Figure 4.8.
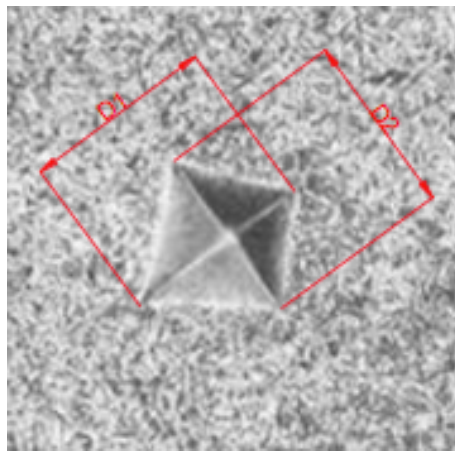

Figure 4.8 Vickers hardness measurements

Vickers hardness measurements were made at approximately 57 locations at 0.5 mm intervals across the middle of the 9.53 mm thickness, and a 3 by 3 square of indentations 0.5 mm apart were also made to measure the hardness at the most critical fracture locations.

Since the welding parameters were kept the same for 6061 properly welded, polished, and kissing bond specimens, they were assumed to share a similar hardness profile represented by the A6PW (Shah, 2017) specimen in Figure 4.9. Between the A6PW, A6TF, and A6LJ samples, the measured hardness profiles varied marginally from each other. The hardnesses

measured in HAZ regions were the lowest on each side for the heat-treatable 6061 alloy, forming a "W" shaped hardness profile for the A6PW, A6TF, and A6LJ samples. This softening phenomenon in the HAZ was a result of coarsening of the strengthening precipitates during the welding process. The crack initiations were expected to take place on the advancing side (AS) for the 6061 PW specimens, where there is an obvious change in hardness profile. This finding aligned with the results of the fatigue tests, where more than 60% of the samples were observed to fracture on the AS.

The hardness profile in Figure 4.9 also suggests that the fatigue strength for the non-heat-treatable 5083 alloy (Shah, 2017) was less influenced by heat during the FSW process, therefore resulting in a higher hardness profile than the 6061 alloy. The measured hardnesses across the weld profile for the 5083 alloys were relatively flat with negligible hardness changes across the welding profile, which may explain why the fracture locations for the 5083 alloys were consistently at the weld root.
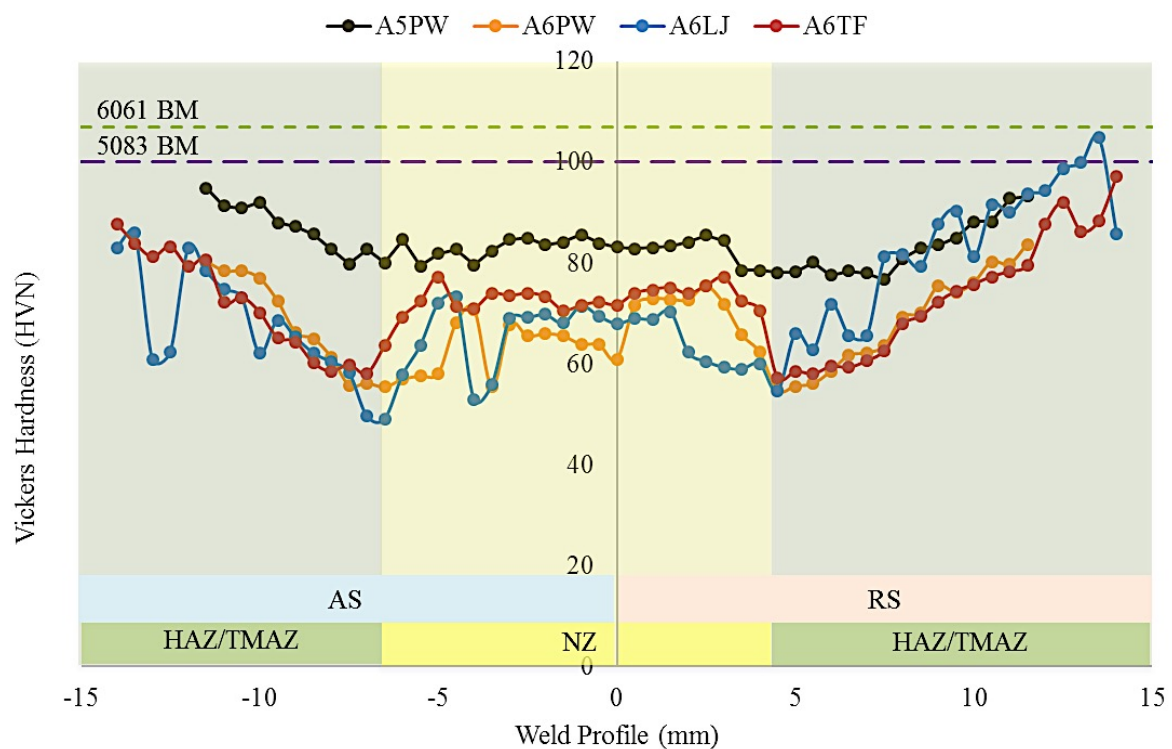

Figure 4.9 Vickers hardness profile from the center of weld

In addition, the hardness was measured at the critical locations at which fracture occurs. For instance, due to the softening in material on the AS and a sudden change in geometry, the A6TF specimens always developed an initial crack at the AS weld toe region as indicated in Figure 4.10 a) with arrows; the A6LJ specimens tended to fail due to a hook defect at the root, where the hardness was measured as shown in Figure 4.10 b).
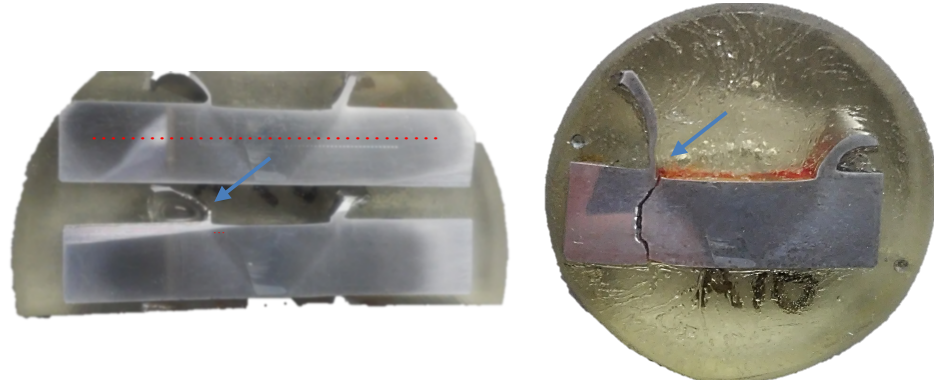
a) Toe flash
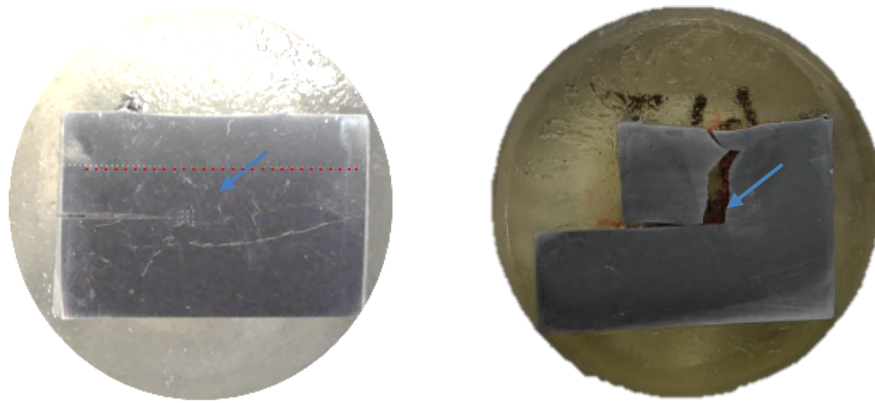
b) Lap joint

Figure 4.10 Fracture locations for A6TF and A6LJ specimens

Nine points in a mesh were measured at the weld toe and root locations for the untested A6TF and A6LJ samples (Figure 4.10) respectively, with their average, minimum, and maximum values presented in Table 4.2. The average values for the mesh was in general lower than the minimum of the hardness profile measured in Figure 4.9. The hardness

gradient at the critical location indicated the induced stress concentration differences, at the location at which fracture occurs.

Table 4.2 Vickers hardness measured at critical locations

Hardness	A6TF	A6LJ
Average	57.5	51.5
Min	44	43
Max	69.4	66.4

4.4 Microstructural Analysis

The microstructural analysis was conducted on selected specimens of interest in parallel with the fatigue testing. The purpose of the microstructural analysis was to relate the fatigue performance to the material microstructure and defect size in the vicinity of the fatigue crack initiation site for each specimen type. In the case of unexpected fatigue test results or abnormal observed failure modes, the associated microstructural analysis or fractography images were examined in an attempt to explain the failure behaviour of the specimens.

4.4.1 6061 Proper Welded Results

Based on the findings in Section 4.3.1, hardness of the materials for heat-treatable alloy 6061 tends to soften in the HAZ on both sides of the FSW nugget zone, especially on the AS. Most of the fracture initiation points should be either on the RS or AS of the welds under properly welded conditions. However, the fracture locations for a few fatigue tested specimens initiated at weld roots, where there was a suspicion of unwanted lack of penetrations or kissing bond defects. Those specimens with suspected small root defects always had a lower fatigue life, and did not align with the other tested specimens, when the results were compared on S-N plots. For instance, Specimen A6PW03A was tested under CA loading with a stress range of 148.5 MPa as shown in Figure 4.11. Since the result appears to be an outlier, a microstructural analysis of the failure location was performed to determine whether this specimen should be included in the same data set, or whether it should be in its own data set as a specimen with a small KB defect that was not detected prior to testing.
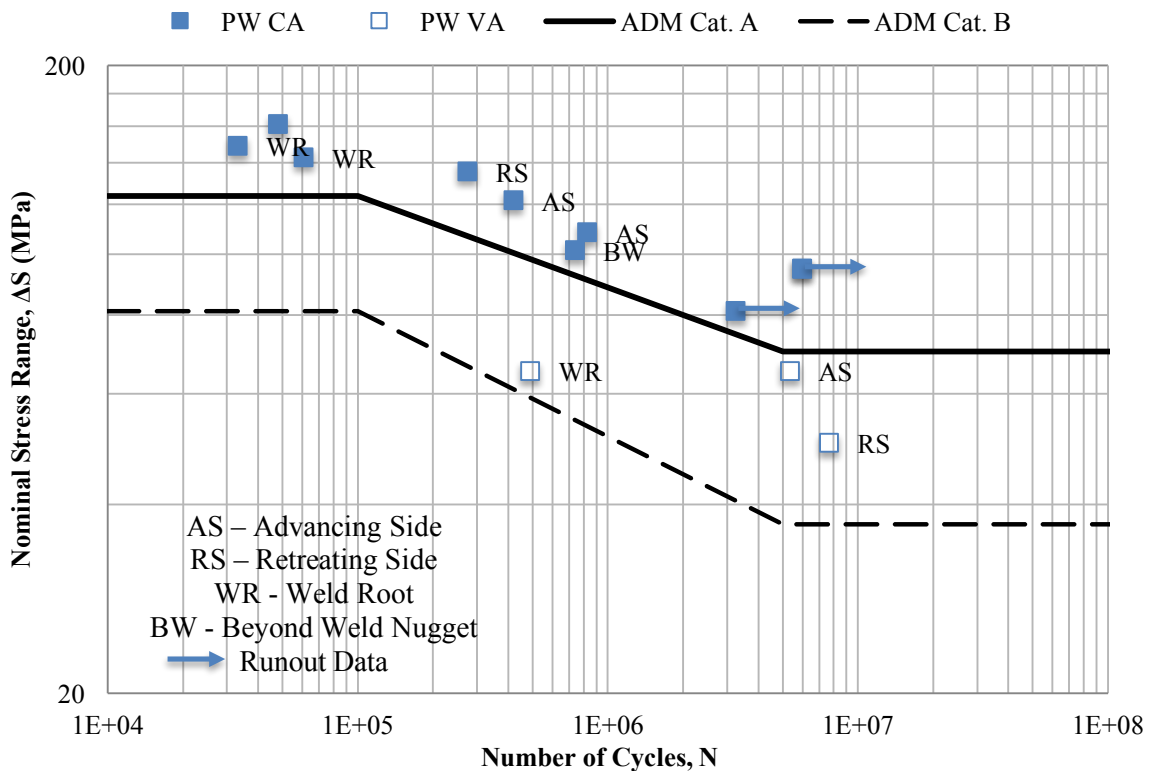
Figure 4.11 Fatigue test results of 6061 proper welds (A6PW) FSW joints compared with ADM standards

Based on the fitted line of the fatigue test results, Specimen A6PW03A was expected to fracture at a fatigue life of 151,643 at the AS location, where in reality it fractured at a fatigue life of 33,235 or one third of the predicted value at the weld root (WR). Specimen A6PW04A tested under VA loading with an equivalent stress range of 65 MPa fractured at a fatigue life of 492,437 at the weld root, whereas another specimen A6PW05C under the same loading conditions failed at a fatigue life of 5,383,609 on the RS. Both fractography images of Specimens A6PW03A and A6PW04A were observed with distinct layers identified in Figure 4.12 and Figure 4.13 at the bottom of the weld with an estimated measurement of 0.238 mm and 0.230 mm respectively. There were multiple micro-cracks developed beyond the white bands, which indicate that the white bands were unbonded layers acting as a kissing bond defect across FSWed region and the cracks initiated at the end of the unbonded layer. Considering these observations for Plate 03 and Plate 04, the rest of the specimens from these

two plates were not tested with the suspicion of similar kissing bond defects. (Note: It is recommended that they should be tested in the future, but that the results should be grouped in a special data set of specimens with ~0.2 mm KB defects).
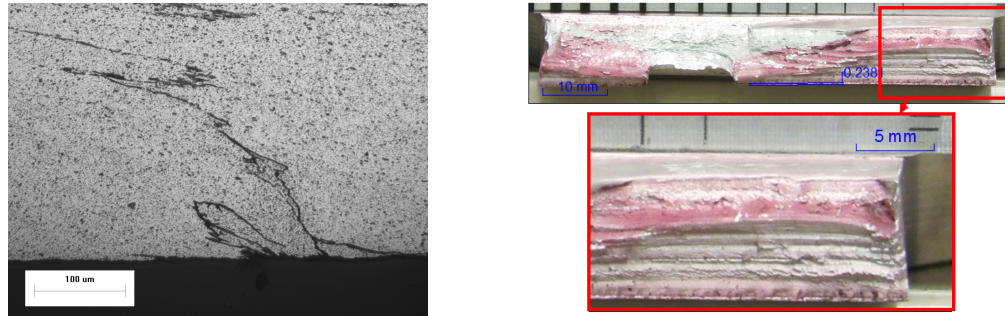
a) Weld root defect under microscope   b) Fractography of the specimen

Figure 4.12 Kissing bond defect detected for A6PW03A

The small specimens were evaluated using a microscope and it was observed that a transient defect was present, which resembled either a kissing bond or a joint line remnant as the KB defect line is not a smooth line. This means that there was a breakage of the aluminum oxide layer at the sample faying surface, which would be difficult to detect using any means since there was still some evidence of metallurgical bonding. The fractography of Specimen A6PW04A appeared to confirm this observation, showing a white band (unbonded region) apart from the bonded region with a height of 0.23 mm.
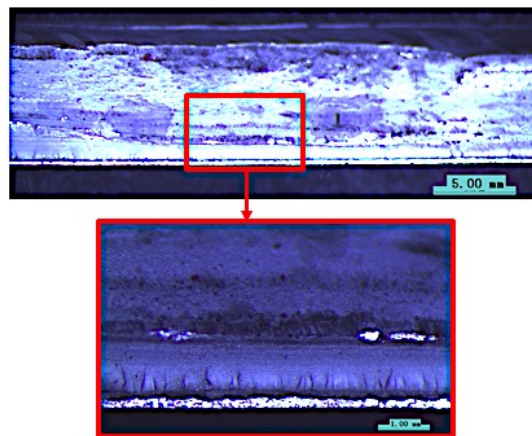

Figure 4.13 Fractography of A6PW04A

4.4.2 6061 Polished Results

As discussed in Section 4.4.2, removal of the top obstacle did not improve the fatigue behaviour of the specimen, but rather made the fracture location unpredictable. The typical fracture locations for A6PO occurred away from the nugget zone as shown in Figure 4.14.
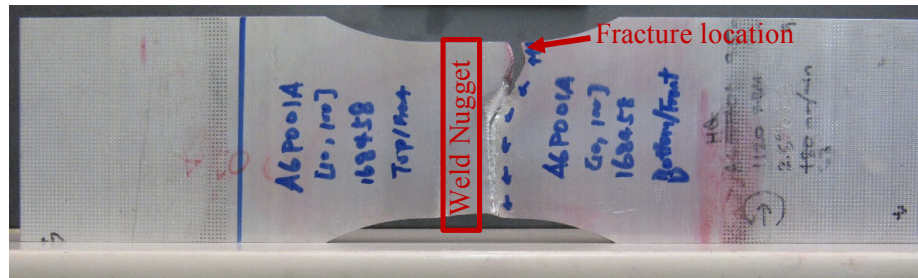

Figure 4.14 Fracture location for A6PO

The fatigue data obtained for A6PO were rather difficult to validate with the support of fractography as the specimens under CA with a stress range of 122 MPa fractured beyond the predicted fitted line. Further measurements were suggested to check if the specimens were improved due to a residual stress change on the surface. As a conclusion for this study, polishing minor toe flashes is not recommended since it does not show any improvement to the fatigue performance and requires additional time.
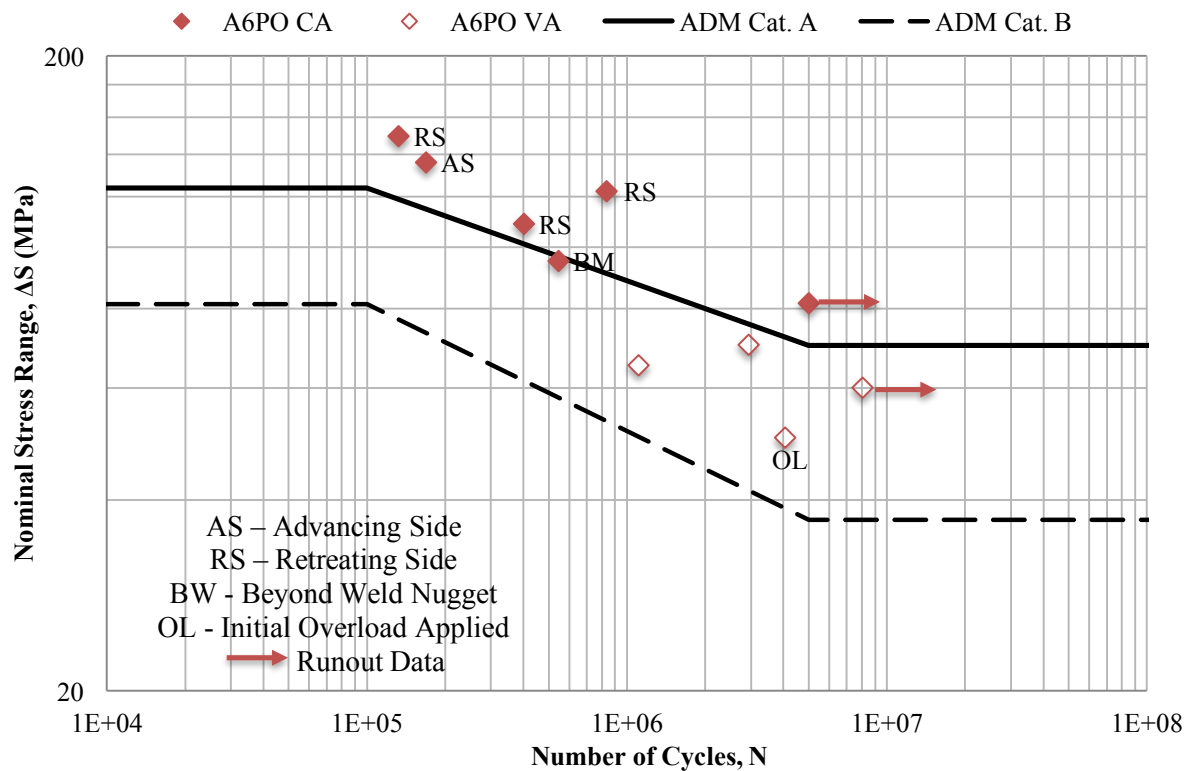
Figure 4.15 Fatigue test results of 6061 polishing (A6PO) FSW joints compared with ADM standards

4.4.3 6061 Toe Flash Results

Due to the softening at the HAZ for the toe flash specimens, the fracture locations were consistently at the AS for the four specimens in Plate 01. The micro-cracks initiated from the weld toe region on the AS fracturing through the HAZ where the lowest hardnesses were detected as shown in Table 4.2. However, the crack initiation for all specimens tested from Plate 02 and Plate 03 were located at the weld root, identified as WR in Figure 4.16. The measured thickness of the specimens in the middle from Plate 01 to 03 using calipers were roughly 8.7 mm, 9.3 mm, and 9.0 mm correspondingly. With a controlled spindle tool of 8.5 mm during the fabrication process, the differences greater than 0.2 mm between the final plate thicknesses to the tool length suggested that in Plate 02 and Plate 03 the tool penetration depths were not fully anticipated during the welding process.
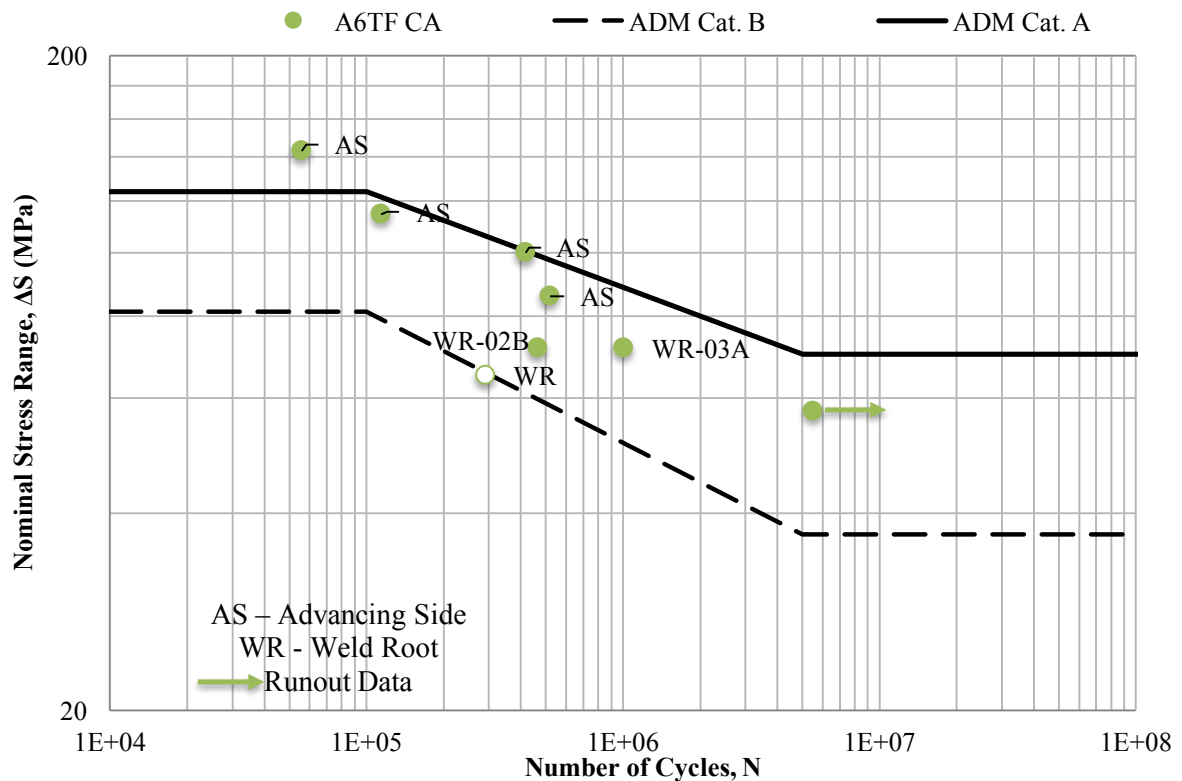
Figure 4.16 Fatigue test results of 6061 toe flash (A6TF) FSW joints compared with ADM standards

The fractography measurements of the fractured specimens from both plates further confirmed that similar white bands to those observed in A6PW03A and A6PW04A also existed. The thickness of the white bands in specimen A6TF02B and A6TF03A were approximately 0.5 mm and 0.68 mm as indicated in Figure 4.17 and Figure 4.18, where the micro-cracks initiated from the end of the consolidation edge. Both of the specimens were tested at a stress range of 71.4 MPa as shown in Figure 4.16, where the specimen with a smaller initial unbonded region fractured at a fatigue life of 1,009,218 cycles, and the specimen from Plate 02, which had a larger kissing bond, fractured at a fatigue life of 466,710 cycles. The fatigue life was significantly reduced by an amount proportional to the reduction in initial kissing bond length. Further fatigue tests on Plate 02 and Plate 03 specimens did not meaningfully contribute values that have the understanding of the toe flash defects because the specimens had a combination of two defects. Since specimens with both

toe flash and kissing bond defects always fractured from the weld root, it can be concluded that when both defects have a magnitude of roughly 1 mm the kissing bond defects are more detrimental than the toe flash defects.
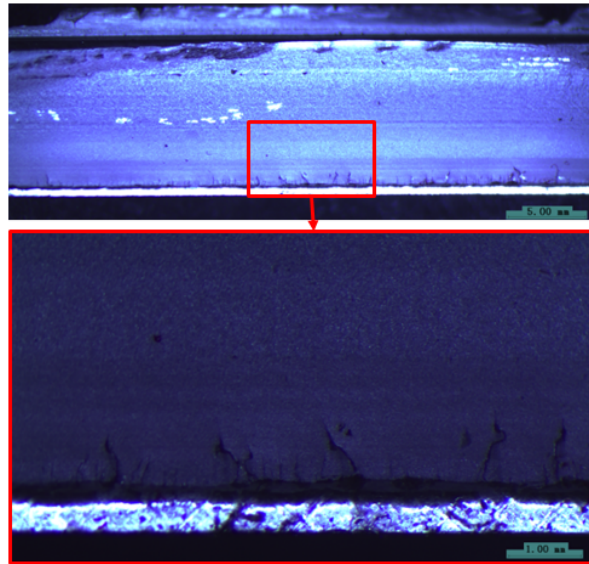

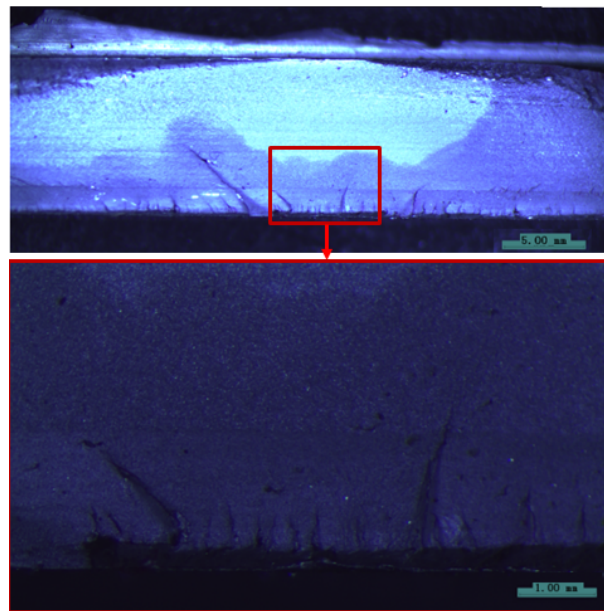**Figure 4.17** Fractography of A6TF02B

Figure 4.18 Fractography of A6TF03

As shown in Figure 4.19, the fracture location in the A6TF specimen from Plate 01 commenced at the weld toe, and propagated through the thickness. There were multiple patterned micro-cracks observed in the weld toe region. The dashed line indicated the boundary between the fracture surface and the development of crack propagation (B) and the yielding fracture (C) regions. The initial micro-cracks developed at the weld toe surface, and propagated into a semi-elliptical shape. Due to the reduction in effective cross sectional area, the specimen failed in a ductile manner where micro-voids (C) observed under a microscope.
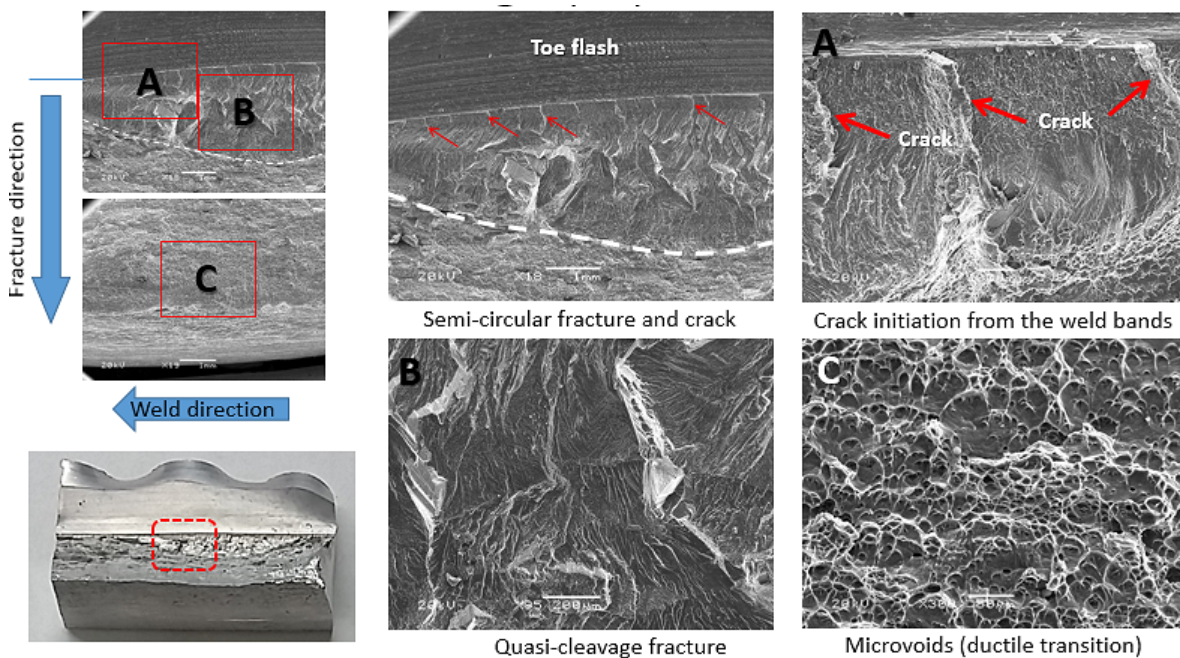

Figure 4.19 Fractograph of fractured specimen from A6TF Plate 01 (Shah, 2017)

4.4.4 6061 Kissing Bond Results

Unlike the other kissing bond defects detected in the categories mentioned above, the kissing bond defect was intended to have a 1 mm gap for the unbonded region in each specimen. Those unbonded regions were examined by two independent organizations CTS and ES using various non-destructive methods, including DP, UT, and RT, where the details of each test were discussed in Section 3.1.3.3. The results for detecting kissing bond defects were not ideal, CTS was not able to find any defects using UT and RT, a very fine dye was observed

after applying dye penetrant shown some indication that a kissing bond defect existed in those plates. CTS concluded the report by saying that it was rather difficult to detect any kissing bond defects less than 1 mm. ES performed the UT on the kissing bond plates by a varying phased array technique, where the 45° linear techniques yield the highest amplitude response. The root of a kissing bond defect is closed and not straight as shown in Figure 4.20. Due to the nature of this defect, it is difficult for the deflection to be detected accurately.
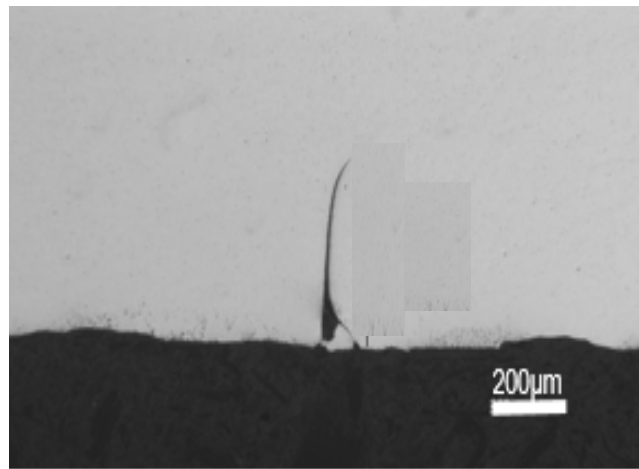

Figure 4.20 Kissing bond defect under microscope (Shah, 2017)

The fatigue life plotted against stress range for all of the A6KB specimens under CA and VA loading can be plotted into two straight lines with little scatter as shown in Figure 4.3, which suggested that the defect types and specimens were consistent. Only selected fractured A6KB specimens were carefully measured in their unbonded region to represent the entire plates, including the kissing bond measurements of 0.95 mm and 0.91 mm for A6KB01B, and A6KB02C respectively (Figure 4.21 and Figure 4.22). These destructive measurements were not accurately reported by CTS nor ES for the kissing bond defects, make along that the kissing bond defects are difficult to detect, and also difficult to avoid with a single side butt weld. The fatigue performance of the A6KB defect significantly reduced the life of the specimens containing the defect since most of the specimens' initiation life was spend developing initial cracks, whereas A6KB act as an initial crack directly proceed to its propagation phase of fatigue life directly. The cracking locations for A6KB were always at

the weld root through the nugget zone even though the HAZ has a lower hardness in comparison, mainly because the fracture path was the most energy efficient one with 1 mm of defect, where the effective area in the middle of the FSW was reduced by almost 10%.
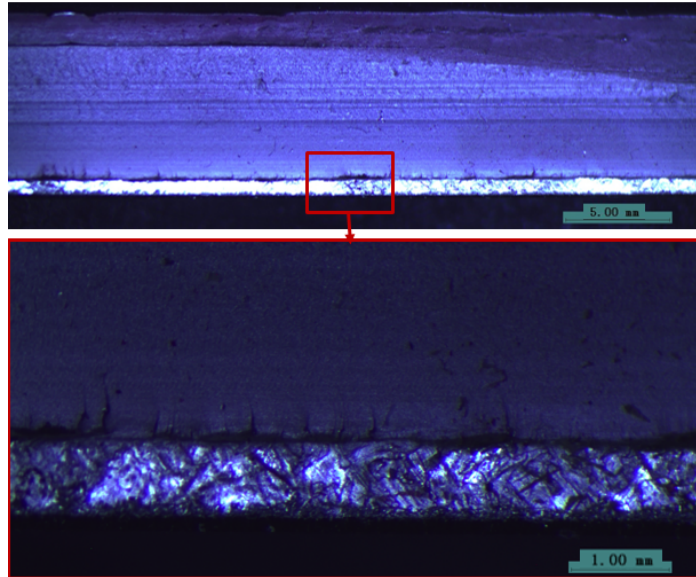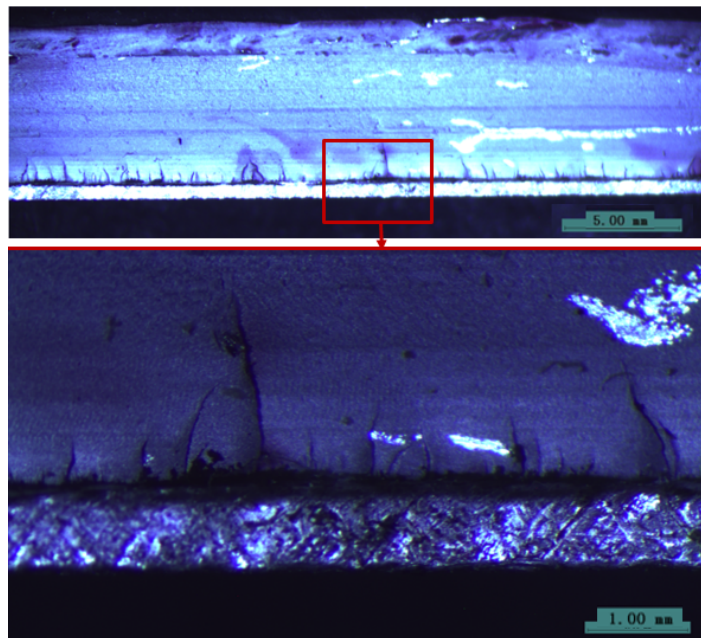

Figure 4.21 Fractography of A6KB01B

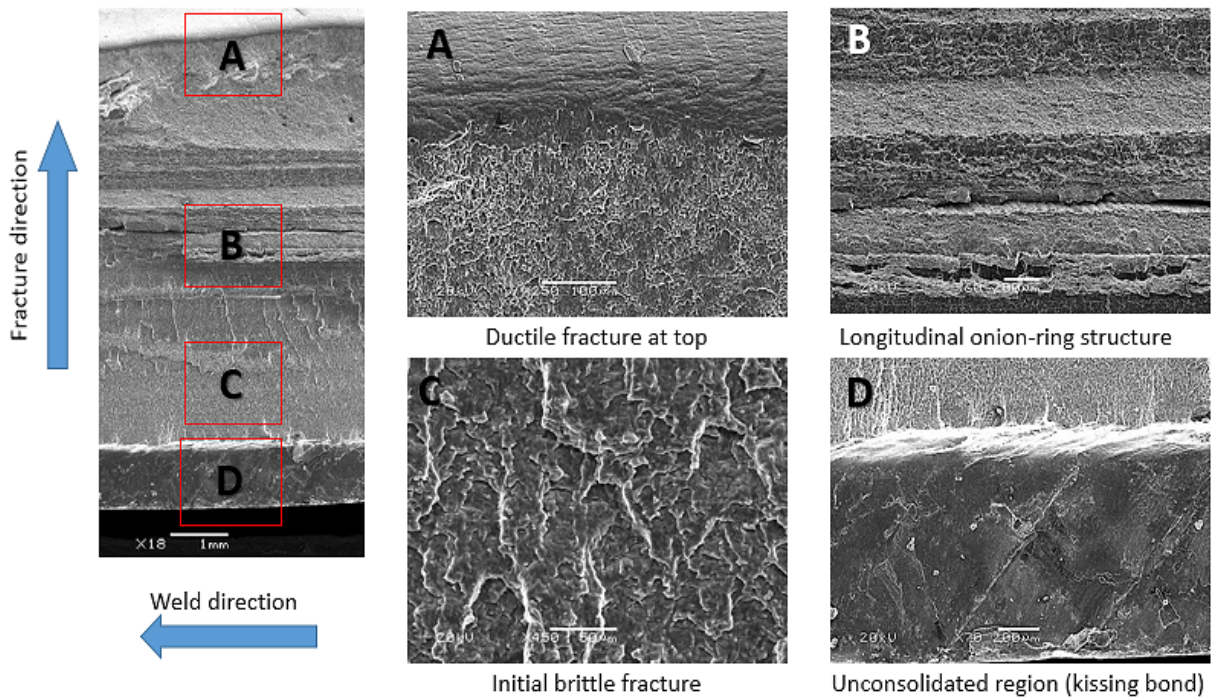**Figure 4.22** Fractograph of A6KB02C

Figure 4.23 Fractography of A6KB specimens (Shah, 2017)

The fracture started in the unbonded region indicated as D in Figure 4.23 at the weld root, and propagated through the thickness. As the KB defect was presented through the longitudinal direction of the weld, the fracture occurred in layers (B) as the accumulative damage was large enough. Finally, as the cross sectional area could not withstand the fatigue loading applied, the material failed by yield of the material (A).

4.4.5 6061 Lap Joint Results

Similar to the A6KB defect, the fatigue performance of the A6LJ defect showed little scatter as the specimens were fabricated with consistent dominant defects. From the cross section of the A6LJ, there is a distinct hook defect observed between the two overlapping plates due to insufficient material flow in this region to consolidate the work pieces together. This hook location as shown in Figure 4.24 was where all of the fracture paths started as it acts as an initial opening for the specimen.
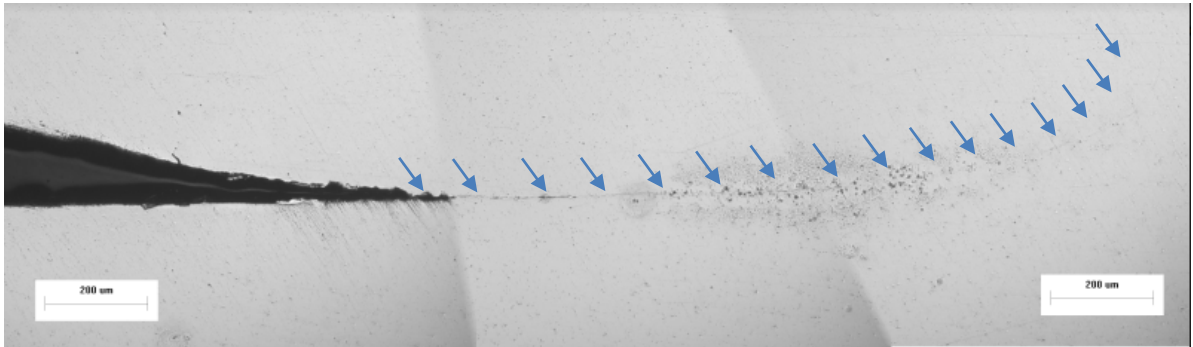
Figure 4.24 Hook crack for A6LJ

In turn, the fatigue lives of the A6LJ specimens were greatly reduced as the crack initiation phase was greatly shortened due to the existing crack like defect at the beginning of the fatigue tests. Since most of the fatigue life were spent at the crack initiation phase, the fatigue life of A6KB and A6LJ were greatly reduced since their initial crack eliminated the crack initiation phase.

4.4.6 5083 Proper Welded Results

The 5083 alloys are non-heat-treatable, the hardnesses across the FSW profile do not fluctuate as much as for the 6061 alloys. As identified in Table 4.3, the grain sizes on the AS and RS of the FSW was almost the same. This finding suggested that the heat distribution was even on both the AS and RS, and that heat has minimal influence on the 5083 material.

Table 4.3 Grain size for 5083 (Shah, 2017)

Region	Height (μm)	Std dev. (μm)	Length (μm)	Std dev. (μm)
Advancing side	17.17	2.24	33.74	3.07
Retreating side	17.58	1.82	35.47	3.63

The stirred 5083 material at the weld root tends to form a joint line of remnant that consists of micro-voids (see Figure 4.25), which may initiate a crack from the weld root. As expected, the fracture path for 5083 always starts from the weld root region.
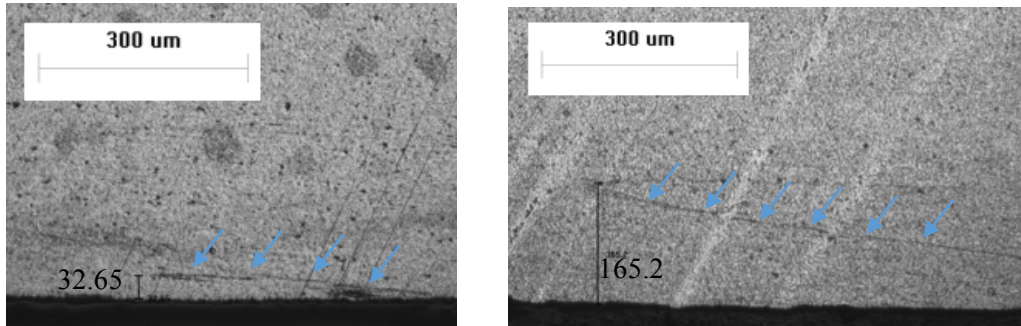
Figure 4.25 Typical micrograph of A5PW

The fatigue test under a CA loading of 113 MPa (A5PW02A) failed in less than 1 million cycles as shown in Figure 4.26, which is almost the same fatigue strength as a sample at a stress range of 155.4 MPa.
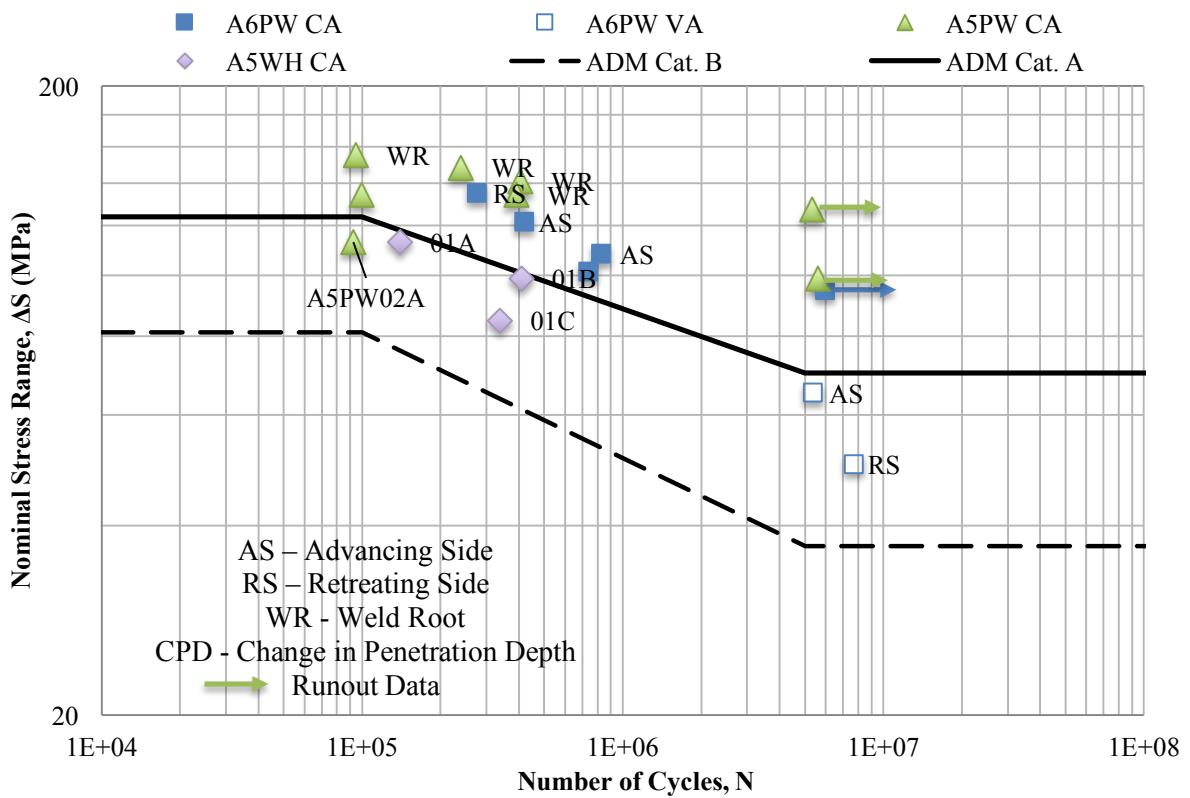

Figure 4.26 Fatigue test results of 5083 properly welded (A5PW) and wormhole (A5WH) FSW joints compared with ADM standards

Specimen A5PW02A was FSWed with two different plunging depths as shown in Figure 4.27, the heat distribution was different due to the re-plunging action, therefore create a stress concentration factor where the specimen failed at a much lower fatigue life. Two other specimens (A5PW03A and A5PW03B) from the same plates were tested with the same stress range of 134 MPa, however, their fatigue lives were dramatically different. Those specimens are still under investigation for their odd behaviours.
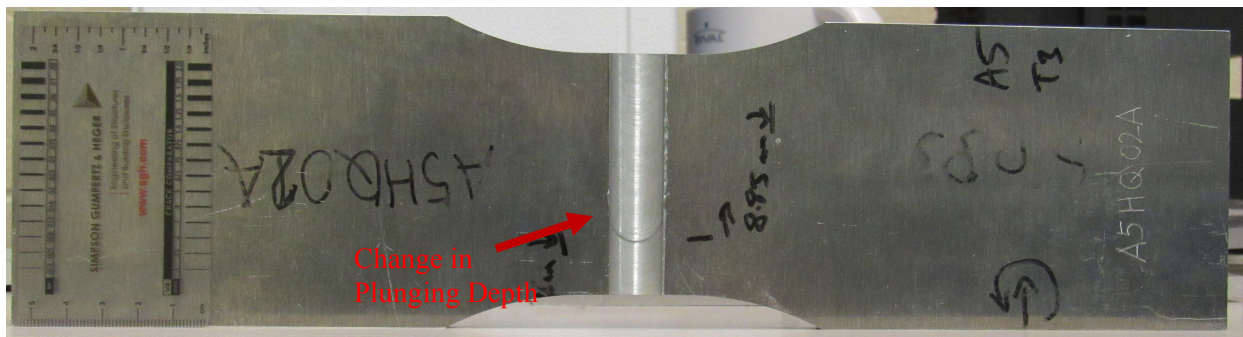
Figure 4.27 A5PW02A with double plunging depth

4.4.7 5083 Wormhole Results

As shown in Figure 4.26, the A5WH fatigue data did not show a clear pattern. The main reason for this scatter was because the geometries of the wormholes in the specimens were not the same. From the fractograph of each specimen in A5WH01 as shown in Figure 4.28, there were indications that the subsurface crack was observed at the beginning of A5WH01A, and continued to develop at the second half of A5WH01C, through the whole specimen in A5WH01D. This observation was confirmed with the CTS ultrasonic scans. The surface wormhole act as an initial discontinues crack that reduced the crack initiation life.

a) A5WH01A
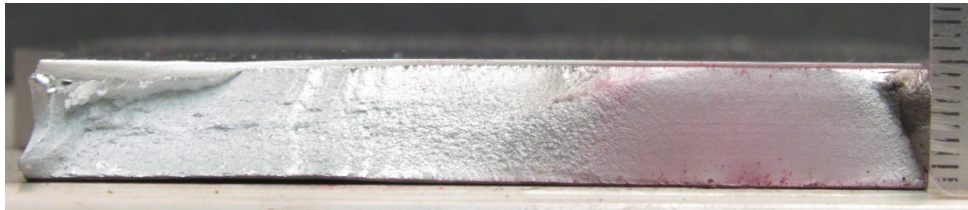
b) A5WH01B
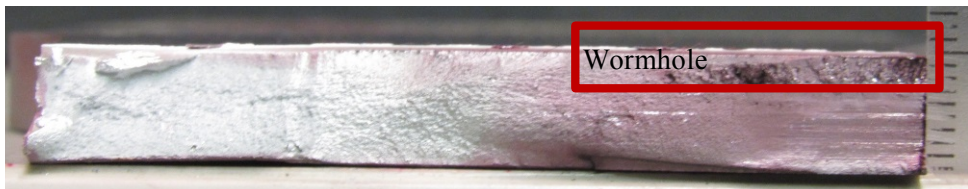
c) A5WH01C
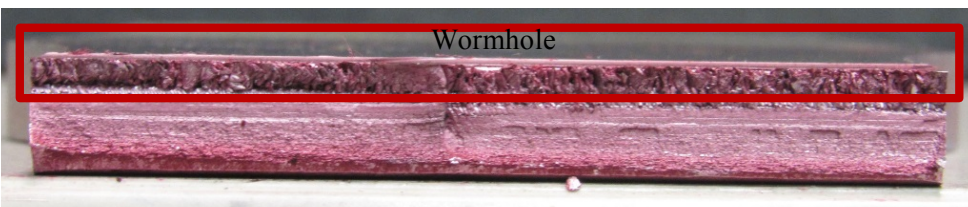
d) A5WH01D

Figure 4.28 Fractograph of 5083 wormhole

Chapter 5

Statistical, Finite Element, and Fracture Mechanics Analysis

This chapter discusses three short analytical studies that were performed to better understand the implications of the fatigue test results presented in Chapter 4. These studies include a statistical analysis based on the methodology prescribed by the International Institute of Welding (IIW), a finite element (FE) analysis of the stress concentrations present in the specimens due to sudden changes in their geometry, and a linear elastic fracture mechanics (LEFM) based prediction of the 6061 PW test specimen fatigue life.

5.1 Statistical Analysis of Fatigue Test Results

This section summarizes the statistical analysis of the fatigue results, including the design and mean S-N curves for the various defect types discussed in Section 4.1.1. Ideally, all of the following effects should be considered for a statistical analysis (IIW, 2016):

- the variance of the data,
- the probability distribution of the mean value by its confidence interval,
- the difference in the distribution of the whole data set and that of the sample,
- the deviation from the assumed Gaussian distribution

For any structural design, safety factors are almost always applied to the mean values of the data sets. The design values used are known as the characteristic values, calculated using the following procedures (IIW, 2016) (in Microsoft Excel, in the current study):

a) take the log of all the data, including the stress range, $\Delta\sigma$ and number of cycles, N

b) calculate exponents, m and constant $logC$ by linear regression, taking the stress range as the independent variable using Equation (5.1):

$$logN = logC - m \cdot log\Delta\sigma \qquad (5.1)$$

(Note: for $n < 10$, a fixed value of m should be taken as derived from other tests under comparable conditions)

a) calculate mean, x_m and standard deviation, $stdv$ of $logC$ using the following

equations:

$$x_m = \frac{\Sigma x_i}{n} \tag{5.2}$$

$$stdv = \sqrt{\frac{\Sigma(x_m - x_i)^2}{n-1}} \tag{5.3}$$

c) calculate the characteristic values x_k by the formula:

$$x_k = x_m - k \cdot stdv \tag{5.4}$$

where, $k = 1.645 \cdot (1 + \frac{1}{\sqrt{n}})$

These characteristic values correspond with the 95% survival probability calculated from mean values, x_m on the basis of two sided tolerance limits of 75% confidence level of the mean.

Since there were not any comparable or similar tests conducted for each defect group, the exponent *m* could not be derived with confidence from other tests. Even though there were only a limited number of specimens tested under each defect category (less than 10 test data), the exponents were obtained using linear regression combining CA and VA loading fatigue data for each category. The following S-N curves from Figure 5.1 to Figure 5.7 were plotted with a log-log scale in comparison with the ADM design curves of Detail Category B, which is representative of fully penetrated butt-welds made from one side using conventional arc welding processes, and the ADM design curve of Detail Category A for aluminum base metal as a reference. Slopes of the mean S-N curves were reported in Section 4.1.1, which are the same as the slopes of the S-N design curves proposed in the following figures summarized in Table 5.1.

Table 5.1 Slopes based on IIW

Defect Type	Mean slopes, m	
	CA	VA
A6PW	3.48	3.48
A6PO	3.15	3.15
A6TF	4.74	-
A6KB	4.95	4.95
A6LJ	3.80	3.80
A5PW	15.15	-
A5WH	2.97	-
ADM Cat. A	6.85	-
ADM Cat. B	4.84	-

From Table 5.1, the slopes in ascending order are properly welded (A6PW), polished (A6PO), toe flash (A6TF), kissing bond (A6KB), and lap joint (A6LJ) fabricated from 6061 alloys, and properly welded (A5PW) and wormhole (A5WH) fabricated from 5083 alloys. Depending on the variance of the fatigue data for each defect type, the design (95%) S-N curves shift to the left of the mean S-N design curves based on the statistical analysis procedure proposed by the IIW (IIW, 2016). The variance largely depends on the consistency in the specimen defect productions, as discussed in Section 4.4. The mean and design S-N curves for the A5PW data set were seen to have the smallest difference. Whereas, the design S-N curves for the A6PO and A5WH data sets deviated substantially from the mean S-N curves, due to the differences in specimen defects in the same category.
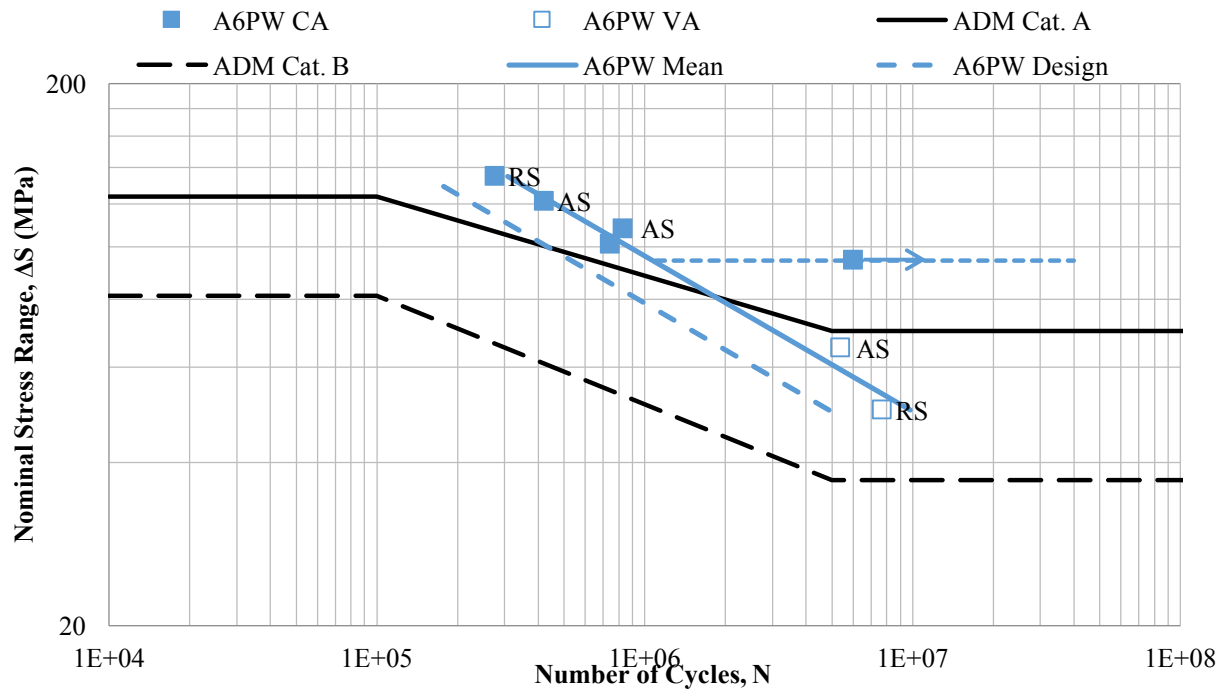
Figure 5.1 Proposed S-N design curves for 6061 properly welded (A6PW) FSW joints

Figure 5.2 Proposed S-N design curves for 6061 polished (A6PO) FSW joints

116

Figure 5.3 Proposed S-N design curves for 6061 toe flash (A6TF) FSW joints
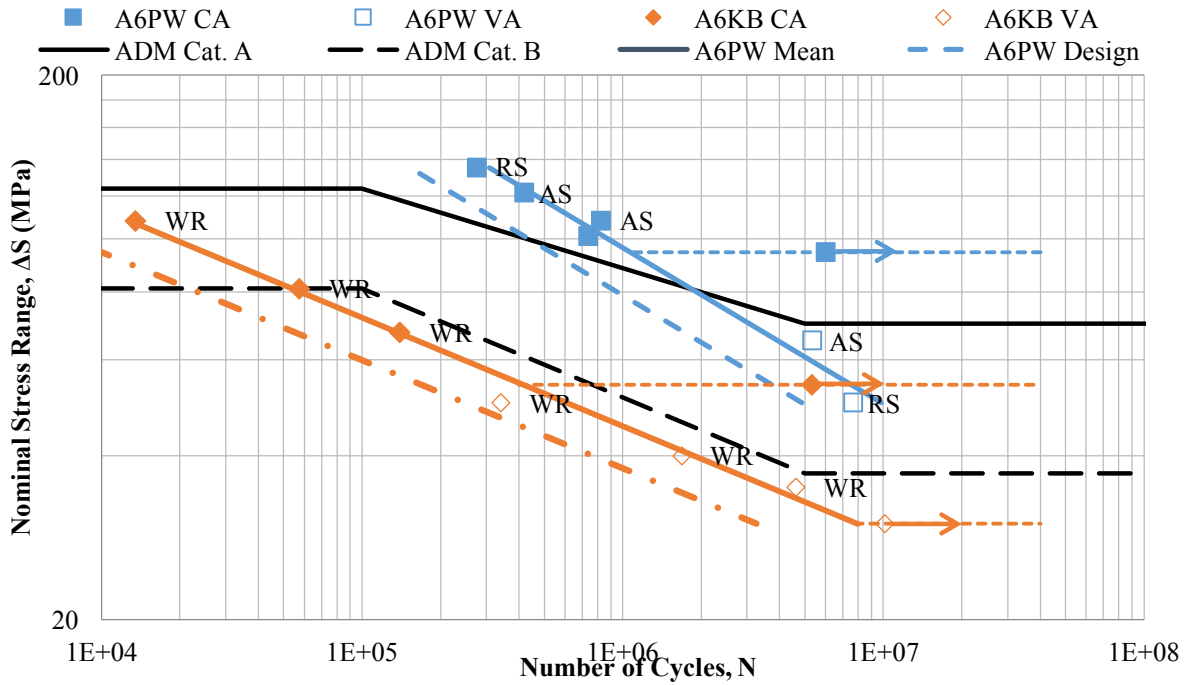
Figure 5.4 Proposed S-N design curves for 6061 kissing bond (A6KB) FSW joints

117

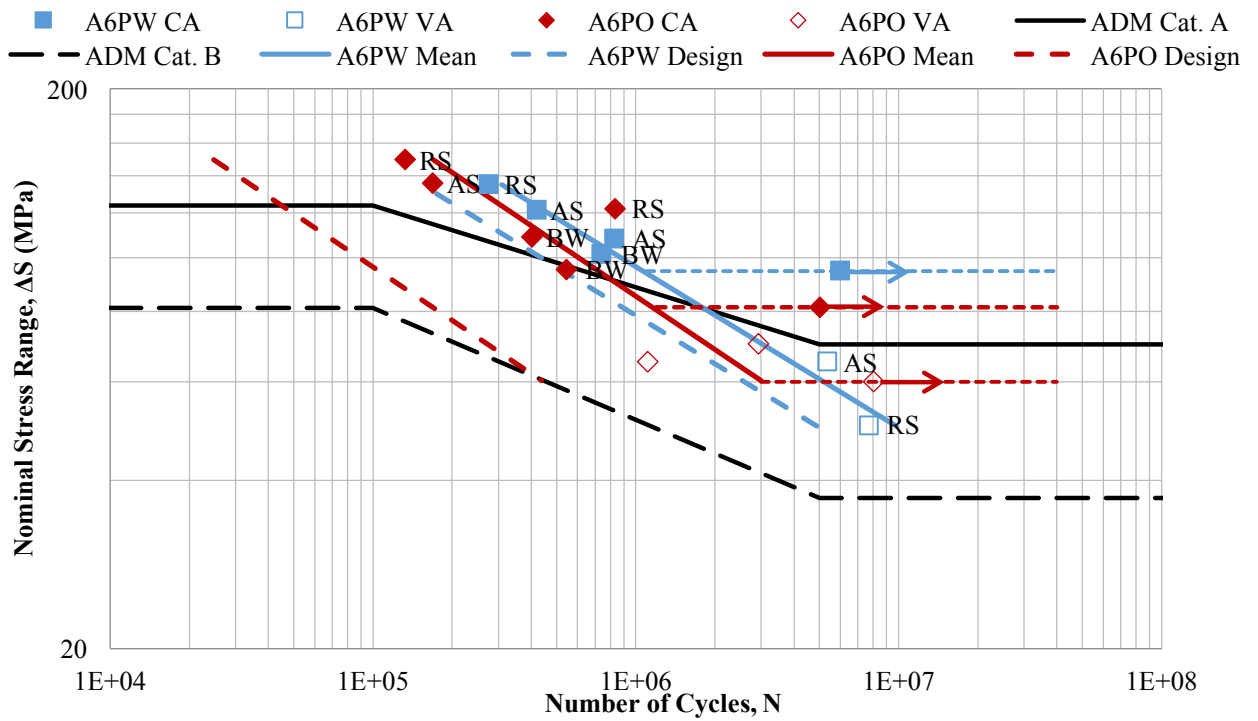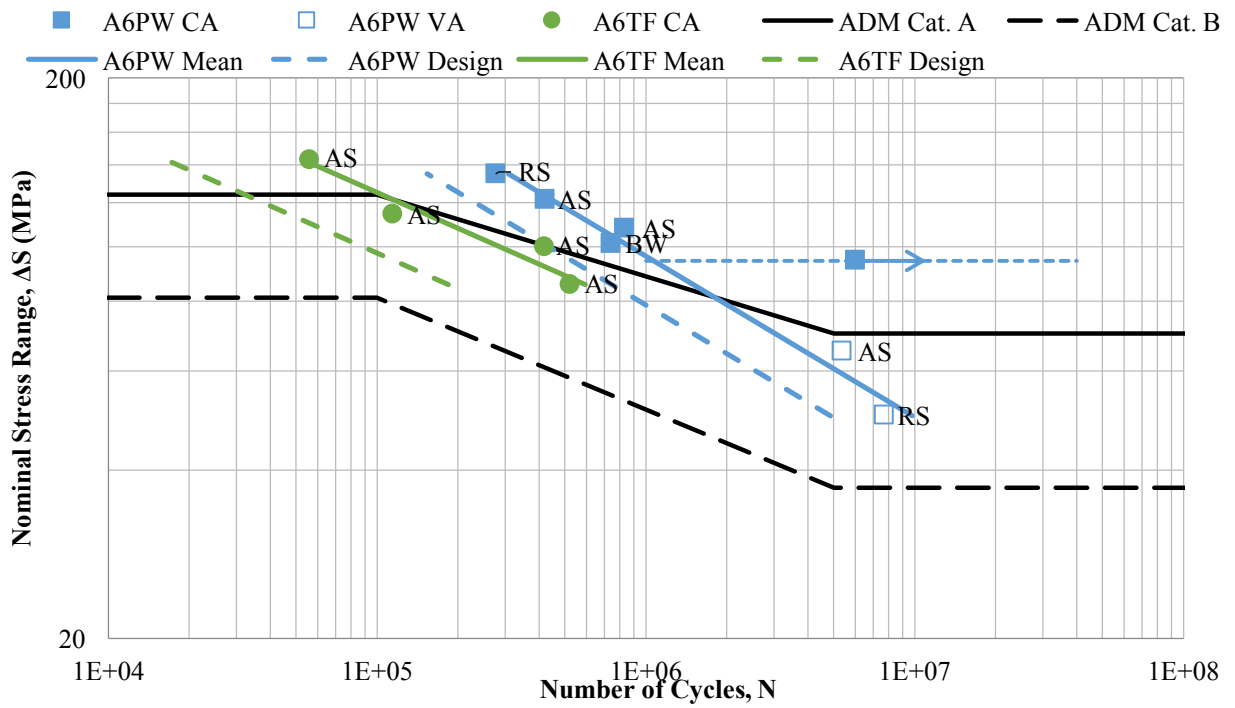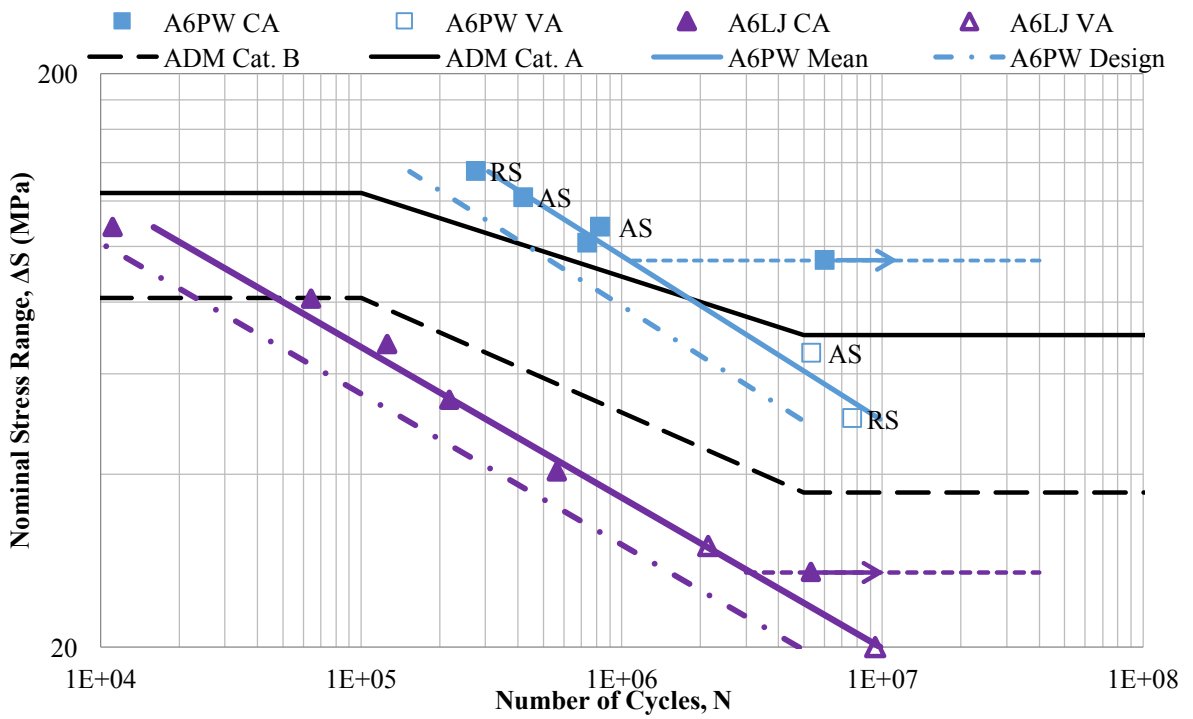**Figure 5.5** Proposed S-N design curves for 6061 lap joint (A6LJ) FSW joints
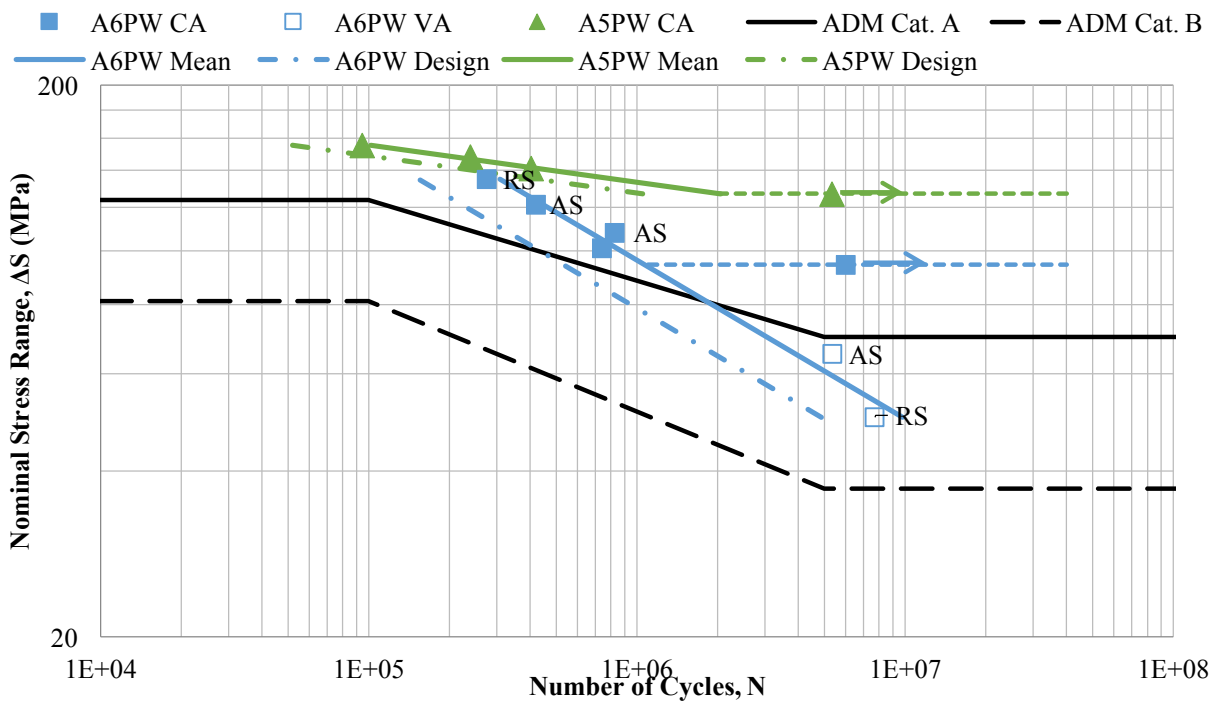
Figure 5.6 Proposed S-N design curves for 5083 properly welded (A5PW) FSW joints

118
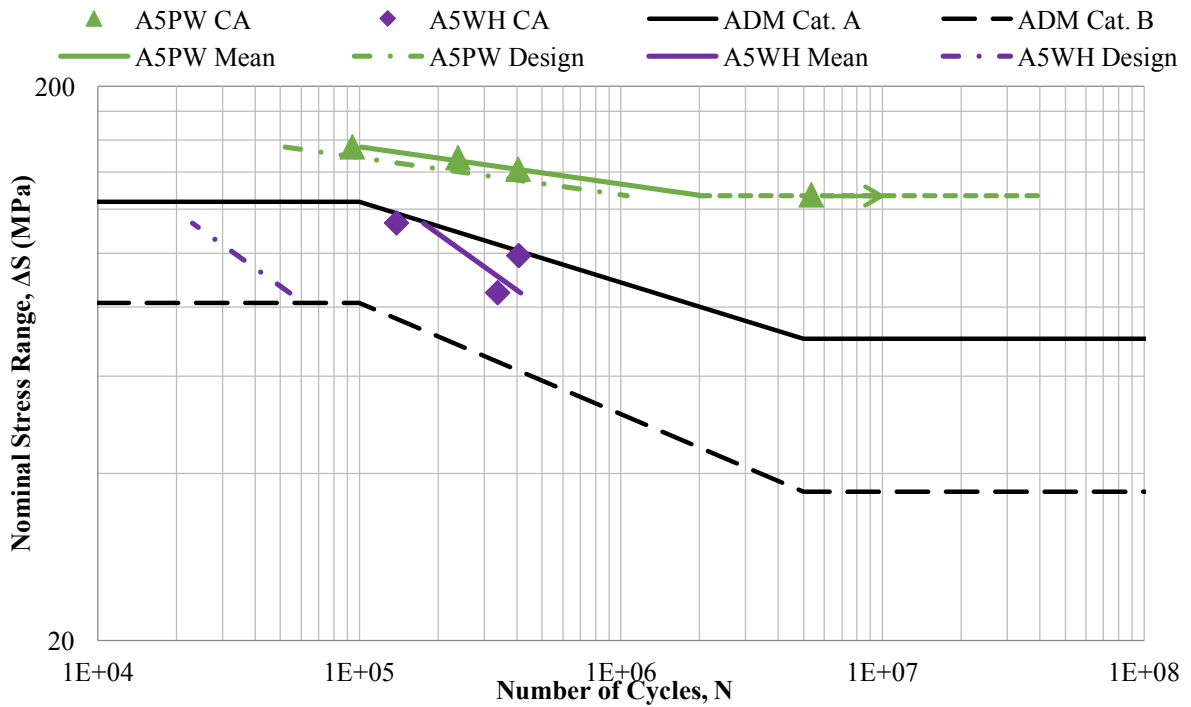
Figure 5.7 Proposed S-N design curves for 5083 wormhole (A5WH) FSW joints

The following statements were made based on the 95% probability design curves (referred as design curves in dashed lines from Figure 5.1 to 5.7) according to IIW procedures. Due to limited fatigue test data (less than 10) for CA and VA, and no comparable conditions for each group, the design curves were obtained by combining the fatigue test data from CA and VA loading conditions. All of the available proposed S-N design curves (dashed lines) were above the current ADM standard Category B, with the exception of S-N design curves for kissing bond and lap joint FSW joints. The lower bound S-N design curves is governed by either A6PO/A6TF in low cycle fatigue, and the upper bound is limited by the properly welded of non-heat-treatable alloy (A5PW). For the proposed S-N design curves below the current design curve in ADM standards with comparable welding condition Category B, A6KB and A6LJ FSW joints were observed with an initial crack-like defect, resulting in a large reduction in fatigue life. Additional fatigue tests for kissing bond defects with varying initial root defects are recommended to correlate initial crack depth and fatigue performance.

5.2 Finite Element Analysis of Stress Concentrations

An understanding of the elastic stress distribution along the crack path is required as one of the inputs for predicting the fatigue life of a welded detail using fracture mechanics. Stress distributions near the weld toe or weld root regions were carried out using ABAQUS (full version 6.11-2/September 2011 and student version 6.14-AP/November 2014) developed by ABAQUS Inc., which is a software suite for finite element analysis used to simulate the elastic and plastic deformation zones of the specimen and present a visual demonstration of the results. The FE models were constructed by tracing the high-resolution weld profile images obtained from microscopy into AutoCAD drafting software, followed by importing the 2-D sketches into ABAQUS for stress analysis. Figure 5.8 illustrated one of the models constructed for a specimen with a toe flash (TF) defect. The assumptions, geometry, boundary conditions, and element types are outlined in this section.
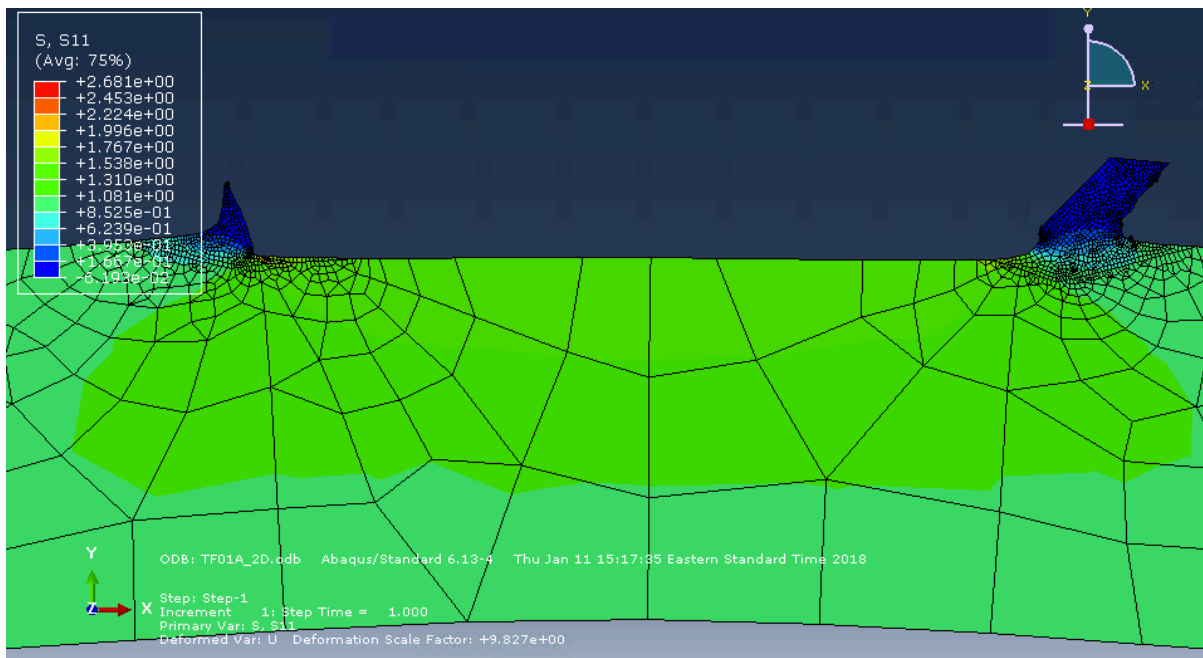
Figure 5.8 Finite element model of toe flash in ABAQUS

For the toe flash model as illustrated in Figure 5.8, material properties of aluminum 6061 were assumed for the FE analysis with a Young's modulus of 70000 MPa, a Possion's ratio

of 0.3 and a density of 2650 kg/m^3. In the FE analysis, the material was assumed to be an isotropic, homogenous solid that had no characteristic material orientations, and the material was modelled with no initial crack-like flaws, as the flaws are introduced later in the fracture mechanics calculation. The geometries of the model were traced based on actual FSW specimens with a thickness of 8.7 mm at the middle of the weld. The thickness of the specimen is relatively small compared with the other specimen dimensions, and the stress acting perpendicular to the specimen was assumed to be zero. A plane stress condition was employed in the ABAQUS model visualized as thin plate with stresses acting only along its longitudinal direction. The stresses around the toe flash region is the most interested area of the 2-D model since it governs the fatigue behaviour of the specimen. In order to improve the accuracy of the stress, strain, and SCF around the weld toe, the singularity a biased seeding of finer meshes (see Figure 5.9) were prescribed to obtain an accurate result.
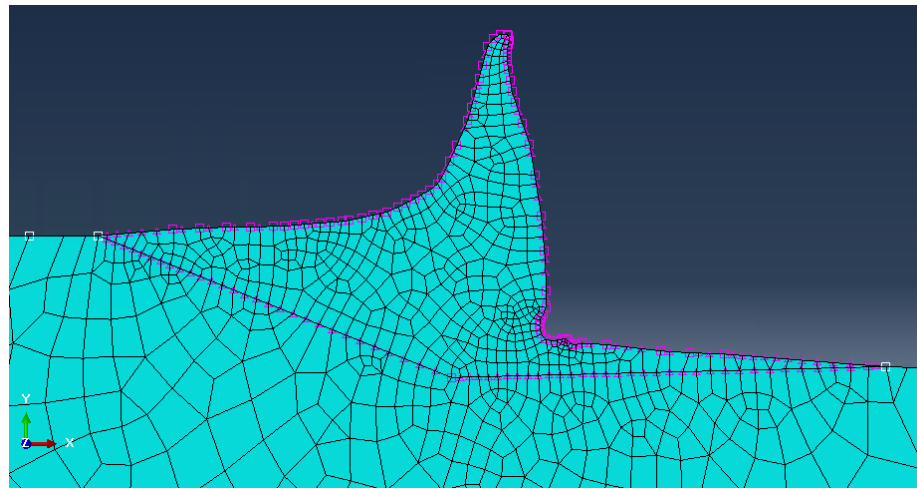
Figure 5.9 Biased seeding for toe flash specimen mesh

The toe flash was modelled with an edge of collapse 4-node bilinear plane stress quadrilaterial elements as shown in Figure 5.9. The accuracy of stress and strain were not compromised with coarse elements in the regions far away from the toe flash. However, the edges of the coarse elements should match with the finer meshes around the crack tip for compatibility. To maintain the accuracy of the results in different regions and save computation time, the regions of separation were discretized into a near field region close to

the toe flash and a far field which was further away from the toe flash. Quadrilaterial elements of 0.5 mm mesh size were used for the near field region, and mesh sizes were increased to 3 mm in the far field as shown in Figure 5.9.

This particular toe flash geometry resulted in a stress concentration factor, SCF of 2.7 (see Figure 5.10), meaning that the local stress at the notch is 2.7 times the nominal stress (applied force/cross section area).
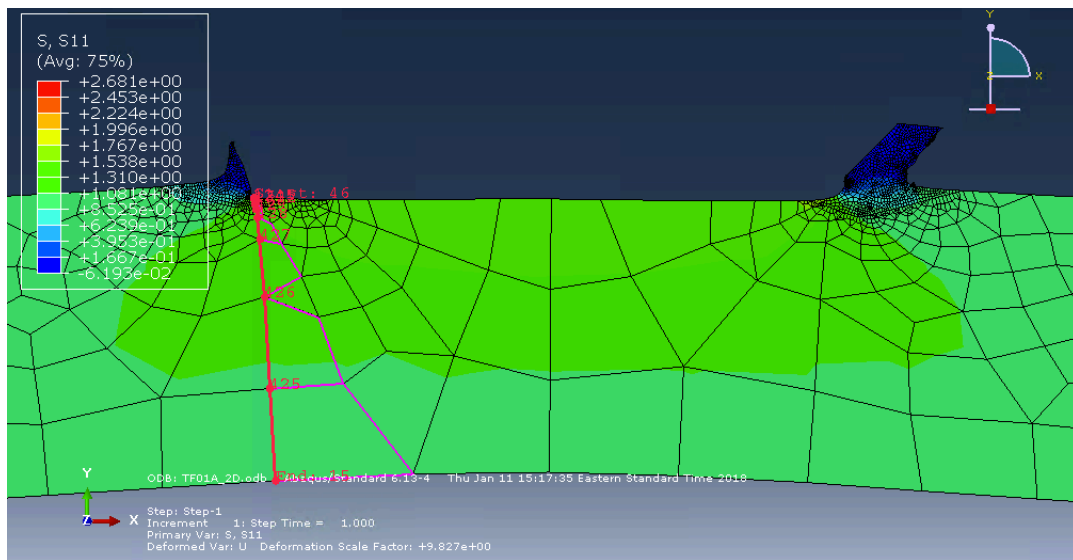
a) Stress along path with the highest local stress
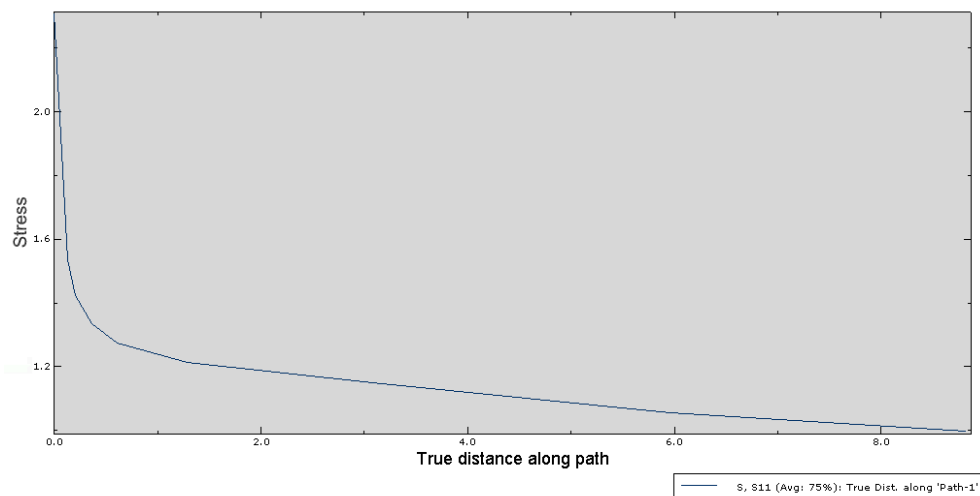
b) Stress concentration factor through the thickness

Figure 5.10 Stress concentration factor for toe flash specimen

The ABAQUS finite element model will produce highly accurate results if the global seeding sizes are very small. However, the computation time for generating these results is not cost efficient from an engineering perspective. To achieve convergence, numerous trials on the types and seeding sizes for the meshing were generated in ABAQUS.

5.3 Linear Elastic Fracture Mechanics

The presence of crack-like defects can significantly reduce the fatigue life of a component or structure. This section introduces the use of LEFM for predicting fatigue crack growth due to the defects induced by FSW. The design parameters in the LEFM model include: the stress intensity factor (K), the fracture toughness (K_c), the applicable fatigue crack growth rate expression, the initial crack size (a_i), and the critical crack size (a_c). In this section, sensitivity studies are performed on the material properties, the initial crack size (a_i), and the crack shape aspect ratio (a/c). The limitations of LEFM are also discussed.

Use of LEFM requires a knowledge of the pre-existing crack (defect) size and shape, based either on experience, engineering judgement, or non-destructive testing. LEFM is used to describe and predict fatigue crack growth life and fracture by assuming the presence of an initial defect. Material conditions are assumed to be predominantly linear elastic during the fatigue crack growth process (Stephens, Fatemi, Stephens, & Fuchs, 2001).

5.3.1 Crack Growth Law

The Paris-Erdogan crack growth law (Equation 5.1), modified to include a threshold SIF range, ΔK_{th}, integrated over a crack depth range, a_0 to a_c is used in the LEFM to predict the growth of an initial crack. The deterministic model was adopted in the model used by Walbridge (2005), which can be applied to any weld toe-like potential crack site.

$$N_c = \int_{a_0}^{a_c} \frac{da}{C \cdot (\Delta K_{app}{}^m - \Delta K_{th}{}^m)} \qquad (5.5)$$

where, N is the fatigue life of a component determined by numerical integration

a_0 is the initial crack depth

123

a_c is the critical crack depth

ΔK_{app} is defined according to Albrecht & Yamada (1977) for crack geometries, configurations, and loadings as:

$$\Delta K_{app} = Y_e \cdot Y_s \cdot Y_w \cdot Y_g \cdot \Delta\sigma_{app}\sqrt{\pi a} \tag{5.6}$$

where, $\Delta\sigma_{app}$, is the applied stress range

Y_e is the shape factor for an elliptical crack

Y_s is the free surface factor

Y_w is the finite thickness of the plate

Y_g accounts for the presence of a non-uniform stress distribution along the crack path.

$$Y_e = \frac{1}{\int_0^{\frac{\pi}{2}}\left(\sqrt{1 - sin^2\emptyset \cdot \left(\frac{c^2 - a^2}{c^2}\right)}\right) \cdot d\emptyset} \tag{5.7}$$

$$Y_s = 1 + 0.12 \cdot \left(1 - 0.75 \cdot \frac{a}{c}\right) \tag{5.8}$$

$$Y_w = \sqrt{\left(\frac{2 \cdot T}{\pi \cdot a}\right) \cdot \tan\left(\frac{\pi \cdot a}{2 \cdot T}\right)} \tag{5.9}$$

where, $\emptyset$ is an angle describing the location around the crack perimeter

a is the crack depth, c is half of the semi-elliptical crack width

T is the thickness of the crack plate

5.4 Input Parameters

The static tensile tests for the materials used in this study 6061 and 5083 were performed previously at the University of Waterloo (Coughlin, 2010 and Ranjan et al, 2016). Those tests provided the mechanical properties for both as-received materials 6061-T651 and 5083-H321. Since the properly welded 6061 specimens always failed in the HAZ and the properly

welded 5083 specimens always failed at weld root, the mechanical properties for both locations are important to determine in order to be best represented in the LEFM model. However, due to the nature of the tensile tests, the fracture locations for each test may not necessarily occur at the weld toe or weld root locations as planned. Therefore, the material properties at the weld toe or weld root were determined using an indirect method. Reid (2010) estimated the mechanical properties of the 6061 alloys in the HAZ using the empirical equations developed by Bauel and Seeger (1990) for aluminum. A linear relationship was developed similar to steel in order to determine the ultimate strength in the 6061 HAZ based on the Vickers hardness, HVN, and ultimate strength, σ_{ult}, for 6061-T651 aluminum and 6061-O aluminum alloys,

$$\sigma_{ult} = 3.2168 \cdot HVN - 45.006 \tag{5.10}$$

Linear interpolations were performed to obtain those parameters based on hardness. The mechanical properties used in the LEFM analysis are summarized in **Error! Reference source not found.**.

Table 5.2 Material properties

Material Properties	6061-T651	6061-O	6061-HAZ	5083-H321	5083-O	5083-Root
Vickers Hardness, HVN	110	51	55	100	87	77
Modulus of Elasticity, E (MPa)	70451	60937	61550	73762	72214	70988
Yield Strength, σ_y (MPa)	287.5	60.9	75.5	240.6	123.7	31.1
Ultimate Tensile Strength, σ_{ult} (MPa)	308.8	119.1	131.3	368.2	328.0	296.1

It should be noted that the material strength was used in the LEFM analysis in the definition of the critical crack size, a_c, based on established ductile and brittle fracture criteria. The resistance for both materials 6061 aluminum and 5083 aluminum alloys against cyclic crack propagation is characterized by the material parameters, C and m in the Paris law in Equation (2.4). The IIW states that when the specified or measured material parameters are absent, the parameters of Paris power law constants for aluminum can be taken as $C = 4.46 \times 10^{-10}$ and

125

$m = 3.0$, which was the approach employed in the current analysis. However, this combination of Paris' constants in the LEFM model did not result a match with the experimental data. Therefore, the Paris' constant C and m was assumed to be $7.88 * 10^9$ and 3.96 in this study under a R-ratio of 0.1 for 6061 aluminum alloys (Collini, Pirondi, & Fersini, 2004).

The input parameters for LEFM analysis were obtained based on material tests conducted in this study or performed by others. Those input parameters include thickness, t, initial crack depth, a_i, aspect ratio, a/c, and stress concentration factor, SCF.

5.4.1 Thickness, t

In the current study, two types of alloys with different thicknesses were evaluated. The parent material of 6061 alloys were measured with a thickness of 9.53 mm, and 5083 alloys were measured with a thickness of 9.1 mm. However, the thicknesses of the specimens at weld nugget regions varied due to the practice of FSW (see Appendix D). For example, the thicknesses for toe flash specimens of 6061 alloys were reduced to approximately 8.7 mm due to the over plunging of the FSW tool. Therefore, the variations in thicknesses can be assumed with a lower bound of 8.7 mm and an upper bound of 9.53 mm. As shown in Figure 5.11, varying the plate thickness within this range has no noticeable influence on the fatigue behaviour, as predicted using the fracture mechanics model.
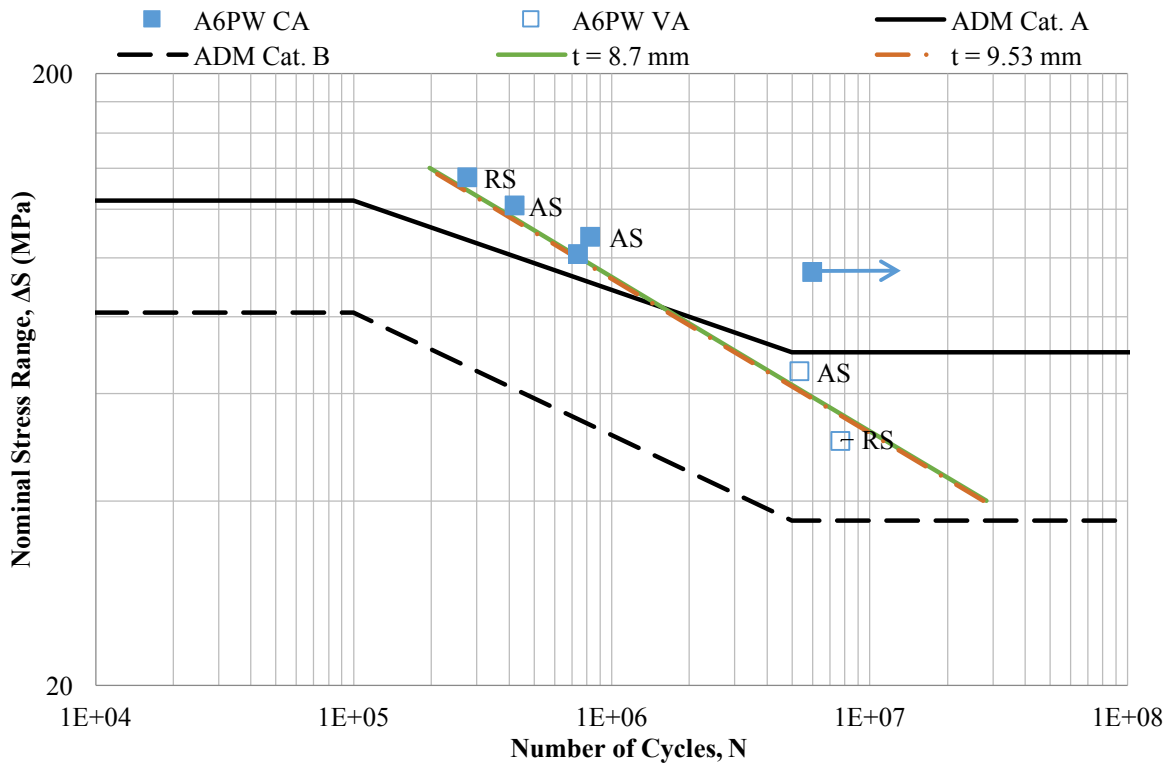
Figure 5.11 Predicted S-N curves with varied thicknesses

5.4.2 Initial Crack Depth, a_i

The initial crack depths were measured either using the non-destructive or the destructive methods described in Section 4.4. Besides the average initial opening of 0.93 mm for the 6061 KB specimens and 0.23 mm for the unintended kissing bond observed in "proper welds", due to the difficulty in measuring small cracks, the initial defect sizes for all other defect types were difficult to quantify precisely. Menzemer (1992) who conducted over 100 defect measurements on arc welded aluminum specimens, suggested that the most common initial crack size was 0.025 mm. In the current study, an initial defect depth of 0.025 mm was assumed for the analysis of fatigue life of specimens failing at the weld toe AS or RS locations, based on the observed initial defects in the 6061 TF specimens.

5.4.3 Aspect Ratio, a/c

Measurements of crack depth were discussed in Section 4.2. In this study, a crack aspect ratio of 0.55 was observed for the 6061 alloy and 0.65 was observed for the 5083 alloy, for the

analysis of weld toe failures. Due to limited crack shape data, the two aluminum groups were combined together, and a crack shape aspect ratio of 0.58 was assumed. As a further simplification, no evolution of the crack shape was considered. In other words, the crack shape aspect ratio was assumed to be constant for the entire fatigue life.

5.4.4 Stress Concentration Factor, SCF

A stress concentration factor (SCF) of 1.0 was assumed for all of the butt joints except those associated with the TF defect. For these specimens, an SCF of 2.7 was assumed, based on the ABAQUS FE analysis results in reported in Figure 5.8. As a simplification and conservative modelling assumption, a uniform stress distribution through the plate thickness was assumed for this specimen type, even though the actual SCF decreases rapidly with depth.

5.5 Constant Amplitude Sensitivity Analysis

LEFM analyses were conducted using MATLAB with different parameters under constant amplitude loading, including material properties, initial crack depth, crack shape, and crack growth parameters. The fatigue results produced using the LEFM model were compared to the fatigue tests obtained in this study in order to assess the validity of the model. Key results of these sensitivity studies and comparisons with test data are presented here.

5.5.1 Properly Welded Specimen Analysis

In the current study, the experimental S-N curves obtained for proper welds of 6061 alloy was used as a baseline for model validation and subsequent analysis of the various defect types investigated experimentally in this research project.
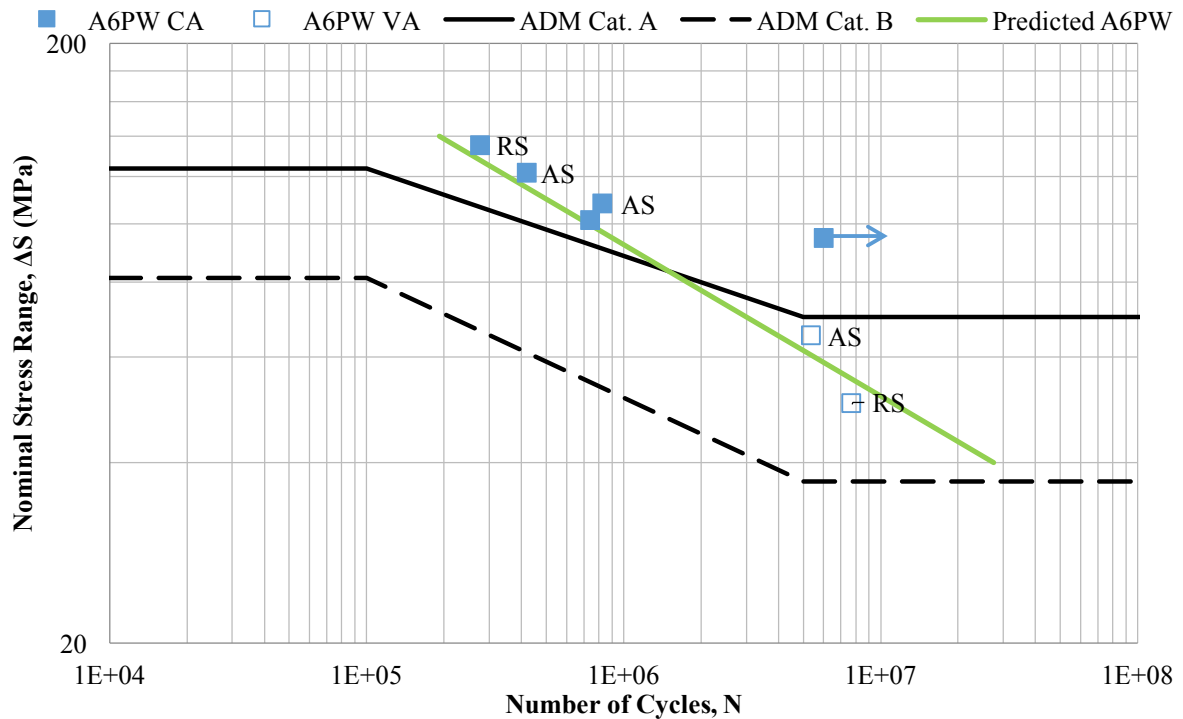
Figure 5.12 Predicted S-N curves for 6061 proper welds (A6PW) FSW joints

In order to accurately predict the S-N curves for 6061 proper welds, the input parameters of the LEFM model were carefully selected. The predicted S-N curve for 6061 properly welded specimens were modelled with the smallest cross-sectional area of 70 mm width by 9.53 mm thickness, an initial crack (center crack) depth of 0.025 mm as suggested by Menzemer (1992), an aspect ratio of 0.58 obtained by measuring the elliptical shapes in all failed specimens, and a stress concentration factor of 1.0. The S-N curves based on experimental results and LEFM model using the selected input parameters were very close as shown in Figure 5.12. Therefore, those input parameters were taken as baseline values and modified to model defects including kissing bond and toe flash defects.

5.5.2 Kissing Bond Specimen Analysis

The kissing bond specimens have unbonded regions at the weld roots, which make them different from the proper welds. The kissing bond defect was modelled using the same LEFM model used for proper welds, except the initial crack depth was changed to 0.93 mm

and the crack was modelled as a through crack (a/c =0). The analysis results are shown in Figure 5.13. The predicted S-N curves for an intended kissing bond of 0.93 mm closely aligned with the experimental results. In order further validate the proposed LEFM model, the unintended kissing bond defects observed in the properly welded specimen set were analyzed in the LEFM model. As identified under Section 4.4.1 of the microstructural analysis, three specimens PW03A, PW03C, and PW04A were found with initial unbonded depth of 0.238 mm, 0.23 mm and 0.23 mm respectively. The corresponding LEFM model was modified with an initial through crack of 0.23 mm shown as a_i = 0.23 mm in Figure 5.13. The predicted S-N curve was moderately close to the three fatigue results with unintended kissing bond defect, and above the ADM standard Category B. Considering the difficulty in detecting such kissing bond defect with nondestructive methods and the dramatic reduction in fatigue life, kissing bond defect in FSW joints should be avoided if possible.
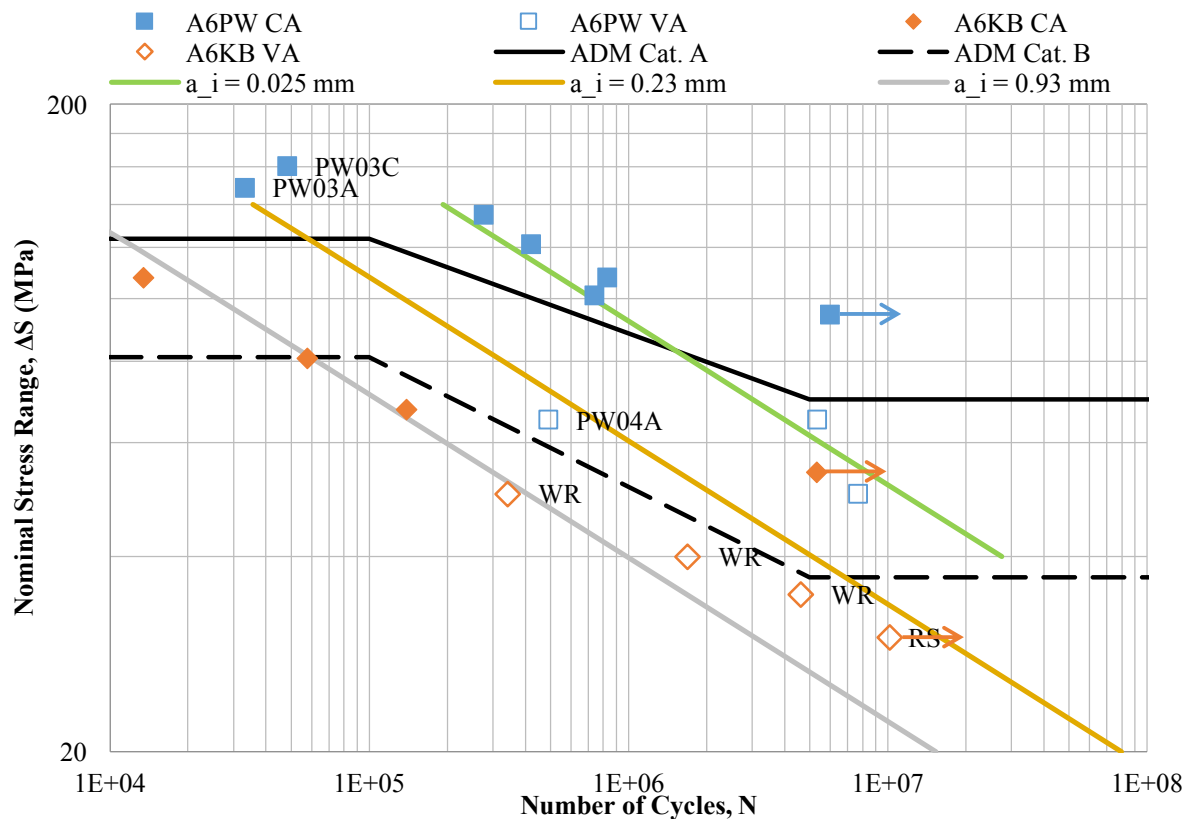
Figure 5.13 Predicted S-N curve for 6061 kissing bond (A6KB) FSW joints

5.5.3 Toe Flash Specimen Analysis

Due to the over plunge of the FSW tool, a concave impression was created at the weld nugget region resulting a reduction in cross-sectional area and a change in profile geometry. In comparison with the proper welds, the LEFM model for toe flash was modelled differently with a cross-sectional area of 70 mm width by 8.7 mm thickness, and a stress concentration factor of 2.7 determined from ABAQUS model. The predicted S-N curve for the toe flash specimens is plotted in Figure 5.14. The predicted S-N curve for toe flash was slightly conservative in comparison with the experimental results. This is likely due to the conservative assumption (made to simplify the fracture mechanics analysis) of a uniform stress distribution (i.e. uniform SCF) through the plate thickness, when in fact, this stress distribution decreases rapidly below the top surface of the plate (see Figure 5.10).
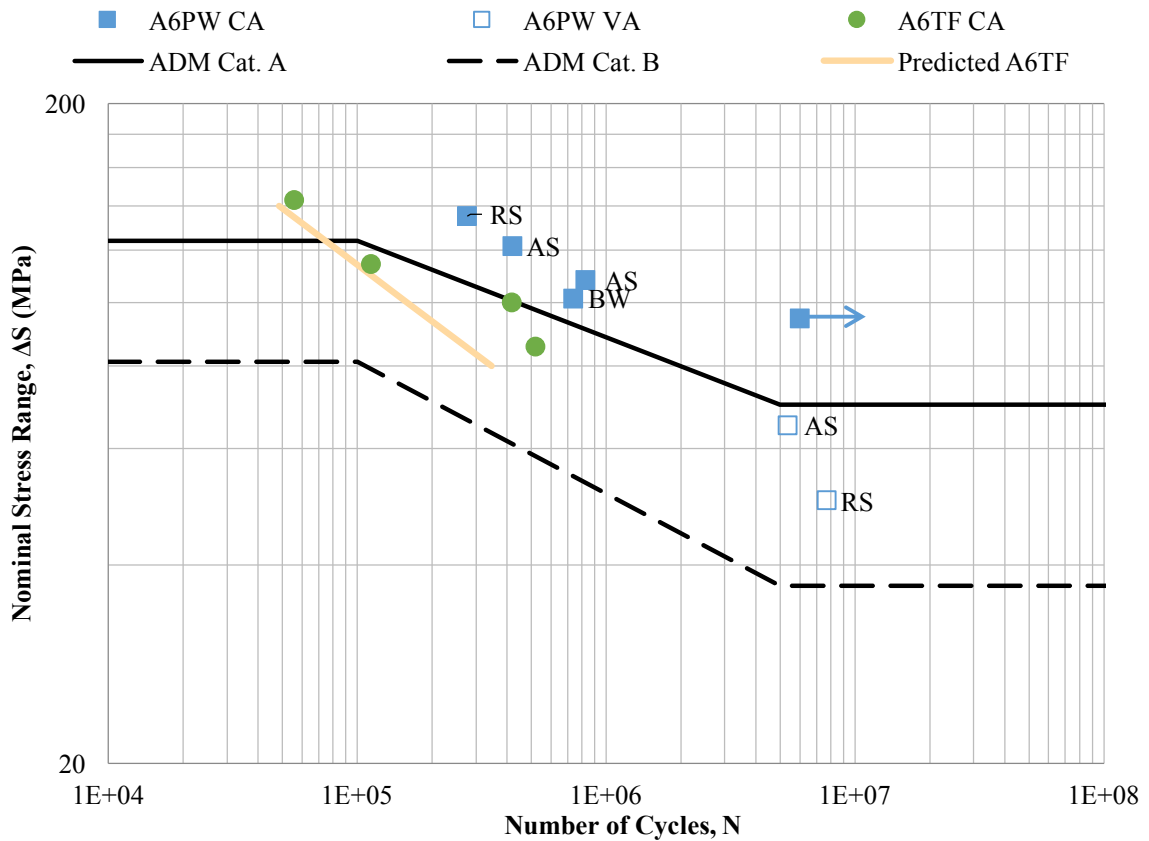
Figure 5.14 Predicted S-N curve for 6061 toe flash (A6TF) FSW joints

5.6 Limitations

The statistical analysis, ABAQUS model, and LEFM model all have limitations that impacted the accuracy of the analyses performed. For the statistical analysis, the number of experimental results was not large enough to generate reliable design S-N curves based on the IIW recommendation. This could be addressed to some degree by grouping data sets together where appropriate (e.g. CA and VA, 6061 and 5083). Due to the nature of the FE method, it can only provide an approximate solution. The FE model in ABAQUS was based on a single TF geometry collected during the fabrication process. The weld geometry could be different from one specimen to another for the toe flash data set. This could be studied with a more in-depth FE analysis on models developed from multiple TF images. Additional FE models should be performed to determine the SCF and degree of bending to due to the lack of symmetry of the lap joint (LJ) specimens.

Chapter 6

Conclusions and Recommendations

This chapter presents the main conclusions and recommendations resulting from the research presented in the previous chapters of this thesis.

6.1 Conclusions

The conclusions resulting from the research presented in this thesis can be separated into two parts, including those based on the experimental data and those resulting from the subsequent statistical, finite element, and fracture mechanics analysis.

6.1.1 Conclusions Based on Experimental Data

Based on the experimental data obtained and the associated metallurgical analysis of the weld specimens, the following conclusions are drawn:

- As 6061 is a heat-treatable aluminum alloy, the mechanical properties associated with this material deteriorate rapidly in its weld region at the middle of the thickness, especially in the HAZ. The HAZ material is softened with finer precipitates identified with low hardness measurements on both the AS and RS, where the AS has a slightly lower value than the RS. The characteristic of a reduction in hardness on the AS or RS was reflected with more than half of the 6061 fatigue specimens fracturing on their AS when other defects do not dominate. Whereas for 5083, the hardness values at the middle of the thickness is relatively consistent in the welded region. Due to the 0.2 mm root gap seen in all of the "properly welded" specimens fabricated with 5083 alloy during the FSW process, the fracture locations for all properly welded specimens were at the weld root due to the existence of a remnant line.

- The experimental fatigue S-N curves obtained for the A6KB and A6LJ specimens showed very little scatter, with a significant reduction in fatigue life in comparison with the other defect types. The fatigue data obtained was showed little scatter because of the consistent root flaw sizes (approximately 1 mm in depth) produced in all of the plates. However, both defect types were difficult to accurately detect using

nondestructive methods, as shown in the certified ultrasonic testing inspection reports (CTS and ES). The defects in the A6KB and A6LJ specimens should be avoided because of the difficulty at detecting those flaws and the significant reduction in fatigue life that results from their presence.

- All of the experimental S-N curves were above Detail Category B (butt-welded) in the ADM standard except A6KB and A6LJ. It can be concluded that the 6061 material is not sensitive to geometry changes as the reduction in fatigue life for the 1 mm toe flash specimens was not significant and the polished samples with smooth surface top did not have an improvement on the overall fatigue life in comparison with the proper welded specimens. Therefore, polishing the excessive toe flash or weld surface is not necessary or beneficial other than for aesthetic reasons.

- The multiple attempts in trying to create wormhole in 6061 alloys by varying the travel speeds were unsuccessful. This finding indicated that the tolerance window of the FSW welding parameters (transvers and rotational speed) is wide.

6.1.2 Conclusions Based on Analytical Studies

Based on the statistical, finite element, and fracture mechanics analysis of the fatigue tests on FSW joined aluminum specimens, the following conclusions are drawn:

- The statistical analyses of 95% survival probability design S-N curves illustrated that the fatigue life significantly decreased for A6PO and A5WH compared with the mean S-N curves due to the large scatter of the collected S-N curves. Surprisingly, based on the available wormhole CA fatigue experimental data, the design S-N curve was above the ADM Category B curve for this defect type. The A6KB and A6LJ mean and 95% S-N curves were below the both ADM design curves, and both 95% curves were close to the mean S-N curves as a result of consistency in defect production. However, several assumptions made by the IIW were not incorporated in the analysis, including the minimal size of the data set. Additional experimental fatigue data should be collected in order to get a high confidence level in the conclusions made.

- 4-node quadrilaterial plain strain elements were employed in the ABAQUS model. The highest stress concentrations were observed near the toe flash where there is a sudden geometry change. The stress concentration factor of the toe flash specimens is approximately 2.7 times greater than the nominal stress.

- An LEFM model was used in this study to predict the fatigue lives of FSW joints under CA loadings, with sensitivity studies performed on several model parameters, including the thickness, initial crack depth, aspect ratio, and stress concentration factor. The model generated predicted S-N curves that were close to the experimental results by using an initial crack size of 0.025 mm, a constant crack shape aspect ratio of 0.58, and a stress concentration factor of 1.0 for 6061 properly welded specimens. Other predicted S-N curves were modelled based on the baseline model with modifications. For instance, the predicted S-N curve of 6061 toe flash FSW joints were modelled by changing the stress concentration factor to 2.7 in order to account for the sudden geometry changes at the weld toe. For the kissing bond FSW joints, the model was modified by changing the initial crack depth to the average measured unbonded depth. Sensitivity analyses were then conducted to examine the impact of individual input parameters in relation to the expected values assumed. All of the individual parameters were compared to determine the input parameters with the greatest influence on the model predictions.

6.2 Recommendations

Recommendations for future work are made here for the following area of study: methods for measuring flaws in FSW joints, experimental tests, and fracture mechanics analysis.

- The inspection reports from both certified ultrasonic testing material inspection labs (CTS and ES) suggested that nondestructive measures for detecting kissing bond defects less than 1 mm may not be reliable. However, the phase array method with a 45° technique can assist in measuring kissing bond defects with a relative smaller error when compared to other methods. A destructive

metallurgical analysis should always be performed using either tensile or bending tests whenever there is a suspicion of a kissing bond in the component. The other inexpensive method is to use a dye penetrate through the weld root. Even after a discontinuous kissing bond identification with dye, the entire component should be investigated for the kissing bond defect depth.

- Additional experimental tests with an emphasis on VA loading tests are recommended to produce complete fatigue curves. Large-scale specimens should be tested to account for residual stresses and plate misalignments that are present in real structures.

- More investigation on polished samples is recommended to find out the reason why the fatigue performance for the polished samples appears to have actually been slightly worse than the proper welded samples.

- Many of the input parameters used in the LEFM analysis were taken from the hypotheses and experimental findings of others. These assumptions were not all validated in the current study. Therefore, it is recommended that further material testing should be conducted for elastic modulus, yield strength, ultimate strength, and the cyclic material constants that are used in the LEFM analysis

Reference

Albrecht, P., & Yamada, K. (1977). Rapid Calculation of Stress Intensity Factors. *Journal of the Structural Division ASCE 103*, 377-389.

Aluminum Association. (2015). *Aluminum Design Manual Part I Specification for Aluminum Structures.* The Aluminum Association.

Arrien, P., Bastien, J., & Beaulieu, D. (2001). Rehabilitation of Bridges using Aluminum Decks. *NRC Research Press*, 992-1002.

Bridges & Structures. (2016, 12 31). Retrieved from Federal Highway Administration: https://www.fhwa.dot.gov/bridge/nbi/no10/defbr16.cfm

BSI. (1992). *BS 8118:1991. Structural Use of Aluminum - Part I Code of Practice for Design.* London.

CEN. (2007). *Eurocode 9 Design of Aluminum Structures.* Milano: UNI.

Chandrashekar, A., Reddappa, H., & Ajaykumar, B. (2016). Influence of Tool Profile on Mechanical Properties of Friction Stir Welded Aluminum Alloy 5083. *International Journal of Chemical, Molecular, Nuclear, Materials and Metallurgical Engineering*, 8-14.

Collini, L., Pirondi, A., & Fersini, D. (2004). *Fatigue Crack Resistance of 6061 and 7005 Aluminum Alloy* . Parma, Italy: University of Parma.

Coughlin, R., & Walbridge, S. (2012). Fatigue Testing and Analysis of Aluminum Welds under In-Service Highway Bridge Loading Conditions. *Bridge Engineering*, Vol. 17, No. 3.

CSA. (2014). *CSA S6-14 Canadian Highway Bridge Design Code.* CSA Group.

Das, S. K., & Kaufman, J. (2007). Aluminum Alloys for Bridges and Bridge Decks. *TMS (The Minerals, Metals & Materials Society)*, 61-72.

Dickerson, T., & Przydatek, J. (2003). Fatigue of Friction Stir Welds in Aluminum Alloys that Contain Root Flaws. *International Journal of Fatigue* , 1399-1409.

Ericsson, M., & Sandström, R. (2003). Influence of Welding Speed on the Fatigue of Friction Stir Welds, and Comparison with MIG and TIG. *International Journal of Fatigue*, 1379-1387.

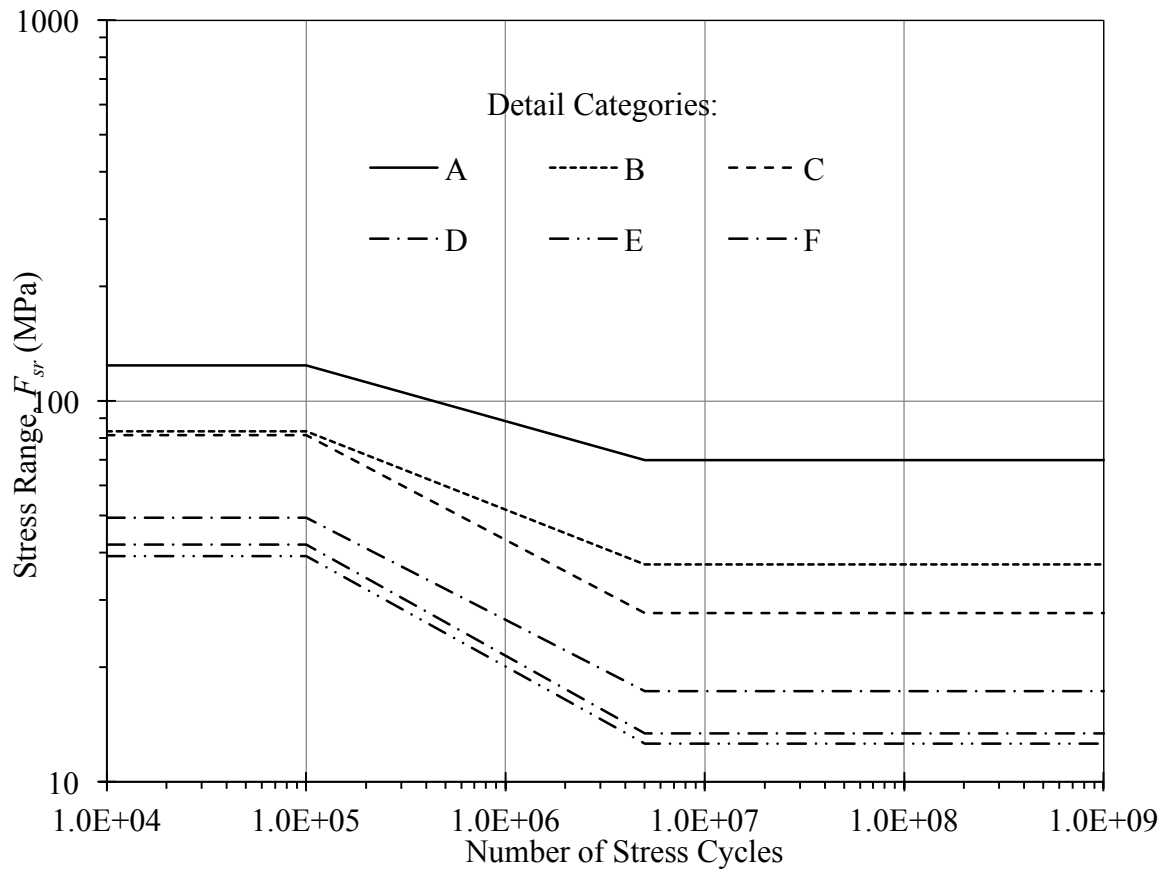*ESAB*. (2017). Retrieved from Welding Automation: http://www.esab.com/automation/en/process/fsw/Tools.cfm

Fujii, H., Cui, L., Maeda, M., & Nogi, K. (2006). Effect of Tool Shape on Mechanical Properties and Microstructure of Friction Stir Welded Aluminum Alloys. *Materials Science and Engineering A419*, 25-31.

Gagnon, M., Gaudreault, V., & Overton, D. (2008). *Age of Public Infrastructure: A Provincial Perspective.* Ottawa: Minister of Industry for Statistics Canada.

Gemme, F., Verreman, Y., Dubourg, L., & Wanjara, P. (2011). Effect of Welding Parameters on Microstructure and Mechanical Properties of AA7075-T6 Friction Stir Welded Joints. *National Research Council Canada. *, 877-886.

Gharaibeh, N., Al-Jarrah, J., & Sawalha, S. (2016). Effect of Pin Profile on Mechanical Properties of 6061 Al Alloy Welded Joints Prepared by Friction Stir Welding. *International Journal of Mechanics and Applications*, 39-42.

Gitter, R. (2006). Aluminium Materials for Structural Engineering – Essential Properties and Selection of Materials. *Structural Engineering International*, 294-300.

Gurney, T. (2006). *Cumulative Damage of Welded Joints.* Cambridge: Woodhead Publishing Limited.

Hobbacher, A. (2016). IIW. *Recommendations for Fatigue Design of Welded Joints and Components*. Switzerland: Springer International Publishing.

Houska, C. (n.d.). *Deicing Salt - Recognizing the Corrosion Threat.* Pittsburgh: TMR Consulting.

Huijbregts, R. (2013, 12 13). *To Modernize Canada's Public Infrastructure - Every Bridge Needs a Switch*. Retrieved 09 25, 2017, from Cisco Canada Blog: https://gblogs.cisco.com/ca/2012/12/13/to-modernize-canadas-public-infrastructure-every-bridge-needs-a-switch/

ISO. (2011). *ISO 25239 Friction Stir Welding - Aluminum .* Switzerland: International Organization for Standardization.

Itharaju, R. (2004). *Friction Stir Processing of Aluminum Alloys.* Lexington: University of Kentucky.

James, M., Hattingh, D., & Bradley, G. (2003). Weld Tool Travel Speed Effects on Fatigue Life of Friction Stir Welds in 5083 Aluminum. *International Journal of Fatigue 25*, 1389-1398.

Kim, S.-Y. (2008). Optimal Welding Parameters of 5083 Al Alloy by Friction Stir Welded. *Research Institute of Industrial Technology* , 115-120.

Kosteas, D. (1994). *Design Recommendations for Fatigue Loaded Structures.* Munich: European Aluminum Association.

Maddox, S. J. (2003). Review of Fatigue Assessment Procedures for Welded Aluminum Structures. *International Journal of Fatigue 25*, 1359-1378.

McDonnell, M., & Miller, R. (2011). *Guidelines for Friction Stir Welding.* Warren: Manufacturing Systems Demonstration.

Menzemer, C. (1992). *Fatigue Behavior of Welded Aluminum Structures.* Ann Arbor: University Microlilms International.

Menzemer, C., & Fisher, J. (1993). Fatigue Design of Welded Aluminum Structures. *Transportation Research Record*, 79-88.

Mishra, R., & Mahoney, M. (2007). *Friction Stir Welding and Process.* Ohio: ASM International.

Podržaj, P., Jerman, B., & Klobčar, D. (2015). Welding Defects at Froctopm Stir Welding . *Metalurgija 54*, 387-389.

Radaj, D., Sonsino, C., & Fricke, W. (2006). *Fatigue Assessment of Welded Joinits by Local Approaches.* Boca Raton: Woodhead Publishing Limited and CRC Press LLC.

Reid, C. (2010). *Fatigue of Aluminum Welds in Canadian Highway Bridges.* Waterloo: University of Waterloo.

Salerno, B. (2007). *Aluminum Structure Design and Fabrication Guide (SSC-452).* Washington: Ship Structure Committee.

Shah, L. (2017). *Characterization of Friction Stir Welded Thick Plate Aluminm Alloys for Structural Applications.* Waterloo: University of Waterloo.

Siwowski, T. (2006). Aluminum Bridges - Past, Present and Future. *Structural Engineering International*, 286-293.

Stephens, R., Fatemi, A., Stephens, R., & Fuchs, H. (2001). *Metal Fatigue in Engineering.* New York: A Wiley-Interscience Publication.

Svensson, L.-E., Karlsson, L., Larsson, H., Fazzini, M., & Karlsson, J. (2000). Microstructure and Mechanical Properties of Friction Stir Welded Aluminum Alloys with Special Reference to AA5083 and AA6082. *Science and Technology of Welding and Joining*, 285-296.

Thomas, W., Johnson, K., & Wiesner, S. (2003, 07). Friction Stir Welding - Recent Developments in Tool and Process Technologies. *Advanced Engineering Materials*, 485-490. Retrieved from TWI.

Threadgill, P., Leonard, A., Shercliff, H., & Withers, P. (2009). *Friction Stir Welding of Aluminum Alloys.* 49-93: International Materials Reviews.

Venkata Rao, C., Madhusudhan Reddy, G., & Srinivasa Rao, K. (2015). Influence of Tool Pin Profile on Microstructure and Corrosion Behaviour of AA2219 Al-Cu Alloy Friction Stir Weld Nuggets. *Defence Technology 11*, 197-208.

Walbridge, S., & de la Chevrotière, A. (2012). *Opportunities for the Use of Aluminum in Vehicular Bridge Construction.* Montreal: Aluminum Association of Canada.

Walbridge, S., & De La Chevrotière, A. (2012). *Opportunities for the Use of Aluminum in Vehicular Bridge Construction.* Montreal : Aluminum Association of Canada.

Zhou, C., Yang, X., & Luan, G. (2005). Fatigue Properties of Friction Stir Welds in Al 5083 Alloy. *Elsevier*, 1187-1191.

Appendix A Fatigue S-N Curves with Detail Category Illustrations

Aluminum Design Manual (Aluminum Association, 2015) and AASHTO Bridge Design Specification (CSA, 2014):

Table 3.1
STRESS CATEGORY

General Condition	Detail	Detail Category	Fatigue Design Details (note 1)
Plain Material	Base metal with rolled, extruded, drawn, or cold finished surfaces; cut or sheared surfaces with ANSI/ASME B46.1 surface roughness ≤ 1000 μin. (25μmm)	A	1, 2
Built-up Members	Base metal and weld metal in members without attachments and built up of plates or shapes connected by continuous full or partial penetration groove welds or continuous fillet welds parallel to the direction of applied stress.	B	3, 4, 5
	Flexural stress in base metal at the toe of welds on girder webs or flanges adjacent to welded transverse stiffeners.	C	6, 21
	Base metal at the end of partial-length welded cover plates with square or tapered ends, with or without welds across the ends.	E	5
Mechanically Fastened Connections	Base metal at the gross section of slip-critical connections and at the net section of bearing connections, where the joint configuration does not result in out-of-plane bending in the connected material and the stress ratio (the ratio of minimum stress to maximum stress) R_s is (note 2)		
	$R_s \leq 0$	B	7
	$0 < R_s < 0.5$	D	7
	$0.5 \leq R_s$	E	7
	Base metal at the gross section of slip-critical connections and at the net section of bearing connections, where the joint configuration results in out-of-plane bending in connected material.	E	8
Fillet Welds	Base metal at intermittent fillet welds	E	
	Base metal at the junction of axially loaded members with fillet-welded end connections. Welds shall be disposed about the axis of the members so as to balance weld stresses.	E	15, 17
	Shear stress in weld metal of continuous or intermittent longitudinal or transverse fillet welds	F	5, 15, 18
Groove Welds	Base metal and weld metal at full-penetration groove welded splices of parts of similar cross section ground flush, with grinding in the direction of applied stress and with weld soundness established by radiographic or ultrasonic inspection.	B	9, 10
	Base metal and weld metal at full-penetration groove welded splices at transitions in width or thickness, with welds ground to slopes ≤ 1: 2.5, with grinding in the direction of applied stress, and with weld soundness established by radiographic or ultrasonic inspection.	B	11, 12
	Base metal and weld metal at full-penetration groove welded splices with or without transitions with slopes ≤ 1: 2.5, when reinforcement is not removed and/or weld soundness is not established by radiographic or ultrasonic inspection.	C	9, 10, 11, 12
	Base metal and weld metal at full-penetration groove welds with permanent backing.	E	22
Attachments	Base metal detail of any length attached by groove welds subject to transverse and/or longitudinal loading, with a transition radius $R \geq 2$ in. (50 mm) and with the weld termination ground smooth:		
	$R \geq 24$ in. (610 mm)	B	13
	24 in. > $R \geq 6$ in. (150 mm)	C	13
	6 in. > $R \geq 2$ in. (50 mm)	D	13
	Base metal at a detail attached by groove welds or fillet welds with a detail dimension parallel to the direction of stress $a < 2$ in. (50 mm)	C	19
	Base metal at a detail attached by groove welds or fillet welds subject to longitudinal loading, with a transition radius, if any, < 2 in. (50 mm):		
	2 in. (50 mm) ≤ a ≤ 12b or 4 in. (100 mm)	D	14
	a > 12b or 4 in. (100 mm)	E	14, 19, 20
	Base metal at a detail of any length attached by fillet welds or partial-penetration groove welds in the direction parallel to the stress, with a transition radius $R \geq 2$ in. (50 mm), and the weld termination is ground smooth:		
	$R \geq 24$ in. (610 mm)	B	16
	24 in. > $R \geq 6$ in. (150 mm)	C	16
	6 in. > $R \geq 2$ in. (50 mm)	D	16
Luminaire Base Welds	Base metal and filler metal at a pair of circumferential fillet welds at least 0.48D apart in a tube's longitudinal direction, where D = the outside diameter of the tube. Fillet welds shall be sufficient to develop the static bending strength of the tube and be placed in the following order: weld the top of the base and the tube, then weld the end of the tube and the bottom of the base. The base shall be for a top mounted luminaire or as a support for a short arm, defined as that producing no more than 5 ksi (35 MPa) tensile dead load stress in the tube at top of the base.	F1	23

Notes:
1. See Figure 3.1. These examples are provided as guidelines and are not intended to exclude other similar details.
2. Tensile stresses are considered to be positive and compressive stresses are considered to be negative.
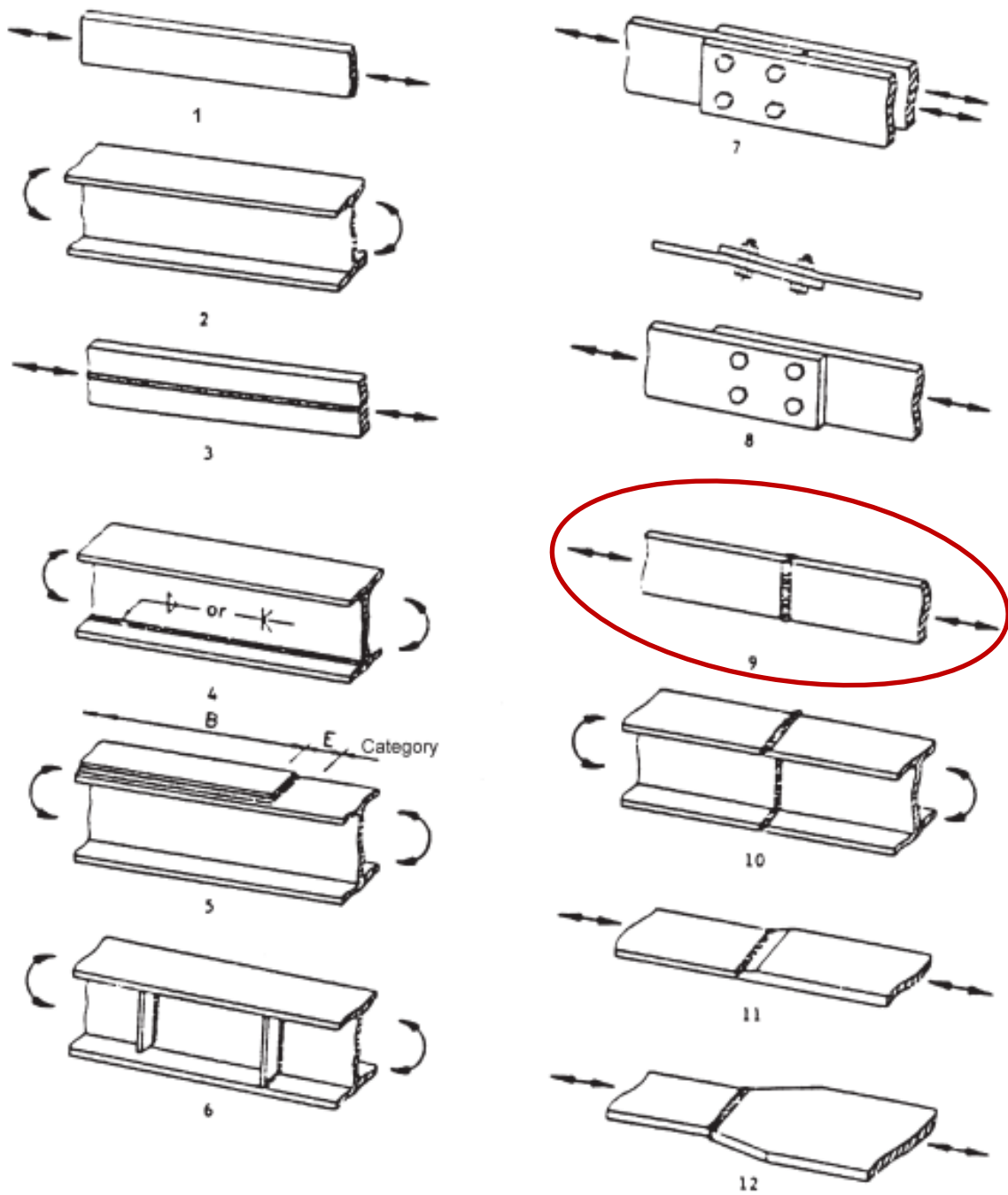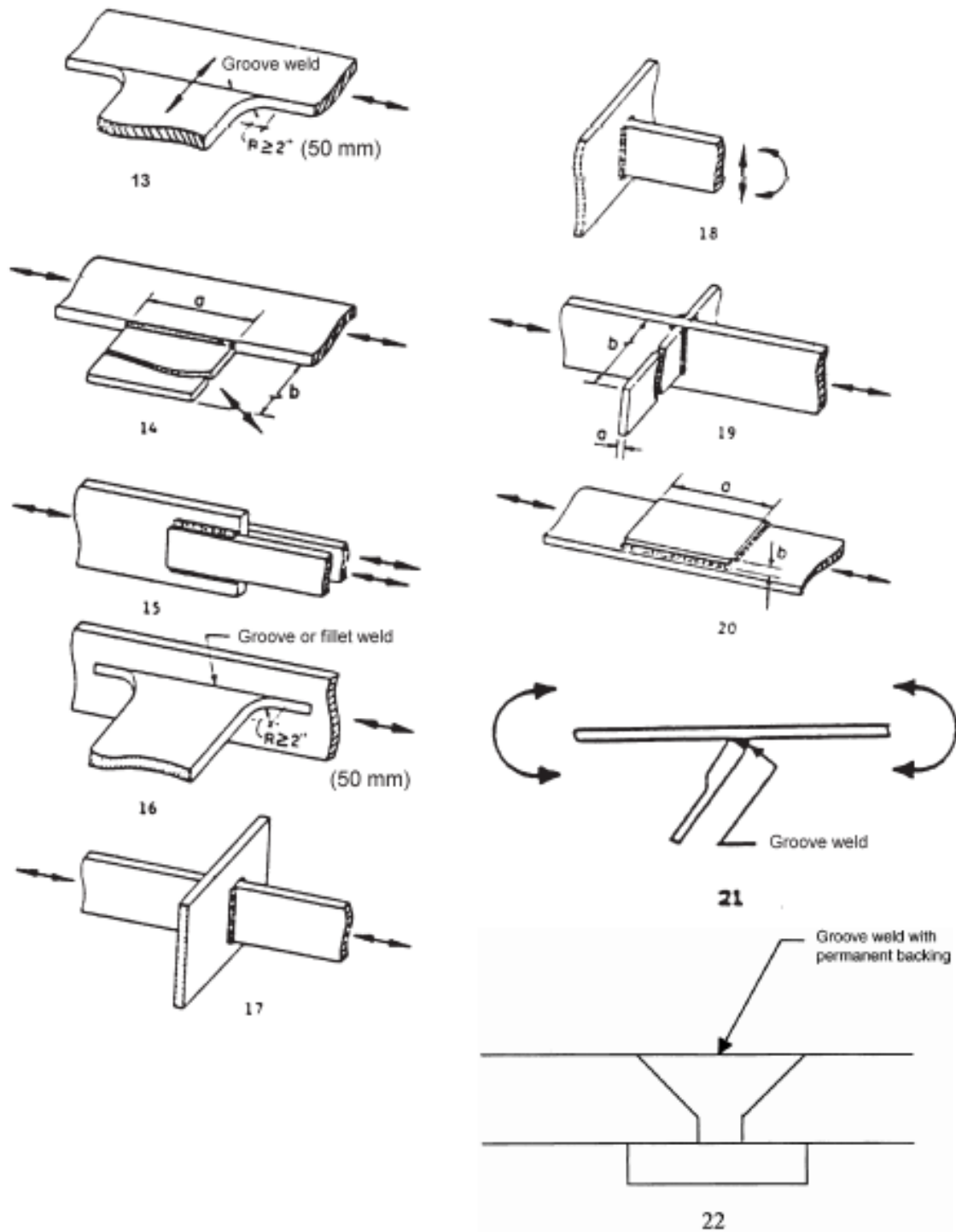
143

Figure 3.1
FATIGUE DESIGN DETAILS

144

Figure 3.1
FATIGUE DESIGN DETAILS (Continued)

145

Eurocode 9 (CEN, 2007)
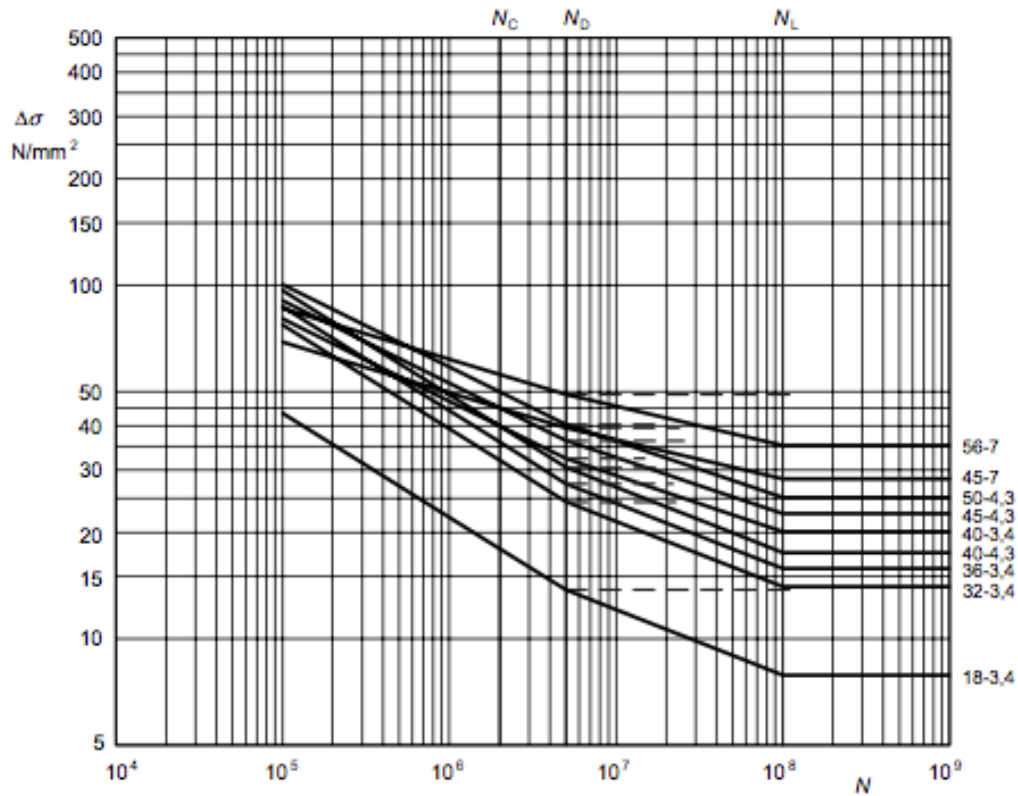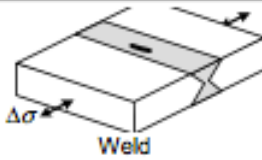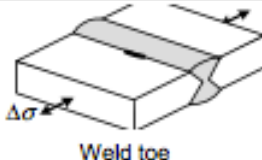
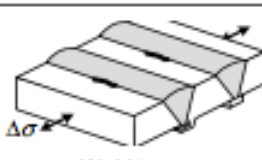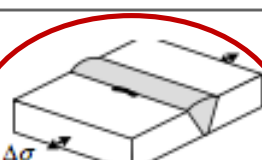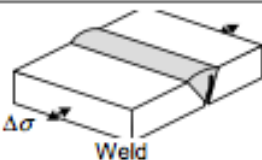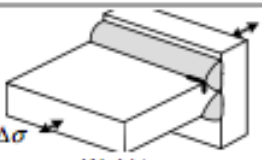Figure J.4 —Fatigue strength curves Δσ-N for butt welded joints between members – detail categories as in Table J.7

Table J.8 – Numerical values of Δσ-N (N/mm²) for butt welded joints between members – detail categories as in Table J.7

Slope		Cycles N						
m₁	m₂	1E+05	1E+06	2E+06	5E+06	1E+07	1E+08	1E+09
7	9	85,9	61,8	56,0	49,1	45,5	35,2	35,2
7	9	69,0	49,7	45,0	39,5	36,6	28,3	28,3
4,3	6,3	100,4	58,7	50,0	40,4	36,2	25,1	25,1
4,3	6,3	90,3	52,9	45,0	36,4	32,6	22,6	22,6
3,4	5,4	96,5	49,0	40,0	30,6	26,9	17,5	17,5
4,3	6,3	80,3	47,0	40,0	32,3	29,0	20,1	20,1
3,4	5,4	86,9	44,1	36,0	27,5	24,2	15,8	15,8
3,4	5,4	77,2	39,2	32,0	24,4	21,5	14,0	14,0
3,4	5,4	43,4	22,1	18,0	13,7	12,1	7,9	7,9

146

Table J.7 – Detail categories for butt-welded joints between members

Detail type	Detail category $\Delta\sigma - m_1$ [1]	Constructional detail / Initiation site	Type of weld	Joint Part	Stress analysis	Welding requirements	Quality level [3] internal	Quality level [3] surface and geometric	additional
7.1.1	56-7	Weld	Full penetration, caps ground flush both sides	Flats, solids	Root ground off	Extension plates used on ends, cut off and ground flush in direction of stress	B	B	6)
7.1.2	45-7			Open shapes			C	C	
7.2.1	50-4,3	Weld toe	Welded from both sides, full penetration	Flats, solids			B	B	4) 6)
7.2.2	40-3,4			Open shapes			B	C	6)
7.2.3	36-3,4						C	C	
7.3.1	40-4,3	Weld toe	Welded one side only, full penetration with permanent backing	Flats, solids	Net section		C	C	6)
7.3.2	32-3,4			Open shapes, hollow, tubular			C	C	
7.4.1	45-4.3	Weld toe	Welded one side only, full penetration without backing	Flats, solids			B	B	5) 6)
7.4.2	40-4,3						C	C	
7.4.3	32-3,4			Open shapes, hollow, tubular			C	C	6)
7.5	18-3,4	Weld	Partial penetration		Net throat		D	D	
7.6	36-3,4	Weld toe	Full penetration		Net section 2)		B	B	

1) $m_2 = m_1 + 2$

2) Stress concentration of stiffening effect of transverse element already allowed for.

3) According to EN ISO 10042:2005

4) Overfill angle ≥150° for both sides of the weld.

5) Overfill angle ≥150°.

6) Taper slope < 1:4 at width or thickness changes

Appendix B CTS Inspection Report

622 Trillium Drive, Kitchener, Ontario N2R 1B6   Tel. (519) 748-2880 Fax (519) 748-2783   Web Site: www.certified-testing.com

INSPECTION REPORT

DATE: Oct. 27-28, 2016

CLIENT: *U of W*   **CLIENT'S P.O. NUMBER:**

ADDRESS: *Waterloo- On.*   **PAGE**   1   **OF**   3
Job site: CTS

REPORT NUMBER	850-2	CTS INSPECTION ORDER	850	CTS INSPECTOR	*D. Molla*
					UT-MT-VT-PT ASNT Level III

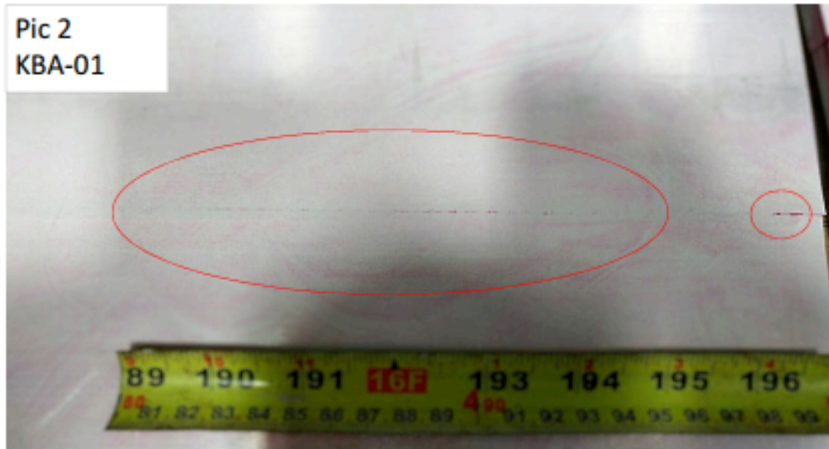### NDT on Dog- Bone Speciemens KB01, KB02, KB03 (root area)

I- RADIOGRAPHIC INSPECTION:

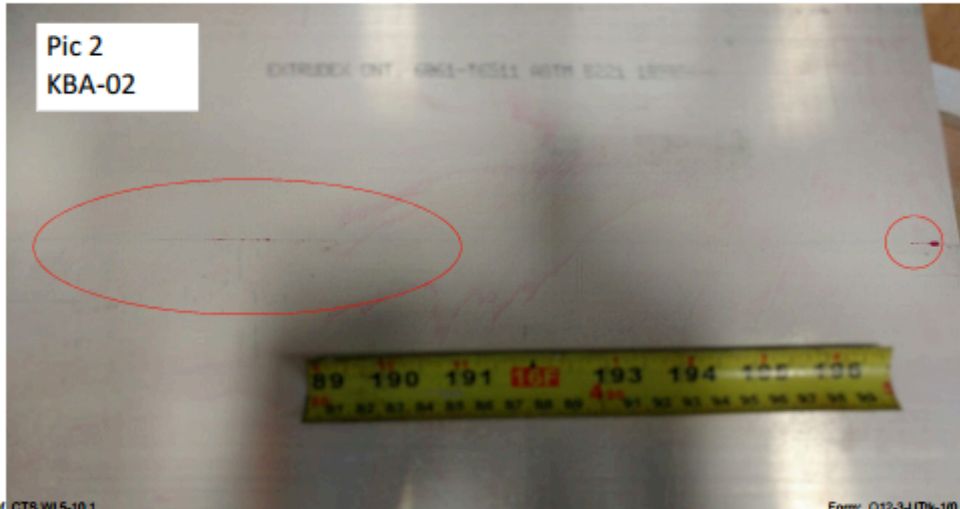The RT didn't detect the defects, RT films are available for review.

2- LIQUID PENETRANT INSPECTION:

The test detected faint indications idicating that the root defects are very shallow. See picture 1, 2 & 3

Pic 2
KBA-01

Pic 2
KBA-02

CTS
NDT
CERTIFIED TESTING SYSTEMS

622 Trillium Drive, Kitchener, Ontario N2R 1E6 Tel. (519) 748-2680 Fax (519) 748-2783   Web Site: www.certified-testing.com

INSPECTION REPORT

DATE: Oct. 27- 28, 2016
PAGE   2   OF   3

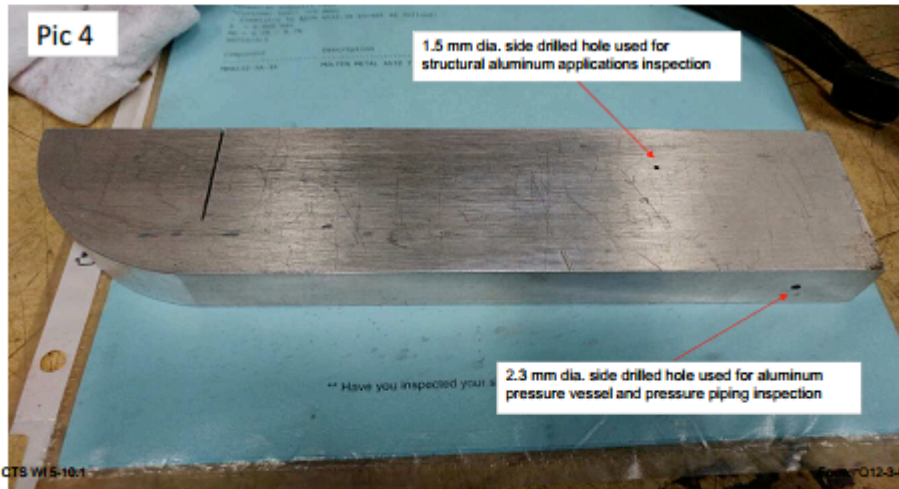| REPORT NUMBER	850-2	CTS INSPECTION ORDER	850	CTS INSPECTOR	D. Molla UT•MT•VT•PT ASNT Level III

Pic 3
KBA-03

3- ULTRASONIC INSPECTION:
The test dectected indications on KB02 and KB03 as marked on the plates picture 5& 6 on page 3.

4-CONCLUSION:
The intended root cracking is too shallow and the joints are welded almost to the full plate thickness. In order for the cracks to be RT/UT detected they have to have a significant depth Min. 1.5mm in order to be detected and evaluated properly.

Picture 4 is showing the UT aluminumin calbiration block showing the reference holes for the most comonly used codes


Pic 4

1.5 mm dia. side drilled hole used for structural aluminum applications inspection

2.3 mm dia. side drilled hole used for aluminum pressure vessel and pressure piping inspection

Ref. CTS WI 5-10.1

![CTS NDT CERTIFIED TESTING SYSTEMS logo]

622 Trillium Drive, Kitchener, Ontario N2R 1E6   Tel. (519) 748-2880 Fax (519) 748-2783   Web Site: www.certified-testing.com

INSPECTION REPORT

		DATE:	Oct. 27- 28, 2016		
		PAGE	3	OF	3

REPORT NUMBER	850-2	CTS INSPECTION ORDER	850	CTS INSPECTOR	D. Molla
					UT•MT•VT•PT ASNT Level III

Pic 5

Pic 6
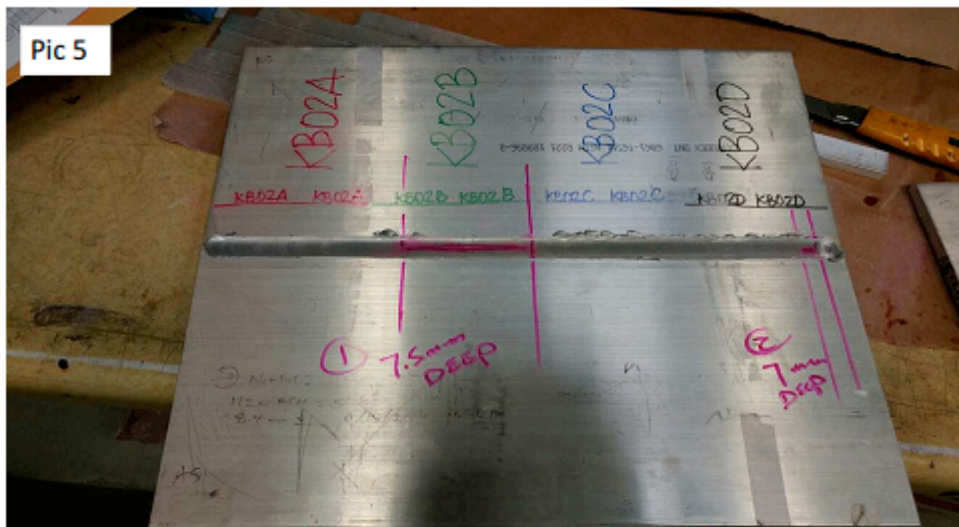
Appendix C ES Inspection Reports

Part 1 Feasibility Study Report

Feasibility Study for Ultrasonic Inspection of Friction Stir Welds in Aluminum

Prepared for:

Lincoln Caissie

Prepared by:

Luís Marka

CSWIP ACFM TOFD PAUT Level 2
Advanced NDT Applications Technician

Reviewed by:

Lincoln Caissie
Director of Sales and Special Services
Eclipse Scientific Inc.

Manager of Acuren Scientific – Eastern Region

Revision Record

Rev. #	Date	Changes since last revision	Author(s)	Reviewer(s)

Prepared by:	Date:	Reviewed by:	Date:
L. Marka	02/10/2017	L. Caissie	02/10/2017

Page 1 of 15

153

Eclipse Scientific.

440 Phillips St. Suite 100
Waterloo, ON N2L 5R9

Research & Development Division

Office: (519) 886-6717

Fax: (519) 886-1102

TABLE OF CONTENTS

Prepared by:	Date:	Reviewed by:	Date:
L. Marka	02/10/2017	L. Caissie	02/10/2017

154

Eclipse Scientific.
Office: (519) 886-6717

440 Phillips St. Suite 100
Fax: (519) 886-1102

Waterloo, ON N2L 5R9

Research & Development Division

TABLE OF FIGURES

Prepared by:	Date:	Reviewed by:	Date:
L. Marka	02/10/2017	L. Caissie	02/10/2017

Eclipse Scientific.

440 Phillips St. Suite 100
Waterloo, ON N2L 5R9

Office: (519) 886-6717
Fax: (519) 886-1102

Research & Development Division

1   INTRODUCTION

This document contains a basic overview of the tests performed to determine the feasibility of friction stir weld testing on aluminum plates.

Testing was performed using Eddy Current and ultrasonic Phased Array methods. Different Phased Array techniques were tested.

2   EQUIPMENT LIST

In order to complete the feasibility study the following specialized equipment was used:

- Olympus Omniscan MX
- Olympus 10MHz 10L64-A2 Phased Array probe
- Olympus SA2-N55S-IHC Phased Array wedge
- Eclipse Scientific ScanLab platform
- Aluminum calibration blocks
- Olympus Nortec 600 Eddy Current instrument
- Eddy Current ML-100KHz-500KHz/A/90.5/6 Eddy Current probe with cable and connector

Standard equipment was also used (camera, pen, paper, ruler, caliper).
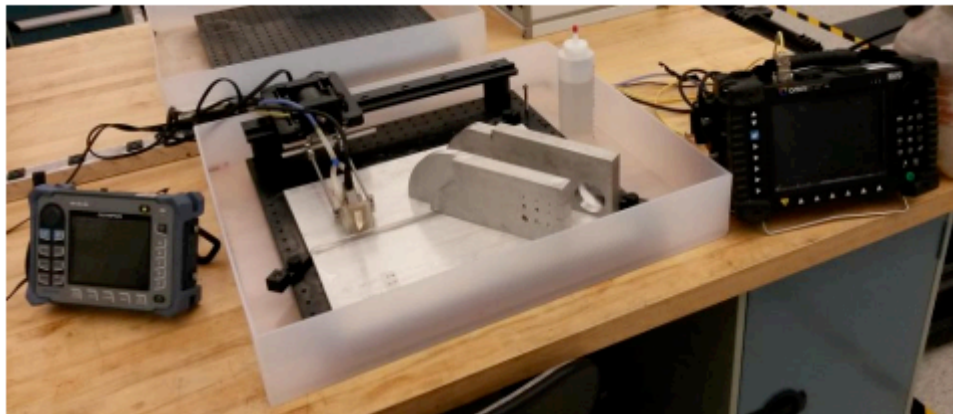
Figure 1: General view of sample piece and testing equipment

Prepared by:	Date:	Reviewed by:	Date:
L. Marka	02/10/2017	L. Caissie	02/10/2017

3 TEST PART DESCRIPTION

One weld joining two 9.5mm thickness 6061-T5 aluminum plates was provided for this feasibility study. Dimension of the welded joint is 425 x 360mm. Images of the section are shown in Figure 2. The different surfaces were labeled A and B for differentiation during scan, as highlighted in the picture below.
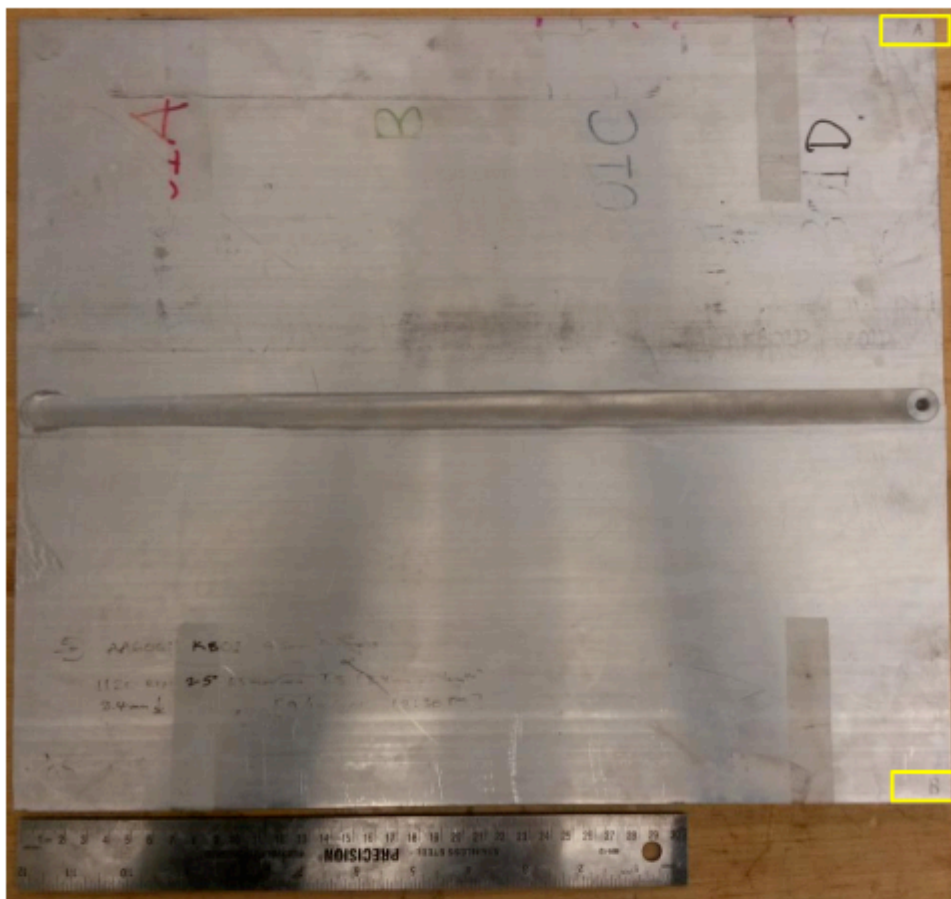

Figure 2: View of welded plate

Prepared by:	Date:	Reviewed by:	Date:
L. Marka	02/10/2017	L. Caissie	02/10/2017

4 PHASED ARRAY TESTS

For the Phased Array tests, different techniques were proposed. Each was designed using specialized software and then translated to a setup in the Omniscan MX Phased Array instrument. Scans using different techniques were performed and the results compared.

As this study does not adhere to any specific Codes, calibration was based on amplitude obtained from small reflectors (1mm Ø side drilled holes in aluminum block) and gain was added in incremental steps to obtain adequate sensitivity with an acceptable signal-to-noise ratio.

4.1 68° Linear Technique

The first technique tested used 68° ultrasonic beams in a linear scan setup. This technique attempted to locate flaws in the weld fusion face by using a beam angle as close as possible to 90°. A diagram of the technique is displayed below.
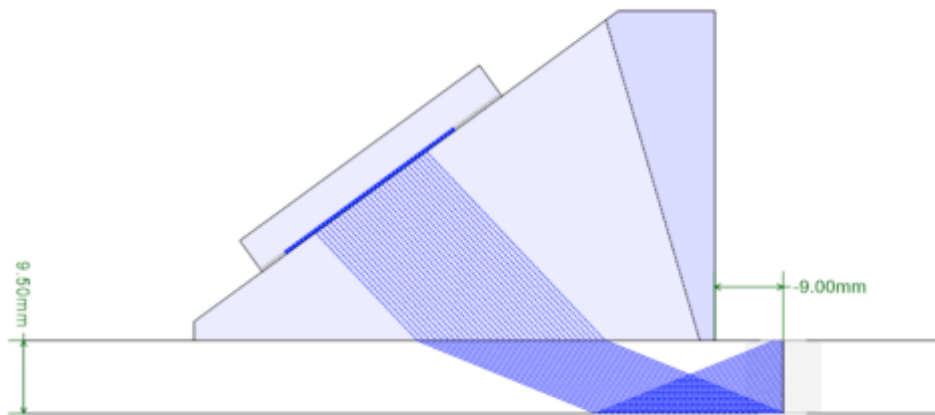
Figure 3: 68° Phased Array technique coverage

Scans performed with this technique could not locate flaws in the welded sample. Geometric signals, however, were clearly visible and matched the expected positions for such signals.

Scan gain was initially based on calibration block reflector amplitude, with additional gain based on background noise level. Scans were performed with the probe positioned at both sides of the weld in order to maximize probability of detection. Vertical flaws, as expected in this type of weld, theoretically should be equally visible from either side of the weld but in practice, small variations introduce fluctuations in response from one side of the weld in respect to the other.

Prepared by:	Date:	Reviewed by:	Date:
L. Marka	02/10/2017	L. Caissie	02/10/2017

Eclipse Scientific.   Office: (519) 886-6717
440 Phillips St. Suite 100 Fax: (519) 886-1102
Waterloo, ON N2L 5R9

Research & Development Division
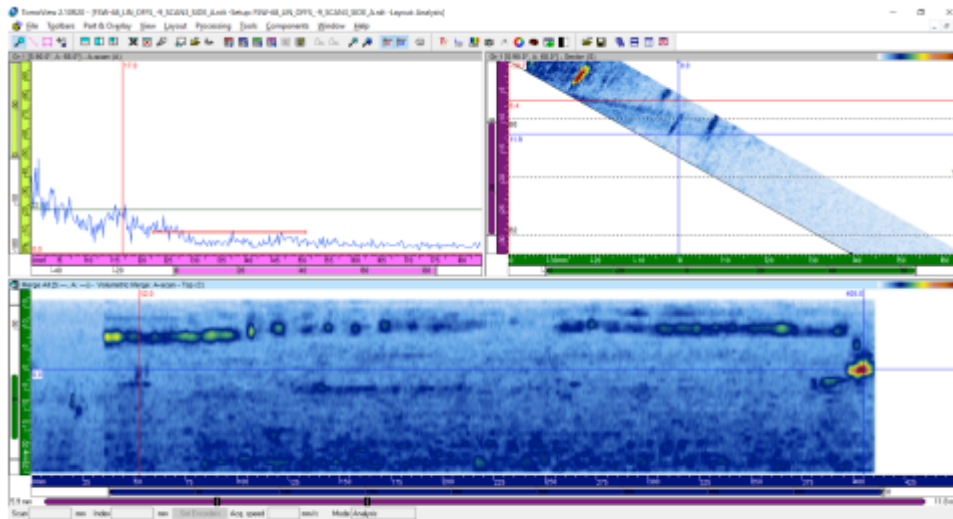
Figure 4: 68° inspection from plate side A
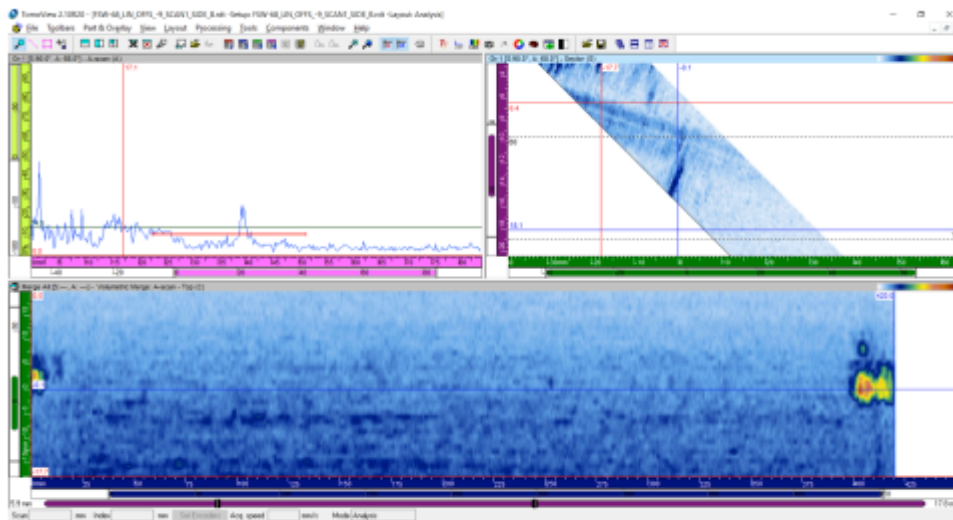
Figure 5: 68° inspection from plate side B

Prepared by:	Date:	Reviewed by:	Date:
L. Marka	02/10/2017	L. Caissie	02/10/2017

Eclipse Scientific.

440 Phillips St. Suite 100

Waterloo, ON N2L 5R9

Research & Development Division

Office: (519) 886-6717

Fax: (519) 886-1102

4.2   55° Linear Technique

A 55° ultrasonic beams in a linear setup scan was attempted. This technique relied on a corner reflection from vertical flaws to obtain a response. A diagram of the technique is displayed in the diagram below.
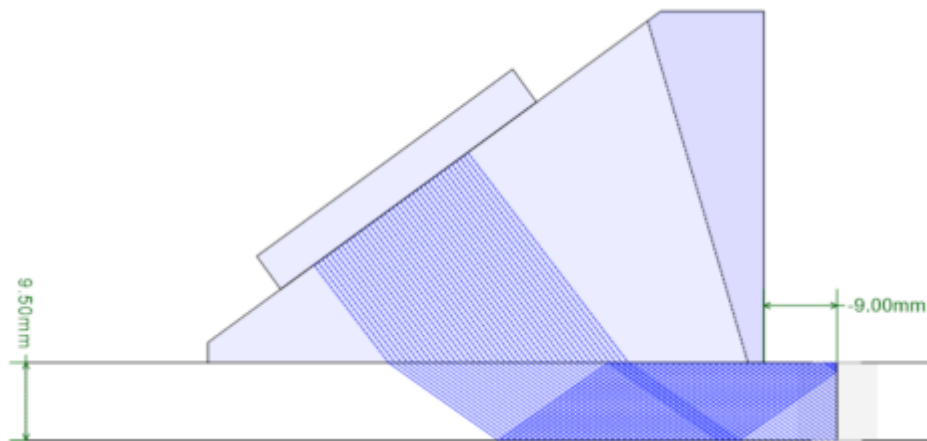
Figure 6: 55° inspection technique

The 55° technique scanning provided response from reflectors located in the root region, as would be expected in this type of weld. The amplitude response was generally low, suggesting that such reflectors have a small vertical extent.

In the scan performed on the A side of the plate, low amplitude reflectors were found in most of the weld extent, with two relatively small regions free of indications as in the images below:

Prepared by:	Date:	Reviewed by:	Date:
L. Marka	02/10/2017	L. Caissie	02/10/2017

Eclipse Scientific.
440 Phillips St. Suite 100
Waterloo, ON N2L 5R9

Office: (519) 886-6717
Fax: (519) 886-1102

Research & Development Division
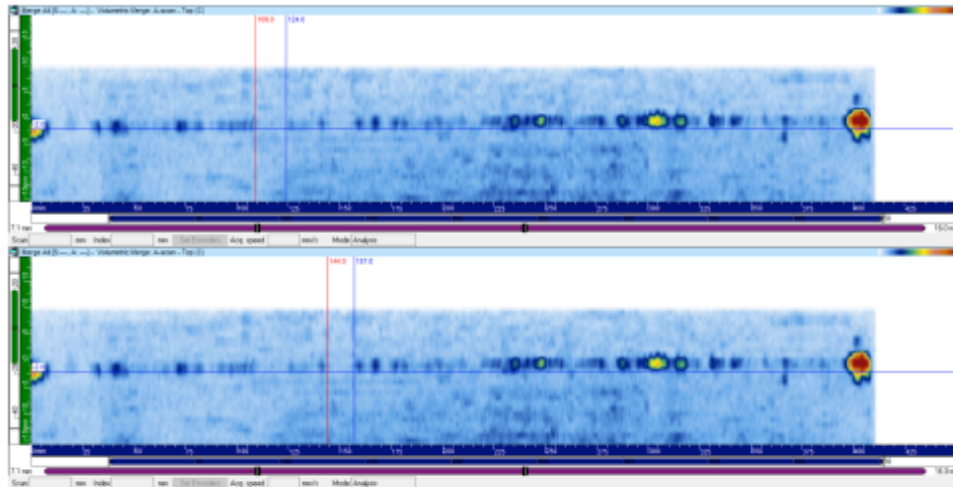
Figure 7: 55° inspection clean regions (side A)

Scan gain was initially based on reflector amplitude, and gain was added based on background noise level. Scans were performed with the probe positioned at both sides of the weld in order to maximize probability of detection. Vertical flaws, as expected in this type of weld, theoretically should be equally visible from either side of the weld but in practice, small variations introduce fluctuations in response from one side of the weld in respect to the other. In fact, response from each side was slightly different although instrument settings were essentially kept the same for each scan.

The images below represent a full view of the inspection results using the 55° setup. Defects are highlighted in the images.

Prepared by:	Date:	Reviewed by:	Date:
L. Marka	02/10/2017	L. Caissie	02/10/2017

Eclipse Scientific.

440 Phillips St. Suite 100
Waterloo, ON N2L 5R9

Office: (519) 886-6717
Fax: (519) 886-1102

Research & Development Division

Figure 8: 55° inspection from plate side A
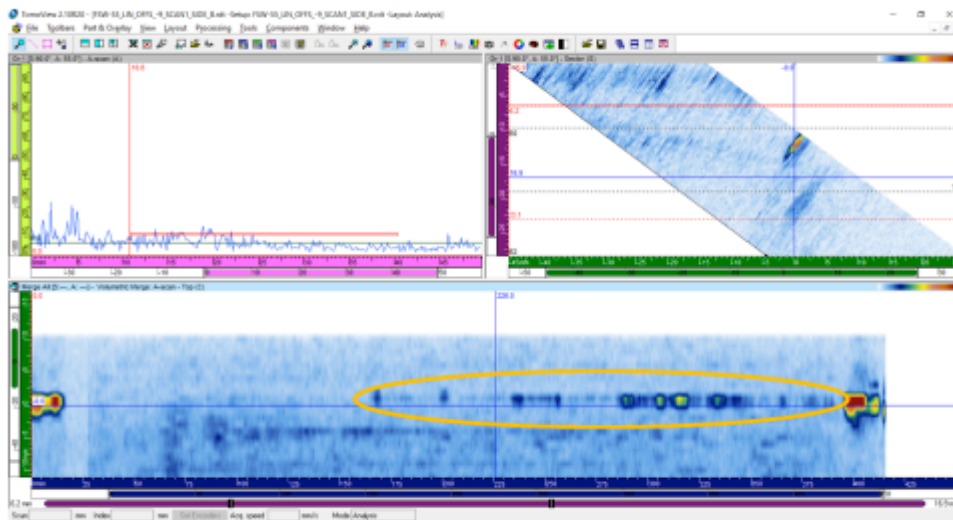
Figure 9: 55° inspection from plate side B

Prepared by:	Date:	Reviewed by:	Date:
L. Marka	02/10/2017	L. Caissie	02/10/2017

Eclipse Scientific.   Office: (519) 886-6717
440 Phillips St. Suite 100   Fax: (519) 886-1102
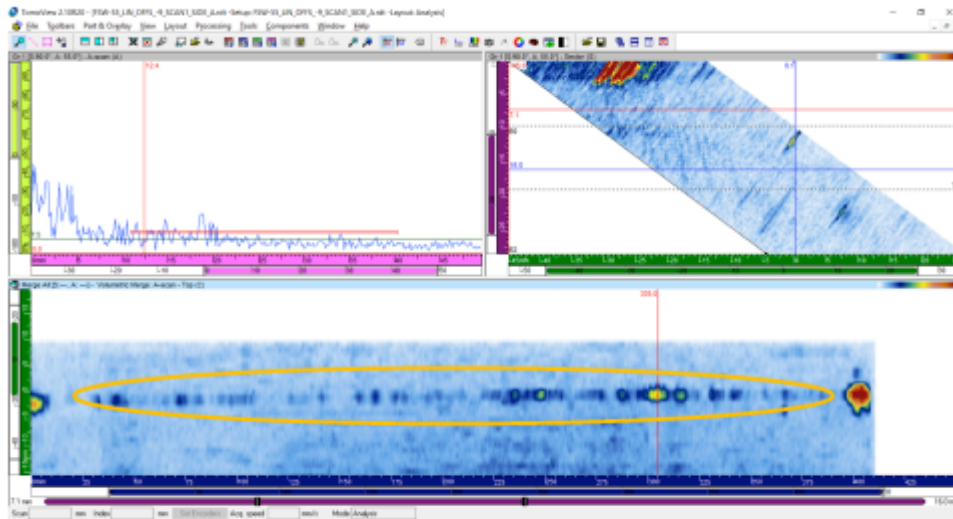Waterloo, ON N2L 5R9

Research & Development Division

4.3   45° Linear Technique

A 45° ultrasonic beams in a linear setup scan was attempted. The corner effect from a vertical reflector should make this technique the most reliable to detect flaws that are open to either surface, but could potentially miss reflectors embedded in the weld. A diagram of the technique is displayed in the diagram below.
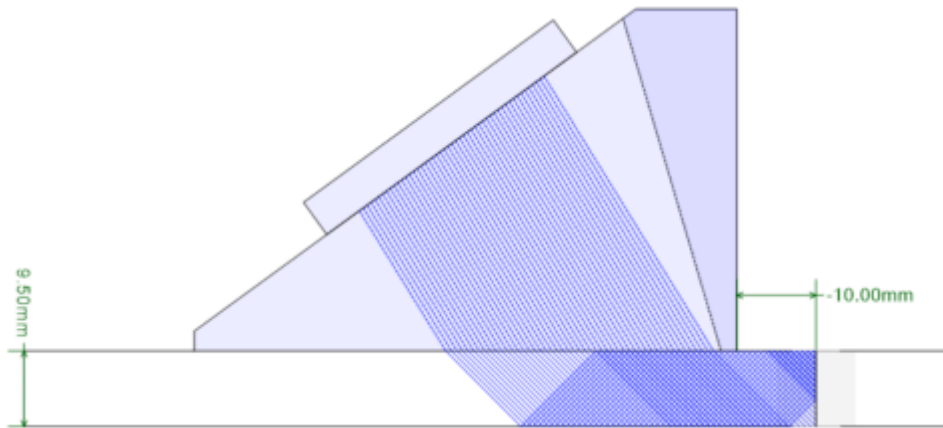
Figure 10: 45° inspection technique

For this technique, probe position was changed from the position used in previous inspection setups. This allows for exit points closer to the front of the edge, resulting in less reflections from the plate top and bottom surfaces.

The 45° technique produced the highest amplitude response from discontinuities in the weld, confirming findings that were detected with the 55° technique. Scans were attempted at different gain settings in order to optimize response without saturating signals.

Both material velocity calibration (3128 m/s in the calibration block) and standard velocity for aluminum (3100 m/s) produced a value that was producing deviations from the actual position in reflections plate edges reflections, both in the measured depth and in distance from wedge face. Reducing the sound velocity to 3000m/s corrected the positioning deviations. It is possible that both the alloy composition and the fabrication process have an influence in the material velocity.

Upon scanning, signals are visible over the full length of the weld, especially when scanning from surface A as displayed in the images below. Defects are highlighted in the images:

Prepared by:	Date:	Reviewed by:	Date:
L. Marka	02/10/2017	L. Caissie	02/10/2017

163
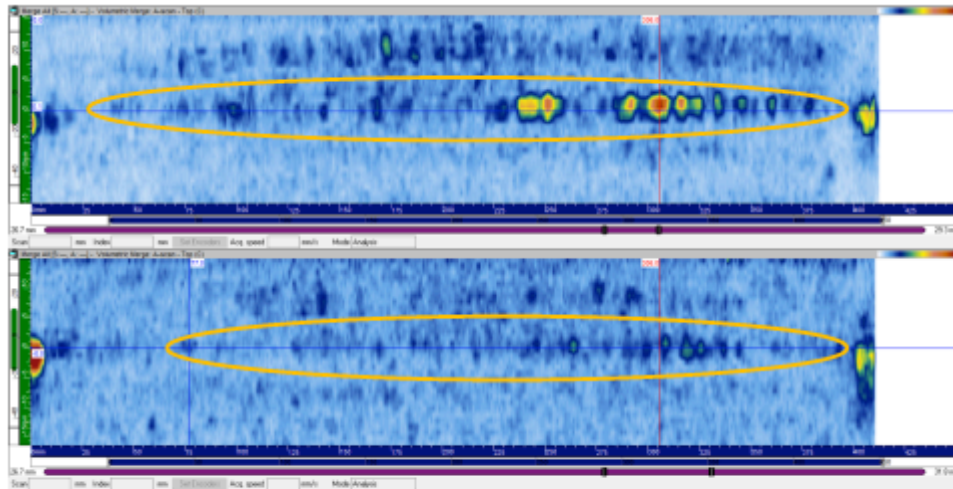
Figure 11: 45° scans for sides A and B

The small height of the discontinuities required a high scan gain. In order to avoid signal saturation, scans were performed ad different gain settings. By adding 15dB to the reference gain, the flaws were detected without saturating signals. The flaw height was estimated at 0.8mm at its larger vertical component, but the corner effect in a 45° beam may oversize the flaw height measurement.

Prepared by:	Date:	Reviewed by:	Date:
L. Marka	02/10/2017	L. Caissie	02/10/2017
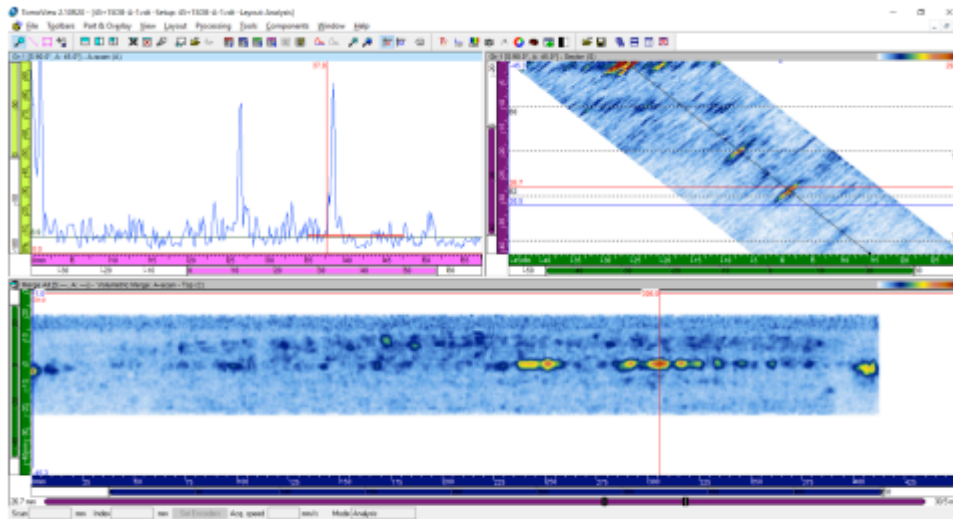
Figure 12: Full view of 45° scan for side A at +15dB gain
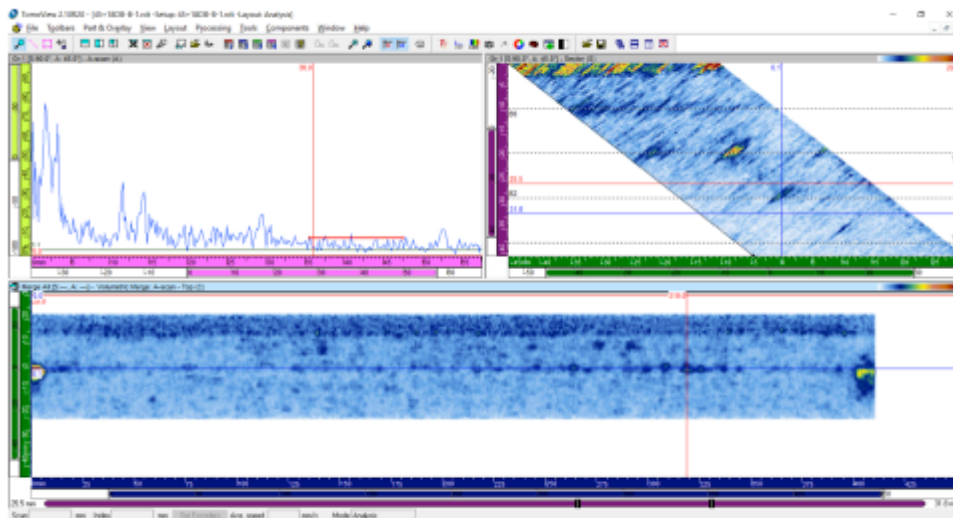
Figure 13: Full view of 45° scan for side B at +15dB gain

Prepared by:	Date:	Reviewed by:	Date:
L. Marka	02/10/2017	L. Caissie	02/10/2017

Eclipse Scientific.
440 Phillips St. Suite 100
Waterloo, ON N2L 5R9

Office: (519) 886-6717
Fax: (519) 886-1102

Research & Development Division

5   EDDY CURRENT METHOD

Eddy currents are well suited for locating surface breaking defects, so this method was chosen for checking the findings with the ultrasonic Phased Array scans, although eddy currents cannot give reliable depth estimates.

The full extent of the weld produced a signal in the Eddy Current instrument consistent with a crack-like indication, except for two areas approximately 10mm long, as per image below:
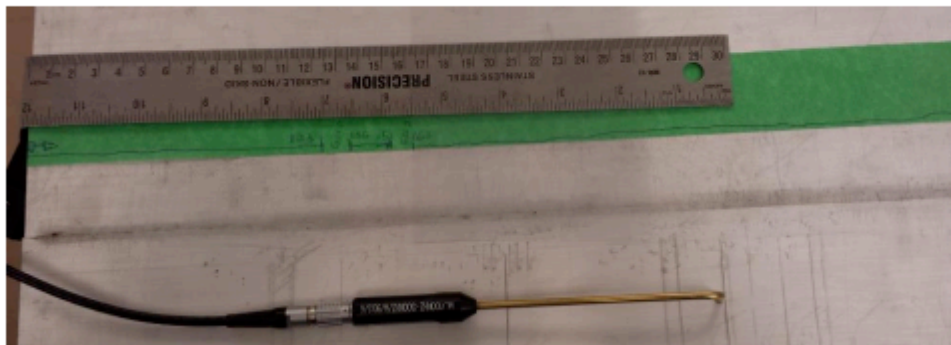
Figure 14: Eddy Current probe and weld scan results
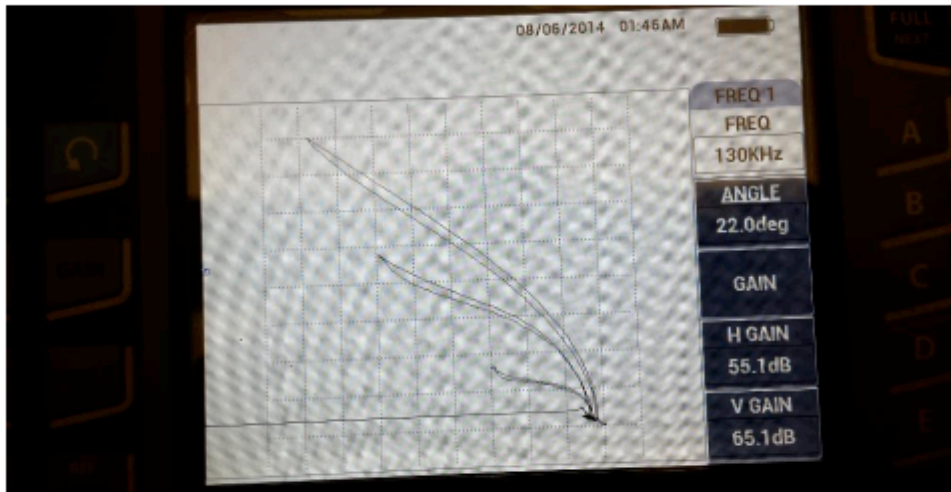
Figure 15: Eddy Current calibration on standard aluminum block

Prepared by:	Date:	Reviewed by:	Date:
L. Marka	02/10/2017	L. Caissie	02/10/2017

6   SUMMARY OF RESULTS

Initial setup using 68° produced very poor results, even with high gain settings. It is possible that the sound velocity difference identified in the 45° scan had an impact on this setup, although this variable would have an influence in the positioning of indications, not in the detection ability.

Setup at 55° showed an improvement over previous setup, with much better detection capabilities. Again, velocity difference generated an error in flaw positioning of about 1mm, which does not seem to have an impact in the technique's ability to detect flaws.

45° setup proved to be the best suited for this application, in accordance with available literature on the subject, where this same angle is recommended for FSW weld inspection. Also, special equipment, not available at this moment in Eclipse Scientific facilities, is required for scanning with the probe oriented 90° from the current scanning orientation.

Eddy current method is an important complement to the ultrasonic method due to its greater sensitivity to defects open to the external surface.

7   RECOMMENDATIONS AND CONCLUSION

These first results show that it is possible to detect flaws in friction stir welds using an ultrasonic Phased Array setup. The small grain size in the alloy tested allows for the use of probes with higher frequency, such as 10 MHz.

Flaw sizing requires a calibration/demonstration block built from the same material as the weld to be inspected, with reflectors machined at precise depths and positions so the amplitude responses can be correlated to the flaw vertical height. Due to differences in velocity found during setup creation, it is recommended that the calibration block provides reflectors suitable for velocity calibration as well.

The ultrasonic method can be complemented by a method that is more sensitive to defects open to the surface, such as Eddy Current, so superficial defects can be detected, even when the vertical dimension is small. Ideally an encoded eddy current system, such as eddy current array, should be used so inspection data can be stored and analyzed.

Available equipment allowed for scanning the weld in a direction parallel to the weld orientation only. However, specialized equipment, such as a water-coupled wedges (immersion) can be used for allowing scans normal to the weld direction, so transverse defects are detectable.

Thresholds for acceptable flaw dimensions should be provided so an acceptance criteria can be applied on the acquired data.

The final recommendation is to perform a sizing accuracy study to ensure the measurements are within needed requirements. With a sizing accuracy study complete, all measurements could be reported with confidence levels.

Prepared by:	Date:	Reviewed by:	Date:
L. Marka	02/10/2017	L. Caissie	02/10/2017

Part 2 *FSW Phase Array Report*

	INSPECTION REPORT	FEASIBILITY STUDY Revision 0		
ECLIPSE SCIENTIFIC	PHASED ARRAY UT	**Date** 02/10/2017		
		Report # 001	**Sheet** 1 of 2	

Project	Customer	Location Waterloo, ON	
Equipment WELDED PLATE	**Welding process** FSW	**Acceptance criteria** N/A	
Material ☐CS ☒AL ☐Other	**Diameter** Plate	**Thickness** 9.5 mm	**Weld preparation**	**Reference block** ALUMINUM IIW
Equipment/serial number OMNISCAN MX	**Software version** TOMOVIEW 2.10	**Couplant** ☐Gel ☒Water	**Scanner type** ES ScanLab	**Scanning direction** L - R
Operator(s) LUIS MARKA / DEEPAK GURJAR			**Technique** ☒PAUT ☐UT

Probe	Size/frequency/pitch	Wedge/refracted angle	Scan type	Aperture / Angle / Start element / # of beams
10L64-A2	50 x 10mm/10MHz /64 Elem./0.6mm	SA2-N55S-IHC/55°	LINEAR	16/45°/1/42

Joint	INDICATIONS						Acceptance		Remarks	Cal/Time
	Type	Side	Start	End	Depth	Height	Acc	Rej		
A6KB01	LOF	A	70	75	9.5	0.2	N/A		Height estimated on amplitude	
A6KB01	LOF	A	91	103	9.5	0.3	N/A		Height estimated on amplitude	
A6KB01	LOF	A	141	144	9.5	0.3	N/A		Height estimated on amplitude	
A6KB01	LOF	A	159	170	9.5	0.4	N/A		Height estimated on amplitude	
A6KB01	LOF	A	221	232	9.5	0.3	N/A		Height estimated on amplitude	
A6KB01	LOF	A	236	381	9.5	0.6	N/A		Intermittent	
A6KB01	LOF	B	261	266	9.5	0.4	N/A		Height estimated on amplitude	

Type: LOF (lack of fusion)   LOP (lack of penetration)   CR (crack)   SI (slag inclusion)   PO (porosity)

Inspector:	Quality manager:	Fiscalization:
Luis S. Marka CSWIP PA Level 2		

Appendix D Fatigue Testing Matrix

ID	Type of Loading	Start Date	End Date	Specimen Dimension (mm)		Load (kN)		Stress (MPa)		Stress Ratio	Stress Range (MPa)	Fatigue Life	Initial Crack Fatigue Life	Frequency (Hz)	Fracturing Location	Notes
				Width	Thickness	Min	Max	Min	Max							
A6PW01C	CA	28-Apr	29-Apr	70	9.68	8	80	11.81	118.06	0.1	106.26	828642	827780	10	Fractured on AS	
A6PW01D	CA	15-May	16-May	70.17	9.79	7.5	75	10.92	109.18	0.1	98.26	741302	-	10	Fractured above (outside) Weld	
A6PW02A	CA	01-May	07-May	70.05	9.63	6	60	8.89	88.94	0.1	80.05	3255068	-	10	-	**Runout**
A6PW02B	CA	05-May	15-May	70.1	9.61	7	70	10.39	103.91	0.1	93.52	6017249	-	10	-	**Runout**
A6PW02C	CA	11-May	12-May	70.03	9.66	9	90	13.30	133.04	0.1	119.74	420979	420348	10	Factured on AS	
A6PW02D	CA	12-May	13-May	70.05	9.6	10	100	14.87	148.70	0.1	133.83	276560	275547	10	Fractured on RS	
A6PW03A	CA	30-May	31-May	70.17	9.74	11	110	16.09	160.95	0.1	144.85	33235		10	Fractured on Weld Root (KB)	Elongated. Slainted KB
A6PW04A	VA	22-Aug	24-Aug	70.06	9.69	11.088	110.88	16.33	163.33	0.1	65.00	492437		10		Minor 0.3mm misalignment
A6PW05A	VA	24-Aug	05-Sep	69.93	9.45	8.53	85.3	12.91	129.08	0.1	50.00	7724571	7701936 (IC at AS)	10		
A6PW05C	VA	05-Sep	19-Sep	70.05	9.44	11.088	110.88	16.77	167.68	0.1	65.00	5383609	5375058 (IC at RS)	10		
A6PO01A	CA	26-Jun	27-Jun	70.01	9.48	10	100	15.07	150.67	0.1	135.60	168458	167320 (IC below AS)	10	Fractured on below weld on AS	
A6PO01B	CA	27-Jun	29-Jun	70	9.47	9	90	13.58	135.77	0.1	122.19	835120	834327 (IC at RS)	10	Fractured on RS	
A6PO01C	CA	29-Jun	30-Jun	70.01	9.46	8	80	12.08	120.79	0.1	108.71	402093	399407 (IC above RS)	10	Fractured above (outside) Weld	
A6PO01D	CA	30-Jun	03-Jul	70	9.47	7	70	10.56	105.60	0.1	95.04	544477	542910 (IC above RS)	10	Fractured above (outside) Weld	
A6PO02A	CA	07-Jul	10-Jul	70.01	9.5	11	110	16.54	165.39	0.1	148.85	132631	132033 (IC at RS)	5	Fractured on RS	
A6PO02B	CA	10-Jul	16-Jul	70.02	9.5	6	60	9.02	90.20	0.1	81.18	5020279	-	10		**Runout**
A6TF01A	CA	12-Jun	12-Jun	70.12	8.75	10	100	16.30	162.99	0.1	146.69	55846	55658 (IC at AS)	10	Fractured on AS	
A6TF01B	CA	12-Jun	13-Jun	70.08	8.72	8	80	13.09	130.91	0.1	117.82	114016	113178 (IC at AS)	5 to 10	Fractured on AS	
A6TF01C	CA	13-Jun	15-Jun	70.04	8.73	6	60	9.81	98.13	0.1	88.31	520841	519353 (IC at AS)	10	Fractured on AS	
A6TF01D	CA	15-Jun	16-Jun	69.97	8.73	7	70	11.46	114.60	0.1	103.14	418103	417573 (IC at AS)	5 to 10	Fractured on AS	
A6TF02B	CA	28-Jul	30-Jul	70.05	9.36	5	50	7.63	76.26	0.1	68.63	467218	466710 (IC at weld root)	15		Possible kissing bond
A6TF02C	CA	01-Jul	03-Jul	69.98	9.33	11	110	16.85	168.48	0.1	151.63	290734	259548	10		Possible kissing bond
A6TF03A	CA	30-Jul	31-Jul	70.01	9.06	5	50	7.88	78.83	0.1	70.95	1009218				Possible kissing bond
A6TF03B	CA	07-Aug	12-Aug	69.98	9	4	40	6.35	63.51	0.1	57.16	5497205	-	15		**Runout**
A6KB01A	CA	16-Jun	16-Jun	70.07	9.63	8	80	11.86	118.56	0.1	106.70	13506	11239 (IC at root)	10	Fractured at Weld Root	
A6KB01B	CA	16-Jun	16-Jun	70.14	9.68	6	60	8.84	88.37	0.1	79.53	57581	55853 (IC at root)	10	Fractured at Weld Root	
A6KB01C	CA	16-Jun	20-Jun	69.93	9.66	4	40	5.92	59.21	0.1	53.29	5322591	-	10&15&20		**Runout**
A6KB01D	CA	21-Jun	21-Jun	70	9.67	5	50	7.39	73.87	0.1	66.48	135466	129251 (IC at root)	10	Weld root	
A6KB02A	VA	19-Sep	20-Sep	69.95	9.54	8.53	85.3	12.78	127.82	0.1	50.00	342040	317896 (IC at root)	10	Weld root	
A6KB02B	VA	20-Sep	02-Oct	69.97	9.54	5.11749	51.1749	7.67	76.66	0.1	30.00	10176309	-	10		**Runout**
A6KB02C	VA	02-Oct	05-Oct	69.96	9.54	6.82332	68.2332	10.22	102.23	0.1	40.00	1692092	1174273 (IC at root)	10	Weld root	

172

|																
A6KB02D	VA	05-Oct	11-Oct	69.97	9.52	5.97	59.7	8.96	89.62	0.1	35.00	4613013	4590378 (IC at root)	10	Weld root	
A6LJ01A	CA	21-Jun	22-Jun	70	18.98	8	80	6.02	60.21	0.1	54.19	13693	11115 (IC at hook)	10	Hook location	
A6LJ01B	CA	22-Jun	22-Jun	69.95	18.92	6	60	4.53	45.34	0.1	40.80	64970	63207 (IC at hook)	10	Hook location	
A6LJ01C	CA	22-Jun	23-Jun	69.94	18.88	5	50	3.79	37.87	0.1	34.08	126227	125188 (IC at hook)	10	Hook location	
A6LJ01D	CA	23-Jun	26-Jun	69.93	18.92	4	40	3.02	30.23	0.1	27.21	219378	218534 (IC at hook)	5 & 20	Hook location	
A6LJ02A	CA	31-Jul	01-Aug	69.98	18.97	3	30	2.26	22.60	0.1	20.34	563711	562960 (IC at hook)	15	Hook location	
A6LJ02B	CA	01-Aug	06-Aug	70.01	19.02	2	20	1.50	15.02	0.1	13.52	5338486		10 & 15	Hook location	
A6LJ02C	VA	11-Oct	16-Oct	69.92	19.02	5.117	51.17	3.85	38.48	0.1	30.00	2144792	2126684 (IC at hook)	10	Hook location	
A6LJ02D	VA	16-Oct	30-Oct	69.9	19	3.411	34.11	2.57	25.68	0.1	20.00	9419241	-	10	Hook location	
A5PW02B	CA	17-May	24-May	70.04	9.16	7	70	10.91	109.11	0.1	98.20	5606722	-	10		**Runout**
A5PW02C	CA	24-May	10-Jun	70.02	9.09	9	90	14.14	141.40	0.1	127.26	2992566	-	8&10		**Runout**
A5PW02D	CA	29-May	29-May	69.97	9.15	11	110	17.18	171.81	0.1	154.63	94494	9347 (IC at back)	10		At weld root
A5PW03A	CA	29-May	30-May	70.15	9.23	10	100	15.44	154.44	0.1	139.00	404680	403990 (IC at back)	10		At weld root
A5PW03B	CA	30-May	30-May	70.18	9.19	10.5	105	16.28	162.80	0.1	146.52	238098	236646 (IC at weld root in middle)	10		At weld root / Fractured at an angle
A5PW03C	CA	31-May	31-May	70.02	9.12	9.5	95	14.88	148.77	0.1	133.89	390320	388164 (IC at back in middle)	5&10		
A5PW03D	CA	20-Jun	21-Jun	70.06	9.09	9.5	95	14.92	149.17	0.1	134.26	99589	-	10		At weld root / Difference maybe due to KB?
A5WH01A	CA	04-Jul	05-Jul	70.02	9.11	8	80	12.54	125.42	0.1	112.87	139337	138454 (IC beside wormhole)	10		At wormhole / Propagation at HAZ of AS
A5WH01B	CA	05-Jul	06-Jul	70.02	9.11	7	70	10.97	109.74	0.1	98.76	408156	405687 (IC at weld root from side)	10		At wormhole
A5WH01C	CA	06-Jul	07-Jul	70.01	9.07	6	60	9.45	94.49	0.1	85.04	338064	334632 (IC at weld root)	10		At weld root
A5WH01D	CA	07-Jul	07-Jul	70	9.03	5	50	7.91	79.10	0.1	71.19	2951	2734 (IC at WH)	10		At wormhole / Fatigue life rather low

Appendix E Sample Calculation for Equivalent Stress Range

Excel macro code for calculating stress ranges:

```vba
Sub Macro1()
num = Cells(Rows.Count, 1).End(xlUp).Row

Dim rr, cc As Integer

rr = 3
cc = 1
counter = 0
Do While rr <= num

If Abs(Cells(rr - 1, cc) - Cells(rr, cc)) <= Abs(Cells(rr, cc) - Cells(rr + 1, cc)) Then
    Cells(num + 3, cc) = Abs(Cells(rr - 1, cc) - Cells(rr, cc))
    Cells(num + 4, cc) = (Cells(rr - 1, cc) + Cells(rr, cc)) / 2
    Range(Cells(1 + 2 * counter, cc), Cells(num, cc)).Copy

    Cells(2 * counter + 3, cc + 1).PasteSpecial
    Range(Cells(rr + 1, cc + 1), Cells(rr + 2, cc + 1)).Delete shift:=xlUp
    counter = counter + 1
    cc = cc + 1
    rr = rr + 2
    check = 1

ElseIf Abs(Cells(rr - 1, cc) - Cells(rr, cc)) > Abs(Cells(rr, cc) - Cells(rr + 1, cc)) Then
    check = 0

ElseIf Abs(Cells(rr - 1, cc) - Cells(rr, cc)) = Abs(Cells(rr - 2, cc) - Cells(rr - 1, cc)) Then
    Cells(num + 3, cc) = Abs(Cells(rr, cc) - Cells(rr - 1, cc))
    Cells(num + 4, cc) = (Cells(rr, cc) + Cells(rr - 1, cc)) / 2
    cc = cc + 1
    rr = rr + 2
    counter = counter + 1
    check = 1
End If

If check = 1 Then
    rr = 2 * counter + 3
ElseIf check = 0 Then
    rr = rr + 1
End If

Loop
End Sub
```

Appendix F Semi-Elliptical Fracture Surface for Crack Shape Ratio

A6PW01C
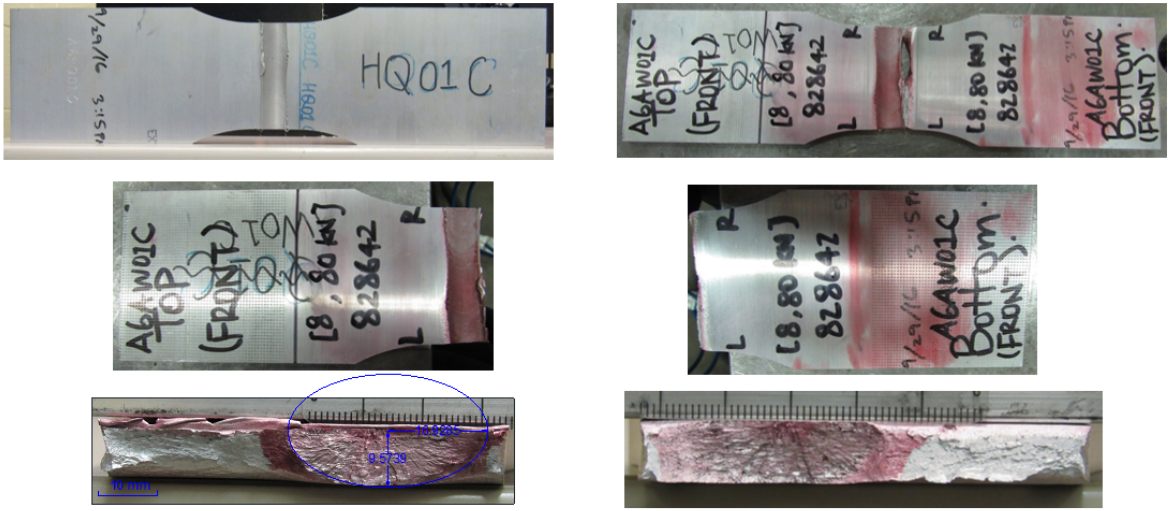
A6PW02C

A6PW02D
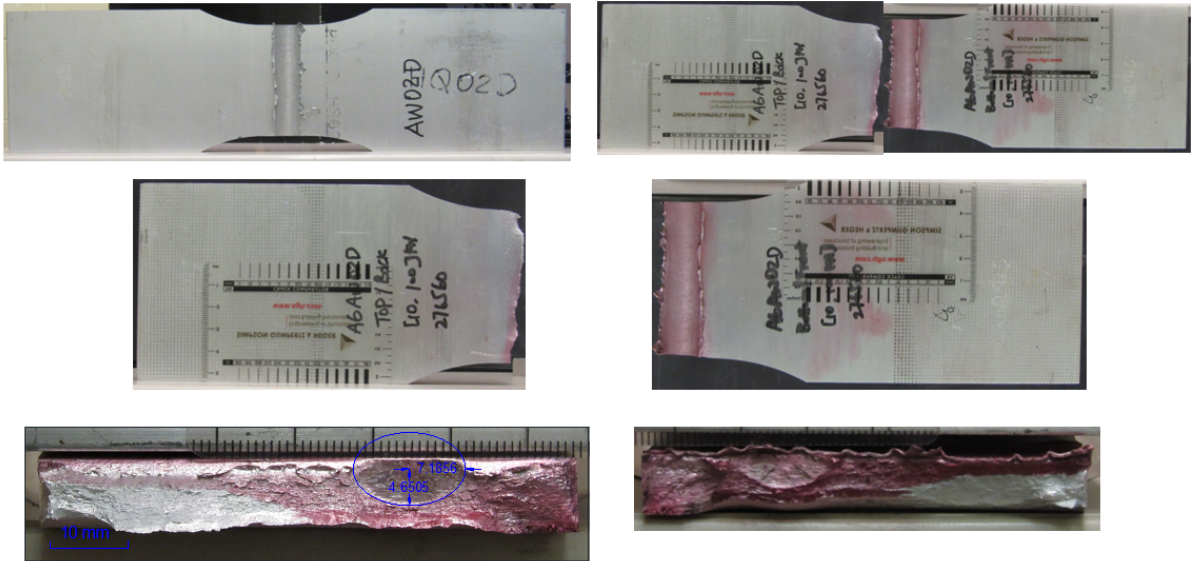
A6PW05A

A6PW05C

A6PO01A

179

A6PO01B

A6PO01C

A6PO03A
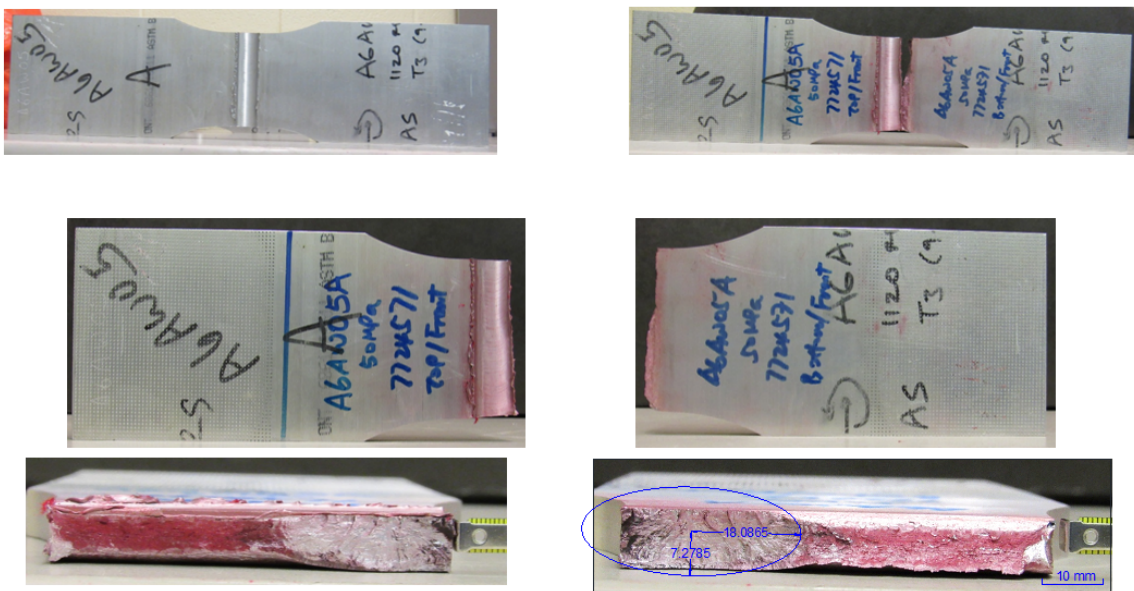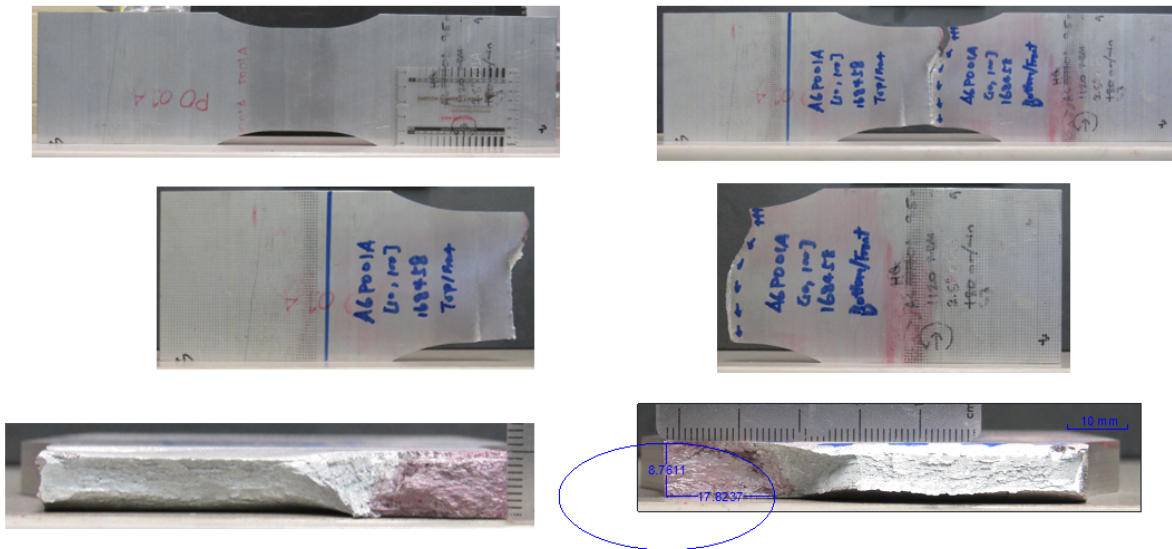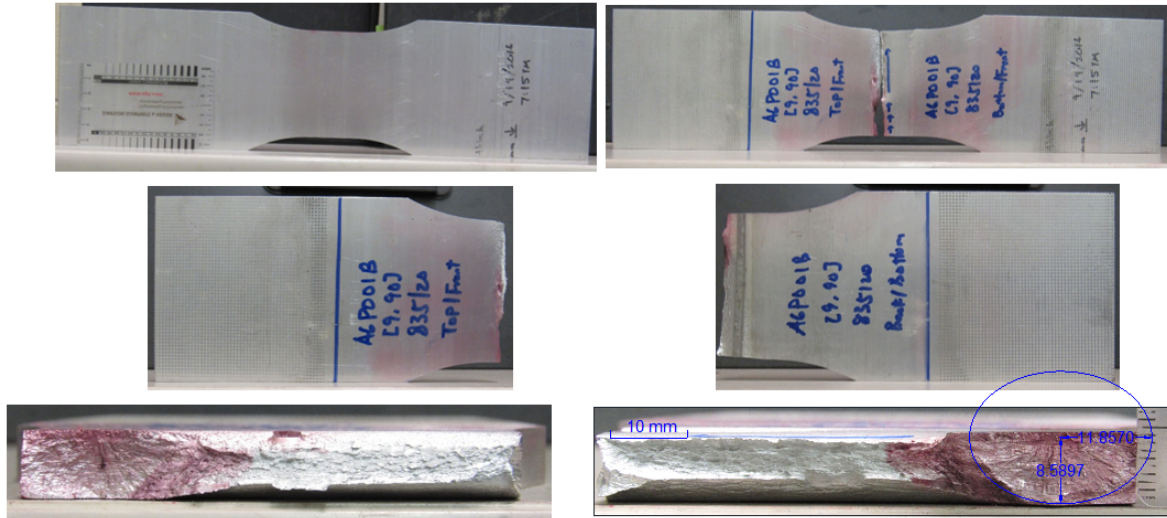
A6PO03B
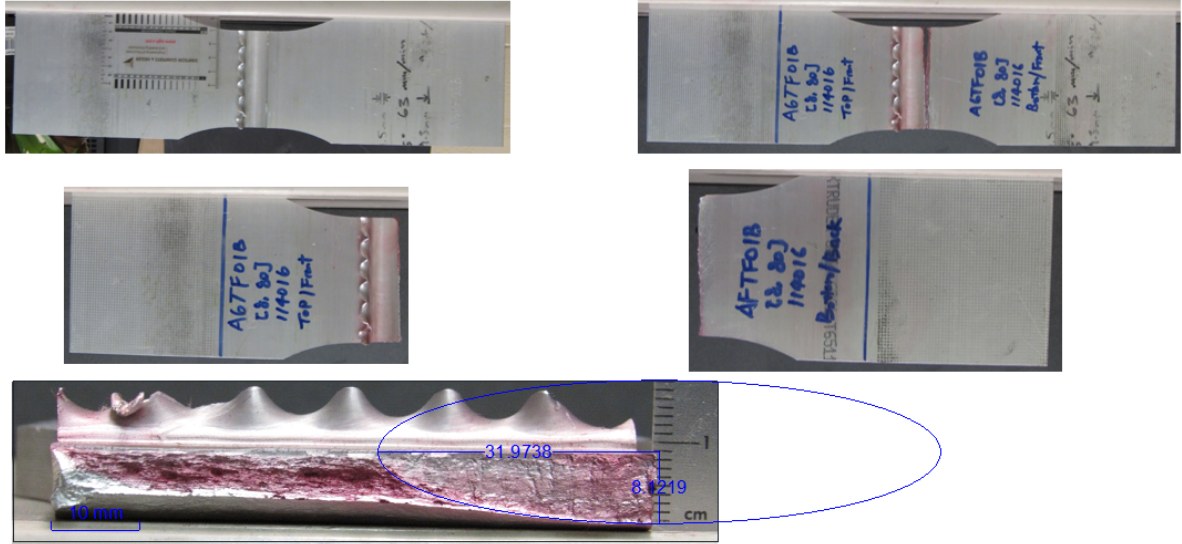
A6TF01B

A6TF01C
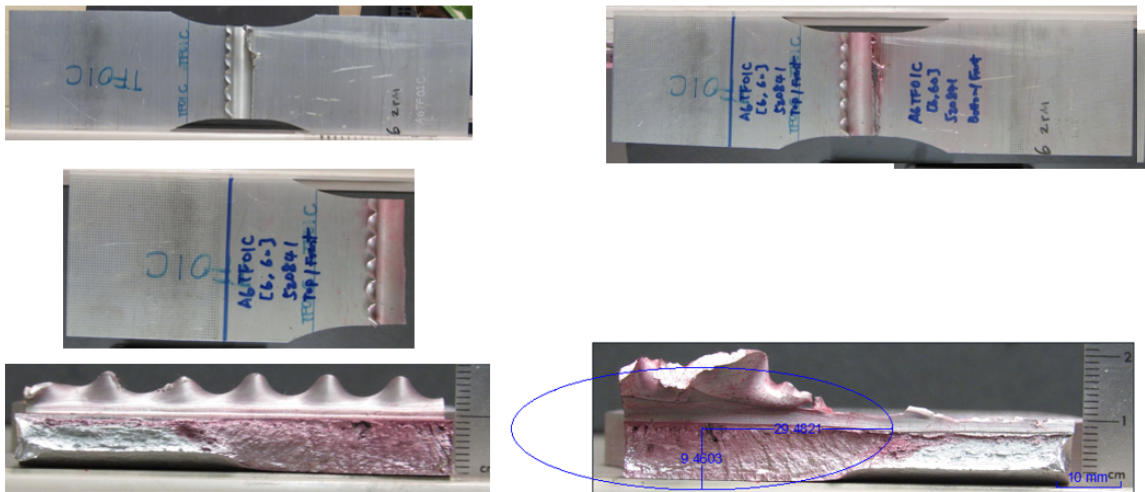
A6TF01D
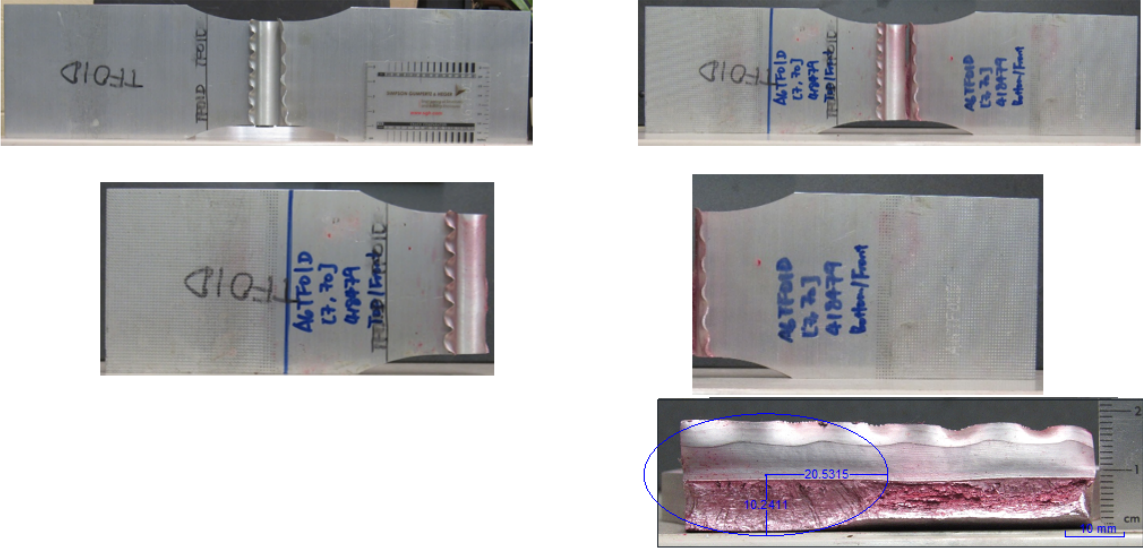
A5PW02D
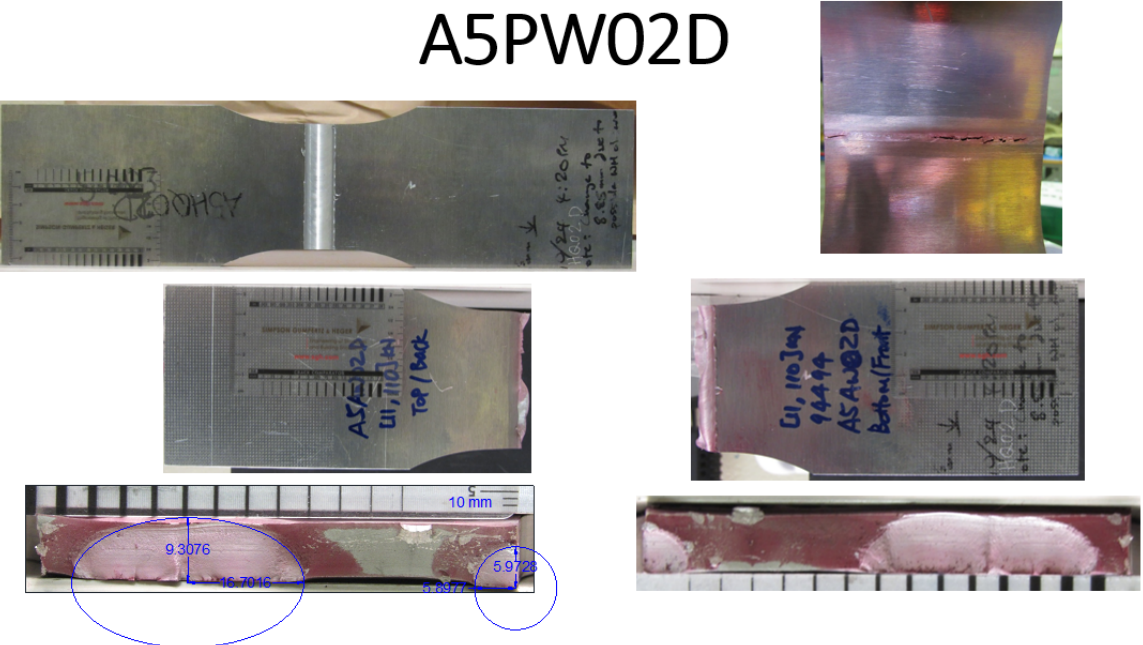
A5PW03A
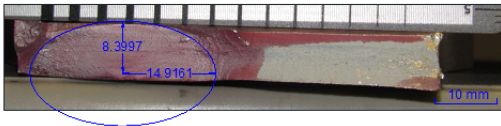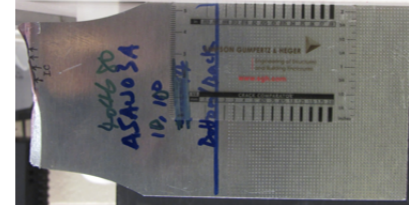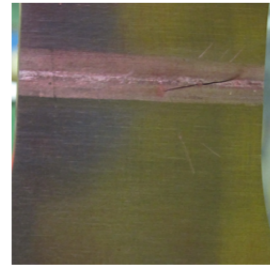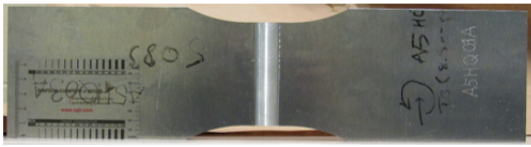
A5PW03B

A5WH01A

A5WH01B

185
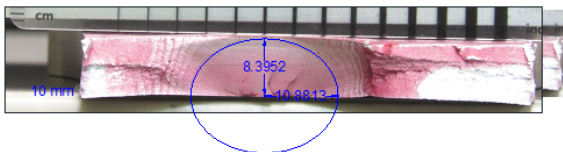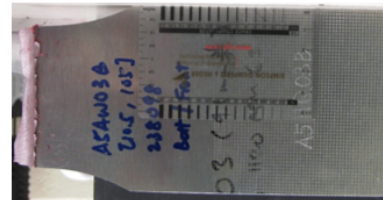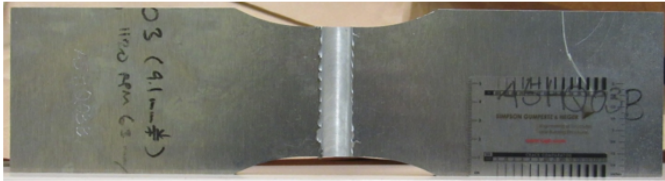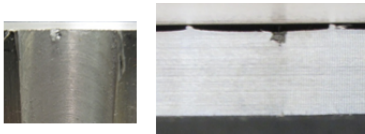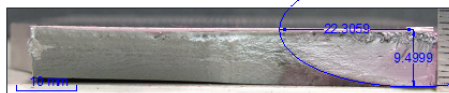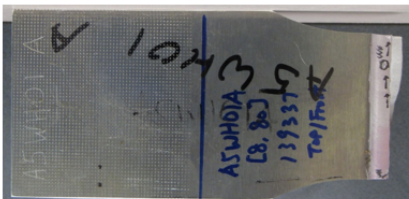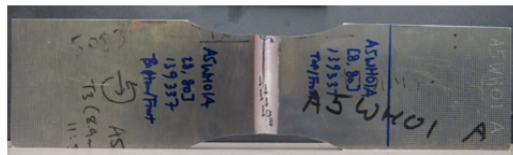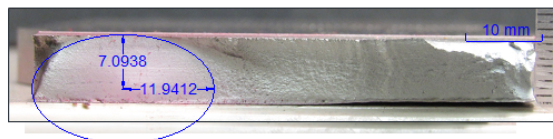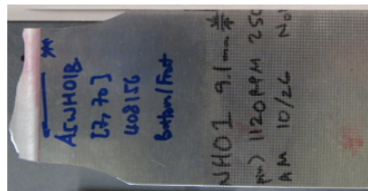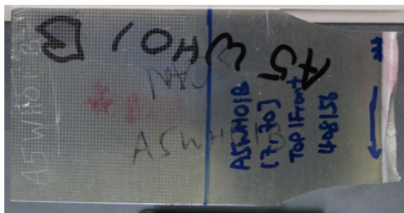
Appendix G Schematic of Specimen Fabrication Drawings

Machined Edge (one side)

Rolling Direction

175

420

Top View

Side View

175

[0.375]
9.53

[0.375]
9.53

420

Front View

Rolling Direction

Machined Edge (one side)

3D View
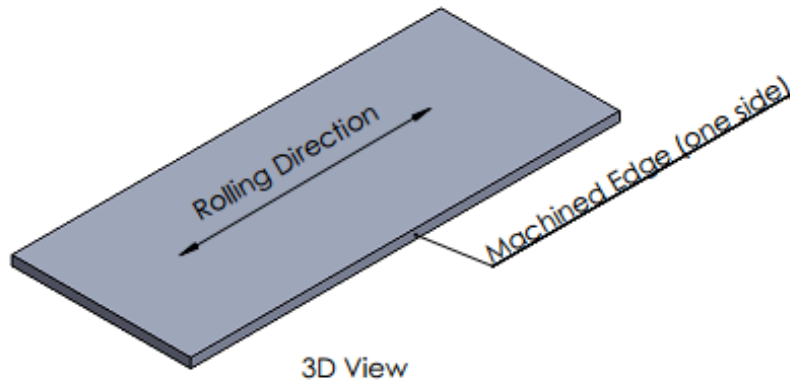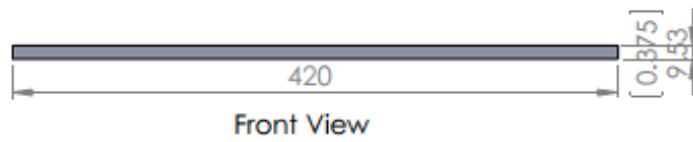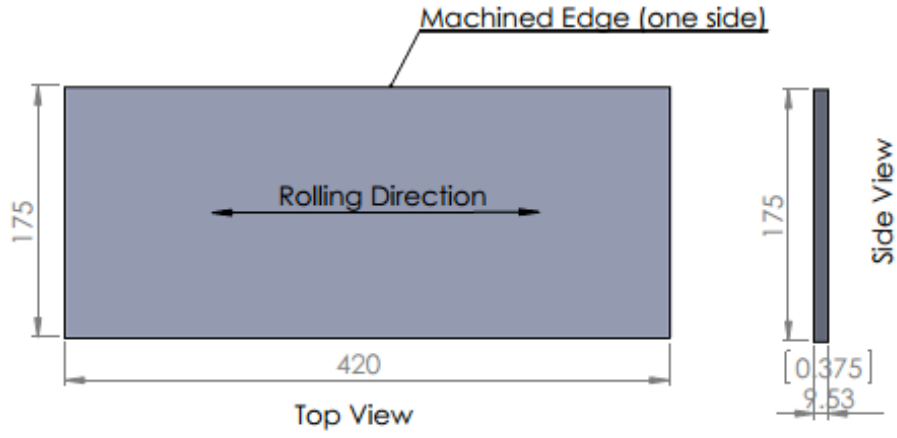
Aluminum 5083 will be provided by the research group.
No need to order material for this job.

UNLESS OTHERWISE SPECIFIED: DIMENSIONS ARE IN MILLIMETERS				DEBUR AND BREAK SHARP EDGES	DO NOT SCALE DRAWING		REVISION
DIMENSIONS IN SQUARE BRACKET ARE IN INCHES					QANTITY:	6 Plates (3 Pairs)	
	NAME	SIGNATURE	DATE		TITLE:		
DRAWN	S. Guo					Friction Stir Weld Plate	
CHK'D							
APPV'D							
MFG							
Q.A					DWG NO.	1	A4
				MATERIAL: Al 5083			
				WEIGHT: 4.2 lbs	SCALE: 1:4		SHEET 1 OF 1

187

ALL DIMENSIONS ARE IN MILLIMETERS

30

5

Rolling Direction

Rolling Direction

	NAME	SIGNATURE	DATE		TITLE:
DRAWN					
CHK'D					
APPV'D					
MFG					
Q.A					DWG NO.

MATERIAL:

Specimencut   A3

WEIGHT: SCALE:1:1   SHEET 1 OF 1

120   40   30   40   120

90

R85   70   R85

90

9.53

9.53

175   175

ALL DIMENSIONS ARE IN MILLIMETERS

	NAME	SIGNATURE	DATE			TITLE:	
DRAWN							
CHK'D							
APPV'D							
MFG							
Q.A				MATERIAL:		DWG NO.	A3
						Specimen Assembly	
				WEIGHT:		SCALE:1:1	SHEET 1 OF 1

UNLESS OTHERWISE SPECIFIED:
DIMENSIONS ARE IN MILLIMETERS
SURFACE FINISH:
TOLERANCES:
  LINEAR:
  ANGULAR:

FINISH:

DEBURR AND
BREAK SHARP
EDGES

DO NOT SCALE DRAWING   REVISION

189

Welding

UNLESS OTHERWISE SPECIFIED: DIMENSIONS ARE IN MILLIMETERS SURFACE FINISH: TOLERANCES: LINEAR: ANGULAR:		FINISH:		DEBURR AND BREAK SHARP EDGES		DO NOT SCALE DRAWING	REVISION
	NAME	SIGNATURE	DATE			TITLE:	
DRAWN							
CHK'D							
APPV'D							
MFG							
Q.A				MATERIAL:		DWG NO.	A4
						lap detail assem	
			WEIGHT:		SCALE:1:5	SHEET 1 OF 1	

190

ALL DIMENSIONS ARE IN MILLIMETERS
UNLESS OTHERWISE STATED

	NAME	SIGNATURE	DATE			
DRAWN						
CHK'D						
APPV'D						
MFG						
Q.A						

UNLESS OTHERWISE SPECIFIED:
DIMENSIONS ARE IN MILLIMETERS
SURFACE FINISH:
TOLERANCES:
 LINEAR:
 ANGULAR:

FINISH:

DEBURR AND
BREAK SHARP
EDGES

DO NOT SCALE DRAWING

REVISION

TITLE:

MATERIAL:

DWG NO.

L Portion Smooth Curve

A3

WEIGHT:

SCALE:1:1

SHEET 1 OF 1